Earthquake Prediction

Edited by
K. Shimazaki
W. Stuart

Springer Basel AG

Earthquake Prediction

Edited by
K. Shimazaki
W. Stuart

Springer Basel AG 1985

Reprinted from Pure and Applied Geophysics
(PAGEOPH), Volume 122 (1984/85), No. 6

Editors addresses:

Kunihiko Shimazaki
Earthquake Research Institute
The University of Tokyo
Bunkyo-ku
Tokyo, Japan (113)

William D. Stuart
U.S. Geological Survey
525 S. Wilson Ave.
Pasadena, CA 91106
USA

CIP-Kurztitelaufnahme der Deutschen Bibliothek

Earthquake prediction / ed. by K. Shimazaki;
W. Stuart.

Aus: Pure and applied geophysics; Vol. 122.
1984/85
ISBN 978-3-7643-1742-3 ISBN 978-3-0348-6245-5 (eBook)
DOI 10.1007/978-3-0348-6245-5

NE: Shimazaki, K. [Hrsg.]

Ursprünglich erschienen bei Birkhäuser Verlag Basel 1985
Softcover reprint of the hardcover 1st edition 1985

PURE AND APPLIED GEOPHYSICS
Vol. 122, No. 6, 1984/85

Contents

PAGEOPH, Vol. 122, 6 (1984/85)

0033-4553/85/060763-01$1.50 + 0.20/0

Introduction

This issue of Pure and Applied Geophysics contains papers presented at the Earthquake Prediction session of the 22nd General Assembly of the International Association of Seismology and Physics of the Earth's Interior. The meeting was held in August, 1983, in conjunction with the XVIII General Assembly of the International Union of Geodesy and Geophysics, at Hamburg, Federal Republic of Germany, and was convened by J. R. Rice and K. Shimazaki. Some papers given at the meeting are not included here, and several papers not given at the meeting but germane to the meeting themes have been added.

The papers given at the meeting and in this issue reflect the wide variety of current international research on earthquake prediction. The contributions also illustrate the recent rapid progress in earthquake prediction, which has been largely due to the increased number and accuracy of field measurements, careful attention to errors in data, and sound application of theoretical principles. Papers dealing with laboratory studies, normally prominent in earthquake prediction symposia, were under-represented at the meeting. In this issue the two main themes are (1) reports and interpretations of new seismological and non-seismological field observations, and (2) theoretical and statistical studies applied to old and new data. Most papers describe possible precursors, and a few papers discuss specific procedures for attempting a prediction.

K. SHIMAZAKI
W. STUART
Guest Editors

PAGEOPH, Vol. 122 (1984/85)

0033-4553/85/060765-16$1.50 + 0.20/0

Temporal Variation of Crustal Deformation During the Days Preceding a Thrust-type Great Earthquake – The 1944 Tonankai Earthquake of Magnitude 8.1, Japan

By KIYOO MOGI[1])

Abstract – The temporal variation in precursory ground tilt prior to the 1944 Tonankai (Japan) earthquake, which is a great thrust-type earthquake along the Nankai Trough, is discussed using the analysis of data from repeated surveys along short-distance leveling routes. SATO (1970) pointed out that an anomalous tilt occurred one day before the earthquake at Kakegawa near the northern end of the focal region of the earthquake. From the analysis of additional leveling data, Sato's result is re-examined and the temporal change in the ground tilt is deduced for the period of about ten days beginning six days before the earthquake. A remarkable precursory tilt started two or three days before the earthquake. The direction of the precursory tilt was up towards the south (uplift on the southern Nankai Trough side), but the coseismic tilt was up towards the southeast, perpendicular to the strike of the main thrust fault of the Tonankai earthquake. The postseismic tilt was probably opposite of the coseismic tilt. The preseismic tilt is attributed to precursory slip on part of the main fault. If similar precursory deformation occurs before a future earthquake expected to occur in the adjacent Tokai region, the deformation may help predict the time of the Tokai earthquake.

Key words: precursory ground tilt, temporal variation of crustal deformation, the 1944 Tonankai earthquake, leveling survey, earthquake prediction.

1. Introduction

Western Japan, along the Nankai Trough, is a typical subduction zone where great thrust earthquakes, such as the 1944 Tonankai earthquake, have occurred with a recurrence time of 100–150 years. Figure 1 shows the rupture zones of these great earthquakes during the past three hundred years. In this region, both seismicity and crustal movement data have been measured. The crustal movement in this region has been discussed by a number of investigators (MOGI, 1970; SATO, 1970, 1977; INOUCHI and SATO, 1975; FITCH and SCHOLZ, 1971; ANDO, 1975). On the basis of triangulation surveys, MOGI (1970) pointed out that the Tokai region is a highly compressed area and so is a potential region for a future great shallow earthquake. As shown in the bottom figure in Fig. 1, this region is also an unruptured region in recent years, namely, a seismic gap of the first kind.

[1]) Earthquake Research Institute, University of Tokyo, Tokyo, Japan.

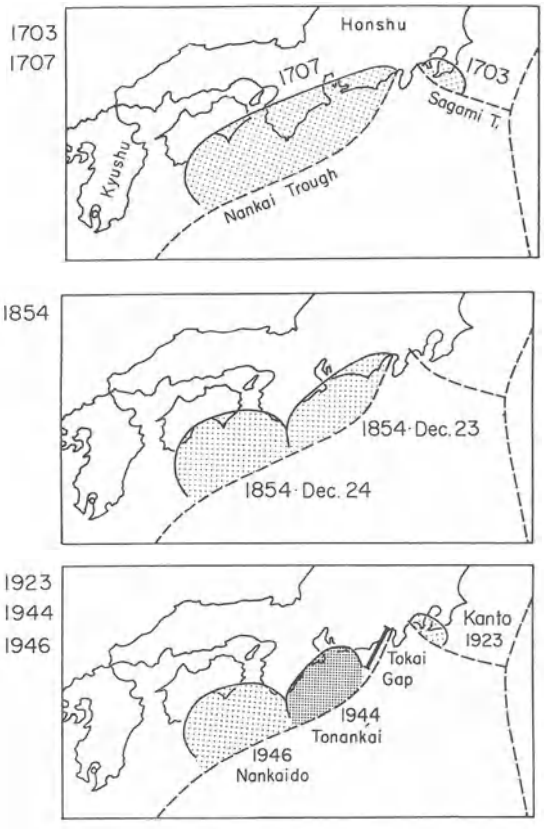

Figure 1

Rupture zones of great shallow earthquakes along the Nankai Trough and the Sagami Trough (northern boundary of the Philippine sea plate) during the last three hundred years. The Tokai region along the Suruga Trough is a seismic gap of the first kind, because the rupture of the 1944 Tonankai earthquake did not extend to the Suruga Trough (bottom figure).

The Coordinating Committee for Earthquake Prediction designated this region as one of the areas that should receive special observation. Subsequently, by considering detailed historical data on the past great earthquakes of 1854 and 1707, ISHIBASHI (1976, 1981) proposed a model of a future rupture zone. The model consists of underthrusting along the Suruga Trough, which is a northeastern extension of the Nankai Trough. For the purpose of predicting the earthquake, a very dense network of various instruments, including seismometers, strain meters and tilt meters, has been set up in the Tokai region (e.g. MOGI, 1981). These data are telemetered to the Japan Meteorological Agency (JMA) in Tokyo, which is staffed 24 hours a day and 7 days a week. When anomalous behavior is observed in these data, the Earthquake Assessment Committee (Chairman, Professor T. Asada) evaluates the data and conveys its finding to the director general of JMA, who reports to the prime minister. On 15 June 1978, the

Large-scale Earthquake Counter-measures Act was promulgated. This law will be applied to the Tokai region.

It may be possible to accurately predict the time of the Tokai earthquake by the observation of short-term precursors. Therefore, it is very important to know whether or not appreciable short-term precursory phenomena can be observed. Unfortunately, there are no precursory data available for earlier earthquakes rupturing the Tokai gap. But the source region of the 1944 Tonankai earthquake is adjacent to the expected rupture zone in the Tokai region, and so the precursory phenomena may be similar.

SATO (1970) was the first to point out a precursory ground tilt immediately prior to the Tonankai earthquake on the basis of leveling data between adjacent benchmarks (5259 and 5260, to be discussed below) for which surveys were carried out repeatedly prior to the earthquake. This result is important, because it suggests the possibility of short-term precursory crustal movement before a future Tokai earthquake. However, since the leveling data analyzed by Sato were very limited in space and time, there is some question about its reliability. Also, the temporal development of the precursory crustal movement, which is a key for predicting the time of an earthquake occurrence, could not be evaluated. THATCHER (1981) reported a deformation curve before and after the Tonankai earthquake on the basis of the leveling data between the same adjacent benchmarks as Sato used, but he did not consider the difference in direction of the leveling route. Also he used the data for the postseismic period differently than in the present study, as mentioned later. He concluded that the data were fragmentary and their precise relation to the Tonankai earthquake was uncertain. Recently the author has found additional leveling data which may help resolve these problems. This paper discusses these additional leveling data and the temporal variation of the tilt prior to the Tonankai earthquake.

2. Leveling surveys near the Tonankai earthquake and previous research

The Tonankai earthquake occurred at 1.35 p.m. on 7 December 1944. Precisely at that time the Army Land Survey (the present Geographical Survey Institute) was carrying out a leveling survey in the vicinity of Kakegawa City in Shizuoka Prefecture, which is located at the northeastern end of the focal region of the earthquake, as shown in Fig. 2. These measurements were being carried out at this time because Professor A. Imamura, then at the University of Tokyo, assumed that the next great earthquake in this area would occur in the near future because earthquakes along the Nankai Trough had occurred at quite regular intervals of about 100–150 years, and ninety years had passed since the preceding (Ansei) Tokai earthquake in 1854 (IMAMURA, 1945).

In carrying out these measurements, Imamura constructed a new leveling route between Kakegawa and Omaezaki (shown in Fig. 4), which yielded much valuable information. Measurement was completed just prior to the earthquake and repeated

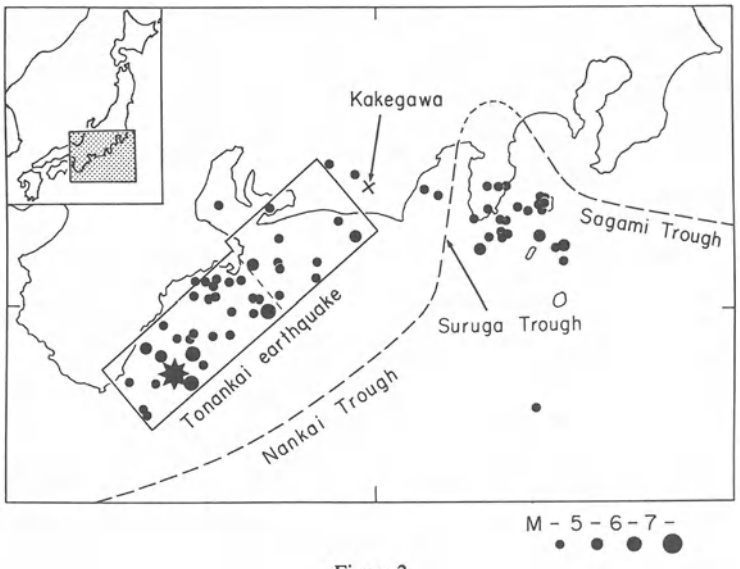

Figure 2

Rectangular Fault plane of the 1944 Tonankai earthquake deduced from leveling data (INOUCHI and SATO, 1975) and the location of aftershocks of the Tonankai earthquake (SEKIYA and TOKUNAGA, 1974).

immediately afterwards, revealing the crustal movements in this region at the time of the Tonankai earthquake.

Figure 2 shows the location of aftershocks of the Tonankai earthquake (SEKIYA and TOKUNAGA, 1974) and the fault plane deduced from the crustal deformation (INOUCHI and SATO, 1975). Solid circles in this figure show earthquakes which occurred immediately after the main shock (star). Aftershocks generally occurred in the focal region of the Tonankai earthquake. However, a number of earthquakes also occurred in the Izu region east of the Tonankai earthquake. This seismic activation in the eastern region may be attributed to the increase of stress in this region due to the accelerated northwest plate motion of the Philippine Sea Plate caused by the Tonankai earthquake, even though the Suruga Trough region remained unslipped. Figure 3 shows the differences of elevations measured before and after the earthquake obtained from the leveling data (INOUCHI and SATO, 1975). These two figures reveal that the rupture zone did not reach Omaezaki, and this is one important piece of evidence for assuming a Tokai earthquake will occur along the Suruga Trough.

Figure 4 shows the leveling routes in this region. Numerals show some of the benchmarks along the route in the north–northwest direction from Kakegawa. IMAMURA (1945) examined these measurements at the time of the earthquake and reported that from the time of the first measurement in 1903 until immediately prior to the 1944 Tonankai earthquake, the southern side – i.e. the Nankai Trough side – of this region had continually subsided. During the earthquake, however, a pronounced uplift of the southern side occurred. SATO (1970) has further scrutinized these measurements

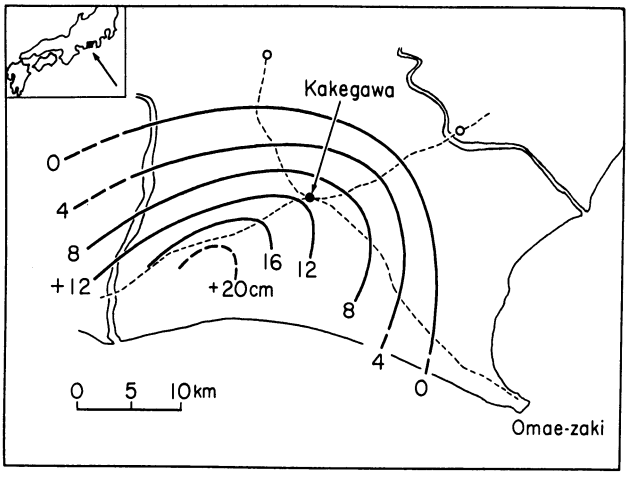

Figure 3
Vertical displacements in the Kakegawa–Omaezaki region before and after the 1944 Tonankai earthquake obtained from the leveling data (INOUCHI and SATO, 1975). Broken lines show leveling routes.

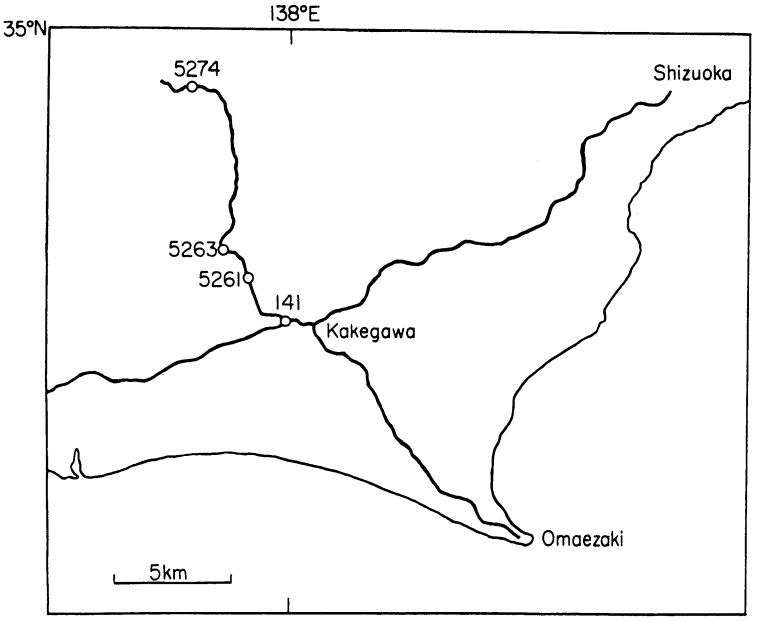

Figure 4
Leveling routes in the Kakegawa–Omaezaki region of the Tokai district.

and reported similar results. Figure 5 shows Sato's version of the movements along the leveling route stretching from Kakegawa to Mikura before (March 1934–December 1944) and immediately after the earthquake. Movements were small in the northern part of the route, but as one moves southwards towards Kakegawa, both long-term

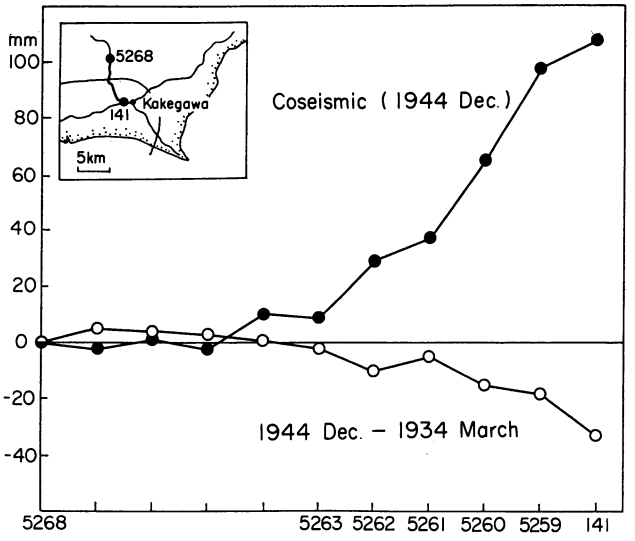

Figure 5
Vertical displacements along the leveling route from BM141 to BM5268. Open circles: March 1934–December 1944 (immediately before the earthquake); solid circles: immediately before and after the earthquake.

subsidence prior to the earthquake and the sudden uplift at the time of the earthquake increase. This crustal movement may be understood as a rebound due to thrust type faulting.

At that time, the leveling survey was carried out in the following manner. In Fig. 6, the leveling route is shown running from Kakegawa in a north–northwesterly direction and passing through Mikura. Benchmarks 5259, 5260, 5261 and 5262 are located at 2 km intervals. Check points were established at locations (represented by solid circles) which further trisected each interval. These are temporary points set up only during the leveling procedure. Each of these sections is further divided into eight sectors, which are measured in turn. Then on the following day or several days later measurements are carried out from the opposite direction in order to check that the measured value of each sector (horizontal distance of about 700 m) lies within a certain range compared to the previous measurement. This means the same sector is measured twice (or more) within several days. In order to make the following discussion easier to understand, I have numbered each sector from benchmarks 5259 to 5262 with numbers from 1 to 9, as shown in Fig. 6.

By chance the sectors between benchmarks 5259 and 5260 were being measured the day before the earthquake and on the day of the earthquake. SATO (1970) noticed that in sectors 2 and 3 there was a difference of 4.3 mm and 4.8 mm per 700 m, and he pointed out that this probably indicates the precursory crustal movement of the Tonankai earthquake. In order to ascertain the significance of these changes, SATO (1977) then took the differences between the two measurements on the outward and

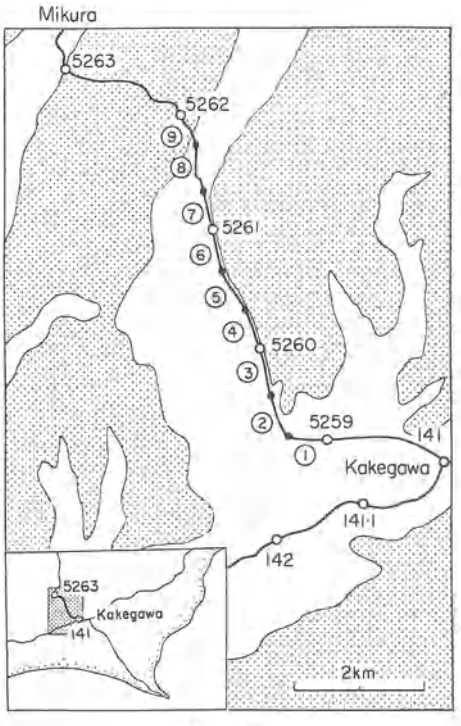

Figure 6

Leveling route along which a survey was carried out immediately before and after the 1944 Tonankai earthquake. Open circles are benchmarks; solid circles are check points (temporary stations). The route between BM5259 and BM5262 is divided into 9 sectors. The length of each sector is about 700 m. Dotted regions are hilly or mountainous areas.

return trip for other sectors that are not thought to have been greatly affected by the earthquake, and studied the measurement errors. He came to the conclusion that such changes of more than 4 mm are extremely rare, and that they are probably significant. However, there was quite a large range of errors in the set of all the measurements assembled by Sato. In some cases there were differences of 2–4 mm per 700 m accounting for as much as 20% of the entire area, and further investigation seemed impossible. Some people were of the opinion that changes greater than 4 mm may have contained errors caused by a strong wind blowing at the time just before the earthquake.

3. Temporal variation of crustal movement prior to the Tonankai earthquake

KOSHIYAMA (1976), who was actually involved in the survey, described the detailed situation at the time of the measurement, particularly the anomalous ground disturbance just before (probably one or two hours) the earthquake. According to his description, a strong wind was blowing, so the author further examined the weather conditions. Figure

7 shows the velocity of the wind and the atmospheric temperature at the Hamamatsu weather station which is located near Kakegawa. This figure does not show any anomalous weather condition during the period before and after the Tonankai earthquake. In particular, the velocity of the wind was not very high immediately prior to the earthquake. So it is not reasonable to attribute the systematic anomalous change in leveling data described below to a change in weather conditions.

The observed values for some of the sectors in Fig. 6 before and after the earthquake are appended at the end of Koshiyama's description. This traverse lies on a straight line running virtually north–northwest from 2 to 9, along which the coseismic tilt is nearly uniform as shown in Fig. 5. Since the times of observations differ, these values may be combined to estimate the temporal progress of the crustal movement prior to a great earthquake (MOGI, 1982).

Furthermore, a check through the original measurement register, which is now preserved at the Geographical Survey Institute, reveals that the measurements shown in Fig. 8 were carried out repeatedly over all nine of the sectors. In some sectors measurements were repeated as many as three times from 1 December until immediately before the earthquake.

Figure 9 shows the vertical displacement curve for sectors 2 and 3. Measurements were carried out a total of four times for sector 3 and five times for sector 2 immediately

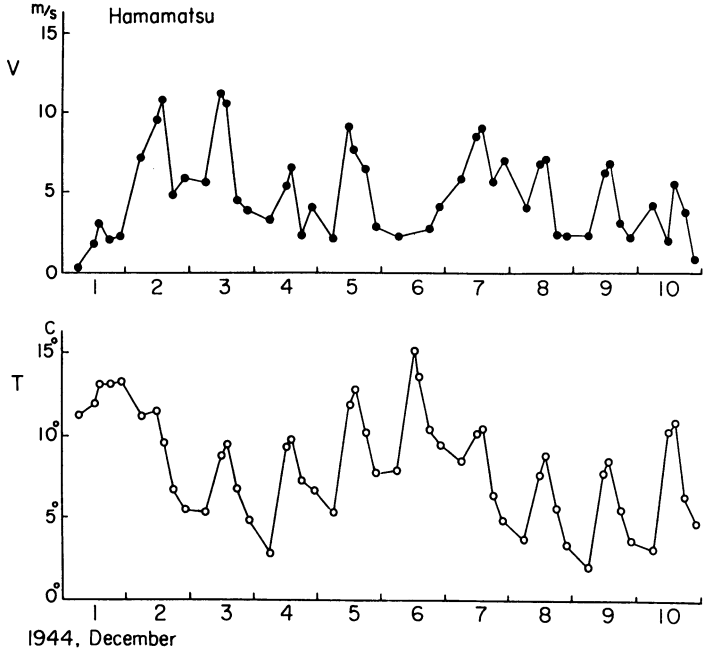

Figure 7
Temporal variation of the wind velocity (upper figure) and the atmospheric temperature (lower figure) at the Hamamatsu weather station during the period before and after the Tonankai earthquake of 7 December, 1944.

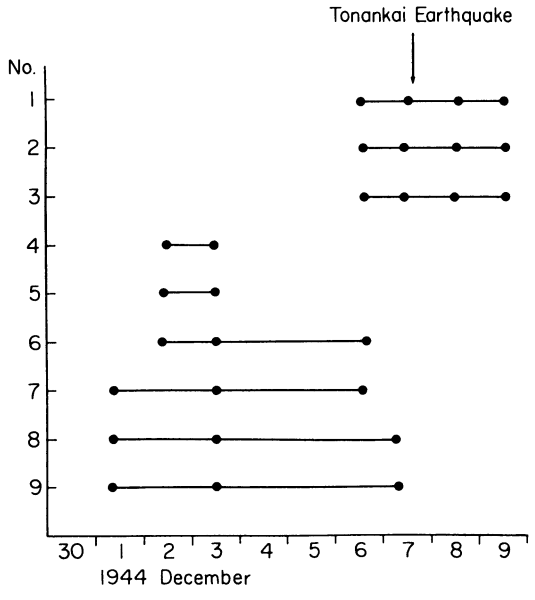

Figure 8
Times of the repeated leveling surveys of each sector. Numerals on the vertical axis are the numbers of the sectors (No. 1–No. 9).

before and after the earthquake. The vertical axis is the amount of uplift on the southern side over a horizontal distance of about 700 m. A glance at this figure shows that before the earthquake a conspicuous uplift began on the southeastern side, then there was a sudden large uplift at the time of the earthquake, and immediately after the earthquake it began to subside. Noteworthy here is the fact that the results for the completely independent sectors 2 and 3 match extremely well. These results strongly suggest that measurement in such flat terrain is considerably accurate. It is deduced from the lower figure of Fig. 10 that the error of the measurement is about plus or minus 2 mm. Consequently the changes prior to an earthquake can be considered real.

The result for sector 1 is not included in Fig. 9. As mentioned later, no precursory movements were seen for this sector. This may be attributed to the difference of the azimuth of sector 1 from that of sectors 2 and 3. This issue is discussed later.

Figure 10 shows the discrepancies when each sector from benchmarks 5259 to 5265 was remeasured, with the horizontal axis showing the benchmark numbers. Solid circles in the upper figure show the situation immediately prior to the earthquake, while the lower figure shows the preceding period. The vertical axis shows the discrepancy between the measurements on these two occasions, assigning a positive value to cases in which the value on the Kakegawa side (southeast side) is larger in the later measurement. This corresponds to uplift on the southeastern side.

The upper figure of Fig. 10 shows the situation immediately prior to the earthquake (solid circles) and spanning the time of the earthquake (double circles). The fact that all of the values are positive and are quite large indicates that prior to the earthquake the

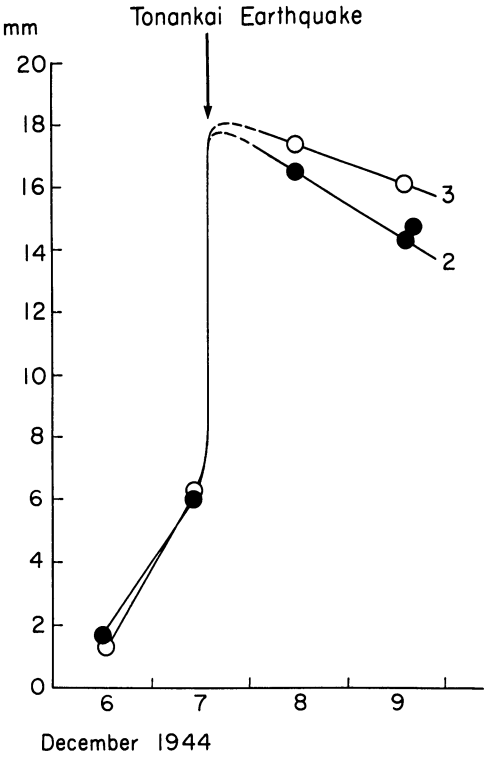

Figure 9
Relative vertical displacement curves for sectors 2 and 3 immediately before and after the 1944 Tonankai earthquake. The vertical axis shows the amount of uplift on the southeastern side.

southern side was uplifted, and that this uplift was appreciable in comparison with the uplift at the time of the earthquake. On the other hand, a look at the period preceding this, shown in the lower figure, reveals that the values are scattered around 0 and that there is no systematic trend. Moreover, the value itself nearly always lies within a range of plus or minus 1.5 mm, except between benchmarks 5262 and 5263. The leveling route between benchmarks 5262 and 5263 curves markedly through an uneven mountain pass increasing the possibilities of errors. However, the remaining measurements in flat areas are thought to be quite accurate.

Summing up the above results and assuming a uniform tilt from sectors 2 to 8, as suggested by Fig. 5, it is believed that it is possible to estimate within a day the temporal changes in the tilt of this region around the time of the Tonankai earthquake. Figure 11 shows a narrow range of curves which includes the measured values from sectors 2 to 8 within the period from 1 December 1944 up until 9 December two days after the earthquake. The shaded band more or less represents the tilt curve for this region. The following is a synopsis of these results.

(1) As can also be seen in Figs. 10 and 11, there was no recognized uplift tendency until about two days before the earthquake.

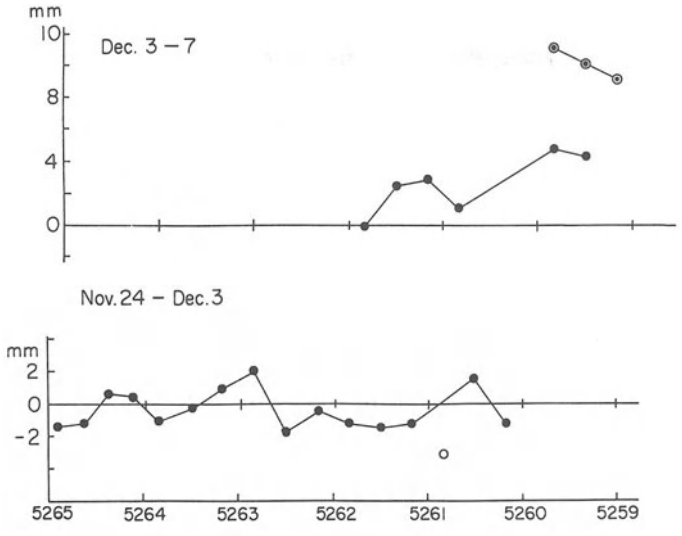

Figure 10

Discrepancies when each sector from BM5259 to BM5265 was remeasured. The horizontal axis shows the benchmark numbers, and the vertical axis shows the discrepancies between the measurements. Positive values correspond to uplift on the southeastern side. Double circles show changes immediately before and after the Tonankai earthquake.

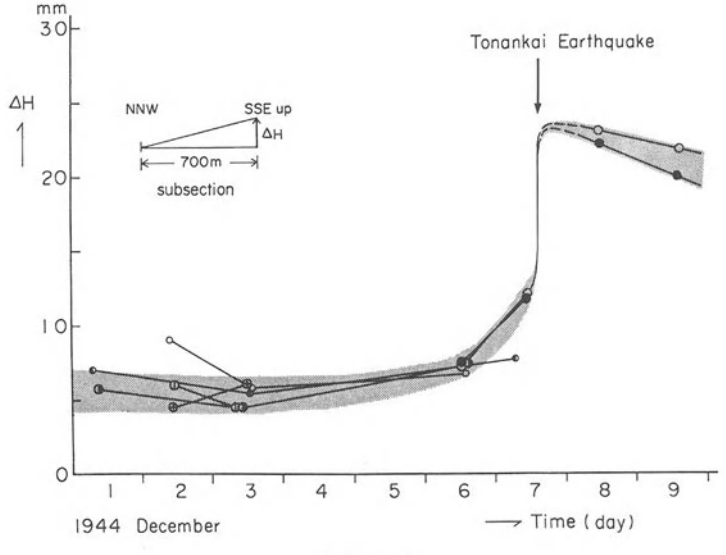

Figure 11

Temporal variation of crustal deformation near Kakegawa before and after the Tonankai earthquake deduced from the repeated surveys of short-distance leveling routes. This curve was obtained by the combination of deformation curves of different sectors, which are shown by different symbols. Positive values on the vertical axis correspond to uplift on the southeastern side of the sectors.

(2) Conspicuous anomalous crustal deformation (tilt as the result of uplift on the southern trough side) began two or three days before the earthquake and gradually accelerated, and, according to Koshiyama's description, this deformation became more rapid one or two hours before the earthquake.

(3) The magnitude of the precursory crustal movement was smaller than the movement during the earthquake (coseismic change), but was striking enough to be clearly noticed.

Figure 11 shows the deformation curve that corresponds to the apparent tilt along the north–northwest route, but the true magnitude of the ground tilt and the direction can be found by comparing the disturbance in sector 1 which runs in an east–west direction, with the disturbances in sectors 2 and 3 which run north–northwest. The fact that movements in sector 1 at the time of the earthquake and immediately after the earthquake were about the same size as in sectors 2 and 3, but almost no precursory movements were seen in sector 1, means that the direction of the precursory ground tilt was up toward the south, but the tilt at the time of the earthquake was up towards the southeast. On 9 December, the surveys of sectors 1 and 2 were carried out twice. THATCHER (1981) used the data of the second survey in which the postseismic change in sector 1 is quite different from those of sectors 2 and 3. In this paper, the data of the first survey are used, because the postseismic changes in all sectors correlates well with the coseismic changes. Figure 12 shows the vectors of tilt at Kakegawa for precursory, coseismic and postseismic periods. The directions of the tilt vectors are completely

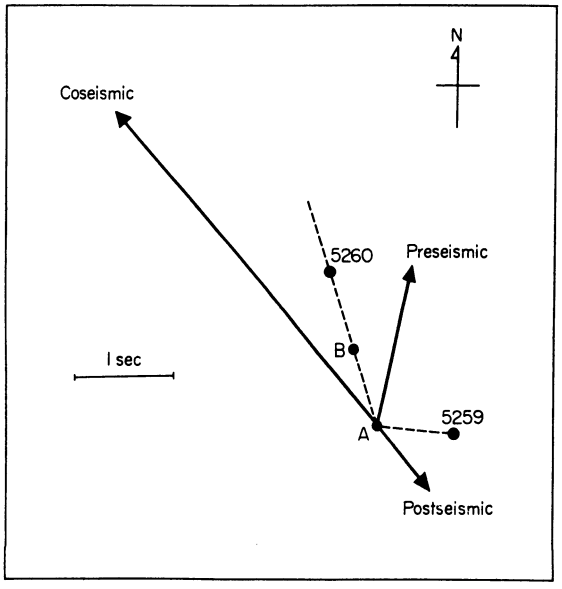

Figure 12

Tilt vectors at Kakegawa for precursory, coseismic and postseismic periods. These vectors were calculated from the vertical displacements along the leveling route from BM5259 to BM5260 shown by a broken line.

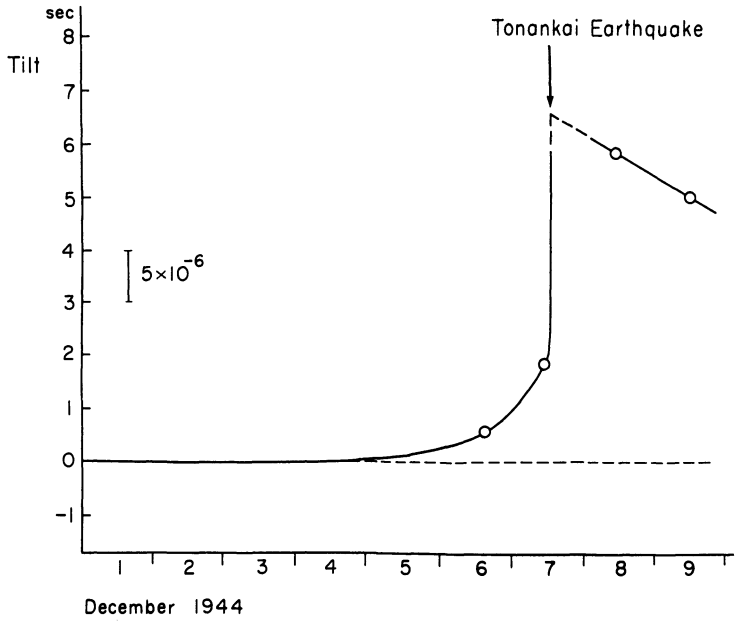

Figure 13
Temporal variation of the ground tilt near Kakegawa deduced from the vertical displacements along the leveling route from BM5259 to BM5262.

reversed between the coseismic and postseismic periods, and they seem to be perpendicular to the strike of the fault of the Tonankai earthquake. Also it is noted that the direction of the vectors are different between the precursory and coseismic times. One possible explanation is that a precursory slip occurred southwest of this leveling route and then the slip extended northeastward at the time of the main rupture. Figure 13 shows the temporal changes in the amount of ground tilt.

If precursory changes in tilt or strain exist on this magnitude, it will be possible to fully detect and track them through the current observation network in the Tokai region. As mentioned above, this result for the Tonankai earthquake is regarded as being probably the most powerful lead in estimating when the Tokai earthquake will occur.

4. Precursory crustal movement prior to the 1946 Nankaido earthquake

On 21 December 1946, the Nankaido earthquake of M 8.1 occurred along the Nankai Trough in a western region adjacent to the focal region of the Tonankai earthquake, as shown in Fig. 1. SATO (1977) pointed out that the difference in tidal level between Tosashimizu in southwestern Shikoku and Hosojima on the east coast of Kyushu, seemed to change appreciably prior to the Nankaido earthquake, as shown in Fig. 14. This result is obtained by correcting the data for the tidal current effect.

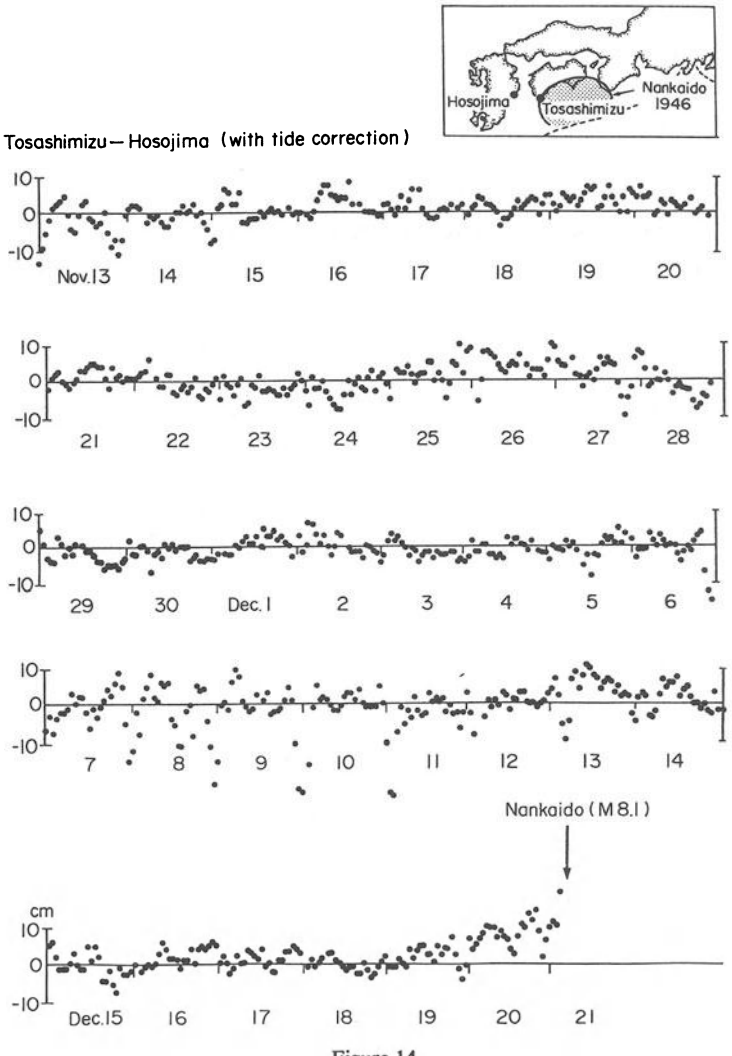

Figure 14

Changes in the relative mean sea level at the Tosashimizu tide station prior to the Nankaido earthquake of 21, December 1946. The vertical axis shows the difference between the mean sea levels at Tosashimizu in southwestern Shikoku and Hosojima on the east coast of Kyushu. Positive values correspond to uplift at Tosashimizu.

Although this tide level data scattered markedly, it is worthwhile to note that the difference seems to increase starting a day and half prior to the Nankaido earthquake. Since Tosashimizu is located on the western border of the focal region of the Nankaido earthquake, this result suggests that the measurable precursory uplift prior to the Nankaido earthquake probably began one or two days prior to the earthquake. Thus an appreciable precursory crustal deformation began one or two days prior to both of the recent great earthquakes along the Nankai Trough.

5. Conclusion

1. Since the leveling measurements for independent sectors immediately before and after the Tonankai earthquake show similar changes, the precursory tilt prior to the earthquake pointed out by SATO (1970) can be considered real.

2. By the use of additional leveling data, the temporal variation of crustal deformation during the days before and after the earthquake is inferred. This crustal deformation curve is obtained by the combination of deformation curves of different sectors of the leveling route near Kakegawa.

3. There was no recognized systematic change in the curve three or four days before the earthquake.

4. Appreciable anomalous crustal deformation (tilt as the result of uplift on the southern Nankai Trough side) began two or three days before the earthquake, and gradually accelerated.

5. The direction of the precursory tilt was up toward the south. However the coseismic tilt was up toward the southeast, and the postseismic tilt was probably opposite to the coseismic tilt.

6. This result on the temporal variation of the crustal deformation prior to the Tonankai earthquake may be helpful for estimating the time of the Tokai earthquake from future measurements of crustal deformation.

Acknowledgments

I thank N. Fujita, H. Haruyama, M. Matsushima and A. Yoshimura of the Geographical Survey Institute for use of the original leveling data and helpful discussions about them. T. Koshiyama kindly described his valuable experience while leveling at the time of the Tonankai earthquake. I also thank Jim Mori for reading the manuscript and helpful comments.

REFERENCES

ANDO, M. (1975), *Possibility of a Major Earthquake in the Tokai District, Japan and its Pre-estimated Seismotectonic Effects*, Tectonophysics *25*, 69–85.

FITCH, T., and SCHOLZ, C. H. (1971), *Mechanism of Underthrusting in Southwest Japan: A Model of Convergent Plate Interactions*, J. Geophys. Res. *76*, 7260–7292.

IMAMURA, A. (1945), *Land Deformations Associated with the Recent Tōkaido Earthquake*, Proc. Japan Academy *21*, 193–196.

INOUCHI, N., and SATO, H. (1975), *Vertical Crustal Deformation Accompanied with the Tonankai Earthquake of 1944*, Bull. Geogr. Surv. Inst., Tokyo *21*, 10–18.

ISHIBASHI, K. (1976), *Re-examination of a Great Earthquake Expected in the Tokai District: Possibility of the 'Suruga Bay Earthquake'*, Abstracts, Seismol. Soc. Japan, 1976 No. 2, 30–34 (in Japanese).

ISHIBASHI, K., *Specification of a Soon-to-Occur Seismic Faulting in the Tokai District, Central Japan, Based upon Seismotectonics*, in *Earthquake Prediction* (eds. D. W. Simpson and P. G. Richard) (Maurice Ewing Series, IV 1981), pp. 297–332.

KOSHIYAMA, T. (1976), *Kokudo Chiriin Kōhō 100*, Suppl., 7–8 (in Japanese).

MOGI, K. (1970), *Recent Horizontal Deformation of the Earth's Crust and Tectonic Activity in Japan (I)*, Bull. Earthq. Res. Inst., Tokyo Univ. *48*, 413–430.

MOGI, K., *Earthquake Prediction Program in Japan*, in *Earthquake Prediction*, (eds. D. W. Simpson and P. G. Richard), (Maurice Ewing Series, IV 1981), pp. 635–666.

MOGI, K. (1982), *Temporal Variation of the Precursory Crustal Deformation Just Prior to the 1944 Tonankai Earthquake*, J. Seismol. Soc. Japan *35*, 145–148 (in Japanese).

SATO, H. (1970), *Crustal Movements Associated with the 1944 Tonankai Earthquake*, J. Geod. Soc. Japan *15*, 177–180 (in Japanese).

SATO, H. (1977), *Some Precursors Prior to Recent Great Earthquakes Along the Nakai Trough*, J. Phys. Earth. *25*, Suppl. S115–S121.

SEKIYA, H., and TOKUNAGA, K. (1974), *On the Seismicity near the Sea of Enshu*, Rep. Coord. Comm. Earthq. Prediction *11*, 96–101 (in Japanese).

THATCHER, W., *Crustal Deformation Studies and Earthquake Prediction Research*, in *Earthquake Prediction* (eds. D. W. Simpson and P. G. Richard) (Maurice Ewing Series, IV 1981), pp. 394–410.

(Received 18th January 1984; revised 25th April 1984; accepted 9th May 1984)

PAGEOPH, Vol. 122 (1984/85) 0033-4553/85/060781-12$1.50 + 0.20/0

On the Interpretation of Slow Ground Deformation Precursory to the 1976 Friuli Earthquake

By MICHELE DRAGONI,[1]) MAURIZIO BONAFEDE[1]) and ENZO BOSCHI[1,2])

Abstract – During three years preceding the 1976 Friuli earthquake, a continuous southward ground tilt was recorded by a tiltmeter placed near Tolmezzo, 15 km north-west of the epicentre of the impending earthquake. The cumulative ground tilt amounted to as much as 3 minutes of arc. Since the tiltmeter was placed in the proximity of an active fault, such a tilt can be explained if the fault slipped aseismically on its shallower section during the same three year period. Aseismic slip on the fault might have been caused by the same mechanism which concentrated stress in the region and eventually produced the 1976 earthquake.

Key words: Precursory tilt, aseismic slip, thrust faulting.

1. Introduction

It is generally recognized that slow crustal deformations play an important role in the earthquake mechanism. They have been often observed both preceding and following larger earthquakes (see e.g. RIKITAKE, 1976). In the present paper, we consider a prolonged, slow ground deformation recorded prior to the 1976 Friuli (Italy) earthquakes. This earthquake sequence consisted of two main shocks of comparable magnitude ($M = 6.5$) which occurred on 6 May and 15 September 1976 respectively, and of a large number of aftershocks (FINETTI *et al.*, 1976; CIPAR, 1981). During three years before the earthquake a tiltmeter placed near Tolmezzo, about 15 km north-west of the epicentre of the earthquake (Fig. 1), recorded an almost continuous ground tilt. The net tilt recorded during the whole period was unusually large: about 3 minutes of arc, approximately in the south direction.

The Friuli region is crossed by several active thrust faults, with strike predominantly in the east–west direction (Fig. 2). While the 1976 earthquake occurred on the Periadriatic fault, the tiltmeter is located close to a secondary thrust fault, north of the Periadriatic fault and nearly parallel to it.

In the present paper we interpret the tiltmeter measurements as being produced by a slow, aseismic slip which occurred on this secondary fault during the three years

[1]) Dipartimento di Fisica, Università di Bologna, Viale Berti Pichat 8, 40127 Bologna, Italy.
[2]) Also at Istituto Nazionale di Geofisica, Roma, Italy.

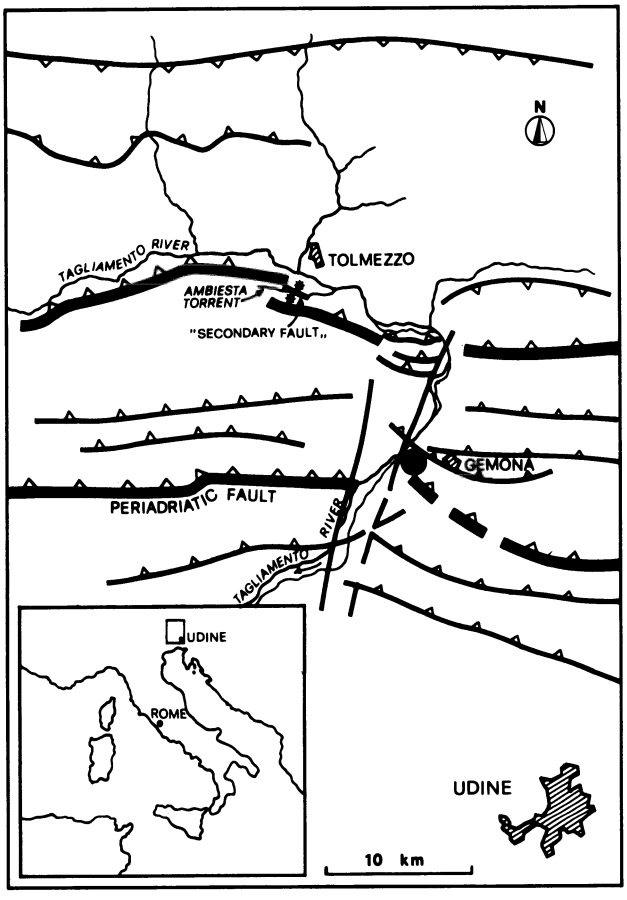

Figure 1
Map of the Friuli region, Italy. The stars denote the tiltmeter sites and the dot is the epicentre of the Friuli earthquake of 6 May 1976.

preceding the 1976 Friuli earthquake. We also show that such a phenomenon can be correlated with a stress concentration mechanism which acted in the lithosphere at depth and eventually produced the earthquake (see BONAFEDE *et al.*, 1983).

2. *The tiltmeter measurements*

A close correlation between ground tilt and seismic activity in the Tolmezzo area was already noticed (CALOI and SPADEA, 1955b; CALOI, 1958, 1962; CALOI and ROMUALDI, 1965). Tilting episodes were often followed by earthquakes: for instance, a ground tilt amounting to 22 seconds of arc in about 20 days was observed prior to a magnitude 4.4 earthquake which occurred on 11 October 1954 (CALOI and SPADEA, 1955b) with approximately the same epicentre as the first 1976 shock.

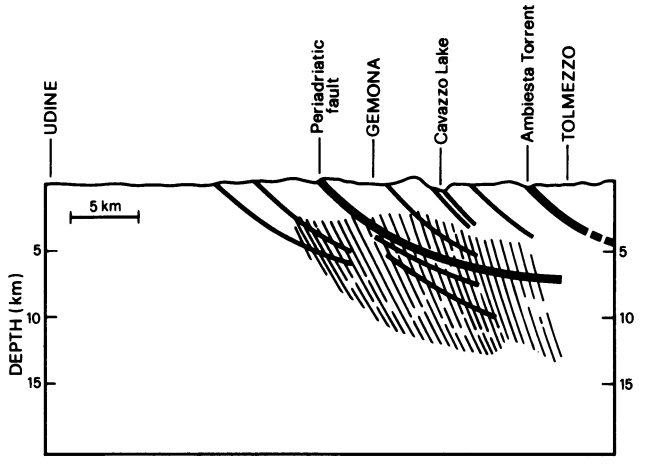

Figure 2
A section view of the Earth's crust in the Friuli region. Several thrust faults are shown. The hatched zone contains the foci of the main shocks and most aftershocks of the 1976 Friuli earthquake.

The tilt measurements used for modelling below are from one of two tiltmeter stations placed on the opposite banks of the Ambiesta torrent, a right tributary of the Tagliamento river (CALOI and SPADEA, 1955a). The distance between the two stations is about 300 m. Each station is composed of two separate tiltmeters measuring the NS and the EW ground tilt component, respectively. The tiltmeters were installed in 1952, in artificial rock caves. They are horizontal pendulums with bifilar Zöllner suspension; their free period is 575 seconds. A detailed description of their technical characteristics is given by CALOI (1950).

Most observations show that the two tiltmeter sites have sharply different behaviours: significant ground tilt episodes were recorded at the site on the left (northern) bank of the Ambiesta torrent, while that on the right (southern) bank showed virtually no tilt. A striking example is shown in Fig. 3, where the tiltmeter records are shown for the period from 1 June to 1 October 1960. In this case, the left bank tiltmeter recorded a tilt of about 70″ approximately in the east direction, while no net tilt was recorded on the right bank. The abrupt change in the tilt direction on the left bank, which occurred after the first half of July, has been connected with a small nearby earthquake ($M \lesssim 4$) on 14 July. In this case, the ground tilt was not followed by a larger earthquake, but was accompanied by an anomalously intense microseismic activity.

This difference in the behaviour of the two tiltmeter sites is ascribed to the fact that the two tiltmeter stations are placed on the opposite sides of a thrust fault which intersects the Earth's surface in correspondence of the Ambiesta torrent (CALOI, 1962; CALOI and ROMUALDI, 1965).

The left bank tiltmeter recorded a significant ground deformation during the three years preceding the 1976 Friuli earthquake (BIAGI *et al.*, 1976). The tiltmeter record is shown in Fig. 4 from 1 January 1972 to 9 September 1976. The trace direction is

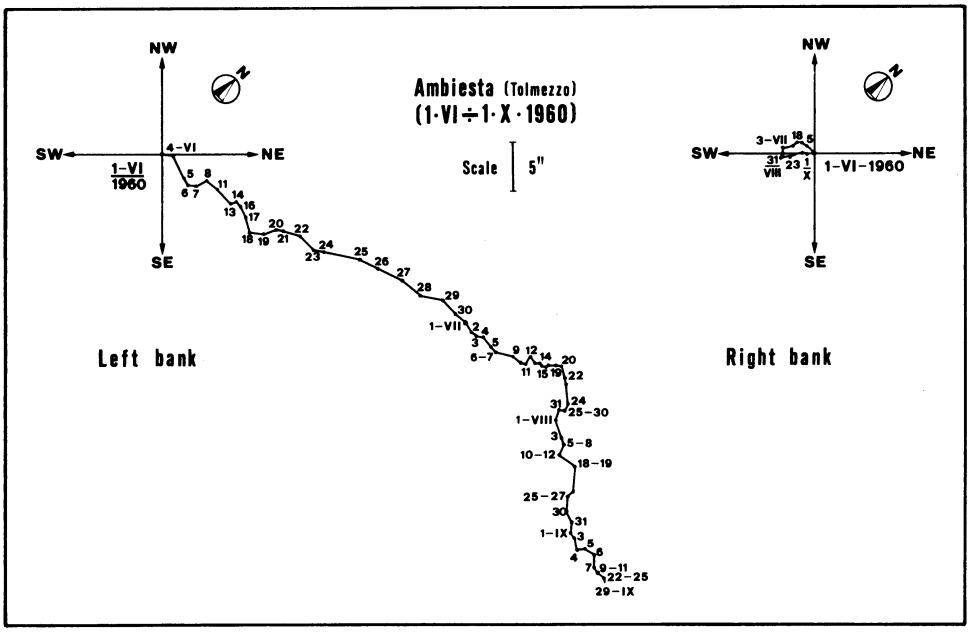

Figure 3
Tiltmeter records from the opposite banks of the Ambiesta torrent for the period 1 June–1 October 1960 (after CALOI, 1962).

approximately southward and this component has been singled out and is shown in Fig. 5 as a function of time. It can be seen that the ground tilt was virtually zero during 1972 and the first half of 1973, while after this date there was a steady increase in tilt at a rate of about 8″ per month until the end of 1974. The southward tilt did not change during the first half of 1975 and, after a series of small shocks of magnitude lower than 4, it started again at about the same rate as before, accompanied by a few small shocks. All these shocks occurred on the secondary fault. The ground tilt stopped again during the first months of 1976, until the large $M = 6.5$ shock occurred on 6 May 1976. In the following sections, this record is interpreted as being produced by a slow dislocation process which occurred on the shallower section of the secondary fault near Tolmezzo during the years preceding the Friuli earthquake. Tilt data from the right bank tiltmeter are unavailable for times after October, 1960.

3. *The model*

The secondary fault is modelled as a rectangular surface embedded in an elastic half-space (Fig. 6). The dip angle is θ. We introduce a downdip co-ordinate ξ, so that the fault surface lies between $\xi = d$ and $\xi = D$, with $D > d$. In the horizontal direction, the fault edges are at $x_1 = -L$ and $x_1 = L$. For the sake of simplicity, we consider a Volterra

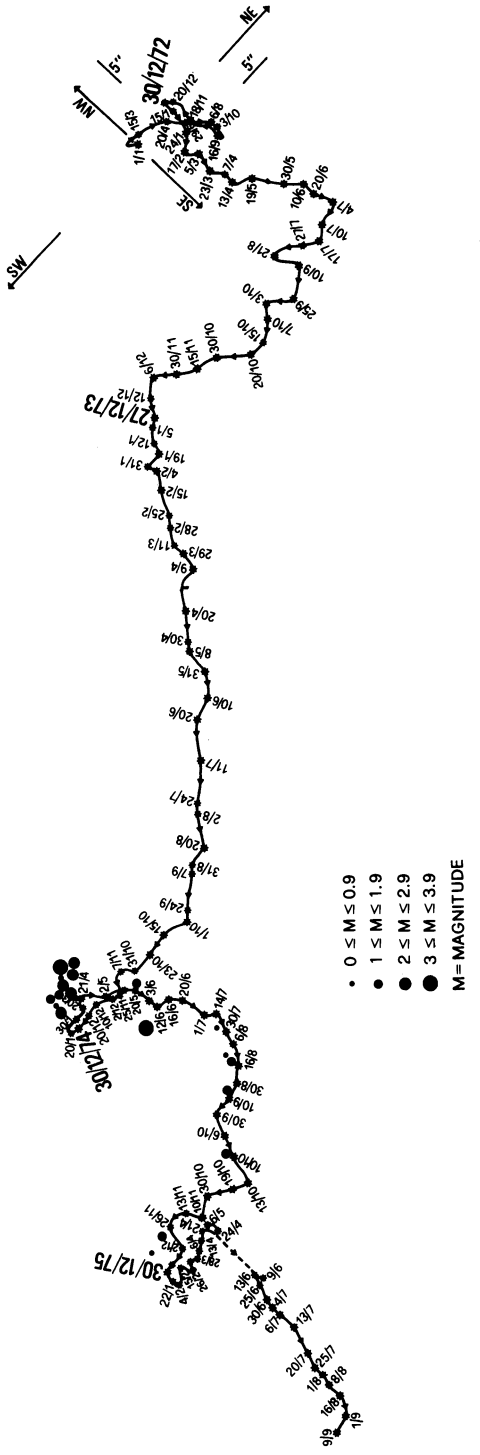

Figure 4
Left bank tiltmeter record during three years preceding the 1976 Friuli earthquake (after BIAGI *et al.*, 1976).

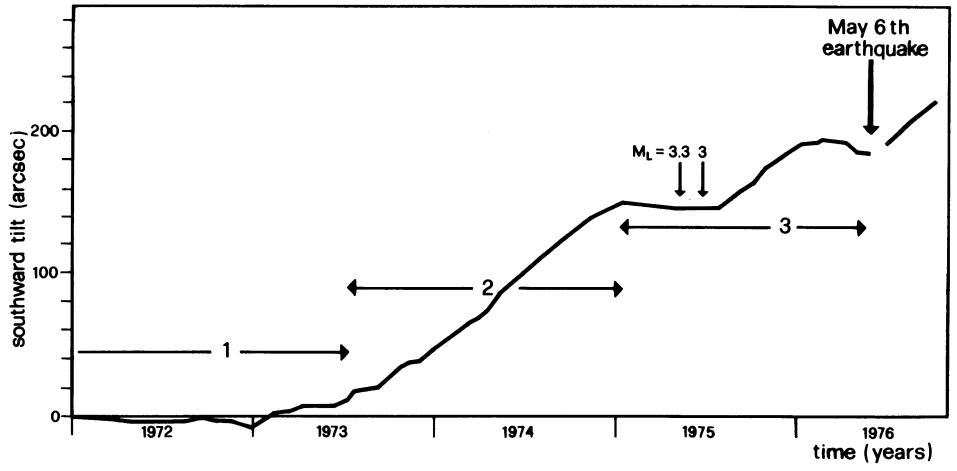

Figure 5
Southward tilt as a function of time as derived from the left bank tiltmeter record (Fig. 4). Three phases are recognizable: (1) negligible tilting and seismic activity; (2) steady increase in tilt; (3) a more irregular tilt variation, accompanied by minor seismic activity.

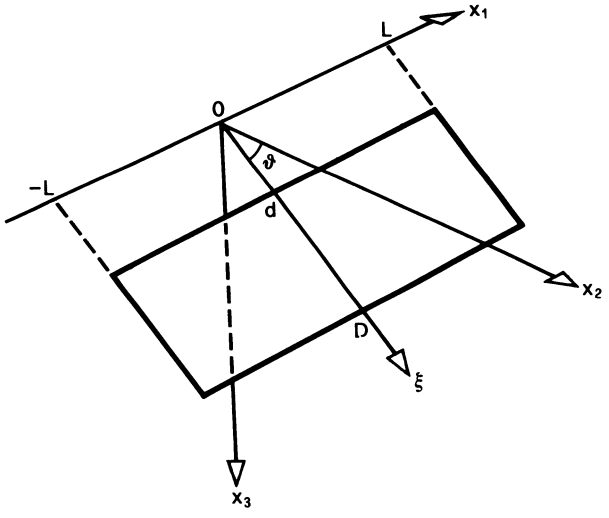

Figure 6
The dislocation model.

dislocation taking place on the fault surface, i.e. a dislocation with uniform slip U. The displacement field produced by such a dislocation has been computed by MANSINHA and SMYLIE (1971). We are interested in the displacement field produced by a dip-slip faulting, i.e.

$$\mathbf{U} = U\hat{\boldsymbol{\xi}} \tag{1}$$

where $\hat{\xi}$ is a unit vector in the ξ direction. In order to compute the ground tilt, we only need the vertical displacement component u_3 at the Earth's surface, $x_3 = 0$. This is given by

$$u_3(x_1, x_2) = \frac{U}{4\pi}\left\{\left[3\,\mathrm{arctg}\,\frac{(x_1-\xi_1)(r_3-\xi)}{r_2 R} - 2\,\mathrm{arctg}\,\frac{(x_1-\xi_1)(x_2-\xi_2)}{(h+\xi_3)(R+h)} - 2\frac{(x_2-\xi_2)\,\xi_3}{R(R+x_1-\xi_1)}\right]\sin\theta - \frac{2\xi_3^2}{R(R+x_1-\xi_1)}\cos\theta\right\}\Bigg\| \tag{2}$$

The displacement u_3 is expressed as an indefinite integral form in the variables ξ_1 and ξ, and we have used CHINNERY's (1961)notation $\|$ to represent the substitution

$$f(\xi_1, \xi)\| = f(L, D) - f(L, d) - f(-L, D) + f(-L, d) \tag{3}$$

In equation (2) the following notations have been also used:

$$r_2 = x_2 \sin\theta \tag{4}$$

$$r_3 = x_2 \cos\theta \tag{5}$$

$$R = [(x_1-\xi_1)^2 + r_2^2 + (r_3-\xi)^2]^{1/2} \tag{6}$$

$$h = [r_2^2 + (r_3-\xi)^2]^{1/2} \tag{7}$$

The ground tilt $\mathbf{t}(x_1, x_2)$ is the gradient of the vertical displacement u_3 projected onto the Earth's surface. Its components are

$$t_1 = \partial u_3/\partial x_1 \tag{8}$$

$$t_2 = \partial u_3/\partial x_2 \tag{9}$$

From equation (2) it is straightforward to obtain

$$t_1(x_1, x_2) = \frac{U}{4\pi}\left\{\sin\theta\left[\frac{2(x_2-\xi_2)\,\xi_3}{R^3} - 2\frac{(x_2-\xi_2)(h+\xi_3)[R(R+h)-(x_1-\xi_1)^2]}{R[(h+\xi_3)^2(R+h)^2 + (x_1-\xi_1)^2(x_2-\xi_2)^2]} + 3\frac{r_2(r_3-\xi)\,h^2}{R[r_2^2R^2 + (x_1-\xi_1)^2(r_3-\xi)^2]}\right] + 2\frac{\xi_3^2\cos\theta}{R^3}\right\}\Bigg\| \tag{10}$$

$$t_2(x_1, x_2) = \frac{U}{4\pi}\left\{\sin\theta\left[-\frac{2\xi_3}{RE} + 2\xi_3(x_2-\xi_2)^2\frac{E+R}{R^3E^2} - 2\frac{(x_1-\xi_1)(R+h)\left[h+\xi_3-(x_2-\xi_2)^2\frac{1}{h}\left(1+\frac{h+\xi_3}{R}\right)\right]}{(h+\xi_3)^2(R+h)^2 + (x_1-\xi_1)^2(x_2-\xi_2)^2} + 3\frac{(x_1-\xi_1)\left[r_2R\cos\theta - (r_3-\xi)\left(R\sin\theta + r_2\frac{x_2-\xi_2}{R}\right)\right]}{r_2^2R^2 + (x_1-\xi_1)^2(r_3-\xi)^2}\right] + 2\xi_3^2\cos\theta(x_2-\xi_2)\frac{E+R}{R^3E^2}\right\}\Bigg\| \tag{11}$$

where

$$E = R + x_1 - \xi_1. \tag{12}$$

4. Discussion

The vertical ground displacement u_3 has been computed for a 1-metre slip occurring over a dislocation surface with $L = 10$ km and dip angle $\theta = 15°$. This value for θ has been chosen assuming that the secondary fault is parallel to the fault surface which broke in the 1976 Friuli earthquake (CIPAR, 1981). The lower fault edge is taken at a depth $A = D \sin \theta = 5$ km. The vertical ground displacement computed for $x_1 = 0$ is plotted in Fig. 7a: three cases are shown, with the upper fault edge reaching depths $a = d \sin \theta$ of 200, 400 and 600 m, respectively. In Fig. 7b the corresponding ground tilt

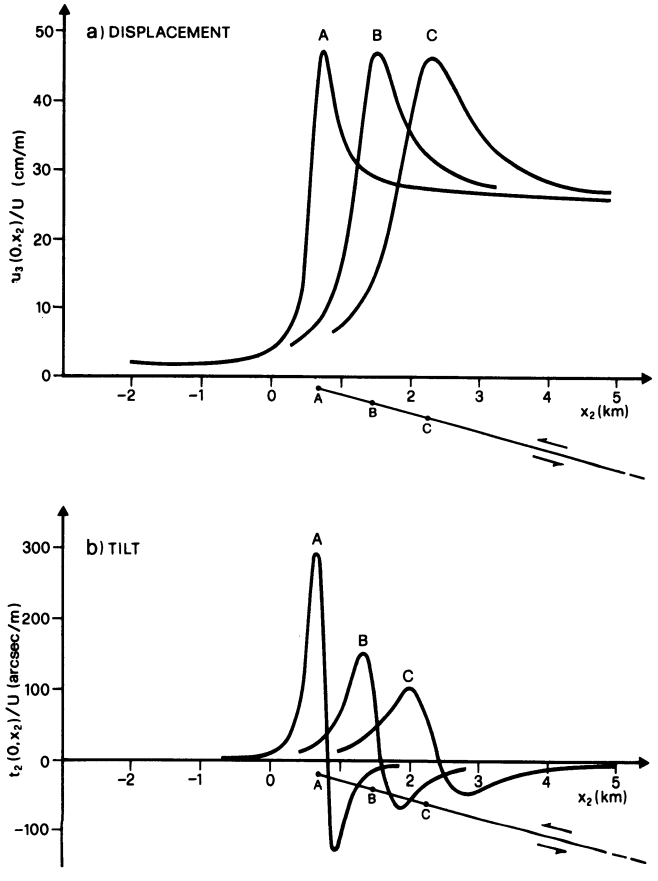

Figure 7
Vertical ground displacement (a) and tilt (b) profiles computed for three different depths of the upper fault edge: $A = 200$ m, $B = 400$ m, $C = 600$ m. A section view of the fault plane is shown.

$t_2(0,x_2)$, the southward component, is plotted. The tilt component t_1 vanishes for $x_1 = 0$. It can be seen that, while the maximum ground uplift is not very different in the three cases, the maximum ground tilt may decrease by a factor 3.

From equations (2), (10) and (11), both displacement and tilt are proportional to the fault slip U. Accordingly, a steady increase in tilt, as occurred in the years 1973–1974 and again in the second half of 1975 (see Fig. 5), may be due to a steadily increasing dislocation amplitude on the fault, i.e.

$$U(t) = kt \tag{13}$$

where k is a constant slip rate. Figure 8 shows the increase of tilt with time in the case of $a = 400$ m and $k = 5$ cm/month, which would fit the data (Fig. 5) reasonably well. This value for the slip rate k is remarkably high, if compared with fault creep rates observed in other parts of the world. It must be stated that an infinity of couples of k and a values would fit the data as well. Smaller a values would imply smaller k values and a narrower zone across the fault where significant tilt occurs. This is shown, as an example, by curve A in Fig. 7. In fact the value inferred for k is likely to be overestimated, since the presence of an upper layer of incoherent rock and sediments, which is not considered in the model, would allow the same ground tilt still to take place with a lower dislocation amplitude.

As has been suggested several times for the Tolmezzo area (CALOI and SPADEA, 1955b; CALOI, 1962; CALOI and ROMUALDI, 1965), such slow deformations as recorded by the Ambiesta tiltmeters indicate that the region is being loaded by tectonic stresses. One may conceive that creep processes were able to release almost continuously the

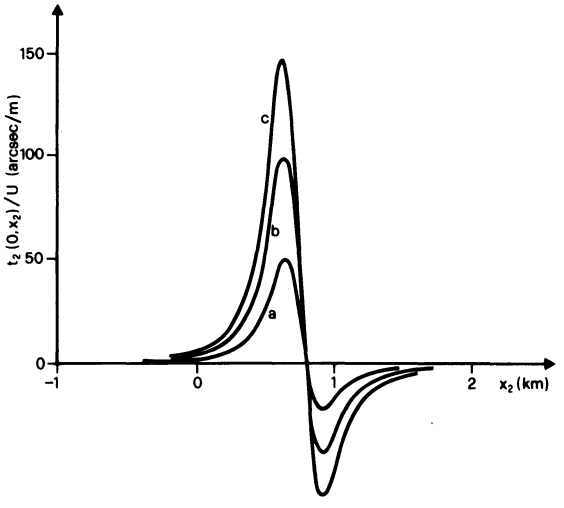

Figure 8

Tilt profiles for a fault with constant creep rate. The upper fault edge is 400 m deep (case *B* in Fig. 7). If $k = 5$ cm/month, the profiles *a*, *b*, *c* refer to 6, 12, 18 months, respectively, after the beginning of the steady tilting phase.

stress which was building up in the region surrounding the secondary fault in the years preceding the 1976 earthquake. Such a release did not take place on the major Periadriatic fault, which was presumably locked in patches at shallow depth (which we may term 'asperities' or 'barriers'; see e.g. LAY *et al.*, 1982), so that stress was accumulated there until it reached a critical value which produced the earthquake.

The creep on the secondary fault was not uniform in time. For instance, the southward tilting had a stop in the first half of 1975, being accompanied by a westward tilting of a few tens of seconds of arc and by small shocks. This westward tilt was then recovered in a few months, while the southward drift resumed (see Figs. 4 and 5). This behaviour can be possibly interpreted as due to locking irregularities on the secondary fault which broke in small earthquakes and left the fault free to slip again uniformly.

Another striking phenomenon was observed during the three years preceding the 1976 Friuli earthquake. The long-period pendulum of the Trieste Earth Tide Station recorded very long period oscillation episodes, each of them lasting several hours (CHIARUTTINI and ZADRO, 1976; ZADRO, 1978). Such oscillations have been interpreted as 'silent earthquakes', that is slow dislocation events occurring on deep fault sections, where the rheological properties of fault gouge play a dominant role (BONAFEDE *et al.*, 1983).

A dislocation process at depth (e.g. on the Periadriatic fault) would concentrate stress onto the barrier zone which was broken in connection with the 1976 earthquake. At the same time, shear stress would increase also on the shallower section of the secondary fault which, if unlocked, would slip aseismically. It is then reasonable that the same mechanism was responsible for both the silent earthquakes on the Periadriatic fault and the aseismic slip on the secondary fault. This is supported by the striking coincidence of the overall duration of both tilt and long period oscillations.

Of course, such inferences suffer from the lack of more data, e.g. tiltmeter records from different sites and geodetic measurements along and across the secondary fault, which could independently test the present interpretation. Existing levelling measurements performed in the Friuli region in 1977 (TALAMO *et al.*, 1978) did not cover the area considered in this paper. However, from a study of possible perturbating phenomena and the fact that the tiltmeter stations are located within caves in stable rock, it has been excluded that the recorded ground tilt has a nontectonic origin (BIAGI *et al.*, 1976). The model presented here, with an extremely localized ground tilt on the upthrusting side of the fault and a negligible tilt on the downthrusting side (Fig. 7b), explains the completely different behaviour at the two tiltmeter sites on the opposite banks of the Ambiesta torrent.

The interpretation given above is also supported by the fact that similar tilting episodes were observed in the past prior to earthquake occurrence in the Tolmezzo area. In particular a ground tilt amounting to 22 seconds of arc in about 20 days was recorded prior to a magnitude 4.4 earthquake which occurred on 11 October 1954.

In this case as well as in the case considered in this paper, the duration of the precursory ground tilt is well correlated with the magnitude of the seismic event,

according to the empirical relation for precursory time versus magnitude derived from analyses performed on several earthquakes throughout the world (RIKITAKE, 1976). A similar curve for precursory time versus fault area has been interpreted in the past in terms of fluid diffusion processes taking place in the focal region (dilatancy-diffusion theory; NUR, 1972). The amplitude of the ground deformation previously described is, however, so high that it is impossible to explain it in terms of any kind of *bulk* deformation occurring at depth. It seems extremely difficult to explain such phenomenon other than in terms of creep episodes on a nearby fault.

The model proposed to interpret the observed ground tilt at Tolmezzo is simplified in some respects. In the first place, displacements and tilts are computed for a homogeneous half-space, while a more realistic model should include at least an upper layer with lower rigidity, representing a sedimentary cover. As was already said, the presence of such a layer would enhance ground deformations. However, this effect is partly compensated by the fact that the MANSINHA and SMYLIE (1971) solution from which our results are derived, employs a uniform slip, Volterra dislocation which gives rise to higher deformation in the proximity of dislocation edges if compared with more realistic dislocation models (see e.g. BILBY and ESHELBY, 1968).

5. *Conclusions*

In the present paper, a tiltmeter record obtained near Tolmezzo, Italy, and relating to three years preceding the 1976 Friuli earthquake, has been interpreted as due to aseismic slip on a neighbouring secondary fault. The observations are reproduced by the model if the fault reached a very shallow depth (less than 1 km) and slipped at a rate of less than a few centimetres per month. Since this fault showed a similar behaviour prior to other earthquakes in the same region, it seems that this fault is able to release the tectonic stress aseismically, whereas in other neighbouring zones stress is accumulated and released catastrophically during earthquakes. It has been suggested that the aseismic slip on the secondary fault may have been caused by the same stress concentration mechanism which produced the very long period oscillations observed at Trieste during the same three-year period preceding the 1976 earthquake (CHIARUTTINI and ZADRO, 1976; ZADRO, 1978; BONAFEDE *et al.*, 1983). If this interpretation is correct, this secondary fault deserves to be more carefully monitored and studied, since its movements may give useful indications on how much stress is being concentrated elsewhere in the Friuli region. The operation of a tiltmeter network is in fact a valuable tool in determining the evolution of stress in the lithosphere and the setting of conditions which make possible the occurrence of larger earthquakes.

Acknowledgments

The authors wish to thank Professor P. Baldi and Dr M. C. Spadea for useful discussions. One of the authors (M.D.) has been supported by the Gruppo Nazionale Difesa dai Terremoti of C.N.R.

REFERENCES

BIAGI, P. F., CALOI, P., MIGANI, M., and SPADEA, M. C. (1976), *Le variazioni d'inclinazione e la sismicità che hanno preceduto il forte terremoto del Friuli del 6 maggio 1976*, Annali Geofis. *29*, 137–146.

BILBY, B. A., and ESHELBY, J. D., *Dislocations and the Theory of Fracture*, in *Fracture – An Advanced Treatise*, vol. 1 (ed. H. Liebowitz) (Academic Press, New York 1968), pp. 99–182.

BONAFEDE, M., BOSCHI, E., and DRAGONI, M. (1983), *Viscoelastic Stress Relaxation on Deep Fault Sections as a Possible Source of Very Long Period Elastic Waves*, J. geophys. Res. *88*, 2251–2260.

CALOI, P. (1950), *Il pendolo orizzontale come clinometro*, Annali Geofis. *3*, 451–457.

CALOI, P., and SPADEA, M. C. (1955a), *Prime indicazioni di registrazioni clinografiche ottenute in zona ad elevata sismicità*, Annali Geofis. *8*, 121–133.

CALOI, P., and SPADEA, M. C. (1955b), *Relazioni fra lente variazioni di inclinazione e moti sismici in zona ad elevata sismicità*, Rc. Accad. naz. Lincei, Ser. 8, *18*, 250–256.

CALOI, P., *About Some Phenomena Preceding and Following the Seismic Movements in the Zone Characterized by High Seismicity*, in *Contributions in Geophysics in Honor of Beno Gutenberg* (Pergamon Press, London 1958).

CALOI, P. (1962), *Moti lenti ed improvvisi nella crosta terrestre e loro reciproche relazioni*, Scientia, Bologna *47*, 1–6.

CALOI, P., and ROMUALDI, G. (1965), *Variazione della verticale apparente e sismicità nella zona di Tolmezzo*, Annali Geofis. *18*, 29–43.

CHIARUTTINI, C., and ZADRO, M. (1976), *Horizontal Pendulum Observations at Trieste*, Boll. Geofis. teor. appl. *19*, 441–455.

CHINNERY, M. A. (1961), *The Deformation of the Ground Around Surface Faults*, Bull. seism. Soc. Am. *51*, 355–372.

CIPAR, J. (1981), *Broad-band Time Domain Modeling of Earthquakes from Friuli, Italy*, Bull. seism. Soc. Am. *71*, 1215–1231.

FINETTI, I., GIORGETTI, F., HAESSLER, H., HOANG, T. P., SLEJKO, D., and WITTLINGER, G. (1976), *Time-space Epicenter and Hypocenter Distribution and Focal Mechanism of the 1976 Friuli Earthquakes*, Boll. Geofis. teor. appl. *19*, 637–655.

LAY, T., KANAMORI, H., and RUFF, L. (1982), *The Asperity Model and the Nature of Large Subduction Zone Earthquakes*, Earthq. Pred. Res. *1*, 3–71.

MANSINHA, L., and SMYLIE, D. E. (1971), *The Displacement Fields of Inclined Faults*, Bull. seism. Soc. Am. *61*, 1433–1440.

NUR, A. (1972), *Dilatancy, Pore Fluids and Premonitory Variations in t_s/t_p Travel Times*, Bull. seism. Soc. Am. *62*, 1217–1222.

RIKITAKE, T., *Earthquake Prediction* (Elsevier, Amsterdam 1976).

TALAMO, R., PAMPALONI, M., and GRASSI, S. (1978), *Risultati delle misure di livellazione di alta precisione eseguite dall'Istituto Geografico Militare nelle zone del Friuli interessate dalle recenti attività sismiche*, Boll. Geod. *37*, 61–71.

ZADRO, M. (1978), *Use of Tiltmeters for the Detection of Forerunning Events in Seismic Areas*, Boll. Geod. *37*, 597–618.

(Received 13th October 1983; revised 16th July 1984; accepted 29th July 1984)

PAGEOPH, Vol. 122 (1984/85)

0033-4553/85/060793-19$1.50 + 0.20/0

Instability Model for Recurring Large and Great Earthquakes in Southern California

By WILLIAM D. STUART[1])

Abstract – The locked section of the San Andreas fault in southern California has experienced a number of large and great earthquakes in the past, and thus is expected to have more in the future. To estimate the location, time, and slip of the next few earthquakes, an earthquake instability model is formulated. The model is similar to one recently developed for moderate earthquakes on the San Andreas fault near Parkfield, California. In both models, unstable faulting (the earthquake analog) is caused by failure of all or part of a patch of brittle, strain-softening fault zone. In the present model the patch extends downward from the ground surface to about 12 km depth, and extends 500 km along strike from Parkfield to the Salton Sea. The variation of patch strength along strike is adjusted by trial until the computed sequence of instabilities matches the sequence of large and great earthquakes since A.D. 1080 reported by Sieh and others. The last earthquake was the $M = 8.3$ Ft. Tejon event in 1857. The resulting strength variation has five contiguous sections of alternately low and high strength. From north to south, the approximate locations of the sections are: (1) Parkfield to Bitterwater Valley, (2) Bitterwater Valley to Lake Hughes, (3) Lake Hughes to San Bernardino, (4) San Bernardino to Palm Springs, and (5) Palm Springs to the Salton Sea. Sections 1, 3, and 5 have strengths between 53 and 88 bars; sections 2 and 4 have strengths between 164 and 193 bars. Patch section ends and unstable rupture ends usually coincide, although one or more adjacent patch sections may fail unstably at once. The model predicts that the next sections of the fault to slip unstably will be 1, 3, and 5; the order and dates depend on the assumed length of an earthquake rupture in about 1700.

Key words: Earthquake prediction; Instability; San Andreas fault.

1. Introduction

This paper describes initial results of an attempt to forecast large and great earthquakes in southern California by combining ground deformation data with an earthquake instability model. Large and great earthquakes (magnitude 7 and 8) are expected on the 500 km long section of the San Andreas fault between Parkfield and the Salton Sea (Fig. 1) because it has had at least six large or great earthquakes at various locations since A.D. 1000 (SIEH and JAHNS, 1984). The last great earthquake was the $M = 8.3$ 1857 Ft. Tejon event, which had a rupture length of about 350 km (SIEH, 1978). The approximate rupture ends are marked by the large brackets in Fig. 1. Based on

[1]) US Geological Survey, 525 S. Wilson Ave., Pasadena, California 91106, USA.

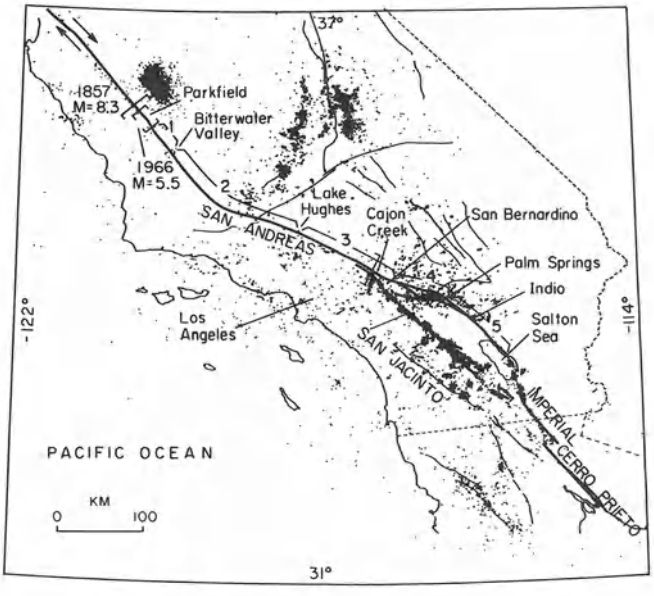

Figure 1

Map of southern California showing seismicity; geographic place names; and San Andreas, Imperial, Cerro Prieto, and San Jacinto fault traces. Dots are epicenters of all earthquakes $M > 0.0$ during 1983. Seismicity data are from the California Institute of Technology – US Geological Survey Seismograph Network, courtesy of C. Johnson. Ruptures of $M = 5.5$ 1966 Parkfield earthquake and $M = 8.3$ 1857 Ft. Tejon earthquake shown by brackets on fault. Numbered sections of fault 1–5 identify sections of brittle patch.

earthquake recurrence times, coseismic slips, and tectonic plate motion, SYKES and NISHENKO (1984) have calculated that several sections of the fault have a high conditional probability of a large or great earthquake occurring in the next 20 years.

The motivation for using an instability model is to make an earthquake forecast more precise than it could be from the use of recurrence times alone. Since individual recurrence intervals for magnitude six and larger earthquakes on the southern San Andreas and Imperial faults differ by as much as 49% from mean recurrence intervals (SYKES and NISHENKO, 1984), predicted times of future events will be comparably uncertain. Several physical factors might contribute to the variation of recurrence intervals at a particular location. One is delayed loading from a nearby earthquake rupture due to viscous relaxation of the deep fault or mantle (LI and KISSLINGER, 1984). Another is the strain field from locked-in dislocations associated with prior earthquakes. A third factor is premature (triggered) seismic slip caused by an earthquake on an adjacent fault section. The model used below takes some account of the last two factors, but not the first. In the model, accelerated faulting and ground deformation precede all instabilities, thus implying an additional way to increase the precision of a forecast (cf. STUART *et al.*, 1985), but the results are not discussed here. This way would be the most precise because many geodetic measurements could be made near the imminent

earthquake rupture, whereas the uncertainties of offsets and dates of past earthquakes are unlikely to be reduced much.

In general terms, attempting a forecast with an instability model involves the use of time-varying geodetic or fault slip data to estimate the values of model parameters that describe the stress-slip law of the fault. The data constrain the shape of the stress-slip law and the variation of fault strength with position. Fault areas where the strength is relatively high are referred to as 'patches', and the goal is to estimate the location and strength of the patches. If the physical model is realistic and the parameter values are well resolved, theoretical and observed curves for past data will coincide. The portions of the theoretical curves corresponding to future times constitute a prediction of future crustal deformation and earthquakes in particular.

At present, this forecast strategy is experimental because most of the theoretical work on instability models is recent (e.g. RICE, 1983), and little field data, especially shortly before earthquakes, has been available to test the models. The antiplane model of MAVKO (1985) simulates repeated earthquakes on a long strike slip fault and is consistent with available triangulation, trilateration, and offset measurements made near the sections of the San Andreas fault that slipped during the Ft. Tejon earthquake and during the $M = 8.3$ San Francisco earthquake in 1906. However, just as for the related model of STUART and MAVKO (1979), no data are available to check the model's prediction of accelerating fault slip prior to instability. In another test, ground uplift during the six years before the $M = 6.4$ 1971 San Fernando, California, earthquake is consistent with the theoretical uplift predicted by a two-dimensional instability model for thrust faulting (STUART, 1979), but the data is in dispute (RUNDLE and MCNUTT, 1981).

In a combined test and forecast attempt, STUART *et al.* (1985) constructed an instability model to forecast the time of a moderate ($M = 5.5$) earthquake expected to occur on the San Andreas fault near Parkfield within the next few years. The next earthquake is expected to resemble earlier earthquakes at Parkfield in 1881, 1901, 1922, 1934, and 1966 which all had similar magnitudes and locations (BAKUN and MCEVILLY, 1979, 1984). The approximate rupture ends of the 1966 event are marked by the small brackets in Fig. 1. Creep and trilateration data measured since 1968 are able to resolve a buried strong patch of about 6 km in diameter and center about 5 km deep. Furthermore, the data constrain the shape of the stress-slip law of the patch to be consistent with unstable failure of the patch (as opposed to stable, aseismic failure), in agreement with the known occurrence of moderate earthquakes. However, the earthquake time cannot be estimated until the field data depart from their linear trends.

A different kind of field data is used to estimate parameters in the model for large and great earthquakes south of Parkfield. This is because the available triangulation and trilateration data span only a fraction of the time of an earthquake cycle (ca. 100–400 years), and because benchmarks generally are not properly located to resolve the spacial variation of fault strength. Instead, I use a set of seismic fault offsets (data and sources given in SIEH and JAHNS, 1984). I find by trial the variation of patch strength along strike that causes the model to produce a sequence of instabilities corresponding to the

observed earthquake offsets. Model instabilities that occur in the part of the simulation representing future times correspond to predicted earthquakes.

This paper presents results obtained from a model simulation that produces instabilities corresponding to the five most recent and best documented large and great earthquakes. This simulation establishes the existence of at least one possible strength variation along the fault; however, the uniqueness of the strength variation is not known. The main purpose of the paper is to show that an instability model is consistent with the field data and therefore is of possible use in predicting future earthquakes.

2. *Qualitative instability model*

Since the model is a slight generalization of the Parkfield model, the discussion here is brief except to describe new features. The reader is referred to earlier papers for physical justification and details of the equations and their numerical solution (STUART *et al.*, 1985; STUART and MAVKO, 1979; STUART, 1981). A qualitative version of the model is presented first, then the mathematical model.

Figure 2 is a sketch of the qualitative model showing a perspective view, looking east, of the San Andreas fault in southern California. At shallow depths, about 0–15 km, the fault zone is assumed to be made of a horizontally elongate patch of brittle rock. The patch is stronger and more brittle than the freely slipping fault at greater depths and than the fault in the continually creeping section north of Parkfield. The patch is many times longer than the circular patch at Parkfield shown at the left in Fig. 2. The variation of patch strength along strike is not known *a priori*, but it is reasonable to assume that the strength distribution is stationary over times much longer than the earthquake recurrence intervals of several hundred years. This would be so, for example, if patch strength is primarily due to fault geometry or to composition of the rocks in contact at the fault. The best evidence supporting a stationary distribution of patch strength is the similarity of recurring earthquake offsets and rupture lengths.

Numerical simulations discussed below indicate that the patch is made of five

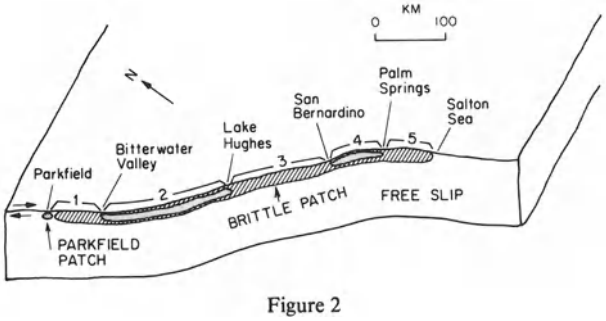

Figure 2
Perspective sketch of southern California showing San Andreas fault plane and hypothetical patch of brittle fault.

sections, each of roughly constant or slowly varying strength. Figures 1 and 2 show the locations of the sections, numbered 1 to 5. Inside and outside of the patch area in the earth there may be small areas of unusual strength or weakness, but these areas cannot be located with available field data. The weak areas, of course, must be strong enough and small enough to disallow substantial surficial fault creep, which is now less than a few mm/yr from 20 km south of Parkfield to the Salton Sea (SCHULZ *et al.*, 1982; BURFORD and HARSH, 1980; LOUIE *et al.*, 1985).

It is assumed that after earthquake failure, the fault patch quickly regains at least a fraction of its former strength by some healing process. The healing would prevent substantial post-seismic slippage and allow renewed storage of elastic strain energy in the surrounding crust needed to produce the next earthquake. The healing need not be immediately complete, but only sufficient to inhibit the tendency for fault slippage induced by the low post-seismic regional stress. Little field data is available to constrain the healing rate after great earthquakes.

The faulting history in the model consists of a succession of unstable slippages, healings, and subsequent reloadings of patch sections. Increasing shear stress due to relative motion of the North American and Pacific tectonic plates induces nearly steady creep on the fault below the patch and at all depths north of Parkfield. Plate motion also causes seismic and aseismic slip on the Imperial, Cerro Prieto, and San Jacinto faults (Fig. 1). Dislocation shear stresses due to fault slip around the patch load it and dominate the much smaller regional shear stress. When one or more patch sections fail unstably, the applied stress (dislocation plus regional stress) that the sections formerly supported is transferred to unfailed patch sections. If the unstable slippage terminates inside the patch, the pileups of edge dislocations near the ends of the slipped length will be locked in and contribute an internal stress that will affect future instabilities. After a patch section has failed, it heals and will fail again in a future instability. Fault geometry, the variation of patch strength along strike, and initial strain determine the timing and length of unstable faulting.

3. Mathematical model

The boundary value problem is stated as a set of simultaneous nonlinear equations, each expressing quasistatic equilibrium at a different position on the fault plane. Each position is at the center of a rectangular dislocation loop that encloses an area of uniform slip. The areas enclosed by dislocation loops are called cells, and they cover the entire fault surface out to distances far from the patch. The different cell slips taken all together correspond to juxtaposed two-dimensional boxcar functions approximating the presumed continuous slip of an actual fault. The model fault approximates the variable strike of the San Andreas, Imperial, and Cerro Prieto faults by a succession of joined flat vertical planes. Planes generally differ from one another in their strike and number of cells. The San Jacinto fault is represented the same way.

Figure 3a shows the map view of the model fault traces. The variable ξ measures the north to south distance along strike of the San Andreas fault. The bottom of Fig. 3b shows the cell boundaries for the faults in side view. The left and right edges of the San Jacinto fault plane intersect the trace of the San Andreas fault plane at $\xi = 738$ km and $\xi = 988$ km respectively. In the model, no slip occurs outside the area covered by fault cells. This assumption is for convenience, and the justification is that stresses acting on the patch due to distant fault slip are small compared to stresses produced by nearby slip. The inferred patch strength shown at the top of Fig. 3b is discussed later.

The equation for shear stress equilibrium at the center of each cell is

$$\tau^r + \sum \tau^d = \tau^f \tag{1}$$

Each stress is the shear stress resolved onto the plane of the cell, acting parallel to local fault strike. τ^r is a term representing the regional stress that increases with time. Usually in models for plate boundary faulting, the cause of the regional stress is assumed to be motion of tectonic plates and is approximated by an antiplane far field stress or displacement. Such boundary conditions seem physically realistic because they allow weak areas of faults to slip and produce dislocation stresses which in turn load nearby strong areas of faults. The regional stress supplements the load due to dislocation

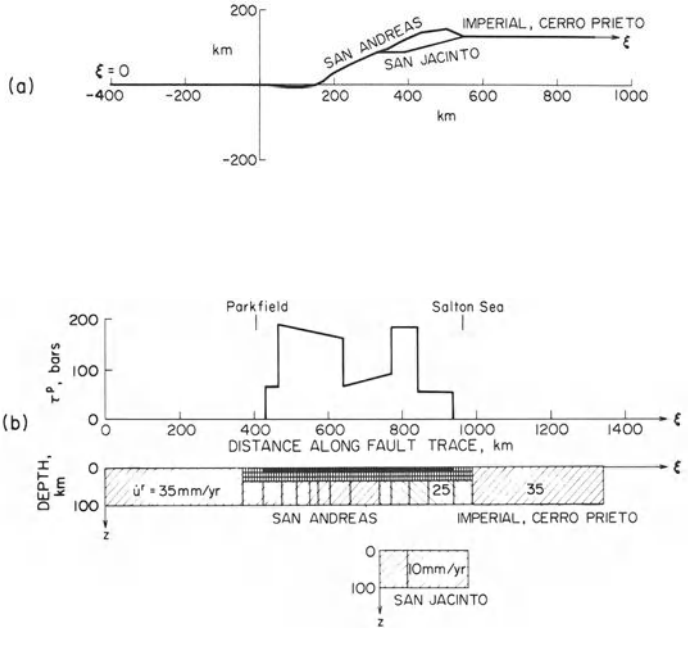

Figure 3

(a) Straight segments of fault trace used in model. Model fault planes are vertical. (b) Bottom two panels are side views of model fault planes (flattened) showing 414 rectangular cells of uniform slip. Slip rates in shaded area are where boundary condition $\dot{u}^r$ is applied. τ^f is non-zero only for the smallest cells. Plot on top shows variation of patch strength along strike.

stresses. For the present model, however, the regional forcing is approximated by imposing an increasing, spacially variable fault slip u^r on the San Andreas fault below and beyond the ends of the fault patch. For the remaining, non-u^r cells, fault slip and stress are computed results. The imposed slip on the San Jacinto fault acts over the entire fault surface. Thus in equation (1) the τ^r for each non-u^r cell is actually the sum of dislocation stresses computed analytically from all u^r cells. The shaded areas of faults in Fig. 3b show the cells where u^r is applied and the numerical values of slip rate $\dot{u}^r$. The reason for the spacial variation of $\dot{u}^r$ is discussed below.

There are three reasons for using the slip boundary condition. First, the complexity of the plate boundary in southern California makes the appropriate orientation of regional stress hard to recognize. Second, slip rate boundary conditions beyond the patch ends ensure that the model is consistent with observed average slip rates. With a far field stress condition, additional patches would have to be included to account for earthquakes such as the 1906 San Francisco event and smaller events on the Imperial, Cerro Prieto, and San Jacinto faults. Third, model simulations with a regional stress boundary condition have failed to produce the observed rates of average slip on the San Jacinto fault. The reason may be the neglect of an additional stress field due to mantle circulation, as suggested by KOSLOFF (1978), BIRD and ROSENSTOCK (1984), and HUMPHREYS and HAGER (1984). The use of the fault slip boundary condition is not to deny that faults are passive features. Slip forcing is only an approximation justified by the fact that dislocation stresses near the patch in the model are generally much greater than far field regional stresses.

The second term of the equilibrium equation (1), $\sum \tau^d$, is the sum of all non-u^r dislocation stresses, including the self stress, acting at the cell center. All dislocation stresses are linear in cell slip and are evaluated from analytic expressions given by CHINNERY (1963; personal communication, 1982).

The third term in (1), τ^f, is the shear stress exerted by the fault zone in resisting fault slippage. As in earlier instability models (STUART and MAVKO, 1979; STUART *et al.*, 1985), τ^f is assumed to be made of two parts. One part expresses the dependence of stress on slip at a specified position on the fault, and the other expresses the spacial variation of strength. The form assumed for τ^f is

$$\tau^f = S \exp\left[-\left(\frac{u-u_0}{a_u}\right)^2\right] \tag{2a}$$

$$S = \tau^p(\xi) \exp\left[-\left(\frac{z-z_0}{a_z}\right)^2\right] \tag{2b}$$

S specifies the peak stress (strength, upper yield stress) at each position on the fault. The bell-shaped Gaussian term in (2b) means that, starting at the ground surface, the fault strength increases with depth z to a maximum value of $\tau^p(\xi)$ at $z = z_0$, then monotonically decreases toward greater depths. $2a_z$ is the characteristic patch height.

Both a_z and z_0 are assumed to be constant along fault strike. $\tau^p(\xi)$ is merely the variation along strike of the patch strength at z_0 and is made of piecewise linear segments as shown at the top of Fig. 3b.

The Gaussian term in (2a) expresses the assumed slip hardening and softening behavior of the fault zone. The left bell-shaped curve in Fig. 4a is a typical plot of (2a) for a position on the fault. The positive slope segment is slip hardening, and the negative slope is slip softening. Both the solid and broken lines describe the material behavior, but when the fault zone is coupled to the elastic surroundings, no quasistatic solutions exist in the broken line sections. At $u = u_0$ fault stress is at its maximum value S. The parameter a_u is a characteristic slip during which failure occurs, and thus $-S/a_u$ is a characteristic weakening stiffness of the fault.

The constitutive law (2a) fails to describe several phenomena known to occur in rocks under laboratory conditions which are possibly appropriate for shallow crustal depths, for example pressure sensitivity, healing after failure, rate dependent strengthening and weakening, and stress corrosion. However, equation (2a) is a simple form that can produce instability, has smooth dependence of stress on slip, and has few enough parameters to be resolved by available field data associated with the large and great earthquakes in southern California.

The healing which is absent in (2a), but required for repeated instabilities, is implemented by a simple procedure which is easiest to describe by referring again to the

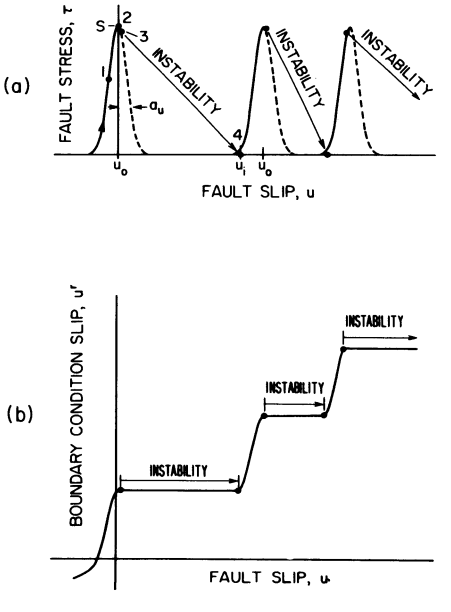

Figure 4

(a) Schematic plot showing stress-slip history for a patch cell. Solid line sections of stress-slip laws allow quasistatic solutions. Broken line sections have no solutions. Unstable slips indicated by arrows. (b) Schematic plot corresponding to (a) showing cell slip u vs. boundary conditions slip u'.

left stress-slip curve in Fig. 4a. This curve represents the possible stress-slip states for a typical cell inside the patch. The curves and slip history would in general differ from cell to cell. The load path, with increasing imposed slip u^r, is at first rightward along the slip-hardening section, passing through point 1, then through the peak stress at point 2, then slip weakening to point 3. From point 3 to point 4 unstable slip and stress drop occur (at fixed u^r), since quasistatic equilibrium is not possible for any values of u between the two points. The post-instability value of τ^f, determined by the left stress-slip law, is essentially zero. Fault healing after instability is approximated by shifting u_0 such that fault slip and stress are now determined by the left, slip-hardening branch of the middle stress-slip law. The formula for the new u_0 is $u_0 = u_i + \sqrt{2}\, a_u$ where u_i is the post-instability value of fault slip. That is, with respect to the middle stress-slip law, $u_i = -\sqrt{2}\, a_u$. Continued increase of u^r will then lead to another instability later. The small difference of stresses given by the left and middle laws at u_i is small compared to S.

The healing of a cell occurs when $(u - u_0)/a_u$ exceeds a preset value and $\dot{u}$ falls below a different preset value. The first condition allows healing only after nearly total stress drop, and the second only after the post-instability rate of fault slip is slow enough. The values of the two empirical constants are the same for all cells and are chosen by trial to allow complete failure of patch sections during one to three time steps and then rapid healing. This healing procedure is no doubt a rough approximation of what might occur in actual fault zones, but is sufficient to simulate the observations.

It is important to note that instability is a property of not just the fault, but of the entire mechanical system of fault plus elastic surroundings. A general condition for unstable slip is that the resisting force of the fault zone decreases faster with increasing regional stress or displacement than the force applied by the elastic surroundings. Thus, just prior to instability, the resisting force (appropriately defined) is declining from an earlier maximum value. In simple two-dimensional models where the fault stress does not vary with position (e.g. STUART, 1981), every position on the fault is in a state of declining stress at the onset of instability. The condition for instability in this case is simply that the rate of weakening $\partial\tau^f/\partial u$ is more negative than $\partial\tau^s/\partial u$, where τ^s is the stress from the elastic surroundings. For fixed geometry, the characteristic fault stiffness S/a_u determines if unstable faulting is possible. For example, if $S/a_u = 0$, as with a horizontal $\tau^f(u)$ curve representing perfect plasticity, instability will not occur because there can be no stress drop. Similarly, the stiffness of the elastic surroundings, which depends on the elastic moduli and model geometry, may be high enough to preclude instability.

In the present model, the average fault stress is also declining before instability, but some locations on the fault are slip hardening or at peak stress when instability starts. Figure 4a illustrates how the pre-instability stress state and amount of unstable slip might differ from one instability to the next at a fault location. Figure 4b shows how the slip rate $\partial u/\partial u^r$ at a position might increase before the same instabilities. The instabilities themselves are shown as jumps of fault slip. In an analytical model the instability would be when $\partial u/\partial u^r \to \infty$, but in the numerical model here the size of

$\partial u/\partial u^r$ is limited by the size of Δu^r during a time step. The area of unstable slip is determined by the number of cells undergoing simultaneous instability.

4. *Earthquake sequence*

The offset geologic markers given in SIEH and JAHNS (1984) are geomorphic features and stratigraphic boundaries that were initially continuous and at high angles to the fault, but became severed by earthquake faulting. At some locations offsets from successive earthquakes have been measured. Figure 5a is a distance–time diagram of earthquake ruptures since A.D. 1000. The horizontal lines show the extent of rupture as

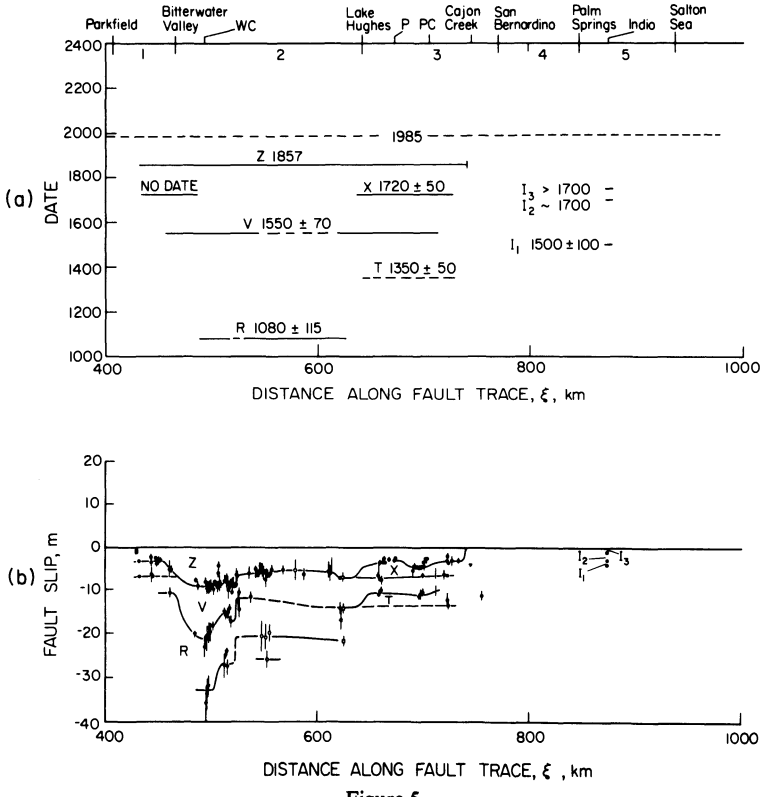

Figure 5

(a) Names, dates, and locations of earthquake offsets given in SIEH and JAHNS (1984). Solid lines indicate more certain correlations than broken lines. Vertical bar at right end of event *Z* indicates well constrained rupture end. Preliminary data for Indio at right are from SIEH (1984b). Numbers 1–5 between ticks at top of figure identify patch sections. WC, P, and PC are locations of Wallace Creek, Palmdale, and Pallett Creek. Broken line labeled 1985 is for reference. (b) Measured fault offsets along San Andreas fault trace. Vertical bars through data points indicate uncertainty of offset. Sub-horizontal solid and broken lines are same correlations as in Fig. 5a. Figure modified from SIEH and JAHNS (1984, Fig. 10). Symbols for data points identify source of data (see SIEH and JAHNS, 1984). Preliminary data near Indio are from SIEH (1984b).

inferred by SIEH and JAHNS (1984) from correlating the dates and amounts of offsets at different locations. Broken lines indicate that the correlation along strike is more tenuous than for solid lines. The broken line labeled 1985 is for reference and does not represent an earthquake. The earthquake names R, T, V, X, and Z above each line are the same as in SIEH and JAHNS (1984), and the dates are historical or from radiocarbon analysis. The uncertainty of the dates represents analytical and stratigraphic uncertainty at approximately the two standard deviation level. Precise locations of rupture ends are not available except for the right end of Z, shown by the vertical bar (WELDON and SIEH, 1985). Events labeled I_1, I_2, and I_3 at the right side of the figure are based on field work in progress at Indio (SIEH, 1984b). The tentative dates are 1500 ± 100, ~ 1700, and > 1700, and the cumulative offsets across one or two of four subparallel fault strands are about 1 m, 2 m, and 1 m respectively. The ~ 1700 event is no later than 1720 (Sieh, personal communication, 1985). The offset values are lower limits because not all fault strands at the Indio site have been excavated. According to Sieh (personal communication, 1984), offsets I_1 and I_2 are probably related to earthquakes, but offset I_3 could be related to either an earthquake or aseismic creep. No other earthquake offset data are available between San Bernardino and the Salton Sea. Furthermore, there is no historical evidence (ca. > 1770) of large or great earthquakes between Parkfield and the Salton Sea for other than the 1857 event.

Figure 5b shows the measured offsets and correlations for events in Fig. 5a. This figure is Fig. 10 of SIEH and JAHNS (1984) turned upside down and modified slightly. The vertical axis is right-lateral slip with respect to the present slip. Oldest fault slips are at the bottom of the figure, and time increases upward. The data-point symbols are the measured values, and the error bars indicate the likely uncertainty in slip measurement. Solid and broken sub-horizontal lines indicate the proposed correlations of offset features. Each line may be thought of as the (negative) right lateral fault slip just before the earthquake which displaces the geologic markers. Earthquake slip is the vertical distance between two sub-horizontal lines. For example, the slip during event Z is the difference between the first line down and the horizontal axis. The slip during event X is the difference between the first and second lines down.

The data for the northern two thirds of the presently locked fault have four prominent features to be explained. First, except near rupture ends, the ratio of slip at a location to the time since the last earthquake is approximately constant. For example, the ratios for V and Z near Wallace Creek (marked WC at the top of Fig. 5a) and for Z, X, and V near Pallett Creek (PC) are all in the range 20 to 33 mm/yr. Thus the single undated, unnamed event near Parkfield with offset of 3 m implies a recurrence interval for similar earthquakes equal to one third that of pairs R–V and V–Z if the maximum slip of 10 m for R, V, and Z is used. One explanation of the relation between slip and recurrence time, of course, is that recurrence intervals are approximately proportional to fault strength and that the loading rate is constant.

Second, the repeated slips at most locations on the fault are roughly the same from event to event and thus weakly dependent on the rupture lengths and magnitudes of the

earthquakes. For example, earthquakes *T*, *V*, *X*, and *Z* have different lengths but comparable slips between Lake Hughes and Cajon Creek. Exceptions are rupture ends such as at Lake Hughes where the successive earthquakes have different slips. More generally, the variation of offsets along strike for events *V*, *Z*, and perhaps *R* appear to be made mainly of sections of nearly constant slip, with the slip changing step-like between sections. These data suggest that fault strength is nearly constant for long segments of the fault, and that strength is re-established to about the same level after each earthquake.

Third, between Lake Hughes and Cajon Creek successive earthquakes seem to have alternately long and short rupture lengths. As will be noted below, this interpretation may be an artifact of not knowing the southern extent of faulting for earthquakes other than the 1857 event. WELDON and SIEH (1985) and SYKES and NISHENKO (1984) have suggested that the offsets between Lake Hughes and Cajon Creek are the right and left tails of ruptures whose maximum slip is alternately to the north and south of the Lake Hughes to Cajon Creek section. Events *X* and *T* would be interpreted as the left tails of a rupture that extended, say, from Lake Hughes to the Salton Sea.

The fourth prominent feature in Fig. 5 is that the maximum slip of the largest events such as *R*, *V*, and *Z*, occurs not in the center of the ruptured section, but at a position shifted to the north.

5. *Instability sequence*

I turn now to fitting the model instabilities to the offset data in Fig. 5. The initial conditions of displacement on the fault and in the elastic halfspace are discussed first, then the boundary condition slip rate $\dot{u}^r$, and finally the parameters describing the patch stress-slip law.

In general it is not obvious what date to choose for the start of a simulation, or what the initial conditions for the model should be once a date is chosen. The strain field in southern California at any time is, of course, unknown and would be spacially variable due to dislocations locked in from prior earthquakes. On the other hand, the similarity of the recurring earthquake offsets in Fig. 5 implies that one or more processes enforce a certain uniformity on the strain field. The earthquakes themselves would tend to smooth the strain field near the ruptured segment, and an earthquake spanning the entire locked fault from Parkfield to the Salton Sea would smooth the strain field for the region.

Thus zero initial strain would appear to be a good approximation for modeling crustal deformation subsequent to an earthquake which had broken the entire locked section. Not enough information is available to say whether any of the offsets in Fig. 5 is associated with such an earthquake, but the most likely candidates would be long events like *R*, *V*, and possibly similar earlier events *N*, *I*, *F*, *D*, *C*, and *B* at Pallett Creek (SIEH 1984a, Fig. 16, Table 2). Events *R* (1080 $\pm$ 65) and *B* (305 $\pm$ 95) at Pallett Creek differ from the other Pallett Creek events in that they seem to define the ends of $\sim$1000 year

seismic cycles, as suggested by SIEH (1984a). Within a cycle, earthquake recurrence intervals decrease with some regularity. Event R would be the first earthquake of the present cycle, and the present time would be near the end of the cycle. Earthquakes N, I, F, D, C, and B would belong to the preceding cycle. SIEH (1984a) cautions that such cycles are conjectural because of uncertainties in radiocarbon dates of several decades. The physical cause of decreasing recurrence intervals is unknown, however, and the model instabilities at the Pallett Creek position do not have regularly decreasing recurrence intervals.

Nonetheless, I assume for simplicity that dislocation stresses shortly after the time of earthquake R were small compared to the patch strength. The assumed initial value of $u^r = 0$ for this time results in computed fault stresses that are small compared to patch strengths and in fault slips inside the patch that have values of about $-a_u$. These initial slips are on the slip hardening sides of stress-slip curves.

There are at least two unattractive alternatives to starting the model right after event R. One is to let initial strains be negligible but perform simulations using various trial $\tau^p(\xi)$ for times representing millennia. The location and time of the next future earthquake would be inferred by trying to find somewhere in the simulation a sequence of instabilities that matches the known earthquakes. The second alternative is similar to the first, except that one could attempt the matching based on shorter simulations evolving from various non-zero initial strains.

The boundary condition slip rate $\dot{u}^r$ varies along fault strike (Fig. 3b) and is set approximately equal to average slip rates determined by offset data. From north of Parkfield to the junction of the San Andreas and San Jacinto faults near Cajon Creek $\dot{u}^r = 35$ mm/yr. This value is close to three estimates from field data. The maximum current slip rate on the creeping section of the fault north of Parkfield is about 32 mm/yr (BURFORD and HARSH, 1980; LISOWSKI and PRESCOTT, 1981). Near Wallace Creek the inferred rate is 33.9 ± 2.9 mm/yr for the past 3700 years (SIEH and JAHNS, 1984). Between Palmdale (marked P) and Cajon Creek, WELDON (1984) determined an average rate of 30 to 40 mm/yr for the past million years. Weldon's rate, however, is not equal to the average rate of 26 mm/yr between Lake Hughes and Cajon Creek computed from Fig. 5b, and the discrepancy has not been resolved.

Between the two junctions of the San Andreas and San Jacinto faults the respective values of 25 mm/yr and 10 mm/yr are adopted for $\dot{u}^r$, following WELDON and SIEH (1985) and SHARP (1981). Near Cajon Creek just south of the junction with the San Jacinto fault, WELDON and SIEH (1985) estimate the rate for the past 14 400 years to be 24.5 ± 3.5 mm/yr. The current combined slip rate of the San Jacinto and San Andreas faults near the Salton Sea is about 35 mm/yr, as determined from the deformation of a 125 km wide trilateration network (SAVAGE, 1983). On the Imperial and Cerro Prieto faults, $\dot{u}^r = 35$ mm/yr, which is the sum of the slip rates of the San Andreas and San Jacinto faults just to the north. The assigned slip rates for the Imperial, Cerro Prieto, and San Jacinto faults are meant to approximate the long term average rate of seismic and aseismic slip.

The free parameters in the model are the lateral variation of fault strength $\tau^p(\xi)$, characteristic fault stiffness S/a_u (the same for all positions), depth of the patch center z_0, and the patch height $2a_z$. Since $\tau^p(\xi)$ and initial conditions are the most important parameters controlling the sequence of instabilities and at the same time least constrained by other information, the values of $z_0 = 6$ km and $a_z = 6$ km are assumed. The value $S/a_u = 0.25$ bar/mm is fixed, but lies in the range $0.15 < S/a_u < 0.30$ giving best agreement of theory and observation. The time step size is five years.

The remaining uncertainty involved in finding $\tau^p(\xi)$ is the earthquake history between Cajon Creek and Indio. Due to lack of field data I assume that in Fig. 5 offset X and the ~1700 Indio offset are due to the same earthquake. The consequences of an alternate assumption about the length of offset X will be discussed below.

The relative frequencies of offsets at patch sections 2 and 3 are approximately in the ratio 1:2, but the frequencies for other sections are poorly known or unknown. For the sake of symmetry, τ^p has been chosen so that instabilities recur in the approximate ratios 9:3:6:2:6 for sections 1–5, and at the same time reproduce the measured offsets. Thus, for example, section 1 fails three times for every time of section 2. These ratios also define an earthquake cycle bounded by simultaneous rupture of the entire patch. There is some freedom in adjusting τ^p of the three weak sections of the patch because failure of an adjacent strong section tends to induce premature instability of the weaker section if the weaker section would normally fail slightly later. A generalization of this statement is that preinstability fault slip of a strong section could induce instability of a weak section; failure of the weak section would be interpreted as a foreshock. This interaction is the opposite of the conventional idea that fault failure associated with foreshocks triggers the mainshock.

The resulting $\tau^p(\xi)$, shown in Fig. 3b, has one maximum at the major bend of the fault south of Bitterwater Valley. The other maximum is at the bend south of San Bernardino. If values of other model parameters are held constant, perturbations of less than a few bars to the strengths of patch sections give essentially the same computed instabilities.

Figure 6a shows the lengths and times of computed unstable slips. The axes are the same as in Fig. 5a. Instabilities corresponding to earthquakes in Fig. 5 are marked with the same names, and the dates are from the simulation. The time scale origin is set by assigning the date 1080 to $u^r = 0$. Between Parkfield and the Salton Sea, faulting occurs episodically as unstable slip, and during the time intervals between instabilities fault slip near z_0 is of order a_u. Sections 1, 3, and 5 fail more frequently than sections 2 and 4, sometimes by themselves, other times in concert with adjacent sections. Instability dates for T, V, and Z are outside the uncertainties of the offset dates in Fig. 5a by 15, 25, and 12 years respectively. The date of instability X is inside the uncertainty of the offset date. Indio instability I_1 occurs in 1455, in agreement with SIEH's (1984b) date of 1500 ± 100. Instability I_2 ($=X$) in 1670 is also in agreement with the offset date of ~1700. However, instability I_3 occurs in 1875, uncorrelated with any known large earthquake. TOWNLEY and ALLEN (1939) report an intensity *IX*

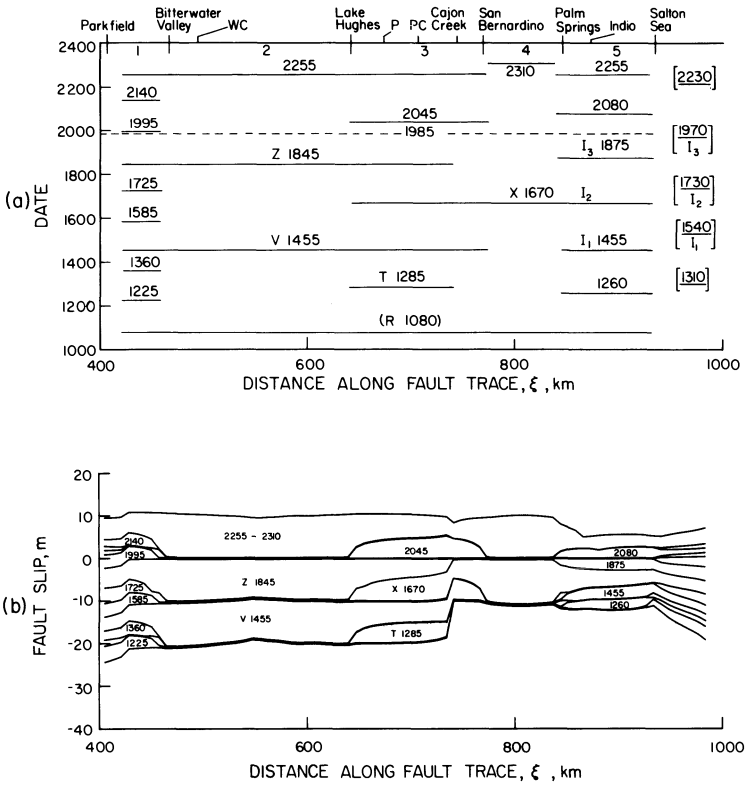

Figure 6

(a) Names, dates, and locations of computed instabilities assuming that earthquake X broke sections 3, 4, and 5. Instabilities T, V, X, Z, I_1, I_2, and I_3 are analogous to measured offsets of the same names in Fig. 5. Numbers 1–5 between ticks at top of figure identify patch sections. WC, P, and PC are locations of Wallace Creek, Palmdale, and Pallett Creek. Broken line labeled 1985 is for reference. Line R is for reference and does not indicate a computed instability. Dates, line segments and names inside brackets at right are results when earthquake X is assumed to have broken only sections 3 and 4. (b) Computed fault slip along the San Andreas fault for times just after instabilities.

(Rossi–Forel) earthquake in 1868 near the northern end of the Salton Sea, but there were no felt reports in Los Angeles, 200 km to the northwest (TOPPOZADA *et al.*, 1981). No other comparable or larger earthquakes near Indio have been reported in historic times (> 1770). Thus the > 1700 event of SIEH (1984b) is unexplained by the model.

Figure 6b shows the computed unstable slips. Each sub-horizontal line is right lateral fault slip with respect to the computed fault slip for the year 1985. The lines have been chosen to indicate slip just after instabilities. As in Fig. 5b, unstable slip is the displacement difference between two adjacent lines. Figure 6b also shows small post-instability slips at the right end of section 1 and left end of section 5, e.g. after 1225 and 1260.

The model produces three of the four main features of the data in Fig. 5 mentioned above. First, the ratios of unstable slip to the time since the previous instability vary by

less than 12% of the mean, except near the ends of unstably slipped segments. The same result can also be obtained to good approximation by a simple model with a single screw dislocation in a half space, assuming that failure occurs when $\tau^d = \tau^p$.

Second, successive unstable slips at fixed locations have nearly equal amplitude except near rupture ends. The reason is that the amount of unstable slip at the fault trace depends mainly on the patch strength and depth instead of on rupture length when the length is much greater than the depth. The sections of nearly constant unstable slip along strike are due to constant $\dot{u}^r$ and nearly constant patch strength. Thus, in field data the nearly constant offsets along strike from one earthquake to the next imply stationary patch strength and depth.

Third, the model results indicate that the rupture lengths from Lake Hughes to Cajon Creek are not necessarily alternately short and long. In the model, X extends from Lake Hughes to the Salton Sea. Instability T and the future one in 2045 at the same position have comparable but unequal lengths. Also, the right ends of instabilities V and 2045 extend farther south than the right end of instability Z. The right ends of V and Z agree with an interpretation of offset data given by WELDON and SIEH (1985). Instabilities V and 2045 extend to San Bernardino because a prestress due to earlier instabilities T or Z, respectively, helps overcome the accumulated local unloading due to slip on the north end of the San Jacinto fault. Since instabilities R and X leave no entrapped dislocations between Cajon Creek and San Bernardino, the right ends of instabilities T and Z terminate near the junction of the San Andreas and San Jacinto faults. In general, however, unstable slips terminate near ends of patch sections.

The fourth main feature in Fig. 5, the northerly location of greatest slip, is not apparent in computed instabilities V and Z. The model slip is too large for most of the fault between Wallace Creek and Cajon Creek. As noted above, the long-term estimate of about 35 mm/yr by WELDON (1984) and the average slip rate computed from data in Fig. 5 between Wallace Creek and Cajon Creek disagree. One explanation may be that offset measurements along this section of the fault are all systematically low. An extreme example is the average slip rate of 9 mm/yr for the Pallett Creek site given by SIEH (1984a).

The next future instability in Fig. 6 occurs on fault section 1 in 1995. The rupture length is about 60 km and the slip is about 3 m. The following instability occurs on section 3 in 2045. This event resembles event T, except that it extends farther south. The third future instability is on section 5 in 2080. The next three instabilities rupture the entire Parkfield to Salton Sea section between 2255 and 2310, thus approximately marking the end of the current earthquake cycle which started with event R.

Finally, by making an alternative assumption that even X broke only sections 3 and 4, it is possible to slightly improve the match of instability and earthquake times at Indio. Raising the strength of section 5 from 53 to 65 bars increases the recurrence interval so that now instability I_1 is in 1540, I_2 in 1730, and I_3 in 1970. The strengths of other patches also have to be adjusted by a few bars to preserve lengths of instabilities to the left of section 5, but the new instability dates there are all within 20 years of those

discussed above. The new results for the Indio instabilities are plotted inside the brackets at the right of Fig. 6a. The dates 1540 for I_1 and 1730 for I_2 are consistent with the estimates of SIEH (1984b), but the >1700 offset in the field would have to be interpreted as aseismic slippage. The 1970 instability would be interpreted as an earthquake that should occur in the next few decades. It appears, however, that neither assumption about the length of offset X gives satisfactory agreement between observation and theory at Indio if offset I_3 is due to a large earthquake.

The dates of instabilities in both simulations are uncertain by a few decades because of large cell size, large time step size, and uncertain values of model parameters. For example, decreasing S/a_u to 0.20 increases the instability times with respect to the year 1080 by about 4%. Overall, the dates and locations of future instabilities are in agreement with dates and locations of future earthquakes estimated by SIEH (1984a), SIEH and JAHNS (1984), and SYKES and NISHENKO (1984) from recurrence intervals. This is because both forecast methods are calibrated by the same set of field data.

6. *Conclusions*

The two main conclusions of this study are that a relatively simple model for earthquake instability is consistent with known earthquake occurrences, and that because of the consistency the model may have application to predicting future earthquakes. The model embodies two concepts that at least qualitatively are generally accepted: a relatively strong brittle zone in the upper 10 to 20 km of the fault is responsible for the current locked state, and unstable fault failure is due to some form of strain weakening. These two concepts underlie other instability models which are consistent with different kinds of geodetic data in other geographic areas having different magnitude earthquakes. Except for the boundary condition fault slip that represents motion of tectonic plates, both pre- and coseismic faulting are computed results instead of assumptions or free parameters.

Times and locations of future instabilities depend on the assumed length of offset X. If X extended from Lake Hughes to the Salton Sea, the next instabilities, in order, are from Parkfield to Bitterwater Valley, from Lake Hughes to San Bernardino, and from Palm Springs to the Salton Sea. But if X extended from Lake Hughes to Palm Springs, the next instabilities are from Palm Springs to the Salton Sea, from Parkfield to Bitterwater Valley, and from Lake Hughes to San Bernardino. The model projections are far from certain, and will require revision when more offsets are measured. The simulation also implies that the strength of the San Andreas fault in southern California varies slowly along sections, but changes rapidly from one section to the next. The consequence is that earthquake ruptures usually terminate near the jumps of fault strength. The most important new field data needed to constrain the model are offsets and dates of consecutive earthquakes between Cajon Creek and the Salton Sea.

Instability models represent the appropriate physical theory for deterministic forecasting of earthquakes because the models simulate ground deformation due to both pre- and coseismic faulting. Values of model parameters can be estimated with past field data, and the estimates can be revised with future data. Because a simulation estimates the time, location, and size of future earthquakes, it can help in the design of a geodetic survey program and in the interpretation of the measurements. Instability models constitute, in a sense, an end member prediction method. Like probabilistic prediction methods, the instability model method uses earthquake recurrence times, but an instability model is additionally constrained by details of the field data and by well-established mechanical principles.

Acknowledgments

I thank T. Heaton, K. Sieh, and R. Weldon for helpful comments and discussions. K. Sieh and R. Weldon also allowed use of material prior to publication. M. A. Chinnery kindly provided unpublished equations.

References

BAKUN, W. H., and MCEVILLY, T. V. (1979), *Earthquakes near Parkfield, California: Comparing the 1934 and 1966 Sequences*, Science, N.Y. *205*, 1375–1377.

BAKUN, W. H., and MCEVILLY, T. V. (1984), *Recurrence Models and Parkfield, California, Earthquakes*, J. Geophys. Res. *89*, 3051–3058.

BIRD, P., and ROSENSTOCK, R. W. (1984), *Kinematics of Present Crust and Mantle Flow in Southern California*, Bull. Geol. Soc. Am. *95*, 946–957.

BURFORD, R. O., and HARSH, P. W. (1980), *Slip on the San Andreas Fault in Central California from Alinement Array Surveys*, Bull Seism. Soc. Am. *70*, 1233–1261.

CHINNERY, M. A. (1963), *The Stress Changes that Accompany Strike-slip Faulting*, Bull. Seism. Soc. Am. *53*, 921–932.

HUMPHREYS, E., and HAGER, B. H. (1984), *Small-scale Convection Beneath the Transverse Ranges, Southern California* (abstr), EOS, Trans. Am. Geophys. Un. *65*, 195.

KOSLOFF, D. D. (1978), *Numerical Models of Crustal Deformation* (California Institute of Technology, Ph.D. Thesis).

LI, V. C., and KISSLINGER, C. (1984), *Stress Transfer and Nonlinear Stress Accumulation at Subduction-type Plate Boundaries – Application to the Aleutians*, Pure Appl. Geophys. *122*, this issue.

LISOWSKI, M., and PRESCOTT, W. H. (1981), *Short-term Distance Measurements Along the San Andreas Fault System in Central California, 1975 to 1979*, Bull. Seism. Soc. Am. *71*, 1607–1624.

LOUIE, J. N., ALLEN, C. R., JOHNSON, D. C., HAASE, P. C., and COHN, S. N. (1985), *Fault Slip In Southern California*, Bull. Seism. Soc. Am. *75*, in press.

MAVKO, G. M. (1985), *Large-scale Earthquakes from a Laboratory Friction Law*, J. Geophys. Res., in press.

RICE, J. R. (1983), *Constitutive Relations for Fault Slip and Earthquake Instabilities*, Pure Appl. Geophys. *121*, 443–475.

RUNDLE, J. B., and MCNUTT, M. (1981), *Southern California Uplift – Is It or Isn't It*, EOS, Trans. Am. Geophys. Un. *62*, 97–98.

SAVAGE, J. C. (1983), *Strain Accumulation in Western United States*, Ann. Rev. Earth Planet. Sci. *11*, 11–43.

SCHULZ, S. S., MAVKO, G. M., BURFORD, R. O., and STUART, W. D. (1982), *Long-term Fault Creep Observations in Central California*, J. Geophys. Res. *87*, 6977–6982.

SHARP, R. V. (1981), *Variable Rates of Late Quaternary Strike Slip on the San Jacinto Fault Zone, Southern California*, J. Geophys. Res. *86*, 1754–1762.

SIEH, K. E. (1978), *Slip Along the San Andreas Fault Associated with the Great 1857 Earthquake*, Bull. Seism. Soc. Am. *68*, 1421–1448.

SIEH, K. E. (1984a), *Lateral Offsets and Revised Dates of Large Pre-historic Earthquakes at Pallett Creek, Southern California*, J. Geophys. Res. *89*, 7641–7670.

SIEH, K. E. (1984b), *Late Holocene Behavior San Andreas Fault*, U.S. Geol. Survey Open-File Report *84–628*, 126–128.

SIEH, K. E., and JAHNS, R. H. (1984), *Holocene Activity of the San Andreas Fault at Wallace Creek, California*, Bull. Geol. Soc. Am. *95*, 883–896.

STUART, W. D. (1979), *Strain-softening Instability Model for the San Fernando Earthquake*, Science, N.Y. *203*, 907–910.

STUART, W. D. (1981), *Stiffness Method for Forecasting Earthquakes*, Bull. Seism. Soc. Am. *71*, 363–370.

STUART, W. D., and MAVKO, G. M. (1979), *Earthquake Instability on a Strike-slip Fault*, J. Geophys. Res. *84*, 2153–2160.

STUART, W. D., ARCHULETA, R. J., and LINDH, A. G. (1985), *Forecast Model for Moderate Earthquakes near Parkfield, California*, J. Geophys. Res. *90*, 592–604.

SYKES, L. R., and NISHENKO, S. P. (1984), *Probabilities of Occurrence of Large Plate Rupturing Earthquakes for the San Andreas, San Jacinto, and Imperial Faults, California, 1983–2003*, J. Geophys. Res. *89*, 5905–5927.

TOPPOZADA, T. R., REAL, C. R., and PARKE, D. L. (1981), *Preparation of Isoseismal Maps and Summaries of Reported Effects for pre-1900 California Earthquakes*, Calif. Div. Mines Geol. Open File Rep. *81–11 SAC*, 182 pp.

TOWNLEY, S. D., and ALLEN, M. W. (1939), *Descriptive Catalog of Earthquakes of the Pacific Coast of the United States 1769 to 1928*, Bull. Seism. Soc. Am. *29*, 1–297.

WELDON, R. J. (1984), *Implications of the Age and Distribution of the Late Cenozoic Stratigraphy in Cajon Pass, Southern California*, in *San Andreas Fault – Cajon Pass to Wrightwood* (eds. R. L. Hester and D. E. Halliger), Pacific Section A.A.P.G. Guidebook 55, 9–16.

WELDON, R. J., and SIEH, K. E. (1985), *Holocene Rate of Slip and Tentative Recurrence Interval for Large Earthquakes on the San Andreas Fault in Cajon Pass, Southern California*, Bull. Geol. Soc. Am., in press.

(Received 11th December 1984; revised 24th January 1985; accepted 24th January 1985)

PAGEOPH, Vol. 122 (1984/85) 0033-4553/85/060812-19$1.50 + 0.20/0

Stress Transfer and Nonlinear Stress Accumulation at Subduction-type Plate Boundaries – Application to the Aleutians

By VICTOR C. LI[1]) and CARL KISSLINGER[2])

Abstract – A study of stress accumulation in seismic gaps and of stress transfer along linear plate boundaries is presented. Time-dependent reloading of plate boundaries following seismic ruptures is modeled by a modified Elsasser model of a coupled lithosphere/asthenosphere plate system. This model is applied to study a series of large earthquakes in the Aleutian Islands and the Alaska peninsula in 1938–1965. It is found that the Rat Island earthquake and the 1948 earthquake in the central Aleutians are likely to have been triggered by adjacent ruptures, in the sense that their occurrence would have come at a later time had their neighboring segments not been ruptured. Stresses in the Unalaska Gap and the Shumagin gap are at a relatively high level and these segments of the plate boundary may be expected to rupture in the near future. In general, in the ten years (about 16% of the earthquake cycle for the Aleutians) following an earthquake, the stress recovery in the rupture zone is highly nonlinear, resulting in a much more rapid stress accumulation than the linear case. Even at a later stage of an earthquake cycle, adjacent ruptures can cause an acceleration of loading rate in addition to the coseismic stress jump. A good example is the influence of the 1964 Alaska earthquake on the 1938 rupture zone. A general conclusion of this work is that long term earthquake prediction models must take into account the nonlinear stress accumulation behavior in seismic gaps. Also, we have shown the interaction of adjacent plate boundary segments, which suggests that some large earthquakes may have been triggered by nearby ruptures.

Introduction

Great earthquakes in subduction zones are the result of stress built up over tens of years on the boundary between two converging plates. Although the process of stress release may be quite complicated, with foreshocks, main shocks, aftershocks and aseismic slip occurring in rather complex temporal and spatial patterns, it may be conjectured that the subduction processes at plate boundaries are largely accommodated by seismic slippage. The presence of inhomogeneities (strength, geometry or otherwise) on any given plate boundary leads to rupturing of finite segments at different times and this is, in fact, what we observe.

[1]) Department of Civil Engineering, Massachusettes Institute of Technology, Cambridge, Mass., 02139.

[2]) Cooperative Institute for Reasearch in Environmental Sciences and Department of Geological Sciences, University of Colorado, Boulder, Colorado, 80309.

A fundamental question in the long term behavior of plate boundary processes is whether the rupturing of one segment influences the behavior of the others. Observational seismology suggests that consecutive time intervals for a series of earthquake ruptures tend to get shorter on the same plate boundary (MOGI, 1977), that ruptures seem to abut each other without much overlap (SYKES, 1971), that large ruptures appear to migrate along a plate boundary (e.g. FEDOTOV, 1965; MOGI, 1968; KELLEHER, 1970), and that a space-time plot of great earthquakes reveals a series of ruptures closely spaced in time followed by a relatively quiet period before the next occurs (SYKES *et al.*, 1981). Although these characteristics often come from studying the behavior of a particular plate boundary, it may be expected that they are shared by other plate boundaries. Such characteristics are supportive of the concept of 'triggering' of ruptures through stress transfer.

It has been shown (MATSU'URA and IWASAKI, 1983; THATCHER and RUNDLE, 1979) that large ruptures have resulted in postseismic deformations at converging plate boundaries that are closely associated with the relaxation of the asthenosphere. Alternatively, the delayed reaction of the asthenosphere must be a source of time-dependent reloading of the lithospheric plate boundary both within the ruptured segment as well as adjacent segments. Hence immediate stress transfer through coseismic elastic stress imposition would be followed by more gradual stress transfer through asthenosphere relaxation.

The concept of seismic gaps (FEDOTOV, 1965; MOGI, 1969, 1979; MCCANN *et al.*, 1979) has been a very useful one for identification of plate segments of high seismic potential. However, its value to forecasting earthquakes is limited by the lack of understanding of the stress accumulation process. Long term prediction models such as the time-predictable model or the slip-predictable model proposed by SHIMAZAKI and NAKATA (1980) depend critically on a knowledge of loading rates. Although linear stress accumulation is often assumed in the literature (presumably based on the assumption of constant relative plate motion, which is probably a valid one in the sense of a long-time average), it is not at all clear that plate boundary loading occurs at a constant rate. Indeed, THATCHER (1983) pointed out that nonlinear stress accumulation may be a result of aseismic slip at deeper parts of the plate boundary or may be a result of asthenosphere relaxation. He showed that postseismic spreading of deformation on the San Andreas Fault is consistent with the prediction of a 2-D (infinite strike-wise) model with either deep aseismic slip or asthenospheric coupling. Data from the San Andreas Fault also suggests a long-term decrease in strain rate (THATCHER, 1983). Obviously, models based on nonlinear stress accumulation would predict very different recurrence time.

In this paper, we address the issue of stress transfer from one plate segment to another, and more broadly, the long-term behavior of stress accumulation in a seismic gap. To do this, we adopt a model of lithospheric deformation which accounts for coupling to a viscoelastic asthenosphere. This model is applied to study the loading, unloading and recovery of stresses in the rupture zones of a series of earthquakes in the

Aleutians and the Alaska peninsula in 1938–65. We hope that this study illustrates some of the ideas discussed above and stimulates a new mode of thought or interpretation of the process of stress accumulation at plate boundaries, which has important implications to earthquake forecasting.

It should be emphasized that the words 'critical stress' will be used in a broad sense in this paper since stress level by itself does not determine plate boundary failures. Rather, earthquakes are results of slip instabilities which depend on the contrasting stiffnesses of the fault and the coupled plate system (see, for example, discussions by STUART, 1979 and LI and RICE, 1983a, b). A constant critical stress level assumes *a priori* that the stiffnesses of the fault and plate system do not change over many earthquake cycles. LI and RICE (1983a) showed, however, that the stiffness of the plate system depends on the length of the seismic gap undergoing slip zone progression towards instability. Similarly, fault stiffness may respond to the rate of loading due to slip rate-dependent friction (e.g. MAVKO, 1983). As explained below, the loading rate in a seismic gap may be altered by adjacent ruptures. Hence a 'critical stress' may at best represent a certain maximum intensity of stressing in a seismic gap as it approaches failure. It is in this context that the calculated stress accumulation level presented in this paper provides a measure of proximity to the next earthquake rupture.

Model of multiple ruptures along plate boundaries

Multiple ruptures are modeled as a sequence of single large earthquakes. The theory of stress transfer due to a large earthquake by means of a modified ELSASSER (1969) model was first proposed by RICE (1980) and further analyzed by LEHNER *et al.* (1981). Essential elements of this model are reviewed to facilitate later discussions. Each earthquake is represented as a distribution of dislocations on a finite portion of a plate boundary formed by the interface of two adjacent semi-infinite plates, which represent the linear elastic lithosphere. These plates are underlain by a viscoelastic asthenospheric foundation (Fig. 1). Thus an earthquake rupture produces a disturbance which propagates horizontally in the lithospheric plate on a time scale determined by the viscoelastic properties of the asthenosphere. It is this transfer of stress which we suggest as providing the time-dependent loading at adjacent plate boundary segments and reloading of the ruptured zone. This loading of plate boundaries will be nonlinear in time and is superimposed on the assumed uniform continuous tectonic loading associated with relative movements between adjacent lithospheric plates. The lithospheric plate of uniform thickness H is treated as undergoing plane stress deformation. Details of the subduction geometry have been deliberately left out from Fig. 1 in order to emphasize the fact that plate boundary ruptures effectively produce horizontal disturbance when viewed with respect to tectonic plate dimensions in the present plane stress model. Indeed, the formulation of the modified Elsasser model is not restricted to any particular type of boundary condition. That is, the model can

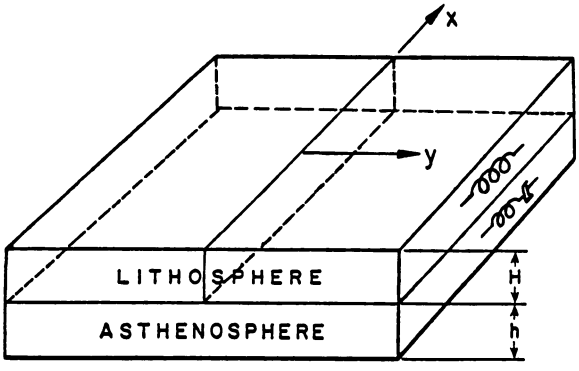

Figure 1
Coupled elastic lithosphere/viscoelastic asthenosphere system, see text for details.

describe subduction or strike-slip stressing processes, and even axisymmetric loading (if such a process has any geophysical meaning).

To further demonstrate the validity of a plane stress formulation in the analysis of the stressing processes at a converging plate boundary, it might be noted that no matter what the detailed tectonic processes are (slab pull, ridge push, etc.) in causing the plates to converge, the plate boundary reacts as if a compressive stress acts in the plane of the plates normal to the strike of the plate boundary. It is this compressive stress in which we are interested in the present study. When a plate boundary segment ruptures, this compressive stress is relaxed in that segment so that the adjacent segments must compensate by bearing more of the loads. The coupling of the lithosphere to a viscoelastic asthenosphere introduces additional complexity in the time delay of this stress redistribution. This is in fact similar to the ideas proposed by ELSASSER (1969) who treated the lithospheric plate as a wave-guide (in plane stress) for diffusion of stress from a converging plate boundary into the plate interior. At any rate, since it is this type of transfer of stress which we shall focus on, details of the local physical processes such as the progressive shear failure of the dipping thrust plane and slab subduction are not included in this paper. However, it is possible to combine the present plane stress analysis with a local cross-section plane strain analysis by a so-called line-spring procedure (RICE, 1972) to yield a more complete description of the deformation processes at the plate boundary. Indeed, a similar point of view was adopted by LI and RICE (1983a, b) in analyzing the stability of slip zone progression and ground surface deformation at strike-slip plate boundaries.

The thickness averaged stress $\sigma_{\alpha\beta}$ is defined as

$$\sigma_{\alpha\beta}(x, y) = \frac{1}{H} \int_0^H \tau_{\alpha\beta}(x, y, z)\, dz \tag{1}$$

where $\tau_{\alpha\beta}$ is the three-dimensional stress tensor. Stress equilibrium requires

$$\partial\sigma_{\alpha\beta}/\partial x_\alpha = \tau_\beta/H \tag{2}$$

where τ_β is the shear stress due to the viscpelastic asthenosphere acting as a thickness-averaged body force which resists motion of the lithosphere. If $u_\beta(x, y)$ is the thickness-averaged displacement, then the stress–strain relation can be written, for plane stress deformation,

$$\sigma_{\alpha\beta} = G\left[\frac{\partial u_\alpha}{\partial x_\beta} + \frac{\partial u_\beta}{\partial x_\alpha} + \frac{2\nu}{1-\nu}\frac{\partial u_\gamma}{\partial x_\gamma}\delta_{\alpha\beta}\right] \tag{3}$$

where G and ν are the shear modulus and Poisson's ratio (with values averaged over the lithospheric thickness). Large earthquakes produce horizontal deformation disturbances with dominant wavelengths typically greater than H, so that the stress components in the thickness direction are in general much smaller than the in-plane components, thus demonstrating the validity of the plane stress model.

It is generally accepted that the viscosity at some depth increases abruptly so that it would be appropriate to model the asthenosphere as a thin channel of thickness h. The in-plane displacements are regarded as varying from $u_\beta(x, y)$ at the lithosphere/asthenosphere interface to zero at the base of the asthenosphere. For a linear Maxwell model, the stress and displacements are related by

$$\dot{\tau}_\beta b/G + \tau_\beta h/\eta = \dot{u}_\beta \tag{4}$$

where η is the viscosity and b is the effective elastic thickness of the asthenosphere. In expectation of displacement response in the short time limit in the plate similar to that in an elastic half-space when the plate boundary suddenly undergoes a uniform stress drop, b may be chosen as $(\pi/4)H$ (LEHNER *et al.*, 1981). The relation between the first term and the right-hand side of (4) may be understood as the average (instantaneous) elastic shear behavior of the asthenosphere, while the second term models the viscous shear relaxation over time. Thus, by enforcing displacement compatibility at the plate/foundation interface, (2) and (4) provide the necessary coupling between the lithosphere and asthenosphere. From (2), (3) and (4), the governing equation for the thickness-averaged displacement field is

$$\left(\alpha + \beta\frac{\partial}{\partial t}\right)\left[\frac{\partial^2 u_\gamma}{\partial x_\rho \partial x_\rho} + \frac{1+\nu}{1-\nu}\frac{\partial^2 u_\rho}{\partial x_\gamma \partial x_\rho}\right] = \frac{\partial u_\gamma}{\partial t} \tag{5}$$

where $\alpha = hHG/\eta$ and $\beta = bH$. The ratio β/α gives the characteristic relaxation time of the viscoelastic foundation. Choosing $h = 100$ km (CATHLES, 1975; STACEY, 1977), $H = 75$ km, $G = 5.5 \times 10^{10}$ Pa, and $\eta = 2.0 \times 10^{19}$ Pa-s (different estimates of η are discussed by LEHNER *et al.*, 1981), the relaxation time is estimated to be about 5 years.

Solutions for (5) are not easily available except for the simplest kind of boundary conditions. For the particular case of converging plate boundaries, in place of (5),

LEHNER *et al.* (1981) propose a simpler, physically-motivated model equation (in which the displacements $u(=u_x)$ and $v(=u_y)$ are uncoupled):

$$\left(\alpha+\beta\frac{\partial}{\partial t}\right)\left[(1+\nu)^2\frac{1-\nu}{2}\frac{\partial^2 v}{\partial x^2}+\frac{2}{1-\nu}\frac{\partial^2 v}{\partial y^2}\right]=\frac{\partial v}{\partial t} \tag{6}$$

For transform plate boundaries, the analogous equation would be

$$\left(\alpha+\beta\frac{\partial}{\partial t}\right)\left[(1+\nu)^2\frac{\partial^2 u}{\partial x^2}+\frac{\partial^2 u}{\partial y^2}\right]=\frac{\partial u}{\partial t} \tag{7}$$

The appropriateness of replacing (5) by either (6) or (7) has been discussed by LEHNER *et al.* (1981) and LI and RICE (1983b). Equations (6) and (7) also show that the solution for the transform mode may be obtained from that for the thrust mode $v=f(x, y, t)$ by simply transforming the length scales:

$$u=f\left(\sqrt{(1-\nu)/2}\,x,\quad \sqrt{2/(1-\nu)}\,y,\quad t\right) \tag{8}$$

If the ruptured segment of the plate boundary remains locked until the great earthquake repeats itself, a dislocation model (which keeps displacement discontinuities fixed in time) would be more appropriate than a crack model (which keeps stress level fixed in time). This choice is also related to the rehealing (or restrengthening) mechanism as well as to aseismic slippage. The physics of rehealing and aseismic slippage is important in analyzing stress redistribution. Unfortunately, very little is known about them. For the present purpose we shall adopt a dislocation model with the understanding that the calculated stresses transmitted across plate boundaries may be modified by these mechanisms. If the magnitude of aseismic slippage is known, and if it occurs shortly before or after the seismic rupture, it may be incorporated in the present model as part of the unloading dislocation. It should also be mentioned that we are dealing with large scale processes, so that although stress drops cannot be expected to be truly uniform within a rupture in a seismic gap we nevertheless adopt this assumption and regard their values as averaged quantities (over the length of the rupture). Modeling of strength heterogeneities in seismic gap zones can be found in LI (1981), DMOWSKA and LI (1982), and LI and RICE (1983a).

The dislocation distribution is assumed to be produced by a semi-infinite crack which suffers a sudden stress drop q on a finite portion L equal to the rupture length. (The use of a semi-infinite crack is for mathematical convenience only.) For uniform stress drop q the dislocation magnitude is given (LEHNER *et al.*, 1981) by

$$\delta(x)=\frac{2q}{G}\sqrt{\frac{\beta}{\pi}}\begin{cases}\displaystyle\int_0^{\lambda_0|x|}\frac{e^{-\rho}}{\sqrt{\rho}}\,\mathrm{erf}\,\{[\rho+\lambda_0(L-|x|)]^{1/2}\}\,d\rho & -L\leqslant x\leqslant 0\\ \displaystyle\int_{\lambda_0(|x|-L)}^{\lambda_0|x|}\frac{e^{-\rho}}{\sqrt{\rho}}\,\mathrm{erf}\,\{[\rho+\lambda_0(|x|-L)]^{1/2}\}\,d\rho & x<-L\end{cases} \tag{9}$$

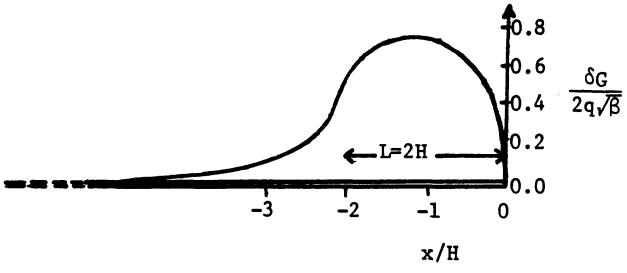

Figure 2
Distribution of dislocation along a rupture zone of length $L = 2H$.

where $\lambda_0 = \{2/[\beta(1 - \nu^2)(1 + \nu)]\}^{1/2}$. Figure 2 shows the dislocation distribution for a rupture length equal to twice the lithospheric thickness. For the boundary condition

$$v(x, 0^+, t) = \begin{cases} \frac{1}{2}\delta(x)H(t) & x < 0 \\ 0 & x > 0 \end{cases} \tag{10}$$

equation (6) yields (LEHNER *et al.*, 1981)

$$\sigma_{yy}(x, 0, t) = \frac{(1 + \nu)\, G}{2\pi} \int_{-\infty}^{0} \tau(|x - \xi|, t) \frac{\delta(\xi)\, d\xi}{|x - \xi|} \tag{11}$$

where

$$\tau(p, t) \equiv \lambda_0\, e^{-\alpha t/\beta} \left\{ K_1(p\lambda_0) + \sum_{\nu=1}^{\infty} \frac{(p\lambda_0\, \alpha t/\beta)^{\nu}}{2^{\nu}(\nu!)^2} K_{\nu+1}(p\lambda_0) \right\}$$

and K_ν is a modified Bessel function of order ν. Equation (11) provides the thickness averaged normal compressive stress change at any point x along the linear plate boundary and at any time t, once the stress drop q and rupture length L are known. Because of the slight asymmetry of the dislocation distribution (Fig. 2), the calculated stress to the left of the rupture is smaller than that to the right. The rupture segment shown in Fig. 2 is oriented so that the tip of the rupture is always directed towards the point at which the stress is calculated when that point is outside the rupture. As indicated by equation (11), the stress inside and outside the rupture is quite non-uniform. It decays rapidly with distance from the tip of the rupture such that less than 20% of the stress drop is felt at a distance of one rupture length ahead (fig. 4 of LEHNER *et al.*). To illustrate the time delay of stress redistribution, the stress at a point of one and a half lithospheric thicknesses from the tip of the rupture both inside and outside the rupture zone is shown in Fig. 3.

If we denote the stress change at any point x and at time t due to a rupture located between x_p and $x_p - L_p$, where L_p is rupture length, and which occurred at time t_p, with

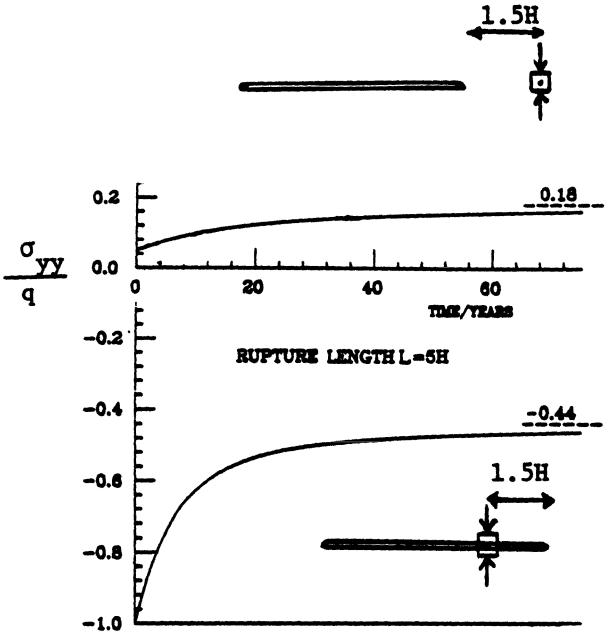

Figure 3
Stress normal to line of rupture at distance $1.5H$ outside and on rupture zone.

stress drop q_p as $g^p(x - x_p, t - t_p; q_p, L_p)$, then by linearity, the stress change at any point x and at time t due to n ruptures ($t_n < t$) is

$$\sigma_{yy}(x, t) = \sum_{p=1}^{n} g^p(x - x_p, t - t_p; q_p, L_p) + \dot{\sigma}_0 t \tag{12}$$

where the second term on the right-hand side of (12) is added to represent the additional stress due to tectonic plate movements, assumed to be uniform far from the plate boundary. Equation (12) is used to study the stress build-up and recovery along the Aleutians and the Alaska peninsula, which we discuss next.

Stress accumulation at the Aleutians

The Aleutian trench is formed by the convergence between the North American Plate and the Pacific Plate (Fig. 4). Relative displacement between 170°E and 155°W is approximately normal to the axis of the trench, although the east and west ends involve some component of oblique convergence. We shall confine our attention to this

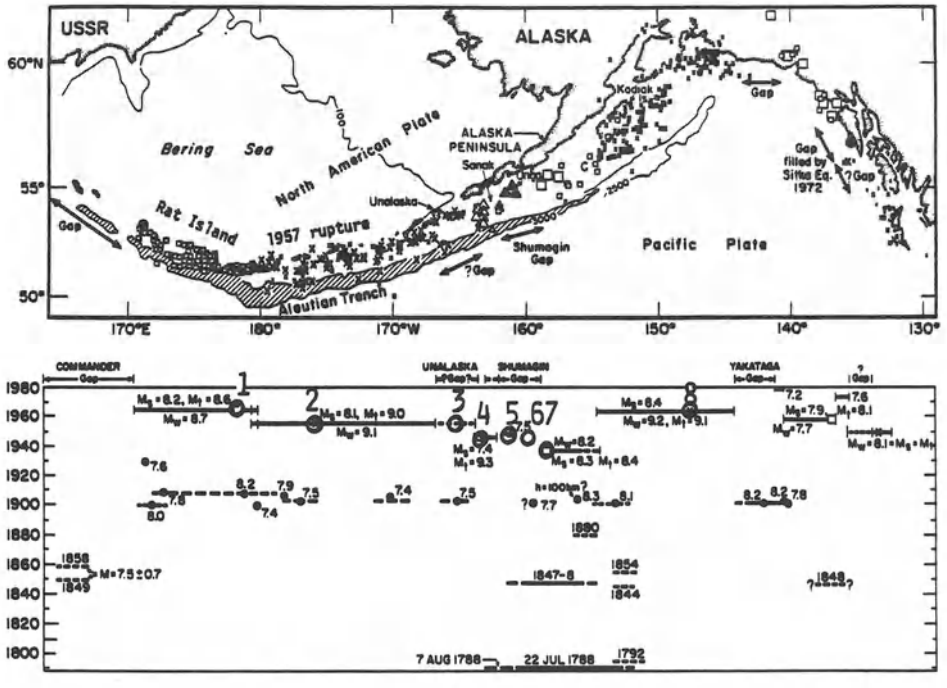

Figure 4

Top: Map of the Aleutians and Alaska, with relocated aftershocks of major earthquakes. Individual aftershock sequences are denoted by crosses: 1949, 1957 and 1964; by squares: 1938, 1958 and 1965; by open circles: 1946; by solid triangles: 1948; by solid circles: 1929, 1972. Larger symbols denote more precise locations. Bottom: Space–time plot of major ruptures. (After SYKES *et al.*, 1981.) The earthquake series around 1950–1960, which are marked with location numbers ruptured the plate boundary segments studied in the present paper.

portion which forms a linear segment of roughly 3080 km. The convergence rate is 7.5 cm/yr (MINSTER and JORDAN, 1978). At least six earthquakes of magnitude M greater than or equal to 7.4 have ruptured most parts of this segment since 1910. The tectonics and the earthquakes at this plate boundary have been under intensive study by many researchers (see e.g. ENGDAHL and KISSLINGER, 1977; SYKES, 1971; SYKES *et al.*, 1981; KELLEHER, 1970; MCCANN *et al.*, 1979). SYKES (1971) noted that the great earthquakes ($M > 7.8$) in this region since 1930 have ruptured zones more than 250 km long, and that they tend to abut each other without much overlap. Another characteristic feature of the earthquake patterns here is that great earthquakes occur as a sequence of events rupturing most of the plate boundary in a relatively short period of time, followed by a period without great earthquakes until the next sequence starts. This may be seen in the 1910 and the 1950/60 sequence in Fig. 4, which shows the space-time pattern of ruptures of $M > 7.4$ from 1784 to 1980 (after SYKES *et al.*, 1981).

The repeat time of great earthquakes is estimated to be 60–80 years (JACOB, 1983, and personal communications). SYKES (1971) also observed that the rupture zones of five large events appeared to form a space-time sequence which progressed from 155°W in 1938 to 171°E in 1965. It might also be noted that the time intervals between these earthquakes 1938–1948 (with the 1946 and 1948 earthquakes regarded as a single rupture), 1948–1957, and 1957–1965 appear to get shorter with time. What emerges is a qualitative picture of stress accumulation and release at the Aleutian Trench. Apart from a few short ruptures, most of the boundary segment was free of strong earthquakes between ~1910 to ~1940. During this period, stress and strain were building up due to tectonic plate movements. The first interruption of this quiet period occurred in 1938 when an earthquake ruptured a 300 km segment east of the Shumagin Gap. This earthquake may have transferred some stress to its adjacent segments, causing the 1946 and 1948 ruptures, which were followed by two great earthquakes in 1957 and 1965. The westward migration of these earthquakes may be regarded as a result of delay triggering through stress diffusion.

We shall use the model described in the previous section to simulate the stress/strain accumulation at eight locations, chosen to coincide with the relocated epicenters given by SYKES *et al.* (1981) and in two identified seismic gap zones (see location numbers in Fig. 4). The relevant tectonic conditions are the lithospheric and asthenospheric thicknesses and their material properties, and the loading rate due to relative plate movements. The relevant earthquake data are the time of occurrence, locations, rupture lengths, stress drops, and the dip of the fault planes. These data are summarized in Table 1. The loading rate (normal to the plate boundary) has been estimated from

$$\dot{\sigma}_0 = \frac{(\Delta\tau \sin 2\phi)\,(W \sin \phi/H)}{T} \tag{13}$$

where ϕ is the angle of dip of the subducting slab, W is the width of the rupture plane, H is the lithospheric thickness, T is the repeat time, and $\Delta\tau$ is the shear stress drop attributed to stress accumulation due to tectonic plate movements. This last parameter is equal to the actual shear stress drop in an earthquake less the stress recovery due to asthenospheric relaxation. Figure 3 shows that asthenospheric relaxation may account for stress recovery of 56% of actual stress drop. Hence using $\phi = 30°$, $W = 100$ km, $T = 70$ yrs, $H = 70$ km, and shear stress drop of 50 bars as representative values for the Aleutians, a rough estimate of the tectonic loading rate would be 0.2 bar/yr. If we also account for stress transfer from adjacent ruptures, the tectonic loading rate would be less. The calculations here are based on $\dot{\sigma}_0 = 0.1$ bar/yr. Although this parameter does not alter the general trend of stress accumulation, it does affect the stress level at any given instant, so that interpretation of current stress state must be kept in perspective with suitable adjustment of this tectonic loading rate.

The thickness-averaged stress normal to the Aleutian Trench as a function of time is shown in Fig. 5a to 5i. Location numbers on the upper right-hand corner of each figure refer to those shown in Fig. 4. The year 1920 is chosen as the reference year when the

Table 1

(a) *Tectonic conditions and material properties:*

Subduction
Loading rate due to relative plate movement $\dot{\sigma}_0 = 0.1$ bar/yr
Poisson ratio $\nu = 0.25$
Shear modulus $G = 5.5 \times 10^{10}$ Pa
Lithospheric thickness $H = 70$ km
Asthenospheric thickness $h = 80$ km
Asthenosphere viscosity $\eta = 2 \times 10^{19}$ Pa-s

(b) *Earthquake data:*

No.	Year	Location (km*)	Rupture length (km)	Rupture width (km)	Dip angle	Stress drop (bars)	References
1	1938	2268	300	120	30	30	KANAMORI, 1977 SYKES, 1971
2	1946	1755	100	110	30	70	SYKES, 1971
3	1948	1836	50	50	30	70	SYKES, 1971
4	1957	1485	850	110	30	75	PURCARU and BERCKHEMER, 1982
5	1964	2916	650	200	10	60	KANAMORI, 1977 PURCARU and BERCKHEMER, 1982
6	1965	594	500	100	15	40	KANAMORI, 1977 PURCARU and BERCKHEMER, 1982

* East end of rupture measured relative to 170°E.

stress is arbitrarily taken to have a zero value at all locations. All stresses in subsequent years should therefore be regarded as alterations from this stress level. Also the influence of the 1910 earthquake sequence is ignored for lack of information on these earthquakes. However, it might not affect the accuracy of our results too much as the most significant portion of asthenosphere relaxation occurs in about ten years after the rupture. It obviously would be possible to include the 1910 sequence of earthquakes in the calculations if such data were available. In what follows, we shall discuss the stress accumulation at each location.

Results and discussion

The 1965 Rat Island earthquake followed the 1957 rupture to its east, which produces a 0.75 bar coseismic stress jump (equal to 1.2 bars shear stress on slab interface) at the Rat Island region (Fig. 5a). If it is assumed that a critical stress level exists for which rupture must occur, then the Rat Island earthquake would not have happened until about 1977 in the absence of the 1957 event. Thus stress transferred

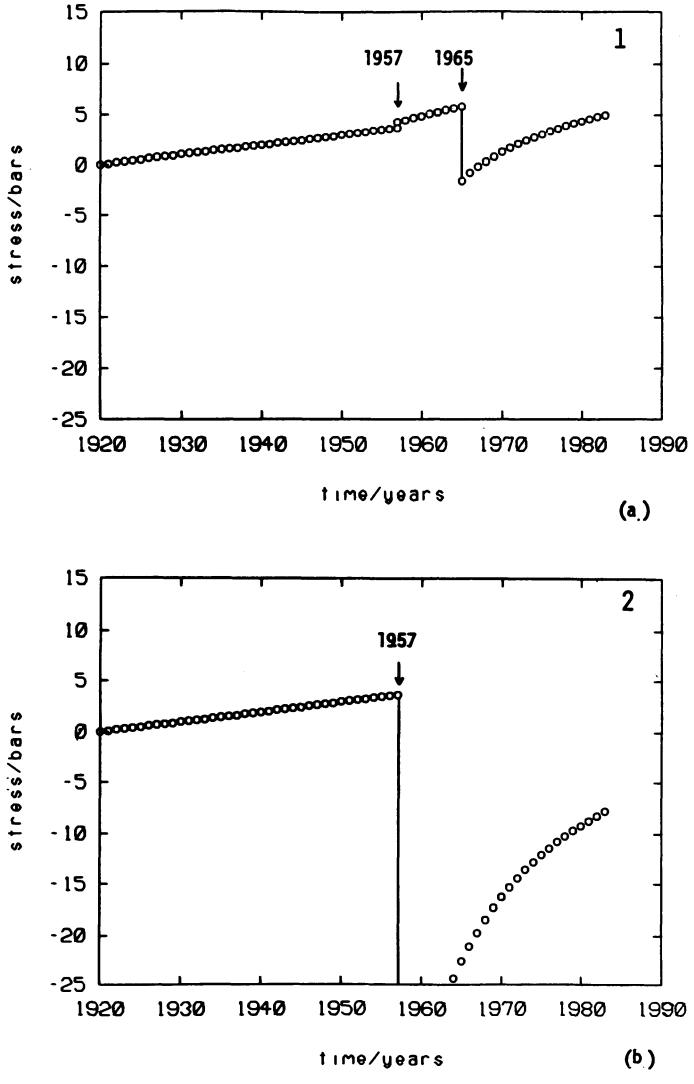

Figure 5a–h

Thickness-averaged stress alteration since 1920 at the eight locations marked in Fig. 4. Figure 5i is a composite of 5a–h, showing the relative stress levels. Note the high stress levels in the Shumagin and the Unalaska Gap. The chart below the time axis indicates the relative locations where stresses have been computed.

from the 1957 earthquake may have accelerated the Rat Island earthquake by as much as 12 years. If stress accumulation at this location continues at the current rate, based on Fig. 5a, it might be speculated that another rupture would occur in 1986–7. This appears to be too short a repeat time for a rupture as large as the Rat Island earthquake. Part of the difficulty may be due to the fact that this location experiences

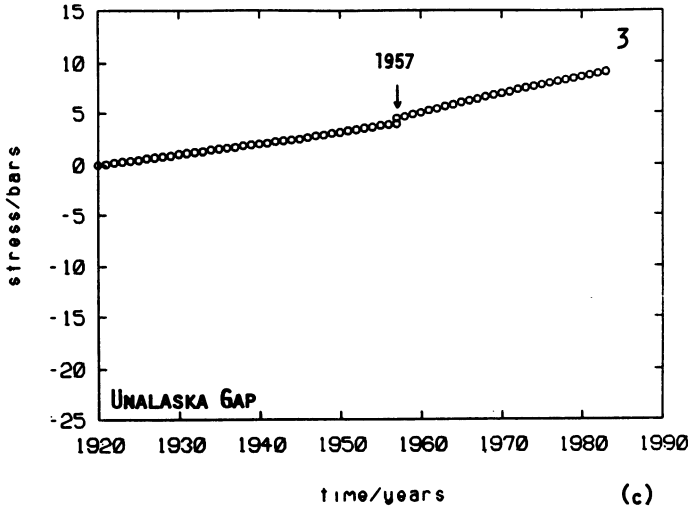

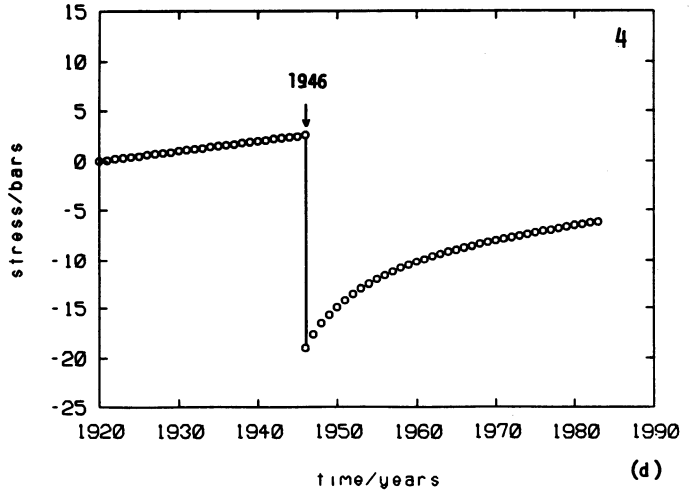

both normal convergence as well as strike-slip movements, due to the bend at longitude 180°. However, the low shear stress drop (40 bars vs ~70 bars elsewhere) may signal an incomplete release of accumulated stress by the Rat Island earthquake in 1965, so that an early return of another rupture at the same location cannot be easily ruled out.

The 1957 rupture between 167°W and 180° was the longest rupture in the Aleutians in this series of earthquakes. As Fig. 5b shows, it does not appear to be triggered by any previous ruptures; the relocated epicenter is at 176°W, at least 800 km from the 1946 or 1948 earthquakes to the east. Although it recovers more than 50% of its stress drop in the subsequent 20 years, another rupture would not be expected for at least another 20–30 years if the current stress accumulation rate persists.

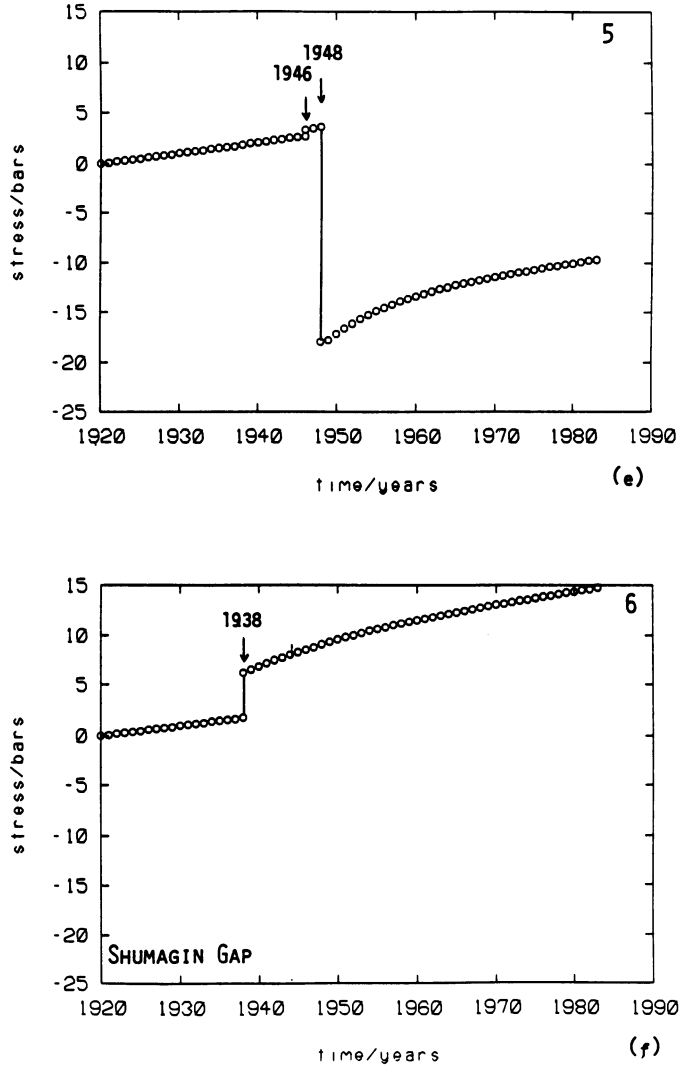

The Unalaska segment at the eastern end of the 1957 rupture is a region of questionable status. If it did not rupture seismically (including aftershocks) or aseismically following the 1957 earthquake, as has been suggested (HOUSE *et al.*, 1981), then the accumulated stress is relatively high at present, above all other segments with the exception of the Shumagin Gap (Figs. 5c and 5f). Thus, this segment may be regarded as a mature seismic gap, with high potential of a large rupture in the near future. It is interesting that the adjacent 1946 and 1948 earthquakes to the east did not cause much stress change in the Unalaska segment, perhaps because of their short rupture lengths. The 1957 rupture, however, did produce a discernible coseismic stress

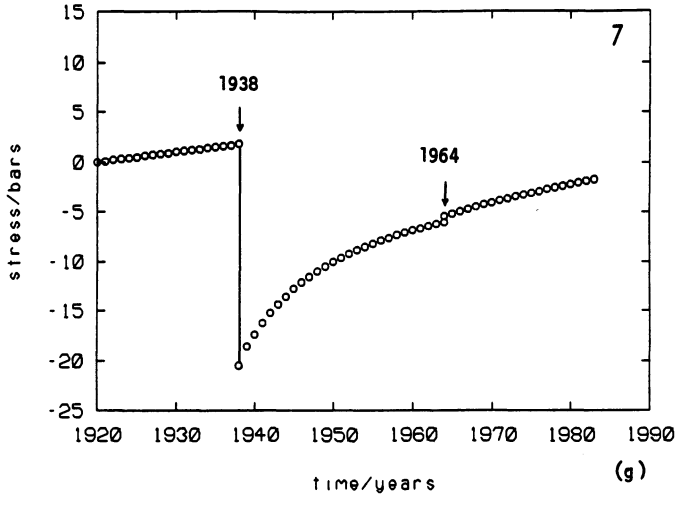

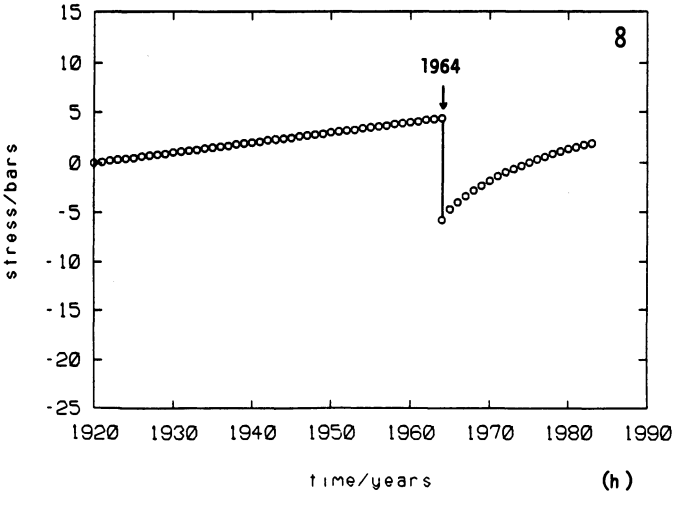

jump and more significantly, almost doubled the stress accumulation rate at the Unalaska Gap.

The 1946 and 1948 earthquakes were both very short ruptures, adjacent to each other. Their proximity in space and time suggests that the latter was triggered by the former. Figures 5d and 5e show the stress drop and recovery. Figure 5e shows the coseismic stress jump just before the 1948 earthquake. Actually the 1948 rupture has such a small down dip dimension that the stress accumulation shown in Fig. 5e may not reflect the much higher stress level in the unruptured ligament (slab interface trench-ward of the 1948 seismic source) in the same location. Indeed this part is generally regarded as the western end of the Shumagin Gap zone.

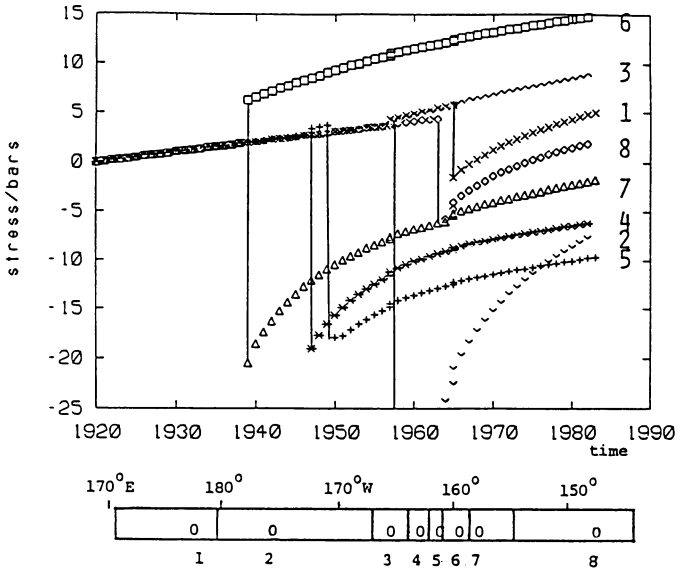

(i)

Figure 5f shows the stress accumulation at the eastern end of the Shumagin Gap, which has not had a great earthquake since the beginning of the century. The steady stress build up was boosted by the 1938 rupture which produces a large coseismic stress jump followed by an accelerated stressing rate. This high rate is apparently sustained by the 1948 rupture. The current high stress level and high stress rate makes this location the most likely candidate for the next large rupture to occur in the Aleutians. The high stress level has been confirmed by the anomalous high stress drops of small earthquakes in this location (HOUSE and BOATWRIGHT, 1980). Based on a statistical study of the recurrence interval of earthquakes along the Aleutian trench, JACOB (1983) has also suggested a high probability of a great Shumagin earthquake in the next ten years. Recently, BEAVAN *et al.* (1983) reported that geodetic measurements at the Shumagin Gap zone indicated deep aseismic slippage of as much as 80 cm during 1978–1980. Such slip would naturally load the upper parts of the lithosphere overlying the slipped zone. Although the present thickness-averaged stress model cannot account for the additional stress increase, it might be safe to assume that aseismic slippage at depth would push the locked seismogenic zone even closer to failure.

The 1938 rupture in the Alaska peninsula was the first one to occur in the sequence of earthquakes in this study. Although the stress recovery has been fairly rapid and was accelerated by the 1964 Alaska earthquake to its east, this location will probably not have another shock for the next twenty years or so (see Fig. 5g). However, if the Shumagin Gap rupture within this period, which is of high probability, stress might be transferred into this region, shortening the return period.

The 1964 Alaskan earthquake is at the eastern end of the aforementioned sequence of ruptures. The epicenter is at least six lithospheric thicknesses from the 1938 rupture so that little stress transfer is felt. Proceeding at the current stress recovery rate, it will take another twenty years to reach the critical stress again, assuming the same nucleation point for the next earthquake. It should be mentioned that the Alaskan region is tectonically quite different from the Central Aleutians. For example, the age of the Pacific Plate in the Central Aleutians is around 70 m.y. whereas the plate near Alaska is much younger, on the order of 30 m.y. (GROW and ATWATER, 1970). According to a thermal model of PARKER and OLDENBURG (1973), the lithospheric thickness in Alaska is about 30% less than the 70 km in the Central Aleutians. This would imply a corresponding 30% increase in thickness averaged stress drop shown in Fig. 5h. Also, according to MINSTER *et al.* (1974), the convergence rate is smaller in Alaska (6 cm/yr) than in the Central Aleutians. The difference in lithospheric thickness and convergence rate would both result in a lower current stress level than is suggested in Fig. 5h, although the indicated trend would still be maintained.

From the above discussions, it appears that the Shumagin Gap and the Unalaska Gap have the highest expectation of seismic rupturing in the near future. It is not possible to pin down the exact time of occurrence, given the lack of data concerning the previous ruptures in these same locations.

Figure 5i shows a composite of the stress-variations at all locations. It might be noted that the failure stress is fairly uniform, on the order of 3–5 bars above the 1960 stress level, at all places with the exception of the seismic gaps which has not yet failed. The higher stress level sustained by the seismic gaps may mean that these locations are unusually strong. But it may also be an artifact of our assuming a uniform stress level for all locations in 1960.

Concluding remarks

A general observation from the above results is that stress recovery in a ruptured segment is rapid and dominates the tectonic loading in the five to ten years after the rupture. This has the effect of shortening the repeat time in a seismic gap zone. Although stress transferred outside of the ruptured zone appears to be much smaller than the stress recovery inside, it is nonetheless significant, particularly at nearby locations. It may be fair to conclude that at least at some locations where the failure stress is approached, an adjacent rupture can be responsible for triggering the earthquake through a sudden coseismic stress jump and subsequent increase of stressing rate (e.g. locations 1 and 5). It is also clear that asthenospheric relaxation modifies the stress accumulation process, which is seen to be highly nonlinear. Seen in this light, the slip-predictable or time-predictable models of earthquake cycles as proposed by SHIMAZAKI and NAGATA (1980) must be modified to reflect this behavior.

We have shown the effect of lithosphere/asthenosphere coupling on the long-term

stress accumulation in seismic gaps and the redistribution of stress due to ruptures. To further understand the behavior in a seismic gap (e.g. is there a critical stress level constant over several earthquake cycles?), it would be necessary to analyze data of older earthquakes. This is a difficult task as an earthquake cycle typically exceeds 50 years, which means that earthquakes before the advent of modern seismological instruments would have to be examined. At any rate it is hoped that this study will establish a more realistic view of long term tectonic loading processes at plate boundaries and provide a useful basis for long range earthquake forecast procedures.

Acknowledgments

The authors would like to thank J. R. Rice for many helpful discussions in the course of this study. Critical reading of the manuscript by K. Aki and R. Dmowska is gratefully acknowledged. Suggestions by M. Matsu'ura and an anonymous reviewer provide improvements of the original manuscript. This work was initiated under contract No. 14-08-0001-20570 from the United States Geological Survey. The Esther and Harold E. Edgerton career development chair in the Department of Civil Engineering at M.I.T. provided support for the completion of this research. V.C.L. would like to thank Claire Benoit for her skilful assistance during the final stages of the preparation of this manuscript.

References

BEAVAN, J., BILHAM, R., and HURST, K. (1983), *Coherent Tilt Signals Observed in the Shumagin Seismic Gap: Detection of Time-dependent Subduction at Depth?*, submitted to J. geophys. Res.

CATHLES, L. M., *The Viscosity of the Earth's Mantle* (Princeton University Press, Princeton, N.J. 1975).

DMOWSKA, R., and LI, V. C. (1982), *A Mechanical Model of Precursory Source Processes for Some Large Earthquakes*, Geophys. Res. Lett. *9*, 393–396.

ELSASSER, W. M. *Convection and Stress Propagation in the Upper Mantle*, in *The Application of Modern Physics to the Earth and Planetary Interiors* (ed. S. K. Runcorn), (Wiley-Interscience, New York 1969), pp. 223–246.

ENGDAHL, E. R., and KISSLINGER, C. (1977), *Seismological Precursors to a Magnitude 5 Earthquake in the Central Aleutian Islands*, J. Phys. Earth *25* (supplement): S243–S250.

FEDOTOV, A. A. (1965), *Regularities of the Distribution of Strong Earthquakes in Kamchatka, the Kurile Islands, and Northeastern Japan*, Tr. Inst. Phys. Earth Acad. Sci. USSR *36*, 66–93.

GROW, J. A., and ATWATER, T. (1970), *Mid-tertiary Tectonic Transition in the Aleutian Arc*, Geological Soc. Amer. Bull. *81*, 3715–3722.

HOUSE, L., and BOATWRIGHT, J. (1980), *Investigation of Two High Stress Drop Earthquakes in the Shumagin Seismic Gap, Alaska*, J. geophys. Res. *85*, 7151–7165.

JACOB, K. H. (1983), *Aleutian Seismic Gaps Quantified: High Probability for Great Shumagin Earthquake in Next 10 years*, EOS *64*, 258.

KANAMORI, H. (1977), *The Energy Release in Great Earthquakes*, J. geophys Res. *82*, 1981–1987.

KELLEHER, J. A. (1970), *Space-time Seismicity of the Alaska–Aleutian Seismic Zone*, J. geophys. Res. *75*, 5745–5756.

LEHNER, F. K., LI, V. C., and RICE, J. R. (1981), *Stress Diffusion Along Rupturing Plate Boundaries*, J. geophys. Res. *86*, 6155–6169.

LI, V. C., *Stressing Processes Associated with Great Crustal Earthquakes at Plate Boundaries* (Ph.D. Thesis, Brown University 1981).

LI, V. C., and RICE, J. R. (1983a), *Preseismic Rupture Progression and Great Earthquake Instabilities at Plate Boundaries*, J. geophys. Res. *88*, 4231–4246.

LI, V. C., and RICE, J. R. (1983b), *Precursory Surface Deformation in Great Plate Boundary Earthquake Sequences*, Bull. seism. Soc. Am. *73*, 1415–1434.

MAVKO, G. M. (1983), *Large-scale Earthquakes from a Laboratory Friction Law*, submitted to J. geophys. Res.

MATSU'URA, M., and IWASAKI, T. (1983), *Study on Coseismic and Postseismic Crustal Movements Associated with the 1923 Kanto Earthquake*, Tectonophysics *97*, 201–215.

MCCANN, W. R., NISHENKO, S. P., SYKES, L. R., and KRAUSE, J. (1979), *Seismic Gaps and Plate Tectonics: Seismic Potential for Major Boundaries*, Pure appl. Geophys. *117*, 1082–1147.

MINSTER, J. B., and JORDAN, T. H. (1978), *Present Day Plate Motions*, J. geophys. Res. *83*, 5331–5354.

MINSTER, J. B., JORDAN, T. H., MOLNAR, P., and HAINES, E. (1974), *Numerical Modelling of Instantaneous Plate Tectonics*, Geophys. J. Royal Astron. Soc. *36*, 541–576.

MOGI, K. (1968), *Migration of Seismic Activity*, Bull. Earthq. Res. Inst. Tokyo Univ. *46*, 53–74.

MOGI, K. (1969), *Some Features of Recent Seismic Activity In and Near Japan (2), Activities Before and After Great Earthquakes*, Bull. Earthq. Res. Inst. Tokyo Univ. *47*, 395–417.

MOGI, K., *Seismic Activity and Earthquake Prediction*, in *A Symposium on Earthquake Prediction Research* (eds. Z. Suzuki and S. Omote) (Seismological Society of Japan, Tokyo 1977), pp. 203–14 (in Japanese).

MOGI, K. (1979), *Two Kinds of Seismic Gaps*, Pure appl. Geophys. *117*, 1172–1186.

PARKER, R. L., and OLDENBURG, D. W. (1973), *A Thermal Model of Oceanic Ridges*, Nature, *242*, 137–139.

PURCARU, G., and BERCKHEMER, H. (1982), *Quantitative Relations of Seismic Source Parameters and a Classification of Earthquakes*, Tectonophysics *84*, 57–128.

RICE, J. R., *The Line Spring Model for Surface Flaws*, in *The Surface Crack: Physical Problems and Computational Solutions* (ed. J. L. Swedlow) (ASME, New York 1972), pp. 171–185.

RICE, J. R., *The Mechanics of Earthquake Rupture*, in *Physics of the Earth's Interior* (eds. A. M. Dziewonski and E. Boschi) (Italian Physical Society/North-Holland, Amsterdam 1980), pp. 555–649.

SHIMAZAKI, K., and NAKATA, T. (1980), *Time-predictable Recurrence Model for Large Earthquakes*, Geophys. Res. Lett. 279–282.

STUART, W. D., and MAVKO, G. M. (1979), *Earthquake Instability on a Strike-slip Fault*, J. geophys. Res. *84*, 2153–2160.

STACEY, F. D., *Physics of the Earth*, 2nd ed. (John Wiley, New York 1977).

SYKES, L. R. (1971), *Aftershock Zones of Great Earthquakes, Seismicity Gaps, and Earthquake Prediction for Alaska and the Aleutians*, J. geophys. Res. *76*, 8021–8041.

SYKES, L. R., KISSLINGER, J. R., HOUSE, L., DAVIES, J. N., and JACOB, K. H., *Rupture Zones and Repeat Times of Great Earthquakes Along the Alaska–Aleutian Arc, 1784–1980*, in *Earthquake Prediction – An International Review* (eds. D. W. Simpson and P. G. Richards) (AGU 1981), pp. 73–80.

THATCHER, W. (1983), *Nonlinear Strain Buildup and the Earthquake Cycle on the San Andreas Fault*, J. geophys. Res. *88*, 5893–5902.

THATCHER, W., and RUNDLE, J. B. (1979), *A Model for the Earthquake Cycle in Underthrust Zones*, J. geophys. Res. *84*, 5540–5556.

PAGEOPH, Vol. 122 (1984/85) 0033-4553/85/060831-17$1.50 + 0.20/0

High-velocity Migration of Large Earthquakes along the Azores–Iran Plate Boundary Segment

By KLAUS MEYER, RUNE OLSSON and OTA KULHÁNEK[1])

Abstract – Between 1 January 1980 and 28 July 1981, a series of large earthquakes with body-wave magnitudes around 7, took place along the western segment of the Alpide belt. The sequence started in the Azores and migrated eastward along the belt at a rate of about 4400 km/yr with consecutive large events in northern Algeria, southern Italy, southern Greece and Iran. Two different methods are employed to identify similar series and corresponding migration velocities during earlier time periods of this century. The data set used contains all earthquakes with body-wave magnitudes larger than 6.3 and covers the time interval 1901–81. The concept of linear migration is tested for eastward and/or westward propagation, considering high migration velocities from 1600 to 11 000 km/yr. Results obtained are not homogeneous with respect to the two opposite migration directions, west–east and east–west, and we interpret this as a net drift of earthquake activity from the west to the east. Our efforts here are concentrated on analysis of observational data and on establishing the uniqueness of migration patterns. Because of the complexity of the tectonic system in question, we did not attempt to establish a mechanism explaining the migration of the observed earthquake sequences.

Introduction

On 1 January 1980, a large earthquake occurred in the Azores, the western extremity of the Eurasian–African plate boundary. About nine months later, on 10 October, another large event took place at El Asnam, northern Algeria, about 2600 km east of the 1 January event. The sequence of large magnitude events in the Azores–Iran area continued with a shock near Naples in southern Italy on 23 November. The west–east progression of the three events with a fairly even migration velocity initiated our interest to discriminate whether or not the series could be attributed to a systematic west–east migration of large earthquakes along the seismically active belt. The succession continued in 1981. On 24 February, 25 February and 4 March 1981, a series of three large earthquakes shook the area of Corinth, southern Greece. The three events fit well the suspected pattern of west–east migration of foci with velocity of about 4400 km/yr. The epicentres of the Corinth sequence themselves moved 40 km eastward between 24 February and 4 March (KIM *et al.*, 1983). Finally, on 11 June and 28 July, two large shocks hit southern Iran, the latter most likely being an aftershock.

[1]) Seismological Department, Uppsala University, Uppsala, Sweden, Box 12019, S-75012 Uppsala, Sweden.

Earthquake migration along various segments of the Alpide belt, such as the Mediterranean area or northern Anatolia in particular, have been studied earlier by PROCHÁZKOVÁ (1973), MOGI (1974), RITSEMA (1975), DEWEY (1976), TOKSÖZ *et al.* (1979), PURCARU and BERCKHEMER (1982), among others. Table 1 provides a list of some of the reported foci migrations along portions of the Alpide belt. It follows from the table that both eastward and westward progressions of earthquakes with a broad range of migration velocities are discernible. In all cases in Table 1, migration patterns of foci were identified visually and consequently suffer from the drawback of being to a large extent subjective, i.e. non-unique. The occurrence of migration in two directions, as well as the wide variation of migration velocities along the active suture (Table 1), may lead to the conclusion that there is no systematic migration in either direction. However, the high-velocity west–east migration of the 1980–81 sequence is so clearly distinguishable that we feel confident in describing this pattern as one mode of migration in the Azores–Iran region that may occur along with other types of migration (reported by previous authors).

There is a wealth of literature dealing with space-time studies in other seismically active regions (see BÅTH, 1979). For example, a summary of results concerning various segments of the Circum–Pacific belt may be found in IDA (1974) or elsewhere. Generally speaking, migration parameters revealed in other regions resemble those derived from investigations in the Alpide belt (Table 1).

In the present study, we address the question of whether or not a dominant linear (i.e. unidirectional, constant-velocity) migration of earthquake hypocentres, similar to the 1980–81 series, does exist along the Alpide system or along some part of it. Seismic

Table 1

Earthquake migration along the Alpide belt

Area	Direction of migration	Velocity of migration (km/yr)	Data used	Reference
Azores fault	westward	~50	1901–1969 $M \geq 5.5$	PROCHÁZKOVÁ (1973)
Hellenic arc	eastward	15–30	1600–1978 $M \geq 6.75$	PURCARU and BERCKHEMER (1982)
Eastern Mediterranean	westward	7–70	1900–1974 $M \geq 7.0$	RITSEMA (1975)
Northern Anatolia	westward	50–90	1901–1969 $M \geq 7.0$	PROCHÁZKOVÁ (1973)
Northern Anatolia	westward	100	1900–1960 $M \geq 7.0$	MOGI (1974)
Northern Anatolia	westward	50–100	1939–1967 $M \geq 6.0$	DEWEY (1976)
Northern Anatolia	westward eastward	50–100 ~10	1910–1976 $M \geq 5.9$ (I > VII)	TOKSÖZ *et al.* (1979)

sequences so far observed along global seismic belts show durations of several decades and corresponding migration velocities are rather low, about 100 km/yr or less. It has to be emphasized that, in contrast, observational data and processing techniques employed in this paper refer to short-duration cycles of 1–3 years and to high-velocity migration of the order of several thousand km/yr.

In spite of many unknowns, established migration patterns of large earthquakes seem to represent a promising method in long- and medium-term prediction. The successful forecast of the 1975 Haicheng earthquake, in which migration observations had been employed, may serve as the best example. However, before individual migration patterns can be accepted as long- or medium-term precursors, their reality and uniqueness must be proved. Also, a physical explanation of the migration mechanism in terms of seismotectonic regimes of the area in question is needed. Below, we present two different methods for identification of migration patterns. One of the methods is complemented with a simple test of the statistical significance of obtained results. Both methods are examined with a real earthquake catalogue.

Earthquake data

The earthquake information used in this study covers the time interval from 1901 to 1981. We concentrated our investigation on the western segment of the Alpide belt extending from the Azores to Iran. Consequently, we limit our search to the region bordered by the latitudes and longitudes of 25–50°N and 40°W–60°E, respectively. Hypocentral data were taken from a wide variety of sources such as Bulletin of the Bureau Central International de Séismologie (BCIS), Bulletin of the International Seismological Centre (ISC), Bulletin of the US Coast and Geodetic Survey (USCGS, later also NOAA, NEIC, NEIS and PDE), COMNINAKIS and PAPAZACHOS (1978), GUTENBERG and RICHTER (1954), International Seismological Summary (ISS), KÁRNÍK (1969), Norwegian Seismic Array (NORSAR), Seismological Bulletin Uppsala and SHEBALIN *et al.* (1974).

An attempt was made to collect all large earthquakes of this century, foreshocks and aftershocks excluded, that fell within the region. For this reason, main shock–aftershock sequences such as the Azores sequence of January 1980 or the Gulf of Corinth sequence of February–March 1981 are here represented by respective main shocks only and cannot be studied in more detail by methods proposed below. An event was considered a foreshock/aftershock if it occurred less than one month before/after and less than one degree from the main shock. All events included in the analysis, altogether 161 earthquakes, are summarized in the Appendix.

Magnitudes listed in the original sources mentioned above, represent a certain problem because different agencies often determine magnitudes in different scales. The fact that surface-wave magnitudes have been reported more systematically only after the adoption of the so-called Moscow–Prague formula of 1962 and also that a number of

events employed (see Appendix) are of intermediate focal depth, requires a consistent application of the body-wave magnitude. To establish a catalogue with homogeneous magnitudes, we therefore decided to make use of Uppsala body-wave magnitudes, hereafter labelled m(UPP, KIR), determined as arithmetic means of magnitudes evaluated separately from measurements of Uppsala and Kiruna seismograph stations. For the interval 1952 to date, m(UPP, KIR) are directly available as they are regularly reported in the Seismological Bulletin Uppsala. For the events prior to 1952, given magnitudes of studied earthquakes usually refer to those listed by KÁRNÍK (1969) or to Pasadena magnitudes. Hence, to arrive at a homogeneous catalogue, we converted the accessible magnitudes m(PAS) and/or M(KAR) for the pre-1952 events into corresponding m(UPP, KIR) values. Linear regression $m(\text{PAS}) \rightarrow m(\text{UPP, KIR})$ has been derived by using magnitude pairs for the time period February 1953–September 1962, i.e. for the entire interval for which both the m(UPP, KIR) and M(PAS) values are on hand. Within this time period and the area studied, parallel magnitude determinations ($5.9 \leqslant m(\text{UPP, KIR}) \leqslant 7.8$; $5.9 \leqslant m(\text{PAS}) \leqslant 8.3$) for 40 events have been collected. The resulting regression reads

$$m(\text{UPP, KIR}) = 1.17\, m(\text{PAS}) - 1.14 \tag{1}$$

The catalogue of KÁRNÍK (1969) spans the period 1901–1955, and hence we have merely four years, namely 1952–1955, of parallel magnitude determinations of m(UPP, KIR) and m(KAR). Thus, when employing Kárnik's magnitudes, rather than performing the direct conversion $m(\text{KAR}) \rightarrow m(\text{UPP, KIR})$ we make use of a two-step conversion such as $m(\text{KAR}) \rightarrow m(\text{PAS}) \rightarrow m(\text{UPP, KIR})$. The first step is carried out through a regression

$$m(\text{PAS}) = 0.86\, m(\text{KAR}) + 0.90 \tag{2}$$

while the second step by using regression (1). Equation (2) is the least-squares fit to all available magnitude pairs m(PAS)–m(KAR) from the interval 1901–1955. Altogether, data from 36 earthquakes, within the magnitude intervals of $5.5 \leqslant m(\text{KAR}) \leqslant 7.9$ and $5.5 \leqslant m(\text{PAS}) \leqslant 8.3$, were collected.

While the choice of a cut-off magnitude is somewhat arbitrary, it should nevertheless ensure the completeness of the data. Nearly all seismic energy released should be considered, but at the same time small events, contributing only to the background noise in space-time diagrams should be avoided. The data set treated here has been limited to cases with m(UPP, KIR) $\geqslant 6.4$. With respect to the selection applied, the list of earthquakes considered is assumed to be homogeneous and as complete as original sources permit. The events have been selected regardless of focal depth.

Methods

By migration of seismic activity we mean a unidirectional progression of earthquake foci within a limited geographical region and time period. The east–west trending plate

boundary between Eurasia and Africa is relatively narrow and simple between the Atlantic and Tunisia, i.e. from 30°W to 12°E, but becomes rather complex, including a number of subplates, between Italy and Iran. Due to the elongated shape of the area studied, only one space coordinate, the longitude of epicentres, has been considered. Available epicentral longitudes were plotted in Fig. 1 as a function of time of occurrence of respective earthquakes. At first sight, a visual check of these diagrams does not provide any evidence of a dominant direction of migration. In order to carry out a more systematic and semi-objective search for possible high-velocity propagation, two different procedures have been used.

Least-squares procedure. By making use of the above longitude–time diagram, the time period 1901–1981 has been divided into intervals of width increasing in steps of 0.2 yr from 0.5 to 6 yr. Intervals of a given width were moved along the time axis with time increments of 0.1 yr. For each interval position, the number of earthquakes within the

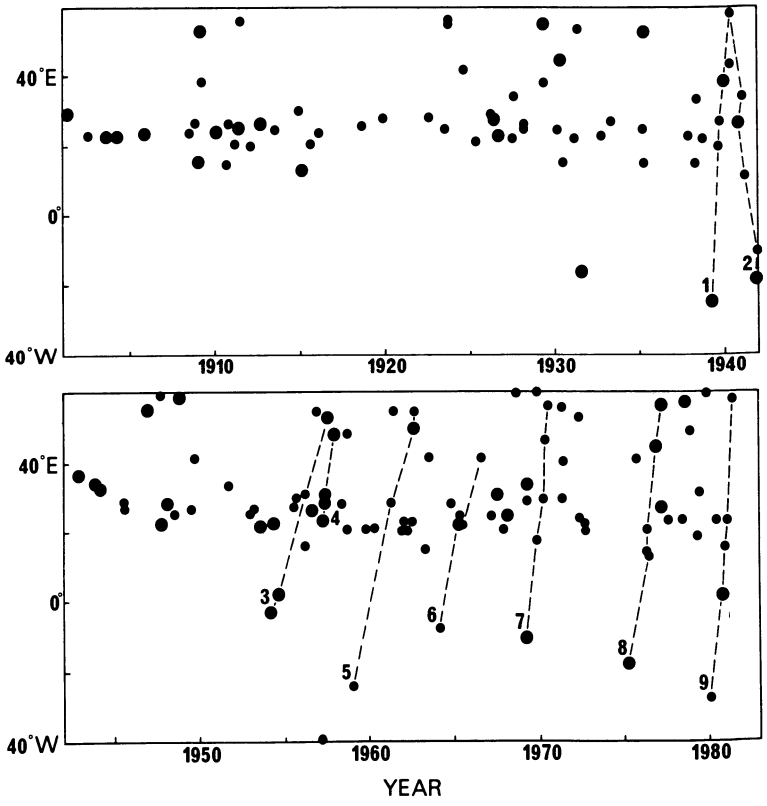

Figure 1

Longitude–time diagram of earthquakes used in this study. Small circles denote $6.4 \leqslant m(\mathrm{UPP, KIR}) < 7.0$; large circles denote $m(\mathrm{UPP, KIR}) \geqslant 7.0$. Depicted epicentres refer to the time interval 1901–1981. Broken lines show the migration sequences: sequence numbers are those used in Table 3.

interval was counted. If the number of shocks was equal to or larger than a chosen number n, we fitted a least-squares straight line to the epicentres in the longitude–time plot and determined the corresponding correlation coefficient, R, between time and longitude. If the number of lines with positive slopes is significantly greater than the number of lines with negative slopes, we interpret this as a net migration in the eastward direction. As the subdivision can be made in an almost unlimited number of ways, we consider selected intervals as a sample and because of the great size of this sample we let it represent the whole population. Hence, the true relative frequency, p_{true}, of positive slopes can be approximated by the same relative frequency, p, computed from the sample. Intervals of confidence are determined by using the formula

$$p - k\sqrt{\frac{p(1-p)}{N_R}} \leqslant p_{\text{true}} \leqslant p + k\sqrt{\frac{p(1-p)}{N_R}} \tag{3}$$

where N_R is total number of regressions and k is a constant, specific for the chosen level of significance. Table 2 lists confidence intervals for a net eastward migration for five different magnitude classes. As most of the correlations are close to zero, even a small change in the condition for the least-squares fitting, such as a change of the minimum number of shocks accepted in each interval, may alter the result. Accordingly, the intervals of confidence are computed only on the basis of correlation coefficients $R \leqslant -0.5$ and $R \geqslant 0.5$. Obviously, these limits are selected arbitrarily but there is no dramatic change in the results if they are chosen somewhat broader or narrower. Results summarized in Table 2 reveal, for example, that the probability that 55–63% of the 63 earthquakes of magnitude 6.9 and greater line up with positive slopes in the longitude–time diagram is 99.99%. The calculation has been based only on a sample (size 1380) of regression coefficients of absolute values $\geqslant 0.5$ and a minimum number of 5 shocks per interval.

Table 2

*Confidence intervals for net eastward migration and level of significance for varying Δm.**

Δm	Interval of confidence for net eastward migration	Level of significance	n	N	N_R
≥ 6.6	0.50–0.54	95%	≥ 5	118	1869
≥ 6.7	0.50–0.54	95%	≥ 5	111	1707
≥ 6.8	0.51–0.55	95%	≥ 5	94	1489
≥ 6.9	0.55–0.63	99.99%	≥ 5	63	1380
≥ 7.0	0.70–0.82	99.99%	≥ 4	50	897

* Δm denotes the magnitude interval considered; n is the minimum number of shocks per interval position; N gives the total number of shocks; N_R is the number of calculated regressions with correlation coefficients $R \leq -0.5$ or $R \geq 0.5$.

It seems convincing from Table 2 that the material used is not homogeneous with respect to the two, eastward and westward, possible directions of migration. The performed statistical test (Table 2) suggests a rather diffuse eastward net shift of epicentres. Calculated results are not listed for smaller, m(UPP, KIR) <6.6, earthquakes, but for no magnitude interval of m(UPP, KIR) $\geqslant 5$, has a significant indication of migration in the westward direction been revealed. Table 2 gives also an impression that the eastward drift is greater for large shocks. This may, however, be partly a consequence of the method, i.e. due to the relatively small number of shocks in these magnitude intervals. There is a clear tendency (not seen in Table 2) of increasing significance of eastward migration with increasing time. This is in agreement with results obtained from the second method and also with the visual impression from the longitude–time plots.

Tilting-window procedure. The second procedure applied to our data is basically a procedure of VIL'KOVICH and SHNIRMAN (1979). Any straight line in the longitude–time diagram represents a constant migration rate. In other words, epicentres that lie on or close to a line form succession at a certain, constant, migration velocity. The angle, α, between the line and the time axis reflects the migration velocity (see Fig. 2). It follows from Fig. 2, that angles $0 < \alpha < 90°$ or $90° < \alpha < 180°$ denote eastward or westward migration, respectively. According to the definition, $\tan \alpha$ has a physical meaning of velocity in longitude degrees per year. In practice, one cannot assume a perfectly linear, i.e. constant-velocity unidirectional migration, but rather a range of velocities and directions is most likely. In longitude–time plots, this implies that the presumed

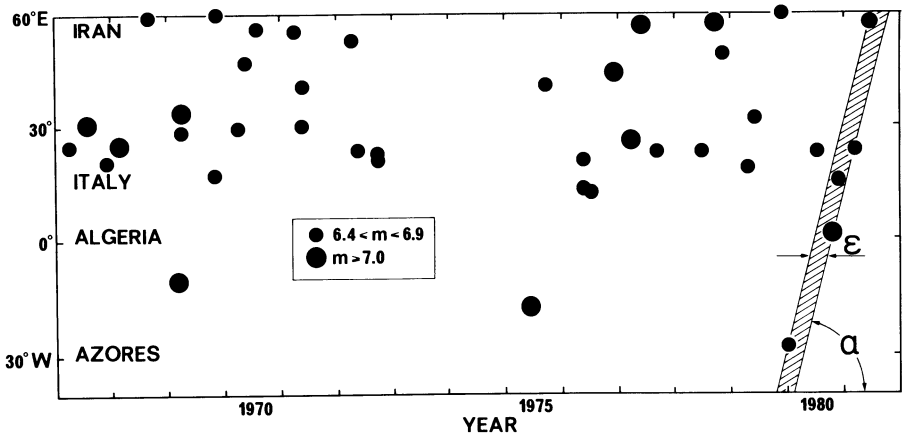

Figure 2

Portion (1967–81) of the longitude–time plot of large earthquakes in the western segment of the Alpide belt used in this study. The hatched area represents a particular position, corresponding to the 1980–81 sequence, of the tilting window with $\varepsilon = 0.3$ yr and $\tan \alpha = 50°$/yr.

earthquake sequence does not necessarily fit a straight line but falls within a time window of width ε. It is obvious, that variations in migration velocity, deviations from the unidirectional, i.e. west–east (or east–west), epicentre wandering and mislocation of events, all contribute to the scatter of points around ideal straight lines in longitude–time plots. In this study, for a given α and ε, we applied windows moving along the time axis at steps of 0.05 yr and define a quality function

$$q(\alpha, \varepsilon) = \sum_{i=1}^{k} [n(t_i)]^4 \tag{4}$$

where t_i denotes position of the ith window along the time axis, $n(t_i)$ is the number of earthquakes within the ith time window and k is the total number of windows applied. The q-function in equation (4) determines the degree of agreement of earthquake foci in a longitude–time plot with a system of parallel strips (of width ε and tilt α) on this plot (VIL'KOVICH and SHNIRMAN, 1979). The fourth power in the right-hand part of equation (4) is used merely to accentuate cases of window positions with large n.

There are some practical difficulties in q calculations. Firstly, due to the local dependence, all foreshocks, aftershocks and swarms should be deleted from the data set. Secondly, the choice of ε is rather critical. In this work, contributions to $q(\alpha, \varepsilon)$ are accepted only if $n \geqslant 4$. Using narrow ε, we approach the ideal linear migration pattern and may expect rather few contributions to $q(\alpha, \varepsilon)$. On the other hand, a wide ε leads to large q-values which, however, hardly have any meaning in the sense of wandering foci. The choice of ε reflects the *a priori* accepted deviations from the ideal linear migration. q-functions have been computed for ε-values of up to 0.5 yr. Velocities, i.e. tan α, varied from 15 to 130°/yr, in 1°/yr increments. Calculated q-values were smoothed taking the maximum, $\bar{q}$, of five successive q-values, i.e. smoothing is performed over moving migration velocity intervals of 5°/yr.

Space-time seismicity of the Azores–Iran segment

In Fig. 3, $\bar{q}$-values versus migration velocity, tan α, are displayed for window widths of 0.2 and 0.3 yr. The dependence of $\bar{q}(\alpha, \varepsilon)$ upon the window-width, ε, is in good agreement with the above discussion. In general, $\bar{q}$-values increase with increasing ε, i.e. there are more contributions to the $\bar{q}$-function when ε is wider. For large ε, $\bar{q}$-values for two opposite migration directions, east–west and west–east, resemble each other. $\bar{q}$-functions for the two directions are practically equal for $\varepsilon \geqslant 0.5$ yr, indicating that a possible dominant migration in either direction is contaminated by the choice of a wide ε. If, on the other hand, the window is as narrow as 0.1 yr, only one or two earthquakes contribute to the $\bar{q}$-values in each interval and it becomes impossible to draw any conclusion from it. Thus, window widths of 0.2 to 0.3 yr are considered as optimal for the purpose of this study.

It can be seen in Fig. 3, that for high migration velocities, $v_m \geqslant 20°$/yr ($\sim$1800

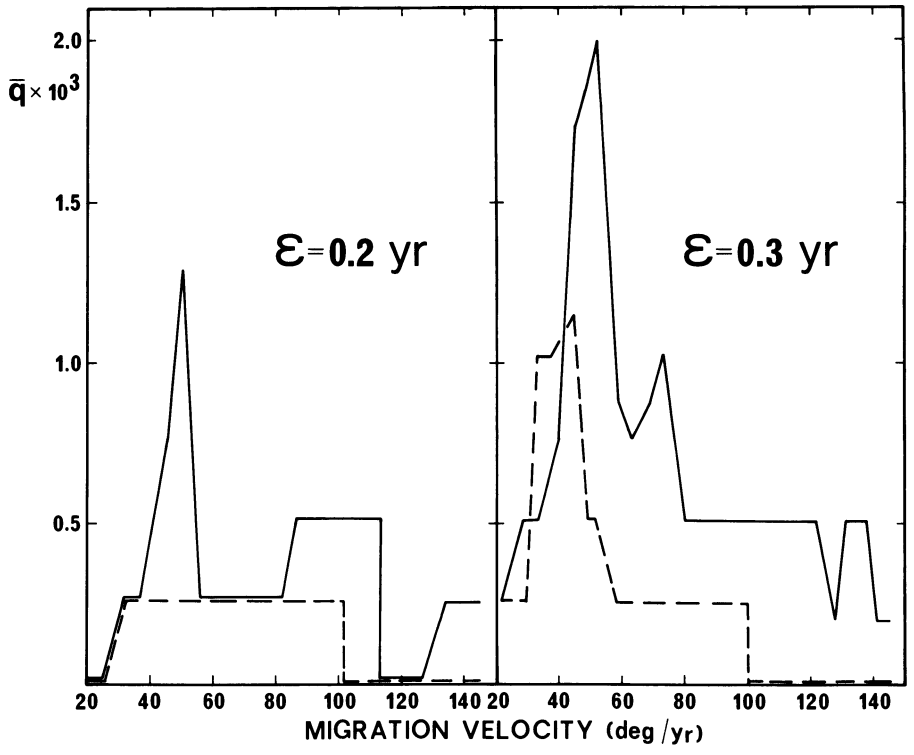

Figure 3

$\bar{q}$-values as function of migration velocity. Results for eastward (solid line) and westward (dashed line) migration and for two different window widths, ε, are displayed. All earthquakes from the time period 1901–1981 within the western segment of the Alpide belt and magnitude interval m(UPP, KIR) $\geqslant 6.4$ have been considered (see Appendix).

km/yr), $\bar{q}$-functions reach their maxima for v_m between 40 and 60°/yr (~3500–5300 km/yr). Within the velocity range of 60 to 120°/yr, calculated $\bar{q}$-functions show a descending tendency even though additional local maxima do occur in the plots. For $v_m > 120$°/yr, the method is hardly applicable due to a poor velocity resolution, i.e. small changes in α result in large changes of v_m ($\tan \alpha$). Displayed $\bar{q}$-functions for eastward migration have higher magnitude when compared with those of the opposite, i.e. westward, migration direction. This is in general agreement with results of the above least-squares procedure and related to the fact that the correlation between longitude and time is greater for windows with positive slopes (eastward migration). Further, it appears that there is no single dominating migration velocity but rather an interval of possible velocities. Considering the present earthquake catalogue, the conclusions from our undertaking read: windows of widths $\varepsilon = 0.2$–0.3 yr are optimal for establishing linear migration waves; $\bar{q}$-functions reach their maxima for v_m between 40 and 60°/yr; $\bar{q}$-functions for the west–east migration are larger than those for the east–west migration.

Table 3

Examples of possible migration sequences

Sequence number	Time interval	Longitude limits	Migration velocity long. degrees/yr	Direction of migration
1	May 1939–May 1940	34°W–58°E	75	eastward
2	May 1940–Dec 1941	58°E–18°W	50	westward
3	Mar 1954–Jul 1957	4°W–53°E	20	eastward
4	Mar 1957–Dec 1957	22°E–48°E	37	eastward
5	Jan 1959–Oct 1962	25°W–55°E	22	eastward
6	Mar 1964–Aug 1966	8°W–42°E	27	eastward
7	Feb 1969–Jul 1970	11°W–56°E	46	eastward
8	May 1975–Mar 1977	18°W–57°E	40	eastward
9	Jan 1980–Jul 1981	28°W–58°E	50	eastward

A question may arise as to whether or not a distinct peak in the $\bar{q}$-function at velocity around 50°/yr, such as in Fig. 3 ($\varepsilon = 0.3$ yr, eastward migration), reflects the existence of a single earthquake sequence during the entire time interval reviewed. To investigate this problem in more detail, the time period of 1952–1981, for which original Uppsala magnitudes are available, was divided into four equal non-overlapping time segments and corresponding quality functions were computed for each segment. Results obtained resemble those corresponding to the whole time interval 1901–1981. Since each independent segment gives the same behaviour, we can conclude that within the area investigated there is a dominant 'time stationary' west–east migration of earthquake foci. From the compiled catalogue, we also tried to select case histories of migration similar to that of 1980–81 which has been described above. In doing this, we counted the number of epicentres per moving window as a function of time and v_m and selected window positions and corresponding velocities with anomalously large numbers of events. Obtained results are listed in Table 3 and depicted in Fig. 1. BÅTH (1979) reports on two earthquake sequences in 1962 and 1976 migrating with high velocity of about 12–14 km/hour from North Atlantic to Burma and from Italy to Iran, respectively. The two sequences comprise also events with m(UPP, KIR) < 6.4 and extend as far as to southern Asia and hence are not detectable in our data set (Fig. 1, Appendix).

Discussion

Generally speaking, the time-space distribution of epicentres within a limited time interval and geographical region follows either a random or a regular pattern. The least-squares procedure, applied to the former case, should in the long run provide a fairly equal division into easterly and westerly oriented migrations. This, however, was

not the case as follows from Table 2. A small but uniform excess of regression lines in positive directions, corresponding to west–east migrations, indicates a non-random space-time distribution of large earthquakes between the Azores and Iran during 1901–1981. The present authors are fully aware of the fact that the migration parameters adopted here are somewhat arbitrary and certainly non-unique, mainly due to the specific selection of data and to a lesser extent also due to the methods used (such as the choice of ε). In this context, we would like to emphasize that the observations employed cover the entire so-called instrumental-time period, the area studied extends practically along the whole western segment of the Alpide belt and the magnitude threshold has been chosen with respect to the completeness of the catalogue. This means that the present data have by no means been chosen in such a way as to 'optimize' the suspected foci migration. Besides, consistent results are confirmed by two different methods. Hence, we conclude that the observed migration is real and independent of any personal preference of the researcher making the measurements.

The studied migration velocities vary from 15 to 130°/yr (~1300–11 000 km/yr). The 1980–81 sequence, the most distinct one among the probable migrations investigated here, has an average eastward migration rate of 4400 km/yr. Velocities of this magnitude imply that the time duration of the sequence from the western to the eastern edge of the segment is less than two years. Only a few earlier investigations (e.g. BÅTH, 1979; KAGAN and KNOPOFF, 1976) report such high velocities. It should be stressed that the resolution of the tilting-window method as applied to the present catalogue (Appendix) does not make it possible to study migration velocities of less than, say, 15°/yr. Consequently, some of the well-established migration sequences in the area studied, the sequence along the north Anatolian fault in particular, can not be revealed by the approach described above. Note that the north Anatolian sequence of 1939–1953 discussed by MOGI (1974) shows a migration velocity of about 0.6°/yr. Such a migration rate, represented by an almost horizontal line in Fig. 1, falls far off the velocity range detectable by the present method (see also Fig. 3). This is also the case for the remaining sequences listed in Table 1.

There are no clear systematic recurrences of migrating series in the Azores–Iran segment (Table 3). Nevertheless, some periodicity may be suggested from the rather regular occurrence of large shocks in the western part of the segment. From the catalogue and the complete space–time diagram in Fig. 1, it is possible to select large earthquakes west of 3°W, occurring at regular time intervals, namely in 1954, 1959, 1964, 1969, 1975 and 1980, i.e. once every fifth year. As follows from Fig. 1, these earthquakes are also starting events for sequences 3, 5, 6, 7, 8 and 9, migrating eastward with velocities from 22 to 50°/yr.

The mechanism that governs propagation of large earthquakes is still poorly understood. Several, rather hypothetical, models have earlier been suggested by other workers to account for possible causal links between tectonic regimes and space-time seismicities. MOGI (1974) presents two possible mechanisms for earthquake migrations. In the first mechanism, the migration of large shocks is considered to be analogous to

the propagatin of a new shear fracture in a laboratory experiment. In the second mechanism, the pre-determined fracture plane is assumed to be the boundary between two tectonic plates. After large earthquakes, stresses are partially or completely released within the focal area. At the same time, stresses may increase, through mechanical coupling, in neighbouring areas and hence earthquakes take place successively along the boundary. In both mechanisms, constant external stresses are assumed. The concept of decoupling earthquakes is discussed in more detail by KANAMORI (1971) and by ANDERSON (1975) for large earthquakes along an arc.

Drawbacks of the above models become apparent when considering real earthquake volumes and velocities of slip propagations. Magnitudes m(UPP, KIR) $\geqslant 6.4$ are usually associated with source dimensions of, say, 30 km and larger. On the other hand, distances between successive events in a single sequence are often several hundreds or thousands of kilometres, i.e. at least of the order of magnitude larger than the linear source dimensions. Thus, it is not possible to explain the observed successions in terms of mechanical couplings. The same applies to the slip propagation with typical velocity slightly less than the S-wave velocity. Such a high velocity would require the events of an entire single sequence to occur practically simultaneously and corresponding epicentres should line up vertically in the longitude–time diagram. This is, however, not the case (Fig. 1) and explanations in terms of the above models become rather unconvincing (VIL'KOVICH and SHNIRMAN, 1982).

The area studied represents a highly heterogeneous tectonic system with different faulting styles and rates of motion. The Azores–Gibraltar line and the north Anatolian fault represent essentially a strike-slip motion and the Hellenic arc and the Zagros fault are thrust-type collisions, whereas most of the activity in the Aegean is due to extensional tectonics. Such a variety of tectonic units *a priori* excludes the idea of a single stress system uniformly affecting all of the earthquake source volumes considered. The problem is rather complex and much remains here to be investigated. Deciphering the triggering mechanisms of earthquake sequences remains a topical research subject because it would constitute a major step toward the eventual prediction of the phenomena. We have enjoyed some success in objectively detecting unidirectional progression of earthquake foci but we lack a plausible explanation for the mechanism generating the observed migration.

Conclusions

The present study offers evidence (via two different methods) of linear migration of earthquake foci in the western segment of the Alpide belt during the interval 1901–1981. The results may be summarized as follows:

1. A prevailing eastward progression of large earthquakes, m(UPP, KIR) $\geqslant 6.4$, has been identified between the Azores and Iran.

2. Propagation velocities for individual probable migration sequences have dominant values of 3500 to 5300 km/yr.

Acknowledgments

This investigation has been carried out at the Seismological Department Uppsala, Sweden, with financial support from the Swedish Natural Science Research Council under the contract G-GU 3164-115. We are grateful to H. Bungum of NORSAR, for complete computer lists with hypocentral parameters. We appreciate comments of the anonymous reviewer who emphasized to us the tectonic complexity of the area in question.

References

ANDERSON, D. L. (1975), *Accelerated Plate Tectonics*, Science *187*, 1077–1079.

BÅTH, M., *Introduction to Seismology*, 2nd edn (Birkhäuser Verlag 1979), pp. 304–308.

COMNINAKIS, P. E., and PAPAZACHOS, B. C., *A Catalogue of Earthquakes in the Mediterranean and the Surrounding Area for the Period of 1901–1975* (Univ. Thessaloniki, Geophys. Lab. Publ. 5, 1978).

DEWEY, J.W. (1976), *Seismicity of Northern Anatolia*. Bull. Seism. Soc. Am. *66*, 843–868.

GUTENBERG, B., and RICHTER, C. F., *Seismicity of the Earth and Associated Phenomena* (Princeton Univ. Press 1954).

IDA, Y. (1974), *Slow-moving Deformation Pulses Along Tectonic Faults*, Phys. Earth Plan. Int. *9*, 328–337.

KAGAN, Y., and KNOPOFF, L. (1976), *Statistical Search for Non-random Features of the Seismicity of Strong Earthquakes*, Phys. Earth Plan. Int. *12*, 291–318.

KANAMORI, H. (1971), *Great Earthquakes at Island Arcs and the Lithosphere*, Tectonophysics *12*, 187–198.

KÁRNÍK, V., *Seismicity of the European Area* (Reidel Publish. Comp. 1969).

KIM, W. Y., KULHÁNEK, O., and MEYER, K. (1984), *Source Processes of the 1981 Gulf of Corinth Earthquake Sequence from Body-wave Analysis*, Bull. Seism. Soc. Am. *74*, 459–477.

MOGI, K. (1974), *Active Periods in the World's Chief Seismic Belts*, Tectonophysics *22*, 265–282.

PROCHÁZKOVA, D. (1974), *Migration of Earthquake Foci in Europe*, Pure appl. Geophys. *110*, 2005–2011.

PURCARU, G., and BERCKHEMER, H. (1982), *Regularity Patterns and Zones of Seismic Potential for Future Large Earthquakes in the Mediterranean Region*, in *Earthquake Prediction*, vol. 85 (eds A. Hales and Z. Suzuki), pp. 1–30.

RITSEMA, A. R., *Seismic sequences in the European Mediterranean*, in *XIVth Gen. Assembly European Seismology Comm. Proc.* (ed. H. Stiller) (NGG Akad. Wissensch. DDR, Berlin 1975).

SHEBALIN, N. V., KÁRNÍK, V., and HADZIEVSKI, D. (Editors), *Catalogue of Earthquakes. Part I, 1901–1970. UNDP/UNESCO Survey of the Seimicity of the Balkan Region* (UNESCO, Skopje 1974).

TOKSÖZ, M. N., SHAKAL, A. F., and MICHAEL, A. J. (1979), *Space-time Migration of Earthquakes Along the North Anatolian Fault Zone and Seismic Gaps*, Pure appl. Geophys. *117*, 1258–1270.

VIL'KOVICH, E. V., and SHNIRMAN, M. G. (1979), *An Algorithm for Establishing the Migration of Strong Earthquakes*, Vychisl. Seismol. *12*, 37–44.

VIL'KOVICH, E. V., and SHNIRMAN, M. G. (1982), *Epicenter Migration Waves: Examples and Models*, Vychisl. Seismol. *14*, 27–37.

Appendix

Large earthquakes, $m \geq 6.4$, from the western segment of the Alpide belt (25–50°N, 40°W–60°E) during 1901–1981.

Year	Date	Or. time (GMT)	Latitude (degrees)	Longitude (degrees)	Depth (km)	Magnitude (UPP)
1901	Mar 31	071000	43.4 N	28.7 E	32	7.2
1902	Jul 5	143200	40.8 N	23.2 E	33	6.4
1903	Aug 11	043254	36.0 N	23.0 E	100	8.7
1904	Apr 4	102600	41.8 N	23.3 E		7.7
1905	Nov 8	220600	40.3 N	24.4 E	35	7.6
1908	May 17	123054	35.0 N	24.0 E	100	6.8
1908	Oct 6	213948	45.5 N	26.5 E	150	6.8
1908	Dec 28	042024	38.0 N	15.5 E		7.7
1909	Jan 23	024818	33.0 N	53.0 E		7.6
1909	Feb 9	112406	40.0 N	38.0 E	60	6.8
1910	Feb 18	050918	36.0 N	24.5 E	150	7.1
1910	Aug 1	104024	39.0 N	15.0 E	200	6.4
1910	Aug 21	161130	34.0 N	27.0 E	170	6.4
1911	Feb 18	213600	41.1 N	20.7 E	33	6.7
1911	Apr 4	154354	36.5 N	25.5 E	140	7.1
1911	Apr 18	181436	32.0 N	56.0 E	50	6.7
1912	Jan 24	162306	38.0 N	20.5 E	60	6.8
1912	Aug 9	012900	40.5 N	27.0 E		8.1
1913	Jun 14	093312	43.5 N	25.5 E		6.8
1914	Oct 3	220700	37.7 N	30.4 E	32	6.9
1915	Jan 13	065242	42.0 N	13.5 E		7.1
1915	Aug 7	150400	38.5 N	20.5 E	18	6.5
1916	Jan 26	073800	46.0 N	24.0 E		6.4
1918	Jul 16	200336	36.3 N	26.3 E		6.4
1919	Nov 18	215438	39.6 N	27.7 E		6.9
1922	Aug 13	000953	36.0 N	28.0 E	40	6.8
1923	Aug 1	031638	35.0 N	25.0 E	150	6.7
1923	Sep 17	070914	35.5 N	55.0 E		6.4
1923	Sep 22	204738	29.0 N	56.5 E		6.9
1924	Sep 13	143405	40.0 N	42.0 E		6.8
1925	Jul 6	121555	38.3 N	21.8 E	120	6.4
1926	Mar 18	140609	35.0 N	29.5 E		6.9
1926	Jun 26	194634	36.5 N	27.5 E	100	8.2
1926	Aug 30	113812	36.8 N	23.3 E	100	7.1
1927	Jul 1	081904	36.8 N	22.8 E	120	6.9
1927	Sep 11	221547	44.5 N	34.5 E		6.4
1928	Apr 14	085953	42.0 N	25.0 E		6.8
1928	Apr 18	192237	41.7 N	26.3 E		6.8
1929	May 1	153730	38.0 N	58.0 E		7.2
1929	May 18	063751	40.0 N	38.0 E		6.4
1930	Feb 14	183820	37.8 N	24.8 E	130	6.8
1930	May 6	223423	38.0 N	44.5 E		7.3
1930	Jul 23	000837	41.0 N	15.5 E		6.4
1931	Mar 8	015019	41.0 N	22.5 E		6.8
1931	Apr 27	165038	38.8 N	46.0 E		6.4

Appendix (continued)

Year	Date	Or. time (GMT)	Latitude (degrees)	Longitude (degrees)	Depth (km)	Magnitude (UPP)
1931	May 20	022249	37.5 N	16.0 W		7.2
1932	Sep 26	192037	40.0 N	23.3 E		6.9
1933	Apr 23	055735	36.8 N	27.3 E	50	6.8
1935	Feb 25	025137	35.8 N	25.0 E	80	6.8
1935	Apr 11	231443	36.5 N	53.5 E		6.8
1935	Apr 19	152322	31.5 N	15.3 E		7.2
1937	Dec 16	173530	35.0 N	23.5 E	100	6.4
1938	Apr 13	024546	39.2 N	15.2 E	270	6.8
1938	Apr 19	105915	39.5 N	33.5 E		6.8
1938	Sep 18	035038	38.0 N	22.5 E	100	6.4
1939	May 8	014650	37.0 N	24.5 W		7.2
1939	Sep 20	001931	38.0 N	20.5 E	80	6.4
1939	Sep 22	003632	39.0 N	27.0 E		6.4
1939	Dec 26	235721	39.5 N	38.5 E	25	8.3
1940	May 4	210154	35.3 N	58.3 E		6.4
1940	May 7	222343	42.0 N	43.0 E	50	6.4
1940	Nov 10	013909	45.8 N	26.5 E	150	7.6
1941	Jan 20	033707	35.0 N	34.0 E	100	6.4
1941	Mar 16	163515	38.5 N	11.5 E	100	6.4
1941	Nov 25	180355	37.5 N	18.5 W	25	8.7
1941	Dec 27	181727	36.0 N	10.5 W	60	6.8
1942	Dec 20	140308	40.5 N	36.5 E		7.4
1943	Nov 26	222036	41.0 N	34.0 E		7.8
1944	Feb 1	032236	41.5 N	32.5 E		7.6
1945	Sep 2	115357	33.8 N	28.5 E	80	6.4
1945	Sep 7	154822	46.0 N	26.8 E	100	6.4
1946	Nov 4	214746	40.0 N	54.5 E		7.7
1947	Sep 23	122808	33.0 N	59.0 E		6.8
1947	Oct 6	195531	37.0 N	22.0 E	28	7.1
1948	Feb 9	125815	35.5 N	27.5 E		7.2
1948	Jul 24	060305	34.4 N	24.5 E		6.9
1948	Oct 5	201205	37.5 N	58.0 E		7.4
1949	Jul 23	150330	38.6 N	26.3 E		6.8
1949	Aug 17	184413	39.4 N	40.9 E	33	6.8
1951	Aug 13	183326	40.9 N	33.2 E		6.8
1952	Dec 17	230357	34.4 N	24.5 E		6.8
1953	Mar 18	190613	40.0 N	27.3 E		6.5
1953	Aug 12	092355	38.5 N	21.0 E		7.4
1954	Mar 29	061705	37.0 N	3.5 W	603	7.1
1954	Apr 30	130236	39.3 N	22.2 E		7.0
1954	Sep 9	010437	36.2 N	1.6 E		7.0
1955	Jul 16	070710	37.6 N	27.2 E		6.6
1955	Sep 12	060924	32.2 N	29.6 E	33	6.5
1956	Feb 1	151051	39.1 N	15.6 E	223	6.4
1956	Feb 20	203137	39.9 N	30.4 E		6.5
1956	Jul 9	031140	36.7 N	25.8 E		7.7
1956	Oct 31	140343	27.3 N	54.4 E		6.7
1957	Mar 5	122437	33.2 N	39.9 W		6.4
1957	Mar 8	122113	39.3 N	22.6 E		7.0

Appendix (continued)

Year	Date	Or. time (GMT)	Latitude (degrees)	Longitude (degrees)	Depth (km)	Magnitude (UPP)
1957	Apr 25	022542	36.5 N	28.6 E	53	7.2
1957	May 26	063334	40.7 N	30.9 E		7.0
1957	Jul 2	004222	36.2 N	52.7 E		7.2
1957	Dec 13	014505	34.4 N	47.7 E	42	7.1
1958	Apr 3	071833	34.9 N	27.5 E		6.4
1958	Aug 16	191344	34.4 N	47.8 E		6.7
1958	Aug 27	151634	37.5 N	20.7 E		6.5
1959	Jan 24	195515	37.3 N	24.4 W		6.4
1959	Nov 15	170843	37.8 N	20.5 E		6.9
1960	May 26	051011	40.5 N	20.6 E		6.4
1961	May 23	024520	36.7 N	28.5 E	65	6.6
1961	Jun 11	051023	27.9 N	54.5 E		7.0
1961	Dec 18	213536	38.4 N	20.2 E	33	6.7
1962	Jan 26	081735	35.2 N	22.7 E	33	6.5
1962	Apr 10	213707	37.8 N	20.1 E	35	6.5
1962	Aug 28	105956	37.8 N	22.9 E	95	6.8
1962	Sep 1	192040	35.6 N	49.9 E	30	7.0
1962	Oct 1	121401	27.9 N	54.8 E	40	6.5
1963	May 19	100005	46.3 N	14.5 E	53	6.7
1963	Jul 16	182713	43.3 N	41.6 E	33	6.8
1964	Mar 15	223026	36.2 N	7.6 W	27	6.7
1964	Oct 6	143123	40.3 N	28.2 E	34	6.9
1965	Mar 31	094726	38.4 N	22.3 E	45	7.1
1965	Apr 9	235702	35.1 N	24.3 E	39	6.5
1965	Jul 6	031842	38.4 N	22.4 E	18	6.6
1966	Aug 19	122210	39.2 N	41.6 E	26	6.9
1967	Mar 4	175809	39.3 N	24.6 E	60	6.8
1967	Jul 22	165658	40.7 N	30.7 E	33	7.3
1967	Nov 30	072350	41.4 N	20.4 E	21	6.5
1968	Feb 19	224542	39.4 N	24.9 E	7	7.0
1968	Aug 31	104741	34.2 N	59.0 E	25	6.7
1969	Feb 28	024031	36.0 N	10.6 W	14	7.7
1969	Mar 28	014829	38.6 N	28.5 E	4	6.6
1969	Mar 31	071554	27.6 N	33.9 E	33	7.0
1969	Oct 27	081058	44.9 N	17.2 E	33	6.5
1969	Nov 7	183404	27.8 N	60.0 E	74	6.8
1970	Mar 28	210223	39.2 N	29.5 E	18	6.9
1970	May 14	181227	43.1 N	47.1 E	33	6.9
1970	Jul 30	005220	37.9 N	56.0 E	22	6.6
1971	Apr 12	190325	28.3 N	55.6 E	37	6.8
1971	May 12	062515	37.6 N	29.7 E	30	6.5
1971	May 22	164359	38.9 N	40.5 E	3	6.7
1972	Apr 10	020650	28.4 N	52.8 E	11	6.7
1972	May 4	213957	35.2 N	23.6 E	14	6.9
1972	Sep 13	041319	38.0 N	22.4 E	75	6.6
1972	Sep 17	140715	38.4 N	20.3 E	33	6.5
1975	May 26	091151	36.0 N	17.6 W	33	7.3
1975	Sep 6	092012	38.5 N	40.8 E	32	6.7
1976	May 6	200012	46.4 N	13.3 E	12	6.8

Appendix (continued)

Year	Date	Or. time (GMT)	Latitude (degrees)	Longitude (degrees)	Depth (km)	Magnitude (UPP)
1976	May 11	165945	37.4 N	20.4 E	33	6.6
1976	Jun 17	142850	46.2 N	12.9 E	35	6.8
1976	Nov 24	122215	39.1 N	44.0 E	10	7.0
1977	Mar 4	192154	45.8 N	26.7 E	86	7.2
1977	Mar 21	211853	27.6 N	56.4 E	24	7.1
1977	Sep 11	231919	35.0 N	23.1 E	4	6.5
1977	Jun 20	200321	40.7 N	23.2 E	3	6.8
1978	Sep 16	153556	33.4 N	57.4 E	33	7.0
1978	Nov 4	152219	37.7 N	48.9 E	34	6.7
1979	Apr 15	061947	42.0 N	18.5 E	33	6.7
1979	May 28	092732	36.4 N	31.8 E	98	6.4
1979	Nov 14	022122	33.9 N	59.7 E	33	6.7
1980	Jan 1	164240	38.8 N	27.8 W	10	6.7
1980	Jul 9	021153	39.3 N	23.0 E	14	6.4
1980	Oct 10	122524	36.2 N	1.4 E	10	7.4
1980	Nov 23	183454	40.9 N	15.4 E	10	6.7
1981	Mar 4	215806	38.2 N	23.3 E	33	6.7
1981	Jun 11	072425	29.9 N	57.7 E	33	6.8

PAGEOPH, Vol. 122 (1984/85) 0033-4553/85/060848-15$1.50 + 0.20/0

A Sequence of Seismic Activity in the Kanto Area Precursory to the 1923 Kanto Earthquake

By MITIYASU OHNAKA[1])

Abstract – The Kanto earthquake (M = 7.9) that occurred along the Sagami Trough in the Sagami Bay on 1 September 1923 was one of the most disastrous earthquakes in Japanese history. The Kanto area includes Metropolitan Tokyo and Yokohama which are densely populated, and hence it has been a matter of great concern, from the viewpoints of earthquake prediction and disaster prevention, whether or not the 1923 Kanto earthquake was preceded by precursory seismicity. A study using the most complete lists of earthquakes catalogued recently by Utsu and the Japan Meteorological Agency reveals that seismic activity in the Kanto area was appreciably higher before and after the Kanto earthquake, and that the Kanto earthquake was preceded by a sequence of anomalous seismic activity, quiescence, and foreshocks. Such higher activity before and after the Kanto earthquake is contrasted with low seismicity during the recent 30-year period. A model is proposed to explain the precursory seismic activity, subsequent quiescence, and foreshocks for the Kanto earthquake. In the model, the transition from precursory seismic activity to quiescence is ascribed to time-dependent fracture due to stress-aided corrosion. Foreshocks are related to an acceleration of premonitory slip shortly before the mainshock slip.

Key words: Precursory seismicity, quiescence, premonitory slip, delayed fracture, stress corrosion.

1. Introduction

The great Kanto earthquake (magnitude M 7.9) that occurred along the Sagami Trough in the Sagami Bay (e.g., KANAMORI and ANDO, 1973; ANDO, 1974) on 1 September 1923 was one of the most disastrous earthquakes in Japanese history. The Kanto area includes Metropolitan Tokyo and Yokohama which are densely populated, and hence it has been of great concern, from the viewpoints of earthquake prediction and disaster prevention, whether or not the 1923 Kanto earthquake was preceded by anomalous seismic activity. IMAMURA (1927, 1929) first argued that seismic activity in the Kanto area increased before the Kanto earthquake. However, the earthquake catalog he used was incomplete, and consequently his suggestion of precursory seismic activity in the Kanto area has not been generally accepted. Recently MOGI (1980) reported that a 'doughnut-shaped pattern' of seismicity could be recognized before the Kanto earthquake.

Using improved catalogs most recently published by UTSU (1979, 1981, 1982b) and the Japan Meteorological Agency (JMA), I wish to show that a distinctive sequence of

[1]) Earthquake Research Institute, University of Tokyo, Bunkyo-ku, Tokyo 113, Japan.

seismic activity preceded the 1923 Kanto earthquake, and then to propose a model derived from studies of time-dependent fracture and friction.

2. Data

The Utsu catalog (1981) is the most complete list of shallow earthquakes (focal depth $\leq$ 100 km) of $M \geq 5.5$ in the area 32°N–38°N latitude and 136°E–144°E longitude during the period 1904–1925. Hence, the data for earthquakes during the period 1904–1925 were taken preferentially from that catalog. The data for the period 1885–1903 were taken from other Utsu catalogs (1979; corrections and supplements in 1982a,b). Data for the period 1926–1982 are from the published Seismological Bulletins of JMA; earthquake data for the period 1926–1960 are from the *Catalogue of Relocated Major Earthquakes in and near Japan (1982)* published by JMA as the Supplementary Volume of the Seismological Bulletin. The JMA magnitude scale is adopted in the Utsu catalogs (1979, 1981, 1982a,b).

The data taken from the Utsu catalog (1979) may be incomplete for earthquakes of $M < 6$ (UTSU, 1979), whereas the data from the new Utsu catalog (1981) and the Seismological Bulletins of JMA are complete for $M \geq 5.5$. The combined catalogs are uniform down to magnitude 5.8 for the period 1904–1982, and 6.0 for the period 1885–1982. I will concentrate on earthquakes in the area 34.4°N to 37.0°N and 138.5°E to 141.6°E (Fig. 1), which will be called Kanto area in this paper.

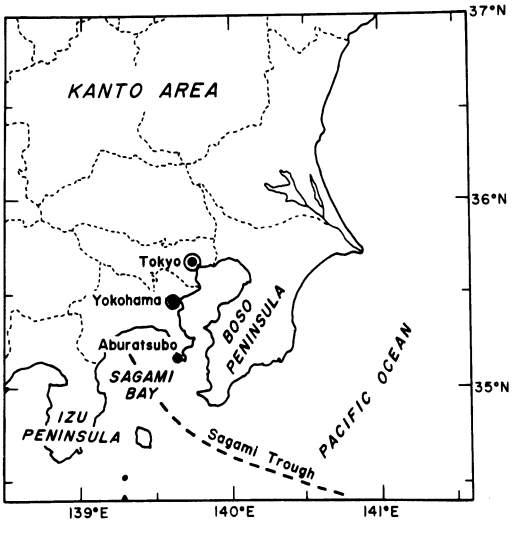

Figure 1
Map of the Kanto area, Japan, showing place names referred to in the text.

3. Precursory sequence of seismic activity

Figure 2 shows epicenters of shallow focus ($h < 80$ km) earthquakes of $M \geq 5.8$ in the Kanto area during the period 1885–1982. This figure gives a general view of seismic activity in the Kanto area, and is useful for understanding the background seismicity. Sizes of circles in Fig. 2 indicate magnitudes of earthquakes, and the focal region of the 1923 Kanto earthquake is indicated approximately by the elliptical boundary. Figure 2c shows the epicenter (largest circle) of the Kanto earthquake and the distribution of aftershocks that occurred within two years. Black circles represent epicenters of the main shock and aftershocks within the first 6 days; hatched circles indicate the epicenters of later earthquakes. In Fig. 2d, black circles indicate the epicenters of earthquakes in the first half of the period, and hatched circles denote the epicenters of earthquakes in the second half of the period. Figures 2c and 2d show that seismic activity after the Kanto earthquake migrated toward the northeast from the focal region.

Figure 3 shows the annual number of earthquakes in the Kanto area vs. time for 1885–1982. Seismic activity in the Kanto area was relatively high before and after the 1923 Kanto earthquake, and the high activity after the Kanto earthquake lasted more than 20 years. This persistent high activity after the Kanto earthquake is surely an aftereffect of the Kanto earthquake, but may be distinguished from the aftershocks in a narrow sense. Such activity may be called aftershocks in a broad sense.

The level of seismic activity during the most recent 30-year period may be regarded as the background level. The average number of earthquakes per year was 0.67 for $M \geq 6.0$ and 1.23 for $M \geq 5.8$. In contrast, the average frequency over the period September 1927–August 1947, for instance, was 1.95 for earthquakes of $M \geq 6.0$ and 3.05 for earthquakes of $M \geq 5.8$. Thus the activity in the Kanto area during the period September 1927–August 1947 was significantly high compared with the activity during the recent 30-year period.

We now turn to seismic activity preceding the Kanto earthquake. Figure 3 shows that there were two conspicuously high activity peaks: one in 1896 (marked A) and the other in 1923 (marked B). The highest peak in 1923 is due to the Kanto earthquake and its aftershocks. According to the Utsu catalog (1982b), the peak in 1896 was caused by a M 7.5 earthquake and its aftershocks in the region off Ibaraki (location A in Fig. 2). When these aftershocks are omitted, the peak in 1896 disappears.

To investigate seismic activity preceding the Kanto earthquake, the period September 1906–August 1926 was divided into four equal time intervals, and epicentral locations of $M \geq 5.8$ earthquakes during each time interval were plotted in Figs. 4a,b,c,d. Twelve earthquakes occurred in the Kanto area between September 1906 and August 1911 (Fig. 4a), and twenty earthquakes between September 1911 and August 1916 (Fig. 4b). The average number of earthquakes per year is 2.4 and 4.0 respectively. In comparison the average frequency for the most recent 30-year period is 1.2.

Only four earthquakes were located in the same area between September 1916 and August 1921 (Fig. 4c), giving an unusually low average frequency of 0.8 per year. Thus

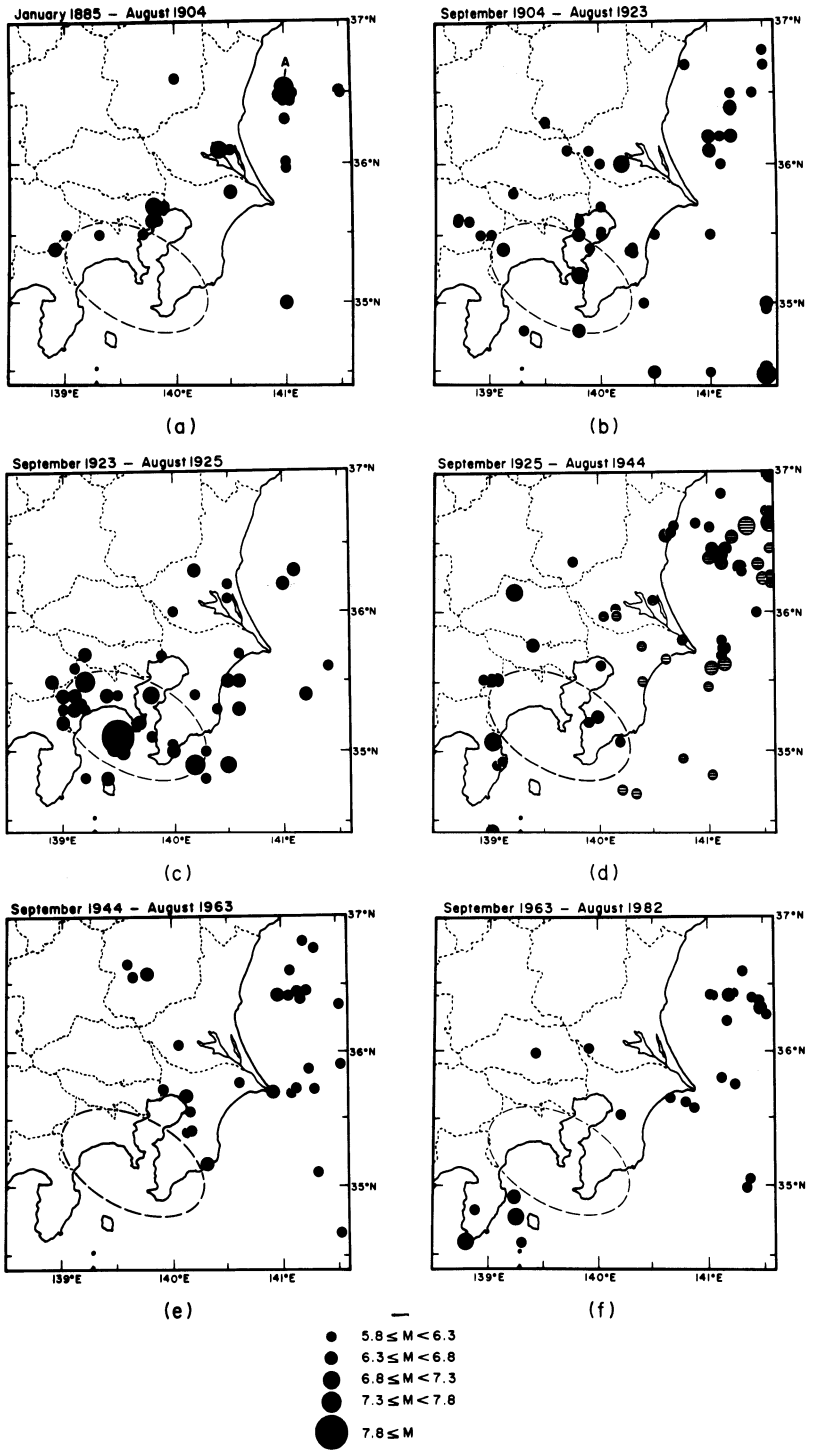

Figure 2

Spacial distribution of epicenters of $M \geq 5.8$ earthquakes in the Kanto area during six different periods. The epicentral region of the 1923 Kanto earthquake is indicated approximately by the ellipse. The cluster

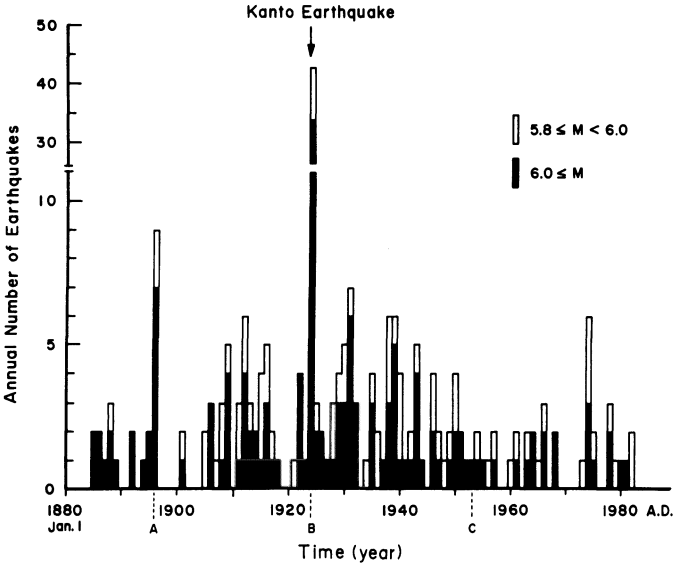

Figure 3

A plot of annual number of earthquakes ($M \geq 5.8$) in the Kanto area, against time for the period 1885 to 1982.

the sequence of high and low activities preceding the Kanto earthquake appears to be anomalous, and the period September 1916–August 1921 may be regarded as a quiescent stage preceding the Kanto earthquake.

Figure 4d shows epicentral locations of earthquakes during the interval September 1921–August 1926. Black circles indicate epicenters of the main shock (largest circle) and aftershocks. The six hatched circles denote epicenters of foreshocks. Earthquakes that occur shortly before a main shock in the focal region are usually called foreshocks in a narrow sense. Only one of the six earthquakes occurred in the area marked by the elliptical boundary indicating the focal region of the 1923 Kanto earthquake (Fig. 4d). However, the other five earthquakes may also be regarded as foreshocks in a broad sense (see later section). KANAMORI (1981) calls this kind of earthquake a preshock.

So far we have investigated earthquakes in the area 34.4°N to 37.0°N and 138.5°E to 141.6°E. In general, if an area selected is too large, any precursory sequence of seismicity may be masked by background seismicity not associated with the 1923 Kanto earthquake. If the selected area is too small, the pattern of precursory activity will be incomplete. To test the effect of area size, the analysis was repeated using the smaller area BCDE shown in Fig. 4. The annual number of $M \geq 5.8$ earthquakes in the

---

marked A in (a) indicates epicenters of an M 7.5 earthquake and aftershocks in 1896. Hatched circles in (b) indicate epicenters of the earthquakes within the latest 3 years before the Kanto earthquake. Black circles in (c) represent epicenters of the Kanto earthquake (largest circle) and aftershocks within the first 6 days; hatched circles indicate epicenters of later earthquakes. Black circles in (d) indicate epicenters of the earthquakes in the first half of the period, and hatched circles denote those of earthquakes in the second half of the period.

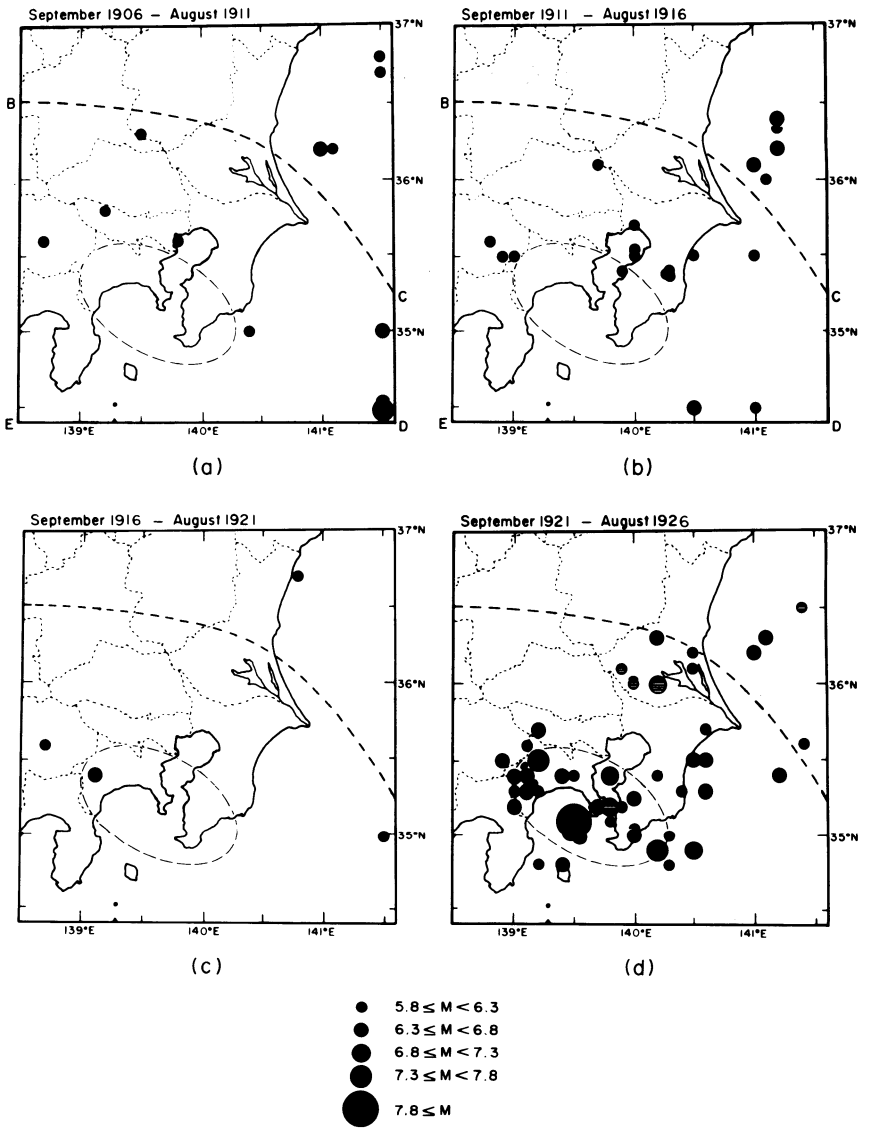

Figure 4

Pre-quiescence seismic activity, quiescence, foreshocks and aftershocks for the Kanto earthquake. The focal region of the Kanto earthquake is indicated approximately by the ellipse. Hatched circles in (d) indicate earthquakes during the period February 1921–August 1923 before the mainshock.

Kanto area from 1904 to 1926 is split into two populations and plotted against time in Fig. 5a. Black portions indicate the annual number of earthquakes in area BCDE, and white portions denote the number of earthquakes outside the area BCDE. For both choices of sample area, it can be seen that the 1923 Kanto earthquake was preceded by a sequence of seismic activity, quiescence, and foreshocks.

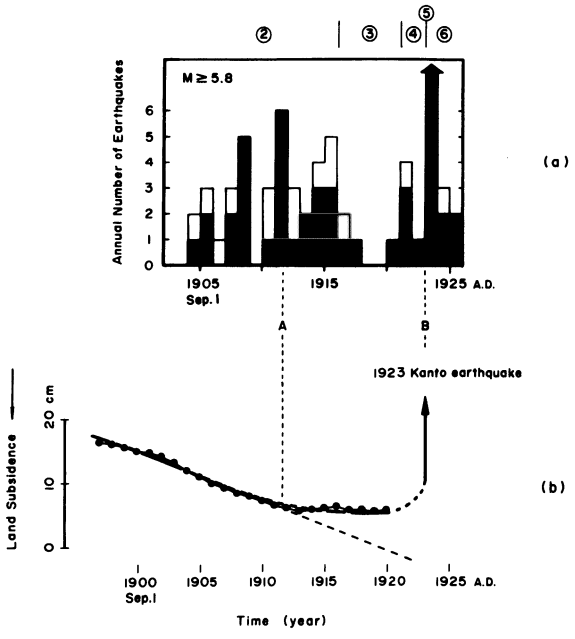

Figure 5

(a) Plot of annual number of earthquakes against time for the period 1904 to 1926. Five seismic episodes can be distinguished: precursory seismic activity ②, quiescence ③, foreshocks ④, mainshock ⑤ and aftershocks ⑥. (b) Plot of the low-pass filtered sea level data at Aburatsubo against time. The thick solid curve indicates the result of low-pass filtering, and the thin curve with black circles is the result of using a running average of 5 points.

4. Relation of precursory seismicity to premonitory slip

Figure 6 shows a plot of the annual mean sea level data (black circles) from a tide gauge at Aburatsubo in the Miura Peninsula (data from COASTAL MOVEMENTS DATA CENTER, 1976). Only data with fewer than 28 days missing observations per year are plotted as black circles. White circles are fictitious points obtained by Lagrangian interpolation. In general, the long-period change in sea level is due to crustal deformation, while the short-period change is caused by an oceanographic effect (TSUMURA, 1971). The short-period components are regarded as noise here and are eliminated by low-pass digital filtering. Before filtering, the 1.4 m coseismic offset in Fig. 6 associated with the 1923 Kanto earthquake was removed, and after filtering the offset was restored. Solid smooth curves in Fig. 6b are the filtered data (30 year cutoff period and 24 dB/octave attenuation slope).

Numerous authors (e.g., TSUMURA, 1971; KAKIMI *et al.*, 1977) have tried to determine if the observed sea level change prior to the 1923 Kanto earthquake derived from crustal deformation. TSUMURA (1971) concluded that the short-period drop in sea

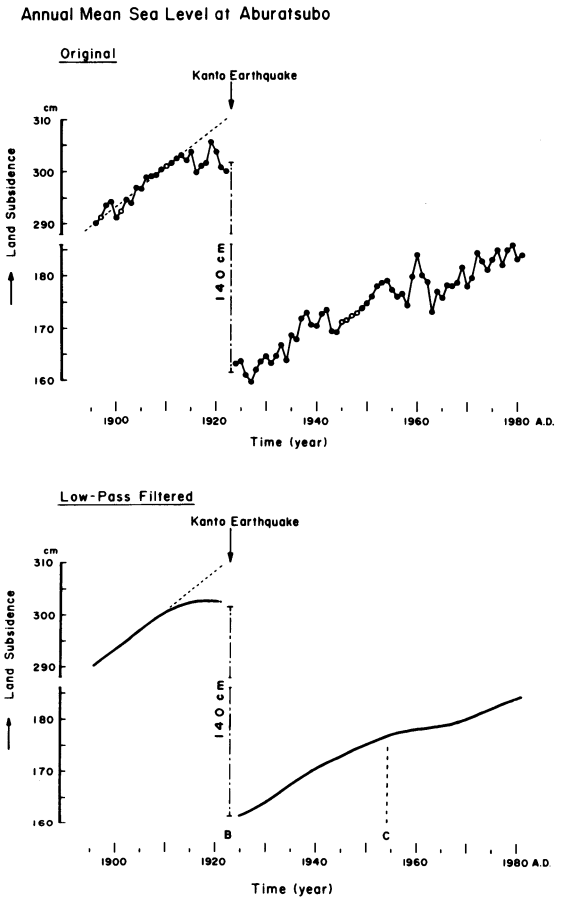

Figure 6

Variation of annual mean sea level at Aburatsubo with time. Data with fewer than 28 days missing observations per year are plotted as black circles. White circles are fictitious points obtained by Lagrangian interpolation. Solid smooth curves in bottom figure are the filtered data.

level during the period 1920–1923 was not due to uplift of the land, but to changes in oceanographic conditions such as motion of a cold water mass. He suggests, however, that systematic deviation of the data points from an extrapolation of the linear upward trend over about 10 years (Fig. 6) could be crustal deformation precusory to the 1923 Kanto earthquake (personal communication, 1980). KAKIMI *et al.* (1977) made the same suggestion.

The low-pass filtered sea level data are compared with the precursory sequence of seismic activity in Fig. 5b. The thick solid line is the filtered sea level data (inverted), and the thin solid line with black circles is the result of a simple running average of 5 points. The beginning of the anomalous subsidence corresponds to the peak of the precursory seismic activity, marked A.

5. *A possible model*

Although the Kanto earthquake was complex, as shown by SCHOLZ and KATO (1978), the mechanism of the Kanto earthquake may be approximated as a frictional contact of an overlying plate with a descending slab (Fig. 7). In terms of plate tectonics, the earthquake slip is due to rupture along the Sagami Trough, which is the boundary between the Philippine Sea and Asia plates (KANAMORI and ANDO, 1973). During the first part of the period before the mainshock, the fault between the plates is locked and the edge of the overlying plate is dragged down together with the descending slab of lithosphere. As a result, the land near the edge of overlying plate subsides. The constant rate of subsidence prior to 1912 in Fig. 5b is consistent with this stage of the model. The steady rate of slab descent would produce a steady increase of the average tectonic stress $\bar{\tau}_{yx}$ in the vicinity of the plate boundary fault.

Figure 7 shows relations among geometry, stress, and motion. The xz plane is parallel to the plate boundary, and the y axis is normal to the plate boundary. The origin of the coordinate system is in the overlying plate at a distance y_0 from the fault, chosen such that the shear stress τ_{yx} may be considered to be negligible (OHNAKA, 1976). The figure shows how an initially straight line (broken) becomes curved due to plate displacement u. The stress $\bar{\tau}_{yx}$ is directly proportional to the displacement, of which the vertical component is sea level change. The plates beneath the Kanto area probably contain a large number of potential stress concentrators such as cracks or faults, as suggested by the great number of micro to moderate intraplate earthquakes (e.g., MAKI, 1984). I suggest that the precursory seismic activity shown in Fig. 8 occurs on such faults and is due to stress buildup while the plates are locked.

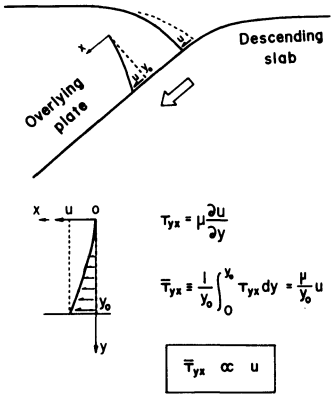

Figure 7

Sketch showing relation among geometry, stress, and motion. An interplate earthquake is generated by elastic rebound motion of the plates. The average shear tectonic stress $\bar{\tau}_{yx}$ caused by elastic deformation is proportional to the displacement u, of which the vertical component is sea level change. y_0 is the distance between the plate boundary and the point where τ_{yx} may be considered to be zero (OHNAKA, 1976).

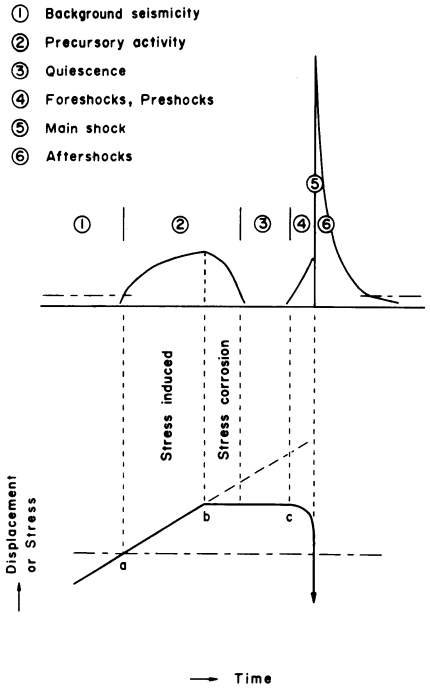

Figure 8

A schematic diagram showing idealized relation between precursory sequence of seismic activity and premonitory slip for the Kanto earthquake. Precursory activity begins at the point in time a, premonitory slip begins at b, and acceleration of premonitory slip beings at c. Fracture is induced by increasing tectonic stress under stress corrosion during the time interval a to b; time-dependent fracture can occur due to stress corrosion even if the stress is constant. Accelerating premonitory slip on the plate boundary can cause a very rapid increase in local stresses at asperities, resulting in foreshocks.

Eventually, friction on the plate boundary in the locked section can no longer resist the rising tectonic stress which has been built up during the deformation of the overlying plate, and premonitory slip starts. The premonitory slip would tend to keep the tectonic stress nearly level until the time of the partial stress drop which precedes the unstable mainshock slip. The subsidence data in Fig. 5b is consistent with an approximately constant $\bar{\tau}_{yx}$ and premonitory slip.

In spite of the constant overall stress $\bar{\tau}_{yx}$, seismic activity in this stage continues as shown in Fig. 5. This might be because local stresses around stress concentrators (faults) can increase through the interaction between two or more slipping faults. However, this effect can be neglected since the interaction is insignificant when the faults are more than a fault length apart (e.g. TADA *et al.*, 1973).

An alternative but more likely process is delayed fracture (stress corrosion) occurring on the intraplate faults, as shown schematically in Fig. 8. Laboratory experiments show that rock strength can be lowered by stress-aided corrosion (e.g., SCHOLZ, 1972; ATKINSON, 1982, 1984), and that the rate of acoustic emission due to

stress corrosion decays as the inverse of time (OHNAKA, 1983a,b). Thus, if acoustic emission is a scale model of seismicity in the Earth (MOGI, 1967), stress corrosion would explain why quiescence follows precursory seismic activity. An equation for the decrease in a number of earthquakes with time can be derived assuming that the average tectonic stress $\bar{\tau}_{yx}$ is held constant at $t = 0$. If there is no interaction between earthquake failures in different regions, and if each region fails only once, the decay rate $n(t)$ of earthquake events can be given as (Ohnaka, 1983a)

$$n(t) \propto \frac{F(\bar{\tau}_{yx})}{t + c} \tag{1}$$

where $F(\bar{\tau}_{yx})$ is a function of $\bar{\tau}_{yx}$, and c is a constant. The seismicity shown in Fig. 9, a plot of the cumulative number of earthquakes from September 1911 to August 1923 (time interval A to B in Fig. 5) against time, has a decay rate in accordance with the relation (1), suggesting that stress corrosion plays a key role in the precursory sequence of seismic activity. In this plot, two events that occurred on 16 November 1915 (Table 1) are removed, since these two shocks are considered to be dependent events.

Thus, the quiescent period marked 3 in Fig. 8 is a result of the decay of precursory seismic activity in this model. However, quiescence need not always appear preceding major earthquakes. For instance, if slip acceleration leading to instability occurs before precursory seismic activity decays completely, then no quiescence appears. This is because fault slip would decrease the average stress in the plates.

In the model, as the time of the mainshock approaches, premonitory slip begins to accelerate. The seismic activity in this stage (called foreshocks in Fig. 5 and 8) may be associated with the accelerating slip. If the fault plane along the plate boundary is held in place at a number of asperities, induced high local stresses could cause fracture of some asperities, resulting in foreshocks in the narrow sense. Foreshocks in the broad sense, which make up five of six earthquakes of $M \geq 5.8$ that occurred shortly before the

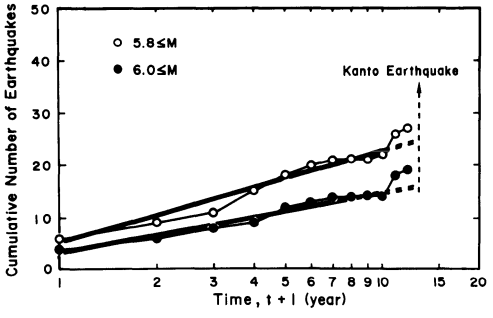

Figure 9

A semi-log plot of the cumulative number of earthquakes against time.

Table 1

Earthquakes which occurred successively in the same focal region within a short time interval (taken from the Utsu catalog (1981))

Date	Locality		Depth	M
	λ(°E)	φ(°N)		
1915, Nov. 12	140.3	35.4	s	5.8
1915, Nov. 16	140.3	35.4	s	6.0
1915, Nov. 16	140.3	35.4	s	5.8

's' means shallow. Only the first event may be regarded as an independent one, and the second and third events as a result of a triggering effect of the first and second shocks, respectively.

Kanto earthquake and can occur outside the focal region of a mainshock, might also be caused by accelerating premonitory slip on the plate boundary fault.

6. Discussion

KELLEHER and SAVINO (1975), EVISON (1977), MOGI (1977), and KANAMORI (1981) suggest that a sequence of seismic activity preceding major earthquakes may usually be described in terms of five episodes: (1) background seismicity, (2) precursory seismic activity, (3) quiescence, (4) foreshocks, and (5) mainshock. These five episodes can be identified in the seismicity preceding the 1923 Kanto earthquake, as discussed above. The model proposed to explain the sequence of seismicity is based on time-dependent fracture and friction, and is different from previous models (KELLEHER and SAVINO, 1975; MOGI, 1977; TSUMURA, 1979; KANAMORI, 1981; DMOWSKA and LI, 1982; MIKUMO and MIYATAKE, 1983).

In the model, premonitory stable slip appears to be a necessary stage preceding seismic unstable slip. In analogous laboratory experiments, for example, frictional stable sliding of rock is associated with fracturing processes at contacting regions or interlocking asperities on mating surfaces (e.g., BYERLEE, 1967; OHNAKA, 1975; ENGELDER and SCHOLZ, 1976). If local fracture occurs at asperities on fault surfaces, the regions around the asperities will relax, and the local stresses will drop; however, stresses at the remaining unfractured asperities will increase, and the increased stresses will increase the probability of further fracture at the remaining asperities. The rate of asperity fracture will eventually accelerate, leading to overall instability, analogous to a mainshock. DAS and SCHOLZ (1981) have showed that an earthquake must be preceded by some precursory slip under stress-corrosive environments. However, premonitory slip can in general occur even if the asperities fracture without any assistance of stress corrosion.

According to the model, quiescence following precursory seismicity is directly related to the premonitory slip. Thus, the low seismicity found around 1900 and 1970

(Fig. 3) cannot be regarded as precursory quiescence, since anomalous seismic activity and slow slip are not found preceding the low seismicity. The relatively high seismic activity during the 20 years after the Kanto earthquake appears to be related to high subsidence rate in Fig. 6 after the Kanto earthquake (steeper slope between B and C). However, this point is beyond the scope of this paper.

I have assumed that stress corrosion has an important effect on an earthquake failure. I will briefly discuss whether the assumption is reasonable at depths of several tens of km. A large number of earthquakes occur at these depths in the Kanto area, where overburden pressure reaches very high levels; nevertheless, earthquakes at these depths are considered to be fracture. Fracture will be difficult under high overburden pressure if pore pressure is absent. Thus, the presence of pore pressure, which reduces the effect of overburden pressure (HUBBERT and RUBY, 1959), would be indispensable at these depths, and pore pressure must open up cracks to some extent. The medium of pore pressure will be liquid water or water vapor, which is the prime corrodent for silicate rocks. Thus, rocks will be weakened at the presence of water by the effects of both pore pressure and stress corrosion.

Water will permeate into the Earth's crust to some depth from the ground surface (or sea bottom). Water at greater depths may be conveyed by the descending slab of oceanic lithosphere from the sea bottom or be released by decomposition reaction of hydrous minerals in the descending slab. The decomposition reaction can occur and release water progressively at different depths (RALEIGH and LEE, 1969; MURRELL and ISMAIL, 1976), resulting in marked weakening and embrittlement of rock containing the hydrous minerals (RALEIGH and PATERSON, 1965; MURRELL and ISMAIL, 1976, 1983). Furthermore, subcritical crack growth in rock by stress corrosion is enhanced by increased temperature (MEREDITH and ATKINSON, 1983). Thus, the assumption that stress corrosion may have an important effect on earthquake failure at depths to several tens of km in a subduction zone is well grounded.

Acknowledgments

Professor T. Utsu provided one of his earthquake catalogs in advance of publication and I am grateful to him for this. I am also grateful to Professor K. Mogi, Dr S. A. F. Murrell, and Dr K. Tsumura for fruitful discussions and critical comments. I wish to thank Dr B. K. Atkinson for providing numerous reprints of his work, Dr S. A. F. Murrell for the provision of a preprint of his study, and Dr P. G. Meredith for providing his experimental results. I thank the Editors of the Special Issue for their helpful suggestions, by which the original manuscript was improved and condensed.

REFERENCES

ANDO, M. (1974), *Seismo-tectonics of the 1923 Kanto Earthquake*, J. Phys. Earth *22*, 263–277.

ATKINSON, B. K. (1982), *Subcritical Crack Propagation in Rocks: Theory, Experimental Results and Applications*, J. Struct. Geol. *4*, 41–56.

ATKINSON, B. K. (1984), *Subcritical Crack Growth in Geological Materials*, J. Geophys. Res. *89*, 4077–4114.

BYERLEE, J. D. (1967), *Frictional Characteristics of Granite under High Confining Pressure*, J. Geophys. Res. *72*, 3639–3648.

CATALOGUE OF RELOCATED MAJOR EARTHQUAKES IN AND NEAR JAPAN (1926–1960) (1982), published by Japan Meteorological Agency, Supplementary Vol. No. 6 Seis. Bull. pp. 1–109.

COASTAL MOVEMENTS DATA CENTER (1976), *Tables and Graphs of Annual Mean Sea Level along the Japanese Coast 1894–1975*, published by CMDC, pp. 1–37.

DAS, S., and SCHOLZ, C. H. (1981), *Theory of Time-dependent Rupture in the Earth*, J. Geophys. Res. *86*, 6039–6051.

DMOWSKA, R., and LI, V. C. (1982), *A Mechanical Model of Precursory Source Processes for Some Large Earthquakes*, Geophys. Res. Lett. *9*, 393–396.

ENGELDER, J. T., and SCHOLZ, C. H. (1976), *The Role of Asperity Indentation and Ploughing in Rock Friction – II. Influence of Relative Hardness and Normal Load*, Int. J. Rock Mech. Min. Sci. & Geomech. Abstr. *13*, 155–163.

EVISON, F. F. (1977), *Precursory Seismic Sequences in New Zealand*, N.Z. J. Geol. Geophys. *20*, 129–141.

HUBBERT, M. K., and RUBEY, W. W. (1959), *Role of Fluid Pressure in Mechanics of Overthrust Faulting*, Bull. Geol. Soc. Amer. *70*, 115–166.

IMAMURA, A. (1927), *On the Seismic Activity of the Kanto District*, Japanese J. Astr. Geophys. *5*, 127–135.

IMAMURA, A. (1929), *Recurrence of Seismic Activity in the Kanto and Kinki Districts and Precursory Phenomena Preceding Great Earthquakes*, Zisin 1st Ser. *1*, 4–16 (in Japanese).

KAKIMI, T., SATO, H., TSUMURA, K., and ISHIDA, M. (1977), *Seismicity, Crustal Movement and Neotectonics in the Kanto District*, Proc. Symp. Earthquake Prediction Research, pp. 21–45 (in Japanese).

KANAMORI, H., *The Nature of Seismicity Patterns before Large Earthquakes*. In *Earthquake Prediction: An International Review*, Maurice Ewing Ser. 4 (eds. D. W. Simpson and P. G. Richards) (AGU, Washington D.C. 1981), pp. 1–19.

KANAMORI, H., and ANDO, M. (1973), *Fault Parameters of the Great Kanto Earthquake of 1923*, Publications for the 50th Anniversary of the Great Kanto Earthquake, 1923, pp. 89–101 (in Japanese).

KELLEHER, J., and SAVINO, J. (1975), *Distribution of Seismicity Before Large Strike Slip and Thrust-type Earthquakes*, J. Geophys. Res. *80*, 260–271.

MAKI, T. (1984), *Focal Mechanisms and Spatial Distribution of Intermediate-depth Earthquakes Beneath the Kanto District and Vicinity with Relation to the Double Seismic Planes*, Bull. Earthq. Res. Inst. Tokyo Univ. *59*, 1–51.

MEREDITH, P. G., and ATKINSON, B. K. (1983), *High-temperature Tensile Crack Growth in Rocks*, Presented at 18th IUGG Meeting, Hamburg.

MIKUMO, T., and MIYATAKE, T. (1983), *Numerical Modelling of Space and Time Variations of Seismic Activity before Major Earthquakes*, Geophys. J. R. Astr. Soc. *74*, 559–583.

MOGI, K. (1967), *Earthquakes and Fractures*, Tectonophysics *5*, 35–55.

MOGI, K. (1977), *Seismic Activity and Earthquake Prediction*, Proc. Symp. Earthquake Prediction Research, pp. 203–214 (in Japanese).

MOGI, K. (1980), *Change in Seismic Activity with Time in a Wide Area Including the Metropolitan Region*. In *Earthquake Prediction in Metropolitan Tokyo and Its Environs*, Report of Regional Committee for Earthquake Prediction, Geographical Survey Inst. 2, pp. 20–21 (in Japanese).

MURRELL, S. A. F., and ISMAIL, I. A. H. (1976), *The Effect of Decomposition of Hydrous Minerals on the Mechanical Properties of Rocks at High Pressures and Temperatures*, Tectonophysics *31*, 207–258.

MURRELL, S. A. F., and ISMAIL, I. A. H., *Mechanical Behaviour Related to Phase Changes of Hydrous Minerals in Several Rocks*. Submitted for publication in *Advances in Physical Geochemistry, Metamorphic Reactions: Kinetics, Textures and Deformation*', vol. 4 (ed. A. B. Thompson) (Springer-Verlag, Berlin 1983).

OHNAKA, M. (1975), *Frictional Characteristics of Typical Rocks*, J. Phys. Earth *23*, 87–112.

OHNAKA, M. (1976), *A Physical Basis for Earthquakes Based on the Elastic Rebound Model*, Bull. Seis. Soc. Amer. *66*, 433–451.

OHNAKA, M. (1983a), *Acoustic Emission During Creep of Brittle Rock*, Int. J. Rock Mech. Min. Sci. Geomech. Abstr. *20*, 121–134.

OHNAKA, M. (1983b), *Acoustic Emission and Fracturing Process to Failure During Creep of Brittle Rock.* Presented at Inter-Disciplinary Symposium 'Time-dependent processes and properties in planetary materials' held at 18th IUGG Meeting, Hamburg.

RALEIGH, C. B., and PATERSON, M. S. (1965), *Experimental Deformation of Serpentinite and its Tectonic Implications*, J. Geophys. Res. *70*, 3965–3985.

RALEIGH, C. B., and LEE, W. H. K. (1969), *Sea-floor Spreading and Island-arc Tectonics*, Proc. Andesite Conference (ed. A. R. McBirney), Oregon, Dep. Geol. Miner. Ind. Bull. *65*, 99–110.

SCHOLZ, C. H. (1972), *Static Fatigue of Quartz*, J. Geophys. Res. *77*, 2104–2114.

SCHOLZ, C. H., and KATO, T. (1978), *The Behavior of a Convergent Plate Boundary: Crustal Deformation in the South Kanto District, Japan*, J. Geophys. Res. *83*, 783–797.

TADA, H., PARIS, P. C., and IRWIN, G. R., *The Stress Analysis of Cracks Handbook* (Del Research Corporation, St. Louis, Missouri 1973).

TSUMURA, K. (1971), *Investigation of Mean Sea Level and its Variation Along the Coast of Japan (Part 2) – Changes in Ground Level at Various Places in Japan as Deduced from Tidal Data and Earthquake Prediction*, J. Geod. Soc. Japan *16*, 239–275.

TSUMURA, K. (1979), *A Model for Temporal Variation of Seismic Activity and Precursors*, Programme and Abstracts, Seis. Soc. Japan No. 1, p. 159 (in Japanese).

UTSU, T. (1979), *Seismicity of Japan from 1885 through 1925—A New Catalog of Earthquakes of $M \geq 6$ felt in Japan and Smaller Earthquakes which Caused Damage in Japan*, Bull. Earthq. Res. Inst. Tokyo Univ. *54*, 253–308 (in Japanese).

UTSU, T. (1981), *Seismicity of Central Japan from 1904 through 1925*, Bull. Earthq. Res. Inst. Tokyo Univ. *56*, 111–137 (in Japanese).

UTSU, T. (1982a), *Seismicity of Japan from 1885 through 1925* (Correction and Supplement), Bull. Earthq. Res. Inst. Tokyo Univ. *57*, 111–117 (in Japanese).

UTSU, T. (1982b), *Catalog of Large Earthquakes in the Region of Japan from 1885 through 1980*, Bull. Earthq. Res. Inst. Tokyo Univ. *57*, 401–463 (in Japanese).

(Received 31st October 1983)

PAGEOPH, Vol. 122 (1984/85) 0033-4553/85/060863-15$1.50 + 0.20/0

Asperities and Barriers along the Japan Trench East of Tohoku from the Distribution of Earthquake Source Areas[1])

By MANFRED BAER[2,3])

Abstract – Barriers and asperities along the Japan trench east of Tohoku (north-eastern Honshu) are outlined by investigating the distribution of source areas of earthquakes with $M \geqslant 6$ in the time period 1926 to 1981. The earthquakes were grouped into three magnitude ranges: A: $6.0 \leqslant M \leqslant 6.4$, B: $6.5 \leqslant M \leqslant 7.0$ and C: $7.1 \leqslant M \leqslant 8.1$.

The following feature is found to be common to all three groups: Either the source areas do not substantially overlap, or they superpose almost perfectly. Only a very small number of events show partial overlapping of source areas. The events of group A tend to align along several NW–SE oriented zones with distinct interspaces. These zones do not follow the regional stress field but show excellent correlation with the direction perpendicular to the magnetic anomaly lineations of the ocean floor in this area. The events of group B and C generally fill in the spatial gaps of group A. In terms of the barrier model this can be explained by barriers of varying strength through which the fracture process of smaller magnitude events does not propagate and that of larger events is not inhibited. The direction of the group A barriers suggests that they have been developed at the time of creation of the oceanic lithosphere and possibly relate to ancient transform faults now buried by sediments. Since the accuracy of epicenter locations is crucial for this kind of investigation, 45 events between 1963 and 1979 have been relocated by the joint epicenter determination method.

Introduction

The observation that the source areas of large ($M \geqslant 7$) earthquakes tend to abut has led to the very successful concept of seismic gaps as possible sites for future large earthquakes (e.g. FEDOTOV, 1965; MOGI, 1968a; UTSU, 1970; SYKES, 1971; KELLEHER *et al.*, 1973; OHTAKE *et al.*, 1977). A seismic gap is thereby defined as a portion of plate boundary which has not ruptured for a relatively long time. The source areas required to outline seismic gaps are usually obtained by assuming that they are represented by the aftershock area involved. This assumption is supported by studies demonstrating that aftershock areas do not significantly overlap (e.g. FEDOTOV, 1965; MOGI, 1968a; KELLEHER, 1970; SYKES, 1971). Occasionally, felt areas of intensities

---

[1]) Contribution No. 456, Institut fur Geophysik, ETHZ.

[2]) Earthquake Research Institute, University of Tokyo.

[3]) Present address: Schweizerischer Erdbebendienst, Institut für Geophysik, ETH Honggerberg, 8093 Zurich, Switzerland.

VIII–IX also have been used to define rupture areas (KELLEHER, 1972; WYSS and BAER, 1981) if accurate aftershock data are not available.

Physical models explaining seismic gaps and abutting source areas are known as the asperity model (MOGI, 1977; LAY and KANAMORI, 1980, 1981) and the barrier model (DAS and AKI, 1977; DAS and SCHOLZ, 1981). In the asperity model, the size and distribution of regions of high stress concentration govern the degree of loading of adjacent asperities when a large asperity fails. The barrier model explains observed features like aftershocks, multiple events, delayed multiple events, postseismic rupture growth, and the stopping of an earthquake. This model has been successfully applied to explain the great earthquake sequence along the Nankai trough by DAS and SCHOLZ (1981) and MIYATAKE (1982). It has been pointed out (e.g. MOGI, 1969) that tectonic features like transform faults, topographic features, and changes in direction of a subduction zone may act as barriers to large earthquakes.

If barriers are responsible for stopping the rupture process of large earthquakes, it seems reasonable that they also could affect the ruptures of smaller magnitude earthquakes. In this paper barriers and asperities are investigated along the Japan trench between 38°N and 41°N by considering the distribution of source areas of earthquakes with magnitudes $M \geqslant 6$.

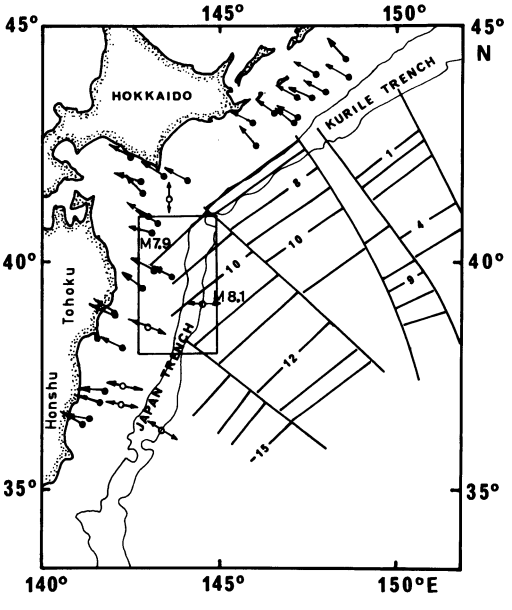

Figure 1
Slip vectors of focal mechanisms along the Japan and Kurile trench (after SENO and EGUCHI, 1982) and magnetic reversal lines of the Pacific plate (after HILDE *et al.*, 1976) (solid circle: thrust fault; open circle: normal fault; double headed arrow: trend of T-axes of normal faulting).

The Japan trench

Figure 1 summarizes some tectonic features of the Japan/Kurile trench. The slip vectors compiled by SENO and EGUCHI (1982) are based on focal mechanism observations. The slip directions are in good agreement with the plate motion calculated by MINSTER and JORDAN (1978) and indicate an underthrusting of the Pacific plate along the Japan trench in a WNW direction nearly perpendicular to the trench axis between 38°N and 41°N. The magnetic reversal lines in this area strike NE and can be followed across the trench (HILDE et al., 1976).

In the past 80 years, 18 large ($M \geqslant 7$) earthquakes occurred in the Japan trench segment (see Table 1). Even though this is a large number, it is difficult to define a recurrence time because of their swarm-like occurrence (UTSU, 1974). The largest event in this region, the Sanriku–Oki earthquake, occurred on 2 March 1933 with a magnitude of 8.1 (JMA). Its epicenter was located seaward of the trench axis, but most of the aftershocks occurred on the landward side. During the following year, the aftershock area expanded to the North, West, and South of the source area (MOGI, 1968b). The focal mechanism was shown to be a normal fault which may have ruptured the entire lithosphere (KANAMORI, 1971a). The epicenter of the Tokachi–Oki earthquake (May

Table 1

Large earthquakes between 1900 and 1981. Source parameters after JMA (Japan Meteorological Agency) improved catalog 1982

Year	Month	Day	Hour (GMT)	Lat. N	Lon. E	*M*
1909‡	06	12	00	39.9	143.0	7.0
1912‡	12	08	23	39.0	143.0	7.3
1915‡	10	13	19	39.3	143.8	7.0
1915‡	10	16	13	39.7	143.6	7.1
1915‡	11	01	07	38.9	143.1	7.5
1916‡	01	25	11	39.0	144.0	7.1
1916‡	03	18	00	40.2	143.7	7.0
1918‡	12	13	21	40.2	144.6	7.3
1919‡	05	03	00	40.0	144.0	7.5
1922‡	05	15	20	40.0	144.0	7.5
1928	05	27	09	39.95	143.25	7.0
1933‡	03	02	17	39.23	144.50	8.1*
1935	10	18	00	40.75	144.35	7.1
1939	10	10	18	38.28	142.78	7.0
1960	03	20	17	39.42	143.43	7.2
1968	05	16	00	40.73	143.58	7.9†
1968	06	12	13	39.42	143.13	7.2
1981	01	18	18	38.60	142.97	7.0

* Mogi (1968a) reported an averaged magnitude of 8.5

† Kanamori and Anderson (1975) reported an averaged magnitude of 8.0.

‡ Not used in this investigation.

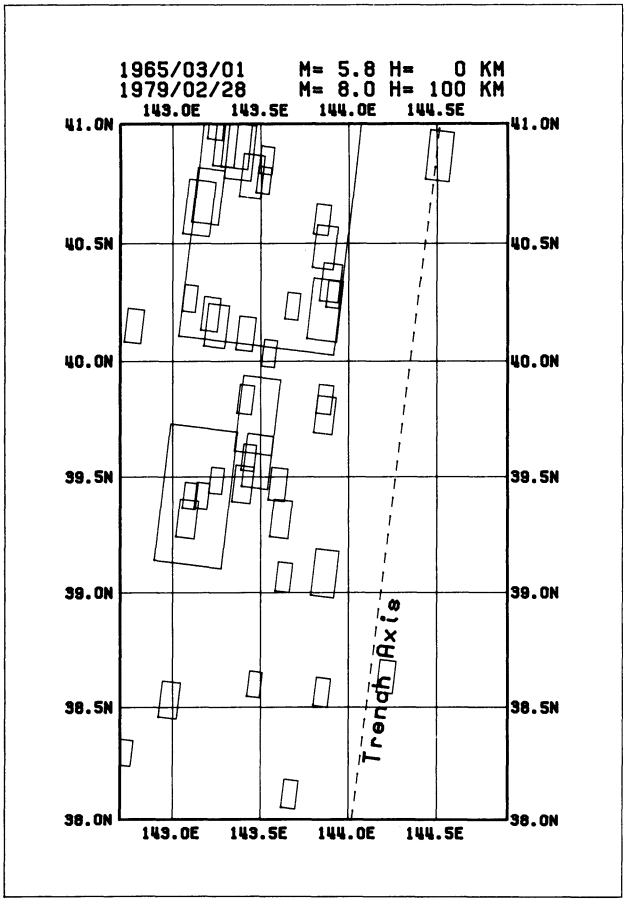

Figure 2(a)
Earthquakes which have been relocated: (a) JMA (Japan Meteorological Agency) determinations; (b) joint epicenter determination (JED) method. The focal depths were fixed at the values reported by ISC from pP–P determinations.

1968, $M = 7.9$) – the second largest event of the area in this century – was located close to the junction of the Japan and Kurile trenches. The focal mechanism is characterized by dip-slip faulting with a strike-slip component (KANAMORI, 1971b).

In general, it has been found (SENO and EGUCHI, 1982) that the average seismic slip along the Japan trench (~2 cm/y) accounts only for one fifth of the relative plate motion, and therefore the major part must be due to aseismic movement.

Data and method

In order to locate possible barriers it is essential to have information on the distribution and size of source areas. The smaller the source area is, the smaller the

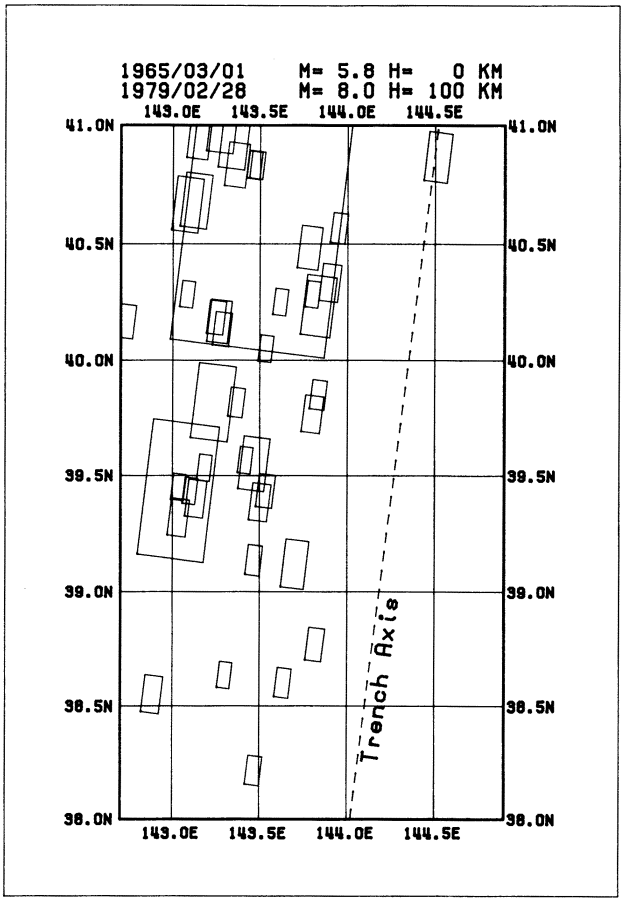

Figure 2(b)

barriers resolved. However, the precision and accuracy of the hypocenter locations set limits to the size of the source areas to be used

The epicenter parameters have been selected from the JMA (Japan Meteorological Agency) data catalogs from 1926 to 1981. For the period from 1926 to 1960 the source parameters are from the improved catalog (JMA, 1982), thus providing the best consistency possible for the entire period. The uncertainties of the epicenter co-ordinates determined by JMA are usually less than 10 km and the location of corresponding source areas of $M > 6$ events can be determined satisfactorily. However, the source areas of $M \sim 6$ events can not be determined from their aftershock distribution because location uncertainties do not allow good definition of the mainstock source area. Furthermore, the data catalog is complete only from $M = 5.0$ before 1950 and $M = 4.0$ by 1980, as shown by an analysis of the log $N - M$ relation in this region.

In this investigation rupture areas are derived from the distribution of aftershocks whenever possible, i.e. when more than three aftershocks were reported. An aftershock was defined as an event of lower magnitude occurring within 24 hours after the

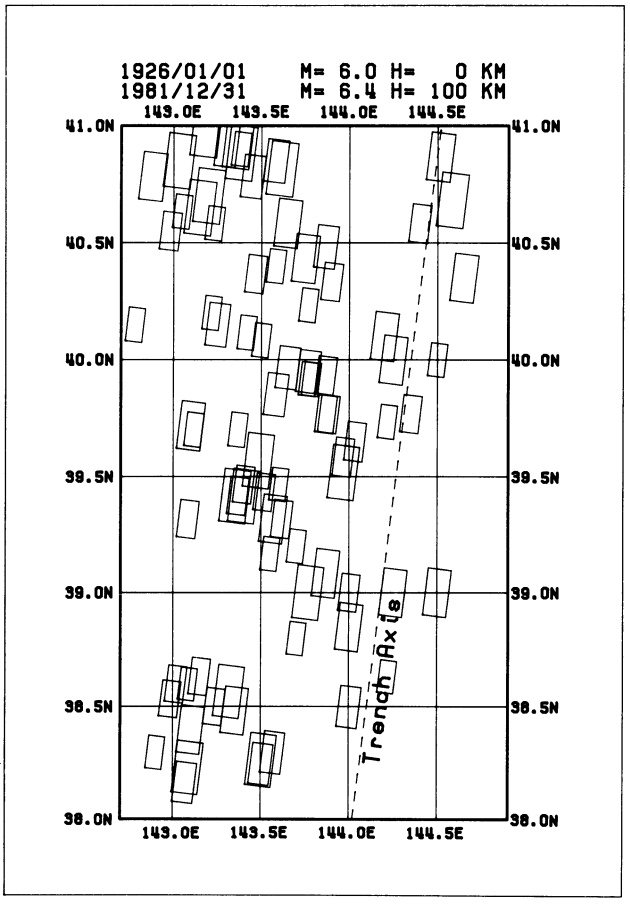

Figure 3(a)
Distribution of source areas for the magnitude range $6.0 \leqslant M \leqslant 6.4$. Source areas have been calculated by $\log S = 1.02M - 4.01$ (UTSU and SEKI, 1955). The dashed line indicates the axis of the Japan trench. (a) Including aftershocks and events with large epicenter uncertainties; (b) excluding aftershocks (within 24 hours) and unreliable events.

mainshock. Since postseismic rupture growth can be explained by barriers whose strength increases with distance, events occurring after 24 hours were not used.

If too few aftershocks were reported, the magnitudes have been transformed to source areas according to the relation $\log S = 1.02M - 4.01$ derived by UTSU and SEKI (1955), where S is the source area in square kilometers and M is the JMA magnitude. This relation was shown by KANAMORI and ANDERSON (1975) to agree with a dislocation model that assumes complete stress drop and a seismic efficiency of one. The source area calculated by this relation was then centered at the instrumentally-determined epicenter. The fault direction was assumed to run parallel to the trench axis, and the length was set equal to twice the fault width (ABE, 1975).

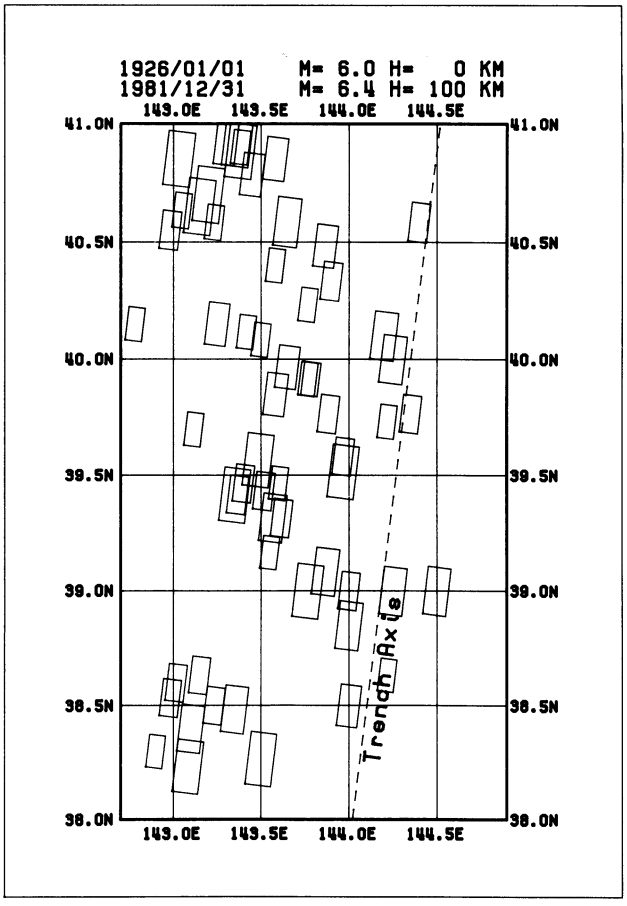

Figure 3(b)

The accuracy of the epicenter locations was determined by relocating 45 events with $M \geqslant 5.8$ in the period 1963 to 1979 using the joint epicenter determination (JED) method (DOUGLAS and LILWALL, 1972). For this purpose, ICHIKAWA and MOCHIZUKI's (1971) traveltime tables have been used for the distance range up to 500 km. Because of the one-sided distribution of the stations and the large distances to the nearest station (~150 km), the focal depth was not calculated but instead was fixed at the values reported by ISC from pP–P observations. These depths differ from the values determined by JMA by as much as 40 km. This discrepancy suggests that the epicentral locations and origin time in the JMA catalogues may be biased (MAKI, 1982). Figures 2a and 2b show a comparison of the locations of the JMA determinations, and the positions relocated by the JED method, respectively. The average north–south adjustment of the focal co-ordinates is less than 2.5 km, with a standard deviation σ of 4 km. Thus the JMA latitude determinations appear to be reliable. However, the longitude seems to have much larger discrepancies. The average adjustments amount to a 8 km west shift with $\sigma = 8$ km. Single events are displaced by as much as 30 km. The large

east–west displacements are partly due to the station distribution (no stations east of the area investigated), but mainly due to the different depth determinations of JMA and ISC. The overall pattern, however, remains unchanged by the systematic west shift. For consistency, only JMA locations were used for further investigations.

An event was excluded from further investigations when either the uncertainty of the focal co-ordinates exceeded 10 km (12 events, all of them before 1947), or if the event was an aftershock (25 events). The Sanriku earthquake was excluded because of its normal faulting mechanism. This event is shown in Fig. 5 only for the sake of completeness. Figure 3a shows the pattern of source distribution when no events are deleted. Figure 3b shows the pattern for earthquakes selected by the above criteria.

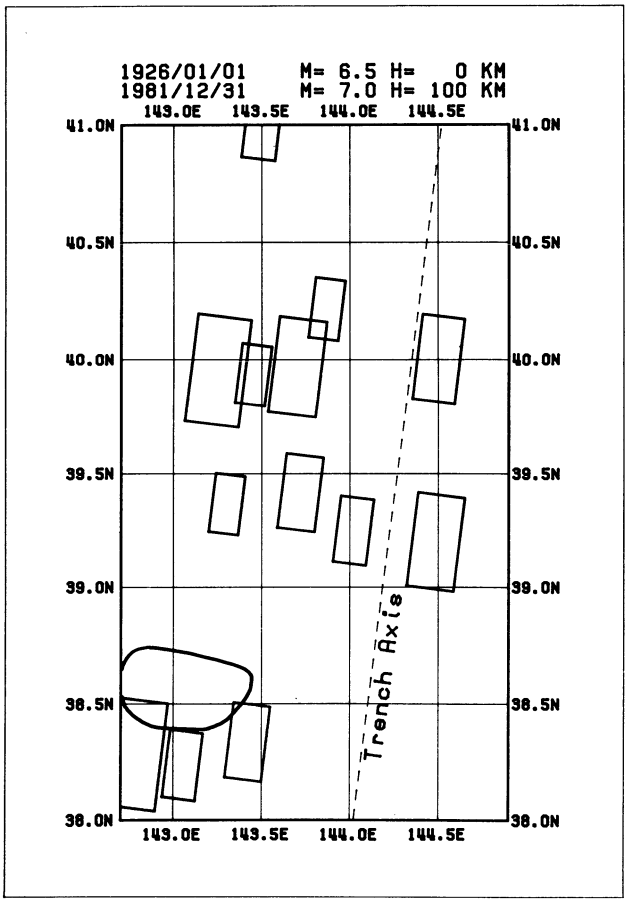

Figure 4

Distribution of source areas for the magnitude range $6.5 \leqslant M \leqslant 7.0$. Source areas derived from $\log S = 1.02M - 4.01$ (Utsu and Seki, 1955) for rectangles, from the distribution of aftershocks otherwise.

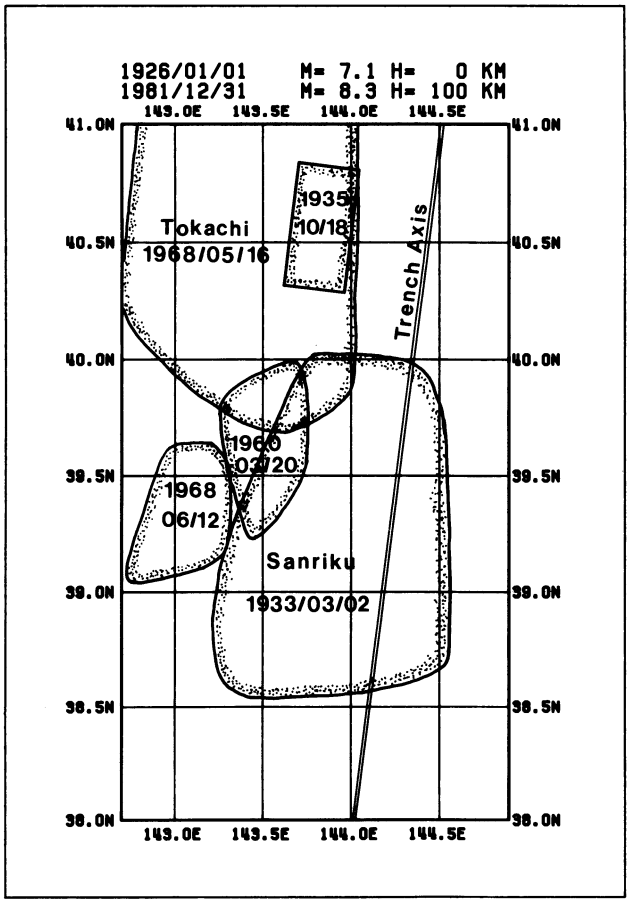

Figure 5
Distribution of source areas for the magnitude range $M \geqslant 7.1$. Source areas derived from $\log S = 1.02M - 4.0$ (UTSU and SEKI, 1955) for rectangles, from the distribution of aftershocks otherwise.

Results

The earthquakes were grouped in 3 magnitude ranges, A ($6.0 \leqslant M \leqslant 6.4$), B ($6.5 \leqslant M \leqslant 7.0$) and C ($M \geqslant 7.1$), with corresponding fault lengths of about 16–25 km, 29–50 km, and >58 km respectively. The geographical distributions of the source areas for each group are depicted in Figs. 3b–5. The source areas of events of comparable size do not in general, overlap; they either abut or superpose almost completely. This is true not only for large earthquakes ($M \geqslant 6.5$), but also for smaller magnitude events down to $M = 6.0$. Furthermore, the events of group A (Fig. 3b) seem to line up along distinct NW–SE trending zones. This trend is not very obvious for groups B and C, probably due to the small number of events. However, these events occupy the interspace between group A zones (Fig. 6) in most cases. Larger events like the

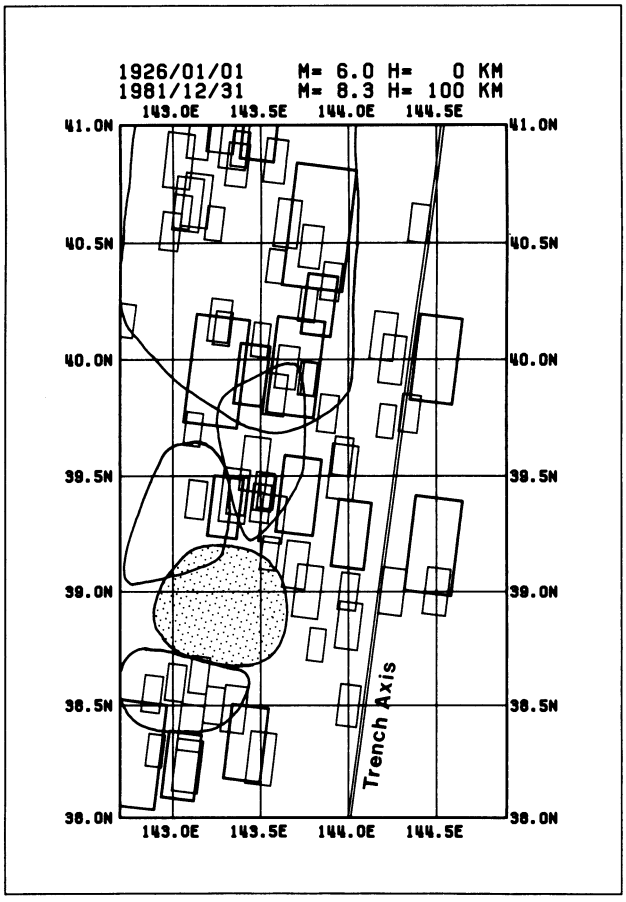

Figure 6
Superposition of Figs 3b–5. Thin lines represent $6.0 \leqslant M \leqslant 6.4$, solid line $M \geqslant 6.5$. The shaded area corresponds to the 1 November 1915 earthquake ($M = 7.5$) which can be considered as a seismic gap at present time.

Tokachi–Oki 1968 earthquake might have ruptured across one or more of the group A zones. The instrumentally-determined epicenter of this event, which might indicate the starting point of the rupturing process, is located in the northernmost zone of group A events propagating subsequently to the south and north-west (KANAMORI, 1971b). Recently, KIKUCHI (1982) analyzed the rupture process of this event in the time and space domain. His results suggest a multiple-event rupture process of about 160 seconds duration where the individual pulses occur in a sequence along NW–SE oriented zones. The zones may correspond to the ones observed in the present study. The dotted area in Fig. 6 indicates the presumed location of the 1 November 1915 earthquake ($M = 7.5$, after CENTRAL METEOROLOGICAL OBSERVATORY CMA, 1952). USAMI (1975) and UTSU (1979) reported for this event a latitude 0.6 degrees further south, with standard errors of 0.2–0.5 degrees. HATORI (1981) estimated its source area

to extend from about 38°N to 39°N. Thus, its actual (CMA) location is in doubt and the earthquake was not included here. However, since this area has not ruptured since 1915 in a large earthquake, it must be considered as a seismic gap with a high seismic potential. Assuming a subduction rate of 10.5 cm/y (after MINSTER and JORDAN, 1978) and no aseismic slip, an accumulated strain of 7 m would result in a stress drop of about 35 bar. SENO and EGUCHI (1982), however, proposed 80% aseismic slip which would reduce the accumulated strain to about 1 m. This seismic gap has been described by many authors (MOGI, 1968b; KELLEHER *et al.*, 1973; UTSU, 1974; HATORI, 1981) and was investigated in detail by SENO (1979). The determination of the size of a future event is difficult. The present results, however, outline and limit the potential source area.

The time sequence of the earthquakes is shown in Fig. 7. For each of the group A zones (numbered 1 to 5 from South to North, see Fig. 8) the events are plotted along the time axis 1926–1980. The top section shows events of $M \geqslant 6.5$, with their approximate rupture areas indicated by the dashed lines. The seismic activity can be observed to migrate between adjacent group A zones. This is best seen in the period from 1940 to

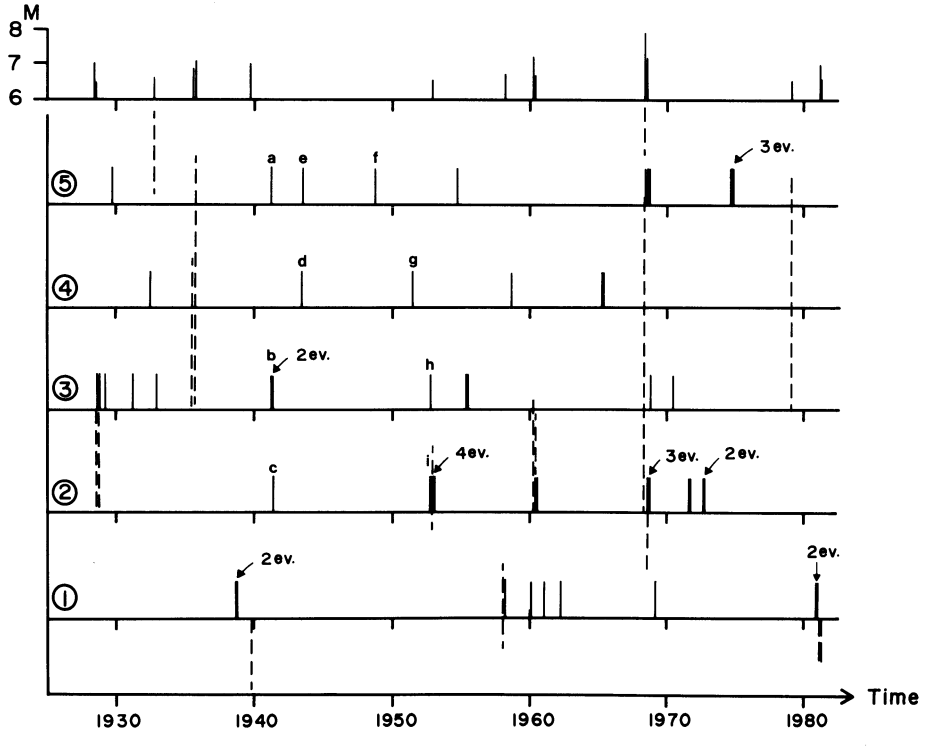

Figure 7

Time sequence of the earthquakes along the various seismic zones. Top: occurrence of earthquakes with $M \geqslant 6.5$. Below: seismicity along the barriers 1 to 5 (see Fig. 8). Dashed lines indicate zones ruptured by $M \geqslant 6.5$ events. Earthquake sequences are labeled a–i (see text).

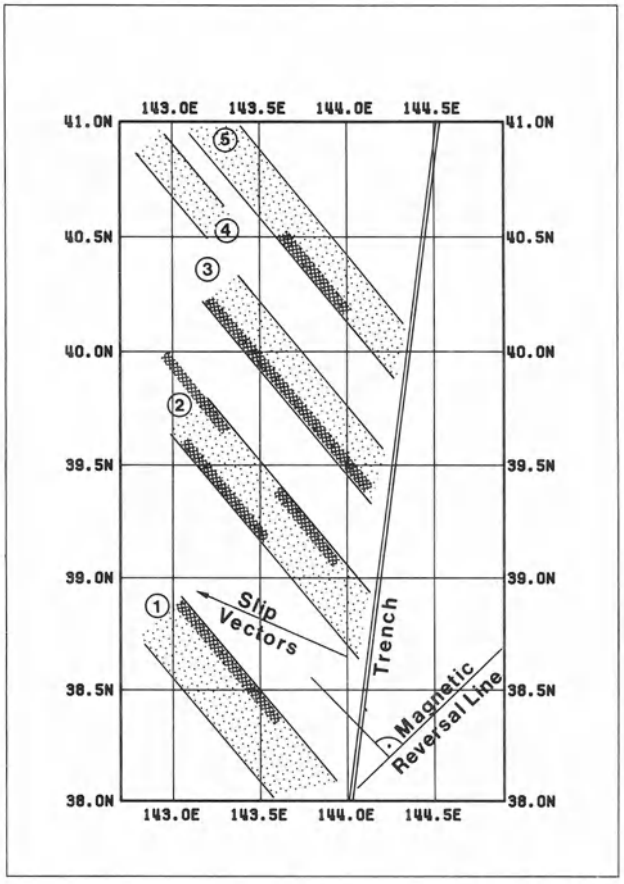

Figure 8

Schematic interpretation of the distribution of the source areas. Light shaded areas indicate the locations of $6.0 \leqslant M \leqslant 6.4$ earthquakes. Barriers for $M \geqslant 6.5$ earthquakes are indicated by dark shading.

1960 where the first event occurs in zone 5, then 2 events in zone 3, followed by one event in zone 2 (sequence a–c). Two years later, zone 4 becomes active, followed by zone 5 (sequence e–d). After a 5 year period of quiescence the activity starts in zone 5 again, moving to the south to zone 2 (sequence f–i).

Discussion

Figure 8 shows a schematic interpretation of the results. The light shaded areas indicate the zones where earthquakes in the magnitude range of 6.0 to 6.4 are most likely to occur. The limits of these zones indicate the position of barriers which cause these low magnitude events to stop rupturing. These zones can also be interpreted as

areas which are strongly coupled to the continental plate. The dark shaded portions indicate the boundaries of the larger magnitude ($M \geqslant 6.5$) events, which would be limited by strong barriers. The relatively large aseismic slip reported by SENO and EGUCHI (1982) may be due to weak coupling in the non-shaded areas. Depending on the time interval between the failure of two or more adjacent, strongly-coupled zones, it is possible to explain large slow earthquakes or multiple-rupture events like Tokachi–Oki 1968. For larger time intervals, swarm type activity of smaller events would result.

The cause of the asperity and barrier alignment is not clear. The displacement vectors of the focal mechanisms in this area point about 290 to 300 degrees clockwise from north (see Fig. 1) in contrast to the 320 degree strike of the barriers. The bathymetry does not have any linear features like seamounts or valleys, nor does the direction of the trench change in this area. However, the direction of increasing age of the oceanic lithosphere i.e. the direction perpendicular to the magnetic reversal lines (Fig. 1), shows excellent agreement with the orientation of the strongly-coupled zones. If these directions are physically related to each other, asperity zones could be related to features formed when the oceanic crust was crested. One such feature could be rock differentiation along the ridge, which seems unlikely, another could be ancient transform faults. Transform faults, in general, are topographic highs. In these elevated areas the sedimentary coverage is less than in adjacent areas thus allowing closer contact with the subducted plate. The arrangement of $6.0 \leqslant M \leqslant 6.4$ earthquakes presented in this paper, therefore, may indicate tectonic features which have not yet been observed by other geophysical methods.

The postulated seismic gap at 39°N and 143°E has apparently existed for at least 67 years. If the 1915 event were located further South, as proposed by UTSU (1979), it could be much older. It is unlikely that this zone is aseismic, since in the earthquake catalog of UTSU (1979) at least 9 events can be found (not counting the swarm of which the 1 November 1915 event was the largest). Even though the earthquake locations are less accurate, this zone is an active one and thus has a high seismic potential. To the north of this seismic gap, the accumulated stress has been released by the 12 June 1968 event ($M = 7.2$) and to the south by the 19 January 1981 earthquake ($M = 7.0$). Assuming that a future event in this gap will probably not propagate across the northern and southern barriers, it can be inferred that the potential fault length is no more than 80–100 km. The magnitude would be about 7.5.

Several assumptions in the course of this investigation are certainly oversimplified, such as the presentation of the rectangular source areas, the equal ratio of fault length to width, and the fault direction parallel to the trench axis. Also the relation between source area and magnitude (UTSU and SEKI, 1955) contains considerable scatter. Nevertheless, the consistent results suggest that mapping source areas for events with magnitudes as low as $M = 6.0$ gives some insight into the detailed physical processes associated with disastrous earthquakes. The major question unresolved by this investigation is the influence of lower magnitude events, including their aftershocks, on the distribution of the barriers.

Conclusions

For the area along the Japan trench east of Tohoku it has been shown that the method of mapping earthquake source areas can be used to obtain qualitative information on barriers and asperities. The source areas of $6.0 \leqslant M \leqslant 6.4$ events align in four separate zones in a NNW direction perpendicular to the magnetic reversal lines of the ocean floor. Earthquakes with $M \geqslant 6.5$ fill in the spatial gaps between these barriers and tend to be limited by them.

Acknowledgments

The access to the new JMA data catalog prior to its publication is gratefully acknowledged. The critical comments and suggestions by Professor T. Utsu and Professor K. Mogi improved the manuscript substantially. This research was supported by the Swiss National Science Foundation and the Japan Society for Promotion of Science.

References

ABE, K. (1975), *Reliable Estimation of the Seismic Moment of Large Earthquakes*, J. Phys. Earth *23*, 381–390.

CMO (CENTRAL METEOROLOGICAL OBSERVATORY) (1952) The Seismological Bulletin of the Central Meteorological Observatory for the Year 1950.

DAS, S., and AKI, K. (1977), *Fault Plane with Barriers: A Versatile Earthquake Model*, J. geophys. Res. *82*, 5658–5670.

DAS, S., and SCHOLZ, C. H. (1981), *Theory of Time-Dependent Rupture in the Earth*, J. geophys. Res. *86*, 6039–6051.

DOUGLAS, A., and LILWALL, R. C. (1972), *Methods of Estimating Travel Times and Epicenters*, Geophys. J.R. astr. Soc. *30*, 187–197.

FEDOTOV, S. A. (1965), *Regularities of the Distribution of Strong Earthquakes of Kamchatka, the Kurile Islands, and Northeastern Japan*, Tr. Inst. Fiz. Zemli Akad. Nauk SSSR *36*, 66–93.

HATORI, T. (1981), *Tsunami Sources in the Sanriku Region in 1979 and 1981, Northeastern Japan – Seismic Gap off Miyagi*, Bull. Earthq. Res. Inst., Tokyo Univ. *56*, 629–640.

HILDE, T. W. C., ISEZAKI, N., and WAGEMAN, J. M., *Mesozoic Sea-Floor Spreading in the North Pacific*, in *The Geophysics of the Pacific Ocean Basin and its Margins* (Geophysical Monograph 19, AGU 1976), pp. 205–226.

ICHIKAWA, M., and MOCHIZUKI, H. (1971), *Traveltime Table for Local Earthquakes In and Near Japan*, Pap. Met. Geophys., Tokyo *22*, 229–290 (in Japanese).

JMA (JAPAN METEOROLOGICAL AGENCY) (1961–1981), Monthly Seismological Bulletin of the Japan Meteorological Agency.

JMA (JAPAN METEOROLOGICAL AGENCY) (1982), *Catalog of Relocated Major Earthquakes In and Near Japan (1926–1960)*, Seismological Bulletin of the Japan Meteorological Agency, Supplementary Volume No. 6.

KANAMORI, H. (1971a), *Seismological Evidence for a Lithospheric Normal Faulting – The Sanriku Earthquake of 1933*, Phys. Earth Planet. Inter. *4*, 289–300.

KANAMORI, H. (1971b), *Focal Mechanism of the Tokachi-Oki Earthquake of May 16, 1968: Contortion of the Lithosphere at a Junction of Two Trenches*, Tectonophysics *12*, 1–13.

KANAMORI, H., and ANDERSON, D. L. (1975), *Theoretical Basis of Some Empirical Relations in Seismology*, Bull. seism. Soc. Am. *65*, 1073–1095.

KELLEHER, J. A. (1970), *Space-Time Seismicity of the Alaska–Aleutian Seismic Zone*, J. geophys. Res. *75*, 5745–5756.

KELLEHER, J. A. (1972), *Rupture Zones of Large South American Earthquakes and Some Predictions*, J. geophys. Res. *77*, 2087–2103.

KELLEHER, J., SYKES, L. R., and OLIVER, J. (1973), *Possible Criteria for Predicting Earthquake Locations and their Applications to Major Plate Boundaries of the Pacific and the Caribbean*, J. geophys. Res. *78*, 2547–2585.

KIKUCHI, M. (1982), *Analysis of Body Waves of Large Earthquakes (IV)*; 2-Dimensional Distribution of Hypocenters, Program and Abstracts, Seismological Society of Japan, *2*, 93.

LAY, T., and KANAMORI, H. (1980), *Earthquake Doublets in the Solomon Islands*, Phys. Earth Planet. Int. *21*, 283–304.

LAY, T., and KANAMORI, H. *An Asperity Model of Large Earthquake Sequences*, in *Earthquake Prediction*. (Maurice Ewing Series 4, AGU 1981), pp. 579–592.

MAKI, T. (1982), *Effects of Observational Conditions on Hypocenter Locations of Intermediate-Depth Earthquakes in Central Japan*, Bull. Earthq. Res. Inst., Tokyo Univ. *57*, 49–82.

MINSTER, J. B., and JORDAN, T. H. (1978), *Present Day Plate Motions*, J. geophys. Res. *83*, 5331–5354.

MIYATAKE, T. (1982), *Great Earthquake Sequence Along the Nankai Trough – a Hypothesis*, Bull. Earthq. Res. Inst., Tokyo Univ. *57*, 103–109 (in Japanese).

MOGI, K. (1968a), *Development of Aftershock areas of Great Earthquakes*, Bull. Earthq. Res. Inst., Tokyo Univ. *46*, 175–203.

MOGI, K. (1968b), *Some Features of Recent Seismic Activity in and near Japan (1)*, Bull. Earthq. Res. Inst., Tokyo Univ. *46*, 1225–1236.

MOGI, K. (1969), *Relationship between the Occurrence of Great Earthquakes and Tectonic Structures*, Bull. Earthq. Res. Inst., Tokyo Univ. *47*, 429–451.

MOGI, K. (1977), *Seismic Activity and Earthquake Prediction*, in *Proceedings of the Symposium on Earthquake Prediction Research (1976)*, pp. 203–214.

OHTAKE, M., MATUMOTO, T., and LATHAM, G. V. (1977), *Seismicity Gap near Oaxaca, Southern Mexico as a Probable Precursor to a Large Earthquake*, Pure and Appl. Geophys. *115*, 375—385.

SENO, T. (1979), *Intraplate Seismicity in Tohoku and Hokkaido and Large Interplate Earthquakes: A Possibility of a Large Earthquake off the Southern Sanriku Coast, Northern Japan*, J. Phys. Earth *27*, 21–51.

SENO, T., and EGUCHI, T. (1982), Seismotectonics of the Western Pacific Region, AGU/GSA Geodynamics Series, Western Pacific, in press.

SYKES, L. R. (1971), *Aftershock Zones of Great Earthquakes, Seismicity Gaps, and Earthquake Prediction for Alaska and the Aleutians*, J. geophys. Res. *76*, 8021–8041.

USAMI, T. (1975), *Nihon Higai Zisin Soran*, Tokyo Univ. Press (in Japanese).

UTSU, T. (1970), *Seismic Activity and Seismic Observation in Hokkaido in Recent Years*, Rep. Coord. Com. Earthq. Pred. *2*, 1–2 (in Japanese).

UTSU, T. (1974), *Space-Time Pattern of Large Earthquakes Occurring off the Pacific Coast of the Japanese Islands*, J. Phys. Earth *22*, 325–342.

UTSU, T. (1979), *Seismicity of Japan from 1855 through 1925 – A New Catalog of Earthquakes of $M > 6$ felt in Japan and Smaller Earthquakes which Caused Damage in Japan*, Bull. Earthq. Res. Inst., Tokyo Univ. *54*, 253–308.

UTSU, T., and SEKI, A. (1955), *A Relation Between the Area of Aftershock Region and the Energy of Mainshock*, Zisin: J. Seism. Soc. Japan *7*, 233–240 (in Japanese).

WYSS, M., and BAER, M., *Earthquake Hazard in the Hellenic Arc*, in *Earthquake Prediction* (Maurice Ewing Series 4, AGU 1981), pp. 153–172.

PAGEOPH, Vol. 122 (1984/85) 0033-4553/85/060878-16$1.50 + 0.20/0

Correlation of Foreshocks and Aftershocks and Asperities

By VINDELL HSU, CHARLES E. HELSLEY, EDUARD BERG and DAVID A. NOVELO-CASANOVA[1]

Abstract – A close correlation in spatial distribution of local seismic activity and energy release patterns before and after the 1979 Petatlan, Mexico earthquake suggests heterogeneity within the fault plane of this major low-angle thrust event associated with subduction along the Middle America Trench. A simple two-asperity model is proposed to account for the complexity. Foreshocks and aftershocks of the neighboring 1981 Playa Azul earthquake showed a similar pattern. As both events occurred at the junction of the Orozco Fracture Zone and the Middle America Trench, we speculate that the observed complex fault plane is caused by subduction of the rugged ocean floor of the Orozco Fracture Zone. Short-term precursory seismicity prior to the Petatlan earthquake can be explained by using the asperity model and migration of a slip front from the south-east to the north-west across the main shock source region.

Key words: Petatlan earthquake; Foreshocks and aftershocks; Asperities.

1. Introduction

The asperity model originated from experiments on rock failure processes in laboratory studies (BYERLEE, 1970; SCHOLZ and ENGELDER, 1976). The concept has been used extensively in seismological studies to model earthquake ruptures (WYSS and BRUNE, 1967; KANAMORI and STEWART, 1978; EBEL, 1980; LAY and KANAMORI, 1980) and to explain local and global seismicities (WESSON and ELLSWORTH, 1973; BAKUN *et al.*, 1980; LAY *et al.*, 1982) and precursory seismic patterns (JONES and MOLNAR, 1979; KANAMORI, 1981; DMOWSKA and LI, 1982). Asperities, defined as areas of relatively higher strength within the fault plane, have been recognized for a number of cases by using strong motion seismograms (WYSS *et al.*, 1983) and seismicity patterns (VALDES *et al.*, 1982; HABERMANN, 1983). In analysis of the foreshocks and aftershocks of the 1979 Petatlan earthquake, we discovered two regions that are possible candidates for asperities. Both areas are within the source region and both showed strain-releasing activity before and after the main shock.

The Petatlan earthquake ($Ms = 7.6$) occurred on 14 March 1979 off the coast of Guerrero, Mexico about 200 km north-west of Acapulco. The epicentral region had not had a major earthquake in the previous 36 years and was designated as a seismic gap

[1] Hawaii Institute of Geophysics, University of Hawaii, 2525 Correa Road, Honolulu, Hawaii 96822.

(McCann *et al.*, 1979). The Petatlan earthquake is a low-angle thrust event typical of major earthquakes along the Middle America Trench associated with convergence of the Cocos and the North American Plates (Molnar and Sykes, 1969; Chael and Stewart, 1982). Long period WWSSN records indicate seismic moments of 2.7×10^{27} and 1.0×10^{27} dyne-cm for surface and body waves, respectively (Chael and Stewart, 1982).

Local seismicity before and after the Petatlan earthquake was monitored by portable seismographs from Hawaii Institute of Geophysics (HIG) and University of Wisconsin, Madison (UW) (Ewing and Meyer, 1982; Valdes *et al.*, 1982; Hsu *et al.*, 1983). The main shock was relocated by the HIG network at 17°27.21'N, 101°27.32'W about 10 km offshore (Gettrust *et al.*, 1981). Using UW stations, Valdes *et al.* (1982) located 255 aftershocks and outlined an aftershock region of 6060 km^2 and a smaller region of concentrated aftershocks about 2620 km^2 inside the aftershock zone. They argued that this smaller region represents an asperity. Hsu *et al.* (1983) located 500 earthquakes during the 6 weeks before the main shock using HIG stations. They found four regions (Zones A, B, C and D shown in Figs. 1 and 6) of relatively higher seismic activity. One of them (Zone A) is 25 km east of the main shock epicenter and is within the eventual main shock source region. Events of Zone A followed a moderate size foreshock (Ms = 5.2, 28 February 1979) and showed migration of epicenters toward the main shock.

In this paper we analyze the spatial and temporal distributions of 1355 earthquakes located by the HIG network covering the four-week period immediately following the main shock and compare them to the foreshocks. We also located 210 aftershocks using joint HIG and UW stations. These events show great improvement in constraining the depths of aftershocks. The two proposed asperities are inferred based on foreshock and aftershock correlation. Both are within the fault plane of the Petatlan earthquake, one beneath Zone A and the other beneath a region of about the same size containing the main shock epicenter.

2. *Aftershocks*

Figure 1 shows the 1355 HIG network located aftershock locations. A circular region about 6000 km^2 of concentrated aftershocks clearly defines the source region affected by the Petatlan earthquake. This region within the one-degree square (17–18°N, 101–102°W) is essentially the same as the region defined by 255 aftershocks located by UW stations (Valdes *et al.*, 1982).

Additional groups of activity are found to the south-east and to the north of the Petatlan source region (Fig. 1). These areas have been found to be more active before the main shock and were designated as Zones B, C, and D (Hsu *et al.*, 1983). Zone D was very active before the main shock and its activity followed three moderate events in the Mexico Volcanic Belt (22, 26 and 28 February 1979, Hsu *et al.*, 1983). Zones B and C were also active before the main shock and their activities followed two moderate

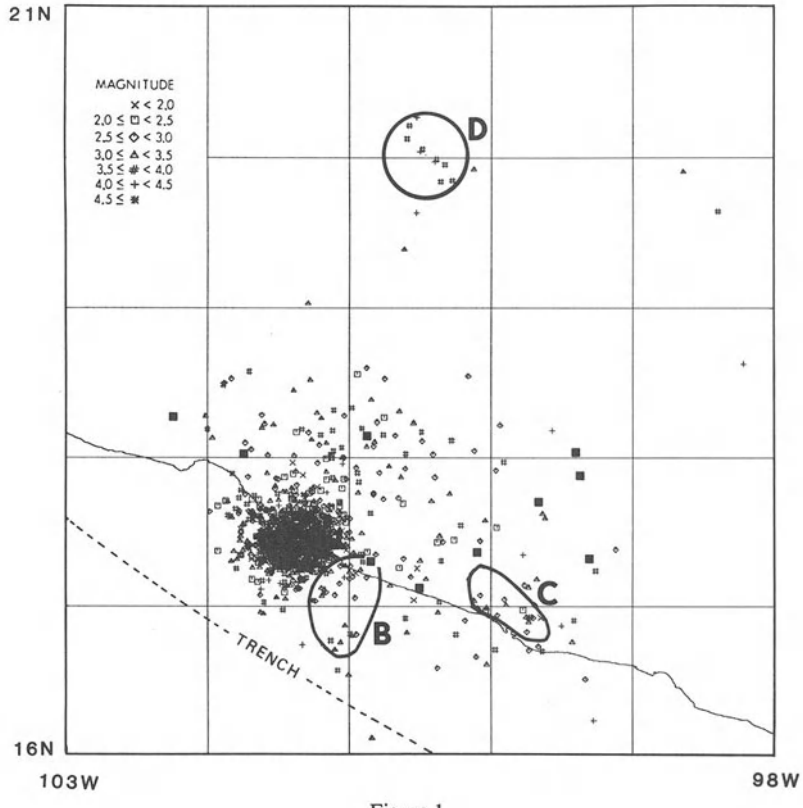

Figure 1

Epicenter locations of 1355 earthquakes located by HIG stations (filled squares) occurring during the four weeks after the Petatlan earthquake. Symbols for different magnitude ranges will be also used for the following figures. Enclosed areas B, C, and D contain activities that are also noted before the main shock. The shapes of the regions are outlined based on activities before the main shock.

events near the Mexican coastline, which occurred on 26 January 1979 ($Ms = 6.6$) and 11 December 1978 ($Ms = 5.0$), respectively (Hsu *et al.*, 1983). Valdes *et al.* (1983) also observed the activities in Zones B and C after the main shock using UW stations and they speculate that these activities may be associated with seismic gap boundaries.

We now examine the aftershock activity of the source region. Figure 2a shows 950 aftershock locations within the one-degree square containing the source region. A two-group distribution of the aftershocks is obvious (Figs. 2a and 2b). The western group contains the main shock epicenter and the eastern group covers the same region as the foreshocks (Zone A) defined by Hsu *et al.* (1983). The two-group pattern was found for the period of 54 hours immediately following the main shock (Novelo-Casanova *et al.*, 1984) and was checked by S–P time distribution (Novelo-Casanova, 1983). We further found the pattern to hold for the entire four weeks after the main shock except for the first 9 hours when aftershocks occurred mostly in the western group (Fig. 3).

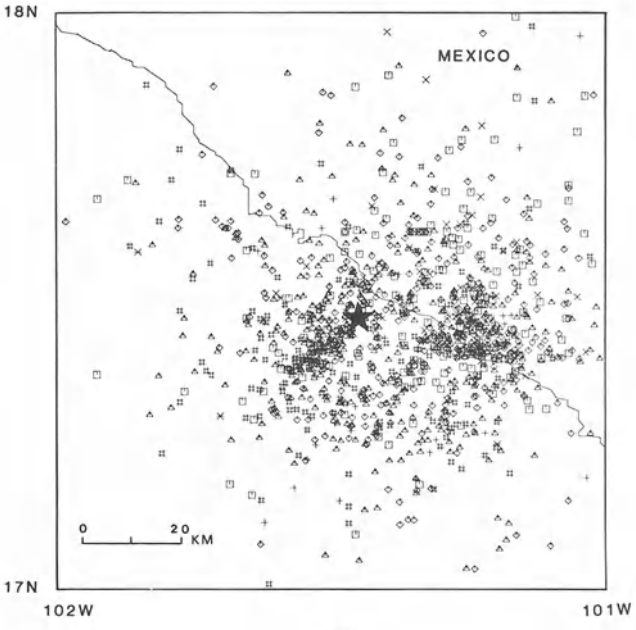

(a)

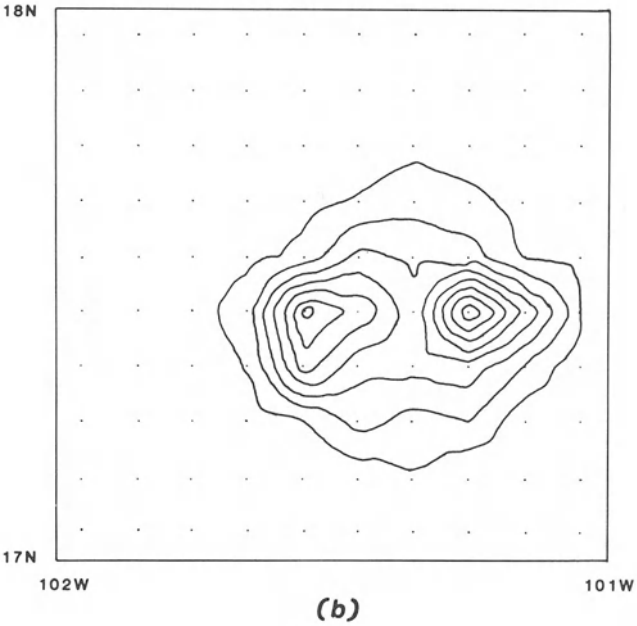

(b)

Figure 2

(a) Epicenter locations of 910 earthquakes occurring within the one-degree square that contains the Petatlan earthquake source region. The main shock is denoted by the filled star. (b) Contour lines of numbers of events within each 0.1 degree square for earthquakes in (a). Contours start at 5 with a contour interval of 5. Peak values are 38 and 43 for western and eastern clusters, respectively.

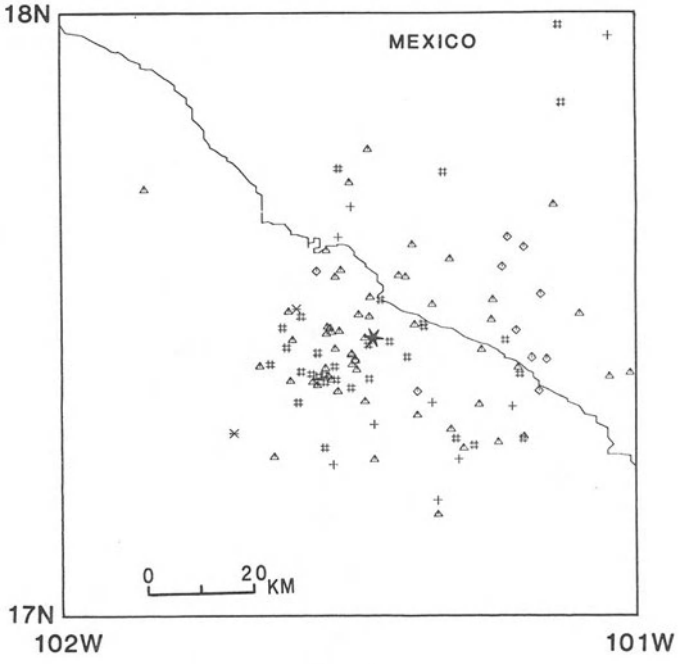

Figure 3
Epicenter locations of 140 events that occurred in the first nine hours after the Petatlan earthquake.

The epicenters shown in Figs. 1 and 2 are located only by HIG stations which spread over a larger area than the Petatlan earthquake source region. Expecting to better constrain the hypocenters, we have included aftershock data from UW stations located very close to the main shock epicenter. Figure 4 thus shows 210 aftershocks located by using combined HIG and UW data. These epicenters change very little from original HIG positions and maintain the two-group distribution. The depth determinations, however, improves significantly as shown in Fig. 5. The improved hypocenters define a plane that dips about 14 degrees to the north-east consistent with the thrust angle obtained from WWSSN long period source mechanism (CHAEL and STEWART, 1982). This angle represents the subduction angle along this segment of the Middle America Trench. The south-western extention of this plane meets the trench axis indicating a constant subduction angle up to 100 km from the trench.

The above result suggests that the more distant HIG stations have poor control of depth and tend to obtain shallower hypocenters by trading the depth for earlier origin time (Lienert, personal communication). Such station distribution was used for locating foreshocks which were found to be shallow and occurred mostly in the continental lithosphere. On the basis of combined HIG–UW network hypocentral depths (Fig. 5) we feel that the foreshocks are likely to occur also at the plate interface.

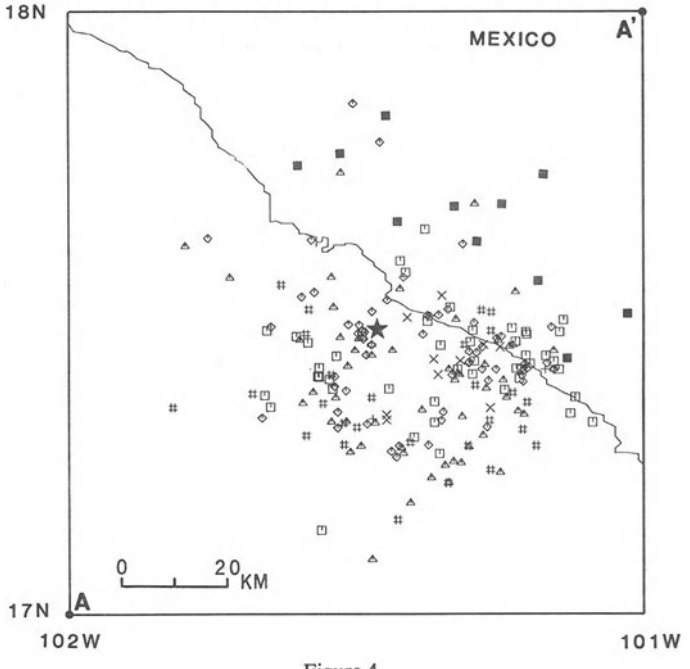

Figure 4

Epicenter locations of 210 aftershocks that were located by joint HIG and UW stations. UW stations are shown as filled squares.

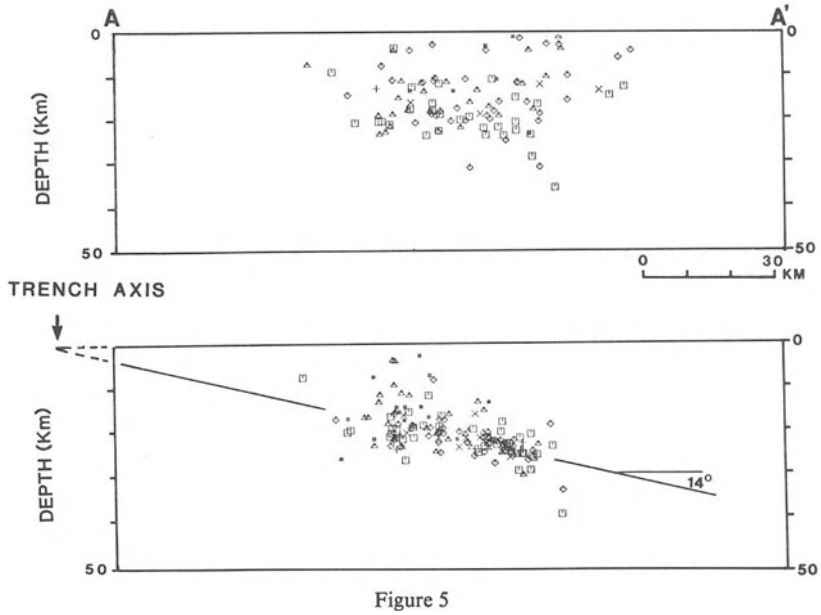

Figure 5

Cross sections (A to A′, Fig. 4) showing hypocenters of events in Fig. 4. Upper plot shows depths by the *HIG stations only* and lower plot shows improved depths by joint HIG and UW stations.

3. Correlation of foreshocks and aftershocks

The first clear correlation between the seismic activities before and after the Petatlan earthquake is of a regional scale. The regions active before the main shock (Zones A, B, C and D) are found to be also active after the main shock (Figs. 1 and 2). Zone A is undoubtedly related to the main shock source. The other three regions, however, are outside the main shock source region. Their activities diminished before the main shock and reactivated afterwards. The relations of these three regions to the Petatlan earthquake are not very clear and we consider that any connections to the Petatlan earthquake would be highly speculative at this time. In this study we concentrate on the 6000 km^2 source region of the Petatlan earthquake.

An even closer correlation in seismic fore- and aftershock activity exists within the

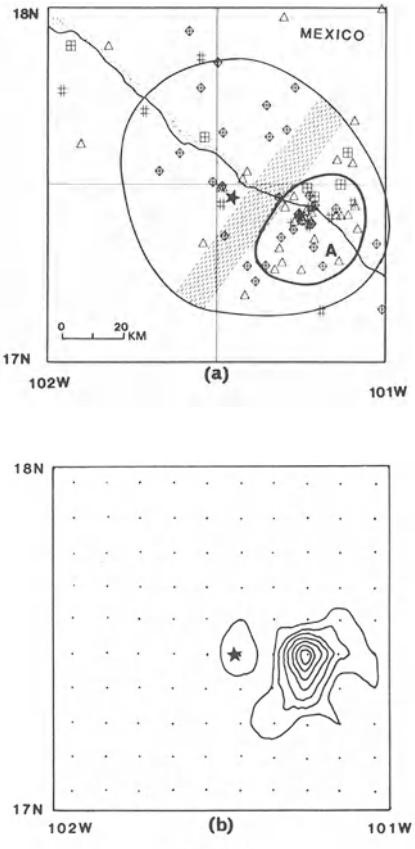

Figure 6

(a) Epicenter locations of local earthquakes occurring in the 14 days before the Petatlan earthquake. The enclosed region of concentrated foreshocks to the east of the main shock is Zone A (Hsu *et al.*, 1983). Shaded region is an aseismic zone separating the foreshock and the main shock. (b) Contour lines for numbers of events within each 0.1 degree square for events shown in (a). Contour interval is 2 and peak values are 4 around the main shock and 16 for Zone A (after Hsu *et al.*, 1983).

source region in terms of number of events and seismic energy release (Figs. 2, 6 and 7). The region of active foreshocks (the 28 February 1979 $Ms = 5.2$ event and its 'aftershocks') continued to be the eastern group of concentrated aftershocks. The western region, which has fewer events (but relatively higher magnitudes) before the main shock, became the western group of concentrated aftershocks. In terms of energy release (Fig. 7) both the east and west regions have characteristic peaks before and after the main shock.

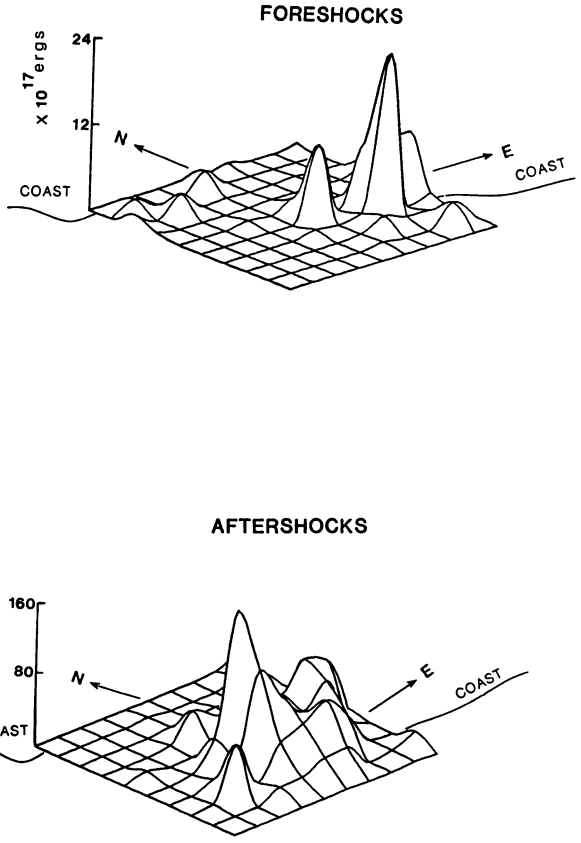

Figure 7

Three-dimensional plots showing spatial distribution of energy release for foreshocks (events in Fig. 6a) and aftershocks (events in Fig. 2). Highest peak values are 24.31 and 163.9 ($\times 10^{17}$ ergs) for foreshocks and aftershocks, respectively. Note that the two-peak configuration correlates well in spatial position. Both figures show views looking toward the continent.

The activities of the eastern and the western regions are not parallel to each other in time. During the first 9 hours after the main shock the western region has much higher activity than the eastern region (Fig. 3). This is also demonstrated by the cumulative difference in energy release between the two areas (Fig. 8). Figure 9 shows the daily numbers of earthquakes from the time of the largest foreshock (28 February 1979) to

30 days after the main shock separately for each region. Clearly, the main shock induced a high number of aftershocks in the western region, while the eastern region had more of a constant activity with a fluctuation caused by the main shock. The difference in the level of aftershock activities induced by the main shock in the eastern and western clusters and the fact that the main shock occurred at the western region indicate that the main shock ruptured the western region but had less effect in releasing stress in the eastern region. Figure 9 remains valid if we also consider some aftershocks not located due to saturation of recording tapes in the first few hours after the main shock, because the saturation affected both regions equally.

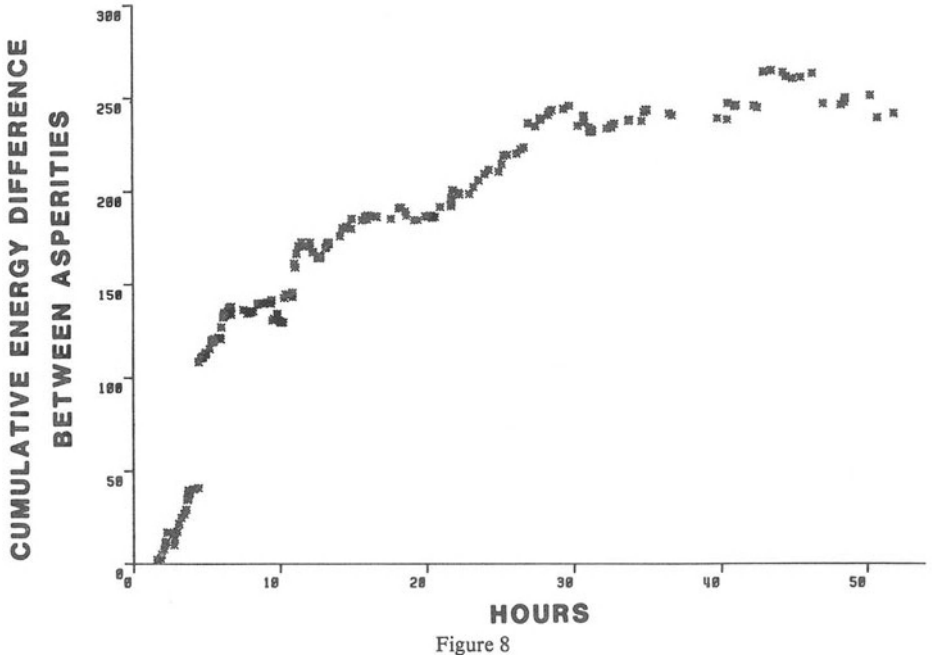

Figure 8

Cumulative difference of energy release (west–east) between the two clusters of aftershocks. The curve is shown until 54 hours after the main shock. Note the dominance of energy release for the western group in the first 9 hours.

A discrepancy seems to exist in correlating depths of foreshocks to depths of aftershocks in the eastern cluster. The foreshocks were reported to be shallower and spread throughout the continental lithosphere (Hsu *et al.*, 1983), while aftershocks are confined along the Benioff Zone (Fig. 5). We showed in the previous section that combined HIG–UW aftershock data relocate shallow and scattered aftershocks to the Benioff Zone. Since foreshocks were recorded by HIG stations only, their shallower depths are likely an artifact of distant HIG stations. As a further qualitative check, the S–P time distributions for events of Zone A before and after the main shock were found similar at all stations. Therefore, we conclude that the foreshocks should also occur on the plate interface and that the correlation is valid.

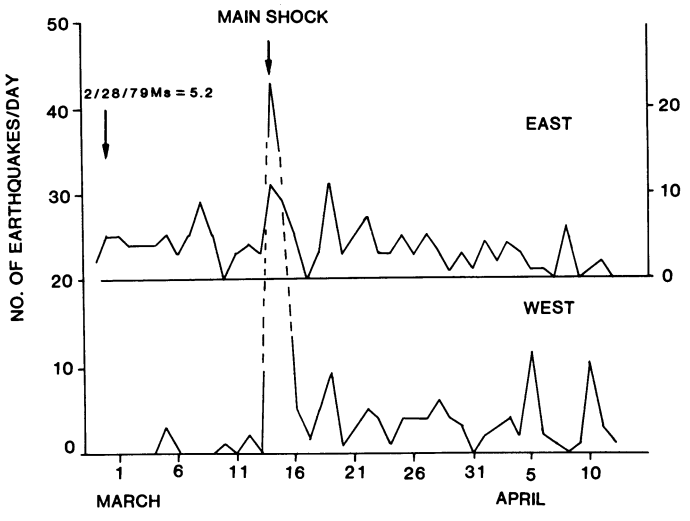

Figure 9

Seismicity level (shown by number of earthquakes per day) for the eastern and the western regions from the largest foreshock to four weeks after the main shock. Note that the main shock induced a large number of aftershocks in the western region but showed a lesser degree of effect on the eastern region.

Within the source region of the Petatlan earthquake (area P, Fig. 10), our results show an interesting correlation between the foreshocks and the aftershocks. Based upon the assumption that aftershocks define the ruptured area, the observation suggests that two regions of higher friction are associated with the rupture plane and that these regions showed premonitory activities before the main rupture. Such an observation, however, is not unique. The Playa Azul, Michoacan earthquake (Ms = 7.3) of 25 October 1981, which occurred in the neighboring seismic gap (area PA of Fig. 10), showed a strikingly similar pattern of foreshock and aftershock sequences (HAVSKOV *et al.*, 1983). For that event, aftershocks also cluster in two groups within the source region and the two-group distribution was verified by two peaks in the S–P time distribution of arrivals recorded at the local station ZIH. Foreshocks of this event could not be located, but S–P time analysis from ZIH indicated their possible presence in the same region as the western group of aftershocks (see Fig. 3 of HAVSKOV *et al.*, 1983).

Several recent major earthquakes along the Middle America Trench have been monitored for detailed aftershock activity. These include the 1973 Colima earthquake (REYES *et al.*, 1979), the 1978 Oaxaca earthquake (SINGH *et al.*, 1980), the 1979 Petatlan earthquake (VALDES *et al.*, 1982; NOVELO-CASANOVA, 1984), and the 1981 Playa-Azul earthquake (HAVSKOV *et al.*, 1983). Only the last two earthquakes show two-group aftershock distribution. As noted previously (HSU *et al.*, 1983), the Orozco Fracture Zone subducts along the portion of the Middle America Trench containing these two events' source regions (Fig. 10). Influence of the topography of subducted ocean floor in both main shock characteristics and seismicity patterns has been noted (VOGT, 1973; KELLEHER and MCCANN, 1976). As the Orozco Fracture Zone is a

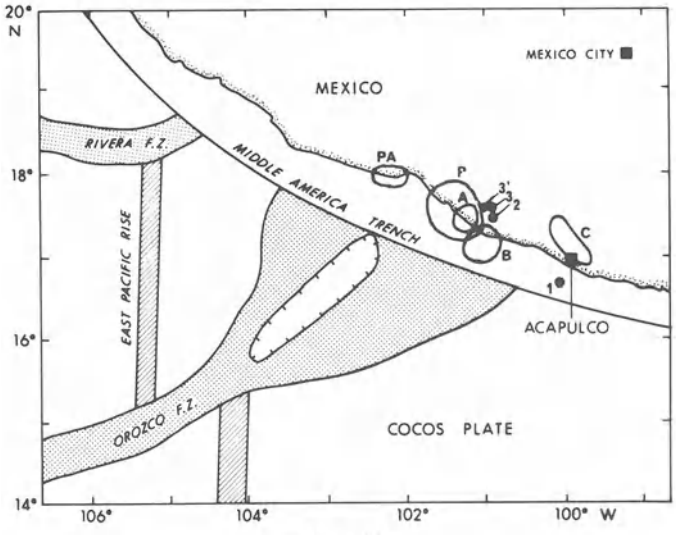

Figure 10

Simplified map showing tectonic features near the Petatlan earthquake epicentral region and some detected areas of earthquake activity. Source regions of the Petatlan earthquake and the Playa Azul earthquake are shown as region P and PA. Regions A, B, and C are areas of activity detected during the six weeks before and four weeks after the Petatlan earthquake. Solid dots 1, 2, and 3 denote PDE locations of the 11 December 1978 ($Ms = 5.0$), 26 January 1979 ($Ms = 6.6$) and the 28 February 1979 ($Ms = 5.2$) moderate events. Solid dot 3′ is the alternate epicenter of Event 3 located by P arrival times at three HIG stations. (After Hsu *et al.*, 1983.)

broad, rugged-surfaced feature, its subduction is likely to cause complex interaction between plates during major stress-releasing events. The regions of concentrated aftershocks are probably surface projections of high-friction spots along the Benioff Zone, which before being subducted were bathymetric highs (such as seamounts). These high-friction regions are interpreted as asperities as described in the following section.

4. The two-asperity model

We propose a simple two-asperity model to account for the observed foreshock and aftershock activities of the Petatlan earthquake. Two regions of higher friction exist within the slip plane of the Petatlan earthquake along the Benioff Zone (Fig. 11), probably as the result of subduction of seamounts. These two areas are of higher strength than surrounding areas and, therefore, represent asperities. The eastern asperity corresponds to Zone A and the western asperity corresponds to the region of the western cluster of aftershocks. Both asperities are also areas of stress concentration before the Petatlan earthquake because they are the major coupling spots between plates. The two asperities are not necessarily equal in strength. In this case, the eastern asperity is relatively weaker.

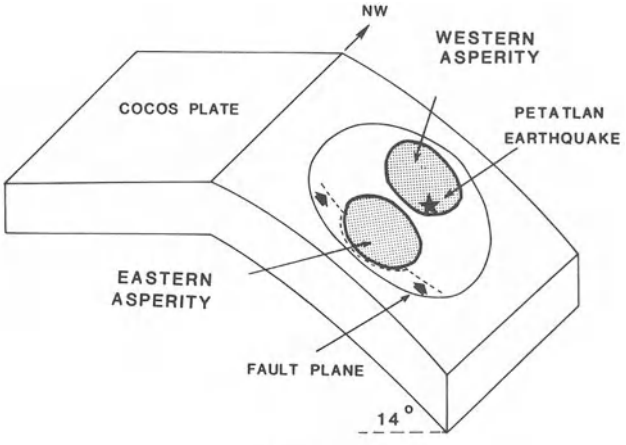

Figure 11

A schematic of the two-asperity model for the subduction of the Cocos Plate containing the Petatlan earthquake source region. The dashed line denotes a slipping front migrating from the south-east toward the north-west and is shown at the instant of meeting the eastern asperity to cause foreshocks.

When the Petatlan earthquake became imminent after a period of accumulation of tectonic stress, the weaker eastern asperity first broke and released seismic energy causing earthquakes in Zone A. The eastern asperity, however, was not completely ruptured because the western asperity could still withstand the tectonic stress load. Eventually, the main shock was initialized at the western asperity when its critical strength was reached. The main shock released stress in the entire source region and induced aftershocks concentrated at both asperities where the plates were strongly coupled.

Following this model, the releasing of stress in the entire source region of the Petatlan earthquake really began with the largest foreshock ($Ms = 5.2$) which partially ruptured the eastern asperity. The stress at eastern asperity was released in two episodes, first by the largest foreshock and then by the main shock. It is hard to estimate exactly how much stress is released by the foreshock and how much by the main shock. However, a major portion should be released by the foreshock because the main shock did not induce a high number of aftershocks at the eastern asperity (Fig. 9).

The stronger western asperity was ruptured during the main shock. Several foreshocks did occur here. One of them with magnitude 3.9 occurred 28 minutes before the main shock at nearly the same spot (MEYER *et al.*, 1980; HSU *et al.*, 1983). These events are likely small ruptures related to minor heterogeneities within the western asperity.

5. Review of precursors

HSU *et al.* (1983) reported in detail the local seismicity during the six weeks before the main shock. It would be worthwhile to re-examine some of the features observed during that period in light of the proposed two-asperity model.

The most distinctive feature is the foreshock activity within Zone A following a moderate event of $Ms = 5.2$ on 28 February (dot 3, Fig. 10). With the two-asperity model, we explain this as a slip at the eastern asperity initializing the stress release of the entire source region. Some characteristics of this group of foreshocks are: (1) the level of seismic activity did not decay like a normal aftershock sequence, (2) they are separated from the main shock by an aseismic zone of about 10 km wide (Fig. 6a) and (3) they migrated toward the main shock during the 14 days before the main shock. In terms of the two-asperity model, the rather constant level of activity probably is a result of the partial release of stress rather than a complete rupture at the eastern asperity. The aseismic zone, previously interpreted as a probable locked fault or region of high strength, is now better explained as a weak, uncoupled region between the two asperities. The foreshocks migrated westward toward the main shock with a velocity of about 1.1 km/day and the main shock occurred near the eastern edge of the western asperity (Fig. 2) at the time when the migrating foreshocks met the aseismic zone (see fig. 10 of HSU *et al.*, 1983). To explain this, we adopt the concept of a migrating slip (or stress) front across asperities (DMOWSKA and LI, 1982), in which a slip front migrates along plate boundaries and can be blocked or slowed by an asperity, causing precursory activities. We assume that a slip front has migrated from the south-east to the north-west across the Petatlan earthquake source region. It first met the eastern asperity to cause the foreshocks (Fig. 11) and when it passed over the eastern asperity it jumped over the weakly coupled zone and initialized the main shock at the eastern edge of the western asperity. The migration of slip front within the eastern asperity causes foreshocks to move toward the main shock.

6. Discussion

We have employed the concepts of asperity and migrating slip front to interpret the observed foreshock–aftershock correlation for the Petatlan earthquake. The designation of the two asperities is based on their concentrated seismic activities both before and after the main shock. The same method was used by VALDES *et al.* (1982) to infer asperity location and size, but they argued that only one asperity existed within the Petatlan earthquake source region characterized by more concentrated aftershocks. This region is equivalent to our two asperities added together. We feel the region is more complicated based on analysis of a more complete list of aftershocks covering the time period immediately following the main shock. We also demonstrated that the two-group aftershock pattern remains true for selected high-resolution events located by joint HIG and UW data. Most important of all, we also base our conclusion on the foreshock distribution.

KANAMORI (1981) and DMOWSKA and LI (1982) used asperity models to explain

the precursory doughnut-shaped seismicity pattern (MOGI, 1969). The model of DMOWSKA and LI (1982) is of great interest in relation to this case study. In their model, a slip front progresses from the bottom of the lithosphere upward. When the front crosses an asperity, the edge of the asperity shows earthquake activity while the center of the asperity remains aseismic (forming a doughnut pattern). If the asperity is elongated in one direction foreshocks will occur at the two ends of the asperity and the disclosed precursory pattern will look very much like foreshock pattern for the Petatlan earthquake (compare fig. 2 of DMOWSKA and LI, 1982 with Fig. 6). HAVSKOV *et al.* (1983) argued that the two groups of aftershocks of the Playa Azul earthquake may occur at the edges of one rupture area or representing two asperities. Our main reason for rejecting the one-asperity possibility is that the two-group pattern persisted until after the main shock. If the single asperity model were used and the asperity were ruptured completely, one concentrated group of aftershocks would be expected. Our simple two-asperity model, however, accounts for both the foreshock and the aftershock spatial occurrence.

The second assumption we have made is a stress migration from the south-east to the north-west across the Petatlan earthquake source region. The concept has been used by many investigators (TURCOTTE and SPENCE, 1974; SAVAGE, 1975; STUART, 1979, PRESCOTT and NUR, 1981; LI and RICE, 1980; NUR, 1981) to model the earthquake rupture process at plate boundaries. They showed that the rupture process starts at the bottom of the lithosphere and that the slip front propagates upward along the plate contact zone perpendicular to the trench. In our application, the slip front moves parallel to the trench. It is not implied that the major stress is acting parallel to the Middle America Trench. In fact, the tectonic stress is perpendicular to the Middle America Trench as evidenced by the thrust mechanisms of the Petatlan earthquake (CHAEL and STEWART, 1982) and the Playa Azul earthquake (HAVSKOV *et al.*, 1983). We infer that the migrating slip front is probably caused by a small component of the tectonic stress not balanced because of the heterogeneity introduced by the Orozco Fracture Zone.

The observed Petatlan earthquake foreshock activity may serve to characterize some of the properties associated with asperities. As HABERMANN (1983) pointed out, it has been unclear whether an asperity would cause quiescence due to high strength or cause seismic activity due to high stress before the main shock. Previous studies suggested quiescence within the asperity due to high strength, while foreshocks occur around it (KANAMORI, 1981; DMOWSKA and LI, 1982) at the weaker edge. In our case study, we have observed foreshock activity associated with the asperities before the main shock. Quiescence, however, was also noticed for the same area (Zone A) before the foreshock sequence while an adjacent region (Zone B) was active (HSU *et al.*, 1983). We have not, however, been able to observe a doughnut-shaped pattern, perhaps because the size of the asperities is small and/or because the HIG network did not have enough resolution to outline it. The answer to the question of quiescence or activity is probably 'yes' for both cases depending on the stages of the stress environment.

Acknowledgments

The authors wish to thank R. P. Meyer and C. Valdes for providing UW aftershock data and E. Herrero for assistance in data processing. We also thank G. Purcaru, R. Pujalet and the two anonymous reviewers for reviewing the manuscript and providing helpful comments. This work is supported by the National Science Foundation grant EAR82-13029. Hawaii Institute of Geophysics Contribution 1523.

References

BAKUN, W. H., STEWART, R. M., BUFE, C. G., and MARKS, S. M. (1980), *Implication of Seismicity for Failure of a Section of the San Andreas Fault*, Bull. seism. Soc. Am. *70*, 185–201.

BYERLEE, J. D. (1970), *Static and Kinetic Friction of Granite Under High Stress*, Int. J. Rock Mech. Min. Sci. *7*, 577–582.

CHAEL, E. P., and STEWART, G. S. (1982), *Recent Large Earthquakes Along the Middle American Trench and Their Implications for the Subduction Process*, J. geophys. Res. **87**, 329–338.

DMOWSKA, R., and LI, V. C. (1982). *A Mechanical Model of Precursory Source Processes for Some Large Earthquakes*, Geophys. Res. Lett. *9*, 393–396.

EBEL, J. E. (1980), *Source Processes of the 1965 New Hebrides Islands Earthquakes Inferred from Teleseismic Waveforms*, Geophys. J.R. astr. Soc. *63*, 381–404.

EWING, J. I., and MEYER, R. P. (1982), *Rivera Oceanic Seismic Experiment (ROSE) Overview*, J. geophys. Res. *87*, 8345–8357.

GETTRUST, J. F., HSU, V., HELSLEY, C. E., HERRERO, E., and JORDAN, T. (1981), *Patterns of Seismicity Preceding the Petatlan Earthquake of 14 March 1979*, Bull. seism. Soc. Am. *71*, 761–770.

HABERMANN, R. E. (1984), *Spatial Seismicity Variations and Asperities in the New Hebrides Seismic Zone*, J. geophys. Res. *89*, 5891–5903.

HAVSKOV, J., SINGH, S. K., NAVA, E., DOMINGUEZ, T., and RODRIGUEZ, M. (1983), *Playa Azul, Michoacan, Mexico, Earthquake of 25 October 1981 (Ms = 7.3)*, Bull. Seism. Soc. Am. *73*, 449–457.

HSU, V., GETTRUST, J. F., HELSLEY, C. E., and BERG, E. (1983), *Local Seismicity Preceding the March 14, 1979, Petatlan, Mexico Earthquake (Ms = 7.6)*, J. geophys. Res. *88*, 4247–4262.

JONES, L., and MOLNAR, P. (1979), *Some Characteristics of Foreshocks and Their Possible Relationship to Earthquake Prediction and Premonitory Slip of Faults*, J. geophys. Res. *84*, 3596–3608.

KANAMORI, H., *The Nature of Seismicity Patterns Before Large Earthquakes*, in *Earthquake Prediction* (ed. D. W. Simpson and P. G. Richards) (Washington 1981), pp. 1–19.

KANAMORI, H., and STEWART, G. S. (1978), *Seismological Aspects of the Guatemala Earthquake of February 21, 1976*, J. geophys. Res. *83*, 3427–3434.

KELLEHER J., and MCCANN, W. (1976), *Buoyant Zones, Great Earthquakes and Unstable Boundaries of Subduction*, J. geophys. Res. *81*, 4885–4896.

LAY, T., and KANAMORI, H. (1980), *Earthquake Doublets in the Solomon Islands*, Phys. Earth Planet. Inter. *21*, 283–304.

LAY, T., KANAMORI, H., and RUFF, L. (1982), *The Asperity Model and the Nature of Large Subduction Zone Earthquakes*, Earthquake Prediction Research *1*, 1–71.

LI, V. C., and RICE, J. R. (1980), *Time-dependent Tectonic Scale Earthquake Instability Model for a Strike-slip Boundary*, EOS, *61*, 1050. (full manuscript in preparation).

MCCANN, W. R., NISHENKO, S. P., SYKES, L. R., and KRAUS, J. (1979), *Seismic Gaps and Plate Tectonics: Seismic Potential for Major Boundaries*, Pure appl. Geophys. *117*, 1087–1147.

MEYER, R. D., PENNINGTON, W. D., POWELL, L. A., UNGER, W. L., GUZMAN, M., HAVSKOV, J., SINGH, S. K., VALDES, C., and YAMAMOTO, J. (1980), *A First Report on the Petatlan Guerrero, Mexico Earthquake of March 14, 1979*, Geophys. Res. Lett. *7*, 97–100.

MOGI, K. (1969), *Some Features of Recent Seismic Activity In and Near Japan. (2) Activity Before and After Great Earthquakes*, Bull. Earthq. Res. Inst. Tokyo Univ. *47*, 395–417.

MOLNAR, P., and SYKES, L. (1969), *Tectonics of the Caribbean and Middle America Regions from Focal Mechanisms and Seismicity*, Bull. geol. Soc. Am. *80*, 1639–1684.

NOVELO-CASANOVA, D. (1983), *First 54 Hours of Aftershocks of the 1979 Petatlan, Mexico, Earthquake*, Master Thesis, University of Hawaii.

NOVELO-CASANOVA, D. A., HSU, V., BERG, E., HELSLEY, C. E., and GETTRUST, J. F. (1984), *Aftershock Activity of the Petatlan Earthquake: The First 54 Hours*, Bull. seism. Soc. Am. *74*, 2451–2461.

NUR, A., *Rupture Mechanics of Plate Boundaries*, in *Earthquake Prediction* (ed. D. W. Simpson and P. G. Richards) (Washington 1981), pp. 629–634.

PRESCOTT, W. H., and NUR, A. (1981), *The Accommodation of Relative Motion at Depth on The San Andreas Fault System in California*, J. geophys. Res. *86*, B2, 999–1004.

REYES A., BRUNE, N., and LOMNITZ, C. (1979), *Source Mechanism and Aftershock Study of the Colima, Mexico Earthquake of January 30, 1973*, Bull. seism. Soc. Am. *69*, 1819–1840.

SAVAGE, J. C. (1975), *Comment on an Analysis of Strain Accumulation on a Strike Slip Fault*, J. Geophys. Res., *80*, 4111–4114.

SCHOLZ, C. H., and ENGELDER, J. T. (1976), *The Role of Asperity Indention and Ploughing in Rock Friction. I. Asperity Creep and Stick Slip*, Int. J. Rock Mech. Min. Sci. *13*, 149–154.

SINGH, S. K., HAVSKOV, J., MCNALLY, K., PONCE, L., HEARN, T., and VASSILIOU, M. (1980), *The Oaxaca Mexico, Earthquake of 29 November 1978: A Preliminary Report on Aftershocks*, Science *207*, 1211–1213.

STUART, W. D. (1979), *Strain-softening Instability Model for the San Fernando Earthquake*, Science *203*, 907–910.

TURCOTTE, D. L., and SPENCE, D. A. (1974), *An Analysis of Strain Accumulation on a Strike-slip Fault*. J. geophys. Res. *79*, 4407–4412.

VALDES, C., MEYER, R. P., ZUNIGA, R., HAVSKOV, J., and SINGH, S. K. (1982), *Analysis of the Petatlan Aftershocks: Numbers, Energy, Release, and Asperities*, J. geophys. Res. *87*, 8519–8527.

VALDES, C., MEYER R. P., and MAHDYIAR, M. (1983), *The Pattern of Earthquakes in Seismic Gaps Adjacent to the Petatlan Earthquake Zone*, EOS *64*, 264.

VOGT, P. R. (1973), *Subduction and Aseismic Ridges*, Nature *241*, 189–191.

WESSON, R. L., and ELLSWORTH, W. L. (1973), *Seismicity Preceding Moderate Earthquakes in California*, J. geophys. Res. *78*, 8527–8546.

WYSS, M., and BRUNE, J. (1967), *The Alaska Earthquake of 28 March 1964: A Complex Multiple Rupture*, Bull. seism. Soc. Am. *57*, 1017–1023.

WYSS, M., WILSON, M., ZUNIGA, R., HARVEY, D., and KOYANAGI, R. (1983), *Four Types of Precursors to an $M = 7.2$ Earthquake and Their Relationship to the Multiple Main Rupture* (abstract), presented at IASPEI, XVIII General Assembly, Hamburg, Federal Republic of Germany.

PAGEOPH, Vol. 122 (1984/85) 0033-4553/85/060894-07$1.50 + 0.20/0

Similarity of Two Liyang Earthquakes

By Xu Shaoxie and Liu Yufen[1])

Abstract – Two moderate earthquakes of magnitudes $M_s = 5.5$ and 6.0 occurred in 1974 and 1979, respectively, in the Liyang region, Jiangsu Province, China. The distance between the two epicenters is less than 20 km and their source mechanisms are very similar. In comparing these two earthquakes, we notice that the similarity of coseismic effects is consistent with a scaling law. The isoseismals of the two earthquakes resemble each other in overall shape but the difference of intensity between pairs of coincident isoseismals is one degree. The precursory seismicity patterns of the two events, such as seismic gaps and preshock swarms, are similar, but do not scale to magnitudes of mainshock. The latter phenomenon may reflect the regional tectonic structure, assuming the entire region to be subjected to the same stress.

Key words: Seismicity Patterns, Seismic Gap, Precursor.

Two destructive earthquakes occurred at almost the same place in the Liyang region of Jiangsu Province in 1974 and 1979 with surface wave magnitude 5.5 and 6.0 respectively. The seismicity of Jiangsu Province is normally very low, with few destructive earthquakes recorded in the last several hundred years, so these two Liyang earthquakes were considered unusual. Since these two earthquakes are separated by more than five years, aftershocks of the first Liyang earthquake of magnitude 5.5 should have ceased, and the preparation of the second Liyang earthquake should be independent of the first one. These events provide a good opportunity for studying the similarity of two independent earthquakes that occurred in the vicinity of each other with similar mechanisms (Table 2) but different magnitudes (Table 1) (Institute of Geophysics, 1982) in a low seismicity region.

These two earthquakes caused damage in a wide area. The overall isoseismal patterns of these two earthquakes (Fig. 1) (Xie, 1980; Mapping Group of Regionalization, 1979) are very similar, although the details differ. The isoseismal V for the 1974 earthquake and isoseismal 6 for the 1979 nearly coincide. The maximum intensity I_0 for the 1974 earthquake is VII and that of the 1979 event is 8. Reports indicate that the areas destroyed by the second earthquake were almost the same as those of the first one, but rather more serious for the earthquake in 1979.

[1]) Institute of Geophysics, State Seismological Bureau, Beijing, China.

Table 1

Parameters of the two Liyang earthquakes

Liang earthquake	1	2
Date	22 April 1974	9 July 1979
Time	08 h 22 m 16.97 ± 1.04 s	18 h 57 m 21.58 ± 0.22 s
Epicenter	ϕ_N 31°592N ± 2.6 km	31°408N ± 3.0 km
Location	λ_E 119°135E ± 2.4 km	119°223E ± 3.1 km
Depth	16 ± 7.8 km	12 km 10 ± 6.4 km (I.S.C.)
Magnitude (M_s)	5.5	6.0

Table 2

Mechanisms of the two Liyang earthquakes

	Node plane I		Node plane II		P axis		T axis	
Earthquake	1	2	1	2	1	2	1	2
Orientation	30°	20°	101°	109°	60°	64°	164°	154°
Dip direction	SEE	SEE	NNE	NNE				
Dip angle	58°	75°	75°	80°	36°	18°	35°	5°

Note: 1: Earthquake with M 5.5 in 1974; 2: Earthquake with M 6.0 in 1979.

An empirical relation between maximum intensity I_0 and magnitude M is often expressed as

$$M = a + bI_0, \tag{1}$$

where a and b are coefficients.

For two earthquakes,

$$\frac{I_0'}{I_0} = \frac{M' - a}{M - a}, \tag{2}$$

where primed and unprimed quantities refer to two different events. If the difference between maximum intensity of two earthquakes is one

i.e. $$I_0' - I_0 = 1,$$

then $$M' - M = b. \tag{3}$$

According to values of a and b given by GUTENBERG and RICHTER (1942)

$$M = a + bI_0 = 1 + \tfrac{2}{3}I_0,$$

LI (1960)

$$M = 1.5 + 0.58I_0,$$

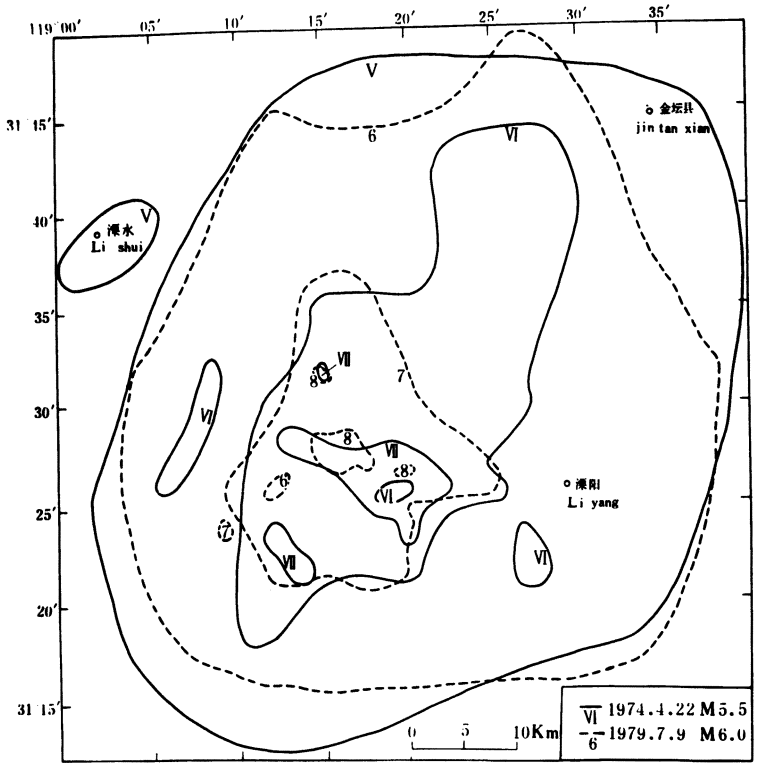

Figure 1
Isoseismals of the two Liyang earthquakes.

TOPPOZADA (1975)

$$M = 1.85 + 0.49I_0,$$

LU (1978)

$$M = 1.45 + 0.60I_0,$$

we can obtain right side values of relation (2) and relation (3). The ratio of maximum intensity of two Liyang earthquakes should be 1.11 (GUTENBERG and RICHTER), 1.13 (LI), 1.14 (TOPPOZADA), 1.12 (LU) respectively, and the observed value of the Liyang earthquakes is $\frac{8}{7}(\approx 1.14)$. The difference between the magnitudes of two earthquakes should be 0.67, 0.58, 0.49, and 0.60 respectively, and the observed value of the Liyang earthquakes is 0.5, thus the magnitudes and intensities of both Liyang earthquakes are consistent with conventional magnitude–intensity relations.

Before the two Liyang earthquakes, precursory seismicity patterns seem to exist around the epicentral area. Gaps (doughnuts) can be recognized around the epicenters of the Liyang earthquakes starting 22 months before and ending 7 months before the earthquakes. The gaps are similar. In Fig. 2, solid circles represent earthquakes before

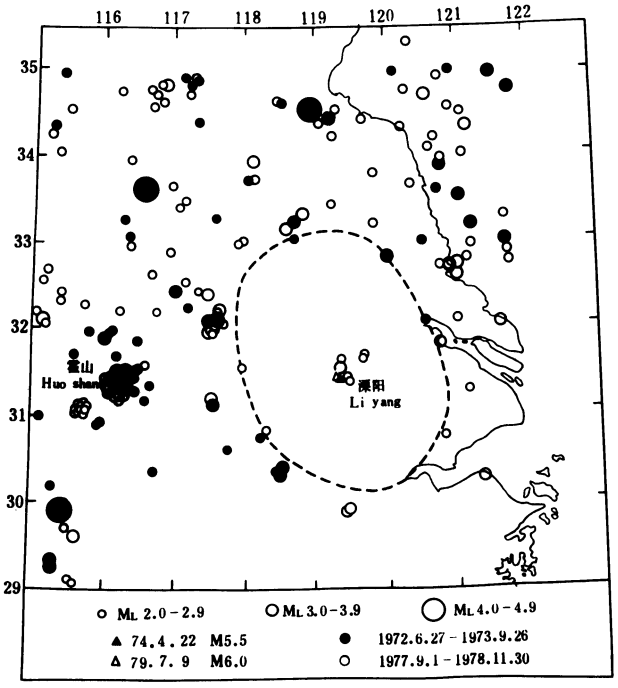

Figure 2
The seismic gaps of two Liyang earthquakes.

the First Liyang earthquake and open circles represent earthquakes before the Second Liyang earthquake. From this figure we can see that epicenters around both Liyang earthquakes are rather scarce, as shown by the dashed line. Figure 3 shows the background seismicity of the region for the 30 month period ending just before the formation of the gaps. Since gaps could not be found in this figure, the gaps shown in Fig. 2 seem to have precursory significance.

Shortly before the two Liyang earthquakes, seismic activity in the Liyang region was concentrated in the north-west part (Fig. 4). Detailed analysis of the seismicity of this region shows that only two moderate earthquakes ($M_L \geqslant 4.5$) have occurred in the ten years since the network was established. One was the Suxian earthquake with magnitude $M_L = 4.5$ on 22 September 1973, and the other was the Guzhen earthquake with magnitude $M_L = 5.4$ on 2 March 1979. Locations of the Suxian earthquake (7 months before the first Liyang earthquake) and the Guzhen earthquake (4 months before the second Liyang earthquakes) are shown in Fig. 4. The parameters of these two earthquakes are shown in Table 3. Sequences $M(t)$ of earthquakes before the two events in areas surrounding them (Fig. 4) are plotted in Figs. 5c and 5d; only magnitude $M_L \geqslant 3.6$ earthquakes are included. The beginning time of Fig. 5 is taken as the formation time of the gap shown in Fig. 2. From this figure, we can see that the seismicity increased before the occurrence of the Liyang earthquakes; the synchronism between two Liyang earthquakes may not be accidental.

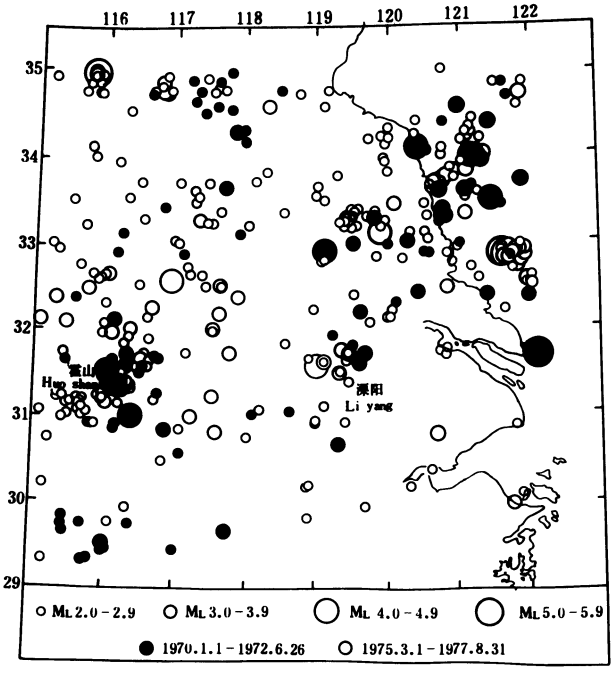

Figure 3
The background seismicity around Liyang earthquake epicenter.

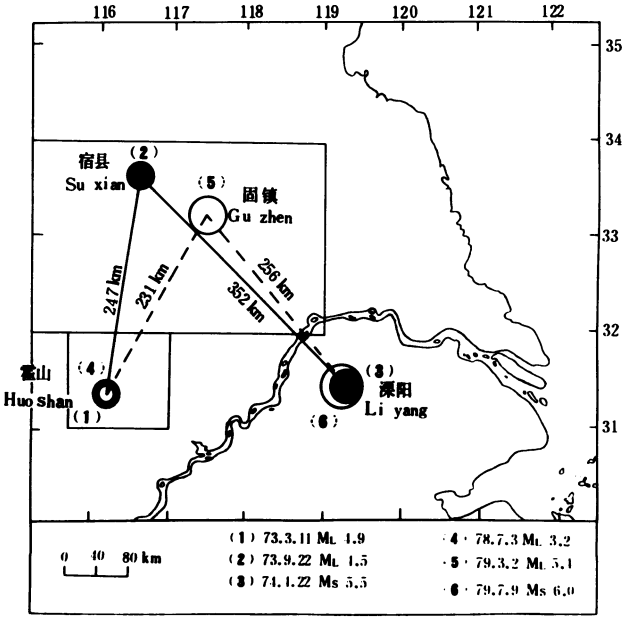

Figure 4
Precursory seismicity before Liyang earthquakes.

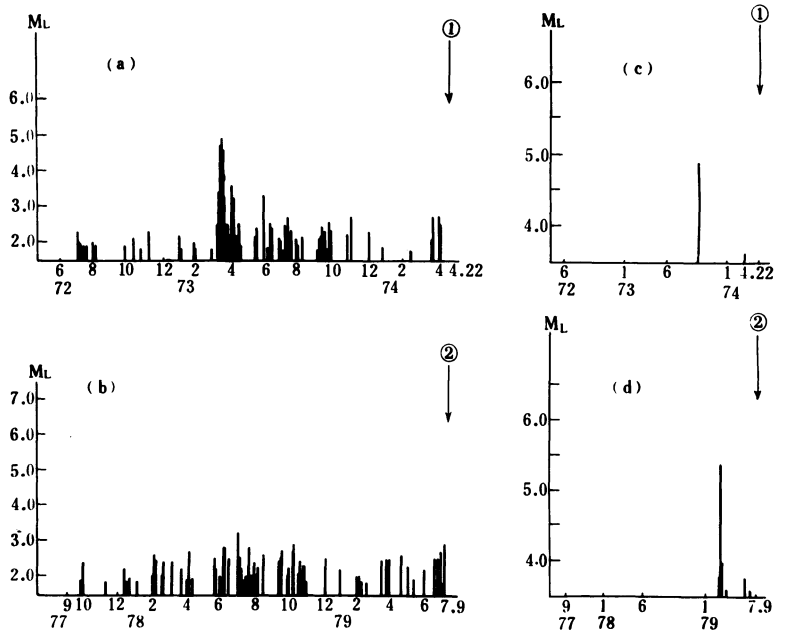

Figure 5

The precursory sequence of seismicity before Liyang earthquakes. (a) June 1972–April 1974 Huoshan swarm ($M_L \geqslant 1.8$). (b) September 1977–July 1979 Huoshan swarm ($M_L \geqslant 1.8$). (c) June 1972–April 1974 earthquakes in Suxian–Guzhen region ($M_L \geqslant 3.6$). (d) September 1977—July 1979 earthquakes in Suxian–Guzhen region ($M_L \geqslant 3.6$). 1 – First Liyang earthquake of M 5.5 on 22 April 1974. 2 – Second Liyang earthquake of M 6.0 on 9 July 1979.

In the Huoshan region west of Liyang swarms have occurred frequently since February 1971. Figures 5a and 5b show $M(t)$ of $M_L \geqslant 1.8$ earthquakes occurring in the small block shown in Fig. 4. Some similarity in $M(t)$ can be found for Figs. 5a and 5b. In both cases the largest earthquakes occurred about one year before respective Liyang earthquakes. The detailed data are given in Table 3.

Table 3

Relation between seismicity around Liyang region and the Liyang earthquakes

Liyang earthquake		1	2
Suxian–Guzhen earthquakes	Magnitude	Suxian $M_L = 4.5$	Guzhen $M_L = 5.4$
	Distance	352 km	256 km
	Time interval	7 month	4 month
Huoshan swarm	Max. magnitude	$M_L = 4.9$	$M_L = 3.2$
	Distance	298 km	292 km
	Time interval	407 day	270 day

XU (1981) showed that precursory seismicity patterns before six strong earthquakes in North China were quite similar. The spatial dimensions of those patterns do not vary, even if the maximum magnitude of the six strong earthquakes ranges from 6 to 7.8. Combining the seismicity pattern of the Liyang earthquakes with those of the six strong earthquakes it is seen that spatial relations of the precursory events with the mainshocks do not seem to vary with the magnitude of the main events. Our conclusion is that coseismic phenomena such as dimensions of isoseismals may vary for different magnitude main shocks, but that the patterns of the precursory seismicity do not. In our opinion, the latter phenomenon may reflect the tectonic structure, but not the characters of the source of main earthquakes, assuming the entire region to be subjected to the same stress.

REFERENCES

GUTENBERG, B., and RICHTER, C. F. (1942), *Earthquake Magnitude, Intensity, Energy and Acceleration*, Bull. seism. Soc. Am. *52*, 162–191.

INSTITUTE OF GEOPHYSICS (1975), *Seismological Bulletin of Chinese Stations 1974*.

INSTITUTE OF GEOPHYSICS (1982), *Bulletin of Seismological Observations of Chinese Stations 1979*.

LI, SHANBANG (1960), *The Catalogue of Chinese Earthquakes*.

LU, RONGJIAN (1978), *Statistical Relation between Isoseismal and Magnitude*, The Reports of Institute of Engineering Mechanics, 78–018.

MAPPING GROUP OF REGIONALIZATION (1979), *Isoseismal Maps of Chinese Earthquakes* (Seismological Publishing House).

TOPPOZADA, T. R. (1975), *Earthquake Magnitude as a Function of Intensity Data in California and Western Nevada*, Bull. seism. Soc. Am. *65*, 1223–1238.

XIE, RUIZHENG (1980), *The Intensity Feature of Liyang Earthquake*, Dispatches of Seismological Work of Jiangsu Province, No. 2, 6–7.

XU, SHAOXIE, and SHEN, PEIWEN (1981), *Seismicity Patterns in China*, Earthquake Prediction, Maurice Ewing Series *4*, 117–125.

ZHOU, BAOZHENG (1980), *Liyang Earthquakes and the Feature of its Sequence*, Dispatches of Seismological Work of Jiangsu Province, No. 2, 29–47.

(Received 12th December 1983; revised 18th July 1984; accepted 29th July 1984)

PAGEOPH, Vol. 122 (1984/85) 0033-4553/85/060901-20$1.50 + 0.20/0

Regional Study of the Anomalous Change in Apparent Resistivity Before the Tangshan Earthquake ($M = 7.8$, 1976) in China

By J. QIAN[1,2])

Abstract – Electrical resistivity measurements have been conducted as a possible means for obtaining precursory earthquake information. Before five great earthquakes ($M > 7$, $h < 25$ km) in China, the apparent resistivity ρ_a showed systematic variations within a region 200 km from the epicenters. In particular, 9 stations in the Tangshan–Tianjin–Beijing region prior to the Tangshan earthquake ($M = 7.8$, $h = 11$ km, 27 July 1976) showed a consistent decrease of apparent resistivity around the epicenter, with a maximum resistivity change of 6% and a period of variation of 2–3 years. Simultaneous water table observations in this region showed a declining water table, and ground surface observations indicated a slight (5 mm) uplift in the epicenter region relative to its surroundings.

In order to develop an explanation for the observed change of apparent resistivity associated with these great earthquakes, we have used Archie's Law to explore the effects of changes in rock porosity, water content and electrolyte resistivity on measured resistivity.

Tentative conclusions of this study are as follows: (1) the apparent resistivity change is opposite to the effect expected from the simultaneous water table trend; (2) the dilatancy needed to give such resistivity variations (assuming Archie's Law holds) is much larger than that needed to explain the observed uplift (by 2–3 orders of magnitude); (3) salinity change in the pore electrolyte is a possible explanation for the variation in resistivity: an increase in the salinity would cause a proportional decrease in resistivity; the data needed to test this hypothesis, however, are lacking; and (4) the effect of changing geometry of rock pores or cracks due to pressure solution may provide an explanation for the decrease in apparent resistivity; it is different in nature from the effect of a volume change in response to stress although the geometry change is also closely related to the stress change.

Key words: earthquake prediction, electrical resistivity.

1. Introduction

The study of the variation of electrical properties of the earth's crust associated with the preparatory process of earthquakes has been one of the attractive subjects in the field of earthquake prediction during the past twenty years. The observations of earth resistivity as a monitoring precursor for this study began in the USSR, Japan and China in the 1960s, and in the United States in the early 1970s. Certain hypotheses for the

[1]) Department of Earth, Atmospheric, and Planetary Sciences, Massachusetts Institute of Technology, Cambridge, MA 02139 USA.

[2]) Permanent address: Lanzhou Earthquake Research Institute, Lanzhou, China.

earthquake preparatory process in the early 1970s (MJACHKIN *et al.*, 1975; SADOVSKY *et al.*, 1972; SCHOLZ *et al.*, 1973) were based in part on such observations before earthquakes.

However, a good understanding of the relation between the variation in electrical resistivity and the earthquake preparatory process must consider the following conditions: (1) a sufficiently long period of observations to establish the temporal aspect of the relation, (2) a set of data taken from an observation net instead of only one point, in order to get at the regional behavior, and (3) an observational net close to the epicenters of studied earthquakes, especially large earthquakes.

A 15% decrease in apparent resistivity occurring over several months in 1969 prior to an earthquake of magnitude 6.0 in Soviet Central Asia (SADOVSKY *et al.*, 1972) was taken as a constraint for the dilatancy-diffusion model (BRACE, 1975). However, only one station was involved (several km from the epicenter), and the observed variation for a period of only several months raised some question as to whether it was a yearly change or a seasonal change. Soviet scientists thought there might be a much larger change of true resistivity at mid-depth in the crust, associated with the earthquake, based on theoretical calculations (BARSUKOV, 1972). In the United States, Mazzella and Morrison reported observations of a resistivity variation exceeding 20% during a period of 60 days prior to an earthquake of magnitude 3.9 which occurred within their array near the San Andreas fault in California in 1973, the year their observations began (MAZZELLA and MORRISON, 1974). Later on, however, the reliability of the data was called into question because no change was observed again prior to another earthquake with the same magnitude and almost the same location, after the recording instruments had been improved (MORRISON *et al.*, 1979). In Japan, coseismic step changes in resistivity were observed by Yamazaki and Rikitake (RIKITAKE and YAMAZAKI, 1969; YAMAZAKI, 1974, 1975) with an electrode separation of a few meters in a mountain cave near the sea. The steps were considered to be an effect of residual strain of earthquakes at the observation point, although most of the earthquakes with magnitude larger than 7 occurred more than 400 miles from the observational point.

A common problem with the observations in these countries is the small number of observation points in both space and time. In China, the observation of apparent resistivity began in 1967 after the occurrence of a strong earthquake in Xintai, in densely populated Hebei Province of North China in March, 1966. The technique then became popular in many seismic belts of the country, and the number of observation stations (called precursory monitoring stations) is now greater than 100. Therefore, when a series of great shallow earthquakes ($M > 7$, $h < 25$ km) occurred in China in the 1970s, at least six of them were located within the nets of stations that had been established several years earlier, so that a long term of records was available on the basis of daily records at related stations. These data provided us with a good opportunity to discuss the relation between the observed variations and the earthquake preparatory process. Some common characteristics of the variation in these great shallow earthquakes were inferred from these data by QIAN *et al.* (1979).

Among these large events, the most important is the Tangshan earthquake ($M = 7.8$, $h = 11$ km, 27 July 1976). Fourteen stations were located within 200 km of the epicenter, a region usually called Beijing–Tianjin–Tangshan (preferably called 'Tangshan–Tianjin–Beijing region' in this study) and most of them had been in operation for over 3 years before its occurrence. In addition to the resistivity observations, some other observations in that region such as water table, levelling, radon content in the water, and seismicity were made during the same period.

This paper deals with a regional study of the apparent resistivity variations before the Tangshan earthquake and tries to develop an explanation for the observed change associated with the great shallow earthquake.

The first section will present the data of apparent resistivity and some relevant data (water table and levelling) observed in the Tangshan–Tianjin–Beijing region. Section 2 deals with the relation between variations of apparent resistivity observed at the surface of a medium and variations of true resistivity within the medium by using a sensitivity analysis. Section 3 discusses the effects of various factors on the true resistivity of the medium when the factors change, assuming Archie's law. Section 4 analyses these various factors, in an effort to select those which might explain the regional variation in apparent resistivity and which are also compatible with the other relevant observations and theory. Section 5 discusses the effect of geometry change as a possible explanation for resistivity decrease. The last section concludes the regional study and makes suggestions for further observation and study.

1.1. The apparent resistivity anomalies associated with the Tangshan earthquake and other relevant observations in Tangshan–Tianjin–Beijing

The Tangshan earthquake occurred in Tangshan, Hebei Province, 150 km away from the capital Beijing (Peking) on 27 July 1976 with a magnitude of 7.8 and focal depth of 11 km. As mentioned above, there were 14 precursory monitoring stations set up within 200 km of the epicenter several years prior to its occurrence. The longest of these records was 8 years; most of them exceeded 3 years. The temporal variations and the spatial distribution of the anomalies associated with these large events are shown in Figs. 1 and 2, respectively.

In Fig. 1, the temporal variation curves taken from 4 typical stations are the monthly averages of apparent resistivity obtained with fixed Wenner arrays with a separation between electrodes of about 1 km. The anomalous amplitude for each curve is represented by the fractional change in apparent resistivity

$$\Delta\rho_a/\rho_a = (\rho'_a - \rho_a)/\rho_a \tag{1}$$

where ρ_a is the normal level several years before the events, and ρ'_a is the level just before the event. Some stations had a kind of periodic behaviour with a period of one year called 'yearly change' or 'seasonal change', which can probably be attributed to the seasonal change of the water table that we will discuss later. For these stations, only

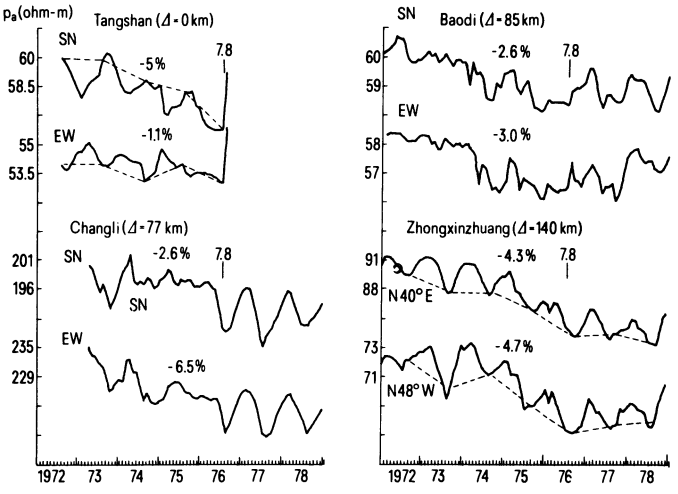

Figure 1

The ρ_a vs. time curves of some stations within the ρ_s anomalous descending region around the epicenter of the Tangshan earthquake. The percentages show anomalous amplitudes and Δ denotes the epicentral distance of individual stations.

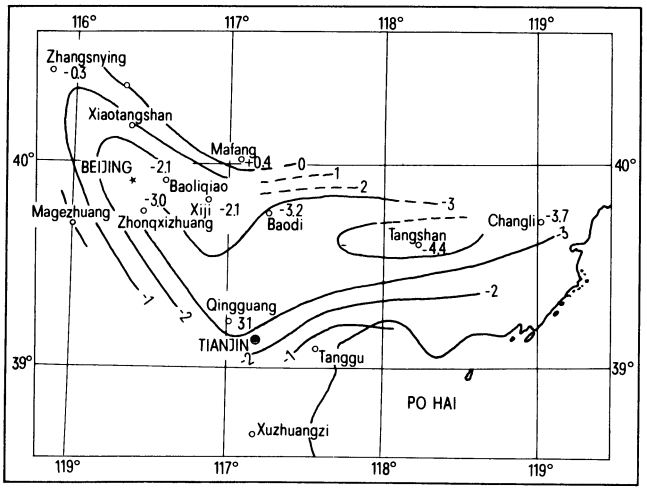

Figure 2

Contour map of anomalous amplitude of ρ_s in the Tangshan–Tianjin–Beijing region. The numerals on the contour lines denote the anomalous resisitivity change (in units of one percent) occurring during the 4–5 year period prior to the Tangshan earthquake; the negative sign indicates a decreasing anomaly.

general trends of the variation lasting for several years, which were superimposed on the yearly change, are taken into account and represented by the dashed lines in Fig. 1. The spatial distribution of the anomalous amplitude calculated from equation (1) is included in Fig. 2, which is a contour map of the anomaly. The minus sign represents the resistivity decrease before the event.

It can be seen from Fig. 1 that declining apparent resistivity was a dominant trend before the earthquake. Figure 2 gives a coherent picture showing that this trend was a consistent phenomenon observed over a certain area about 300 km long E–W and 100 km wide N–S. This is referred to as the ρ_a negatively anomalous region surrounding the epicenter. This trend continued at most stations until the month the earthquake occurred.

A systematic feature in apparent resistivity, seen in Fig. 1, at several stations over that region is a change in the decreasing trend at the approximate time of the earthquake. Furthermore, the apparent resistivity exhibits no sudden recovery immediately after the earthquake.

Other relevant observations which were conducted over the same region, especially for the study on earthquake prediction, such as water table changes and leveling changes, are available and are shown in Fig. 3 (WANG, 1979) and Table 1 (ZHANG *et al.*, 1981), respectively.

In Fig. 3, it is seen that the water table level was also decreasing with time. The static water levels were different from well to well and so were the decreasing amplitudes over several years. Generally the static water levels were in the range 20–100 m, and the average decrease in level before the event was about 10 m.

The leveling data in Table 1 were taken from 9 observation points within about 100 km of the epicenter. The measurements were not regularly repeated year by year at these points. The last column in Table 1 shows the leveling changes during 1972–75, and indicates only a few millimeters uplift in the area close to the epicenter relative to the area at greater distance.

Table 1

*Vertical ground variations in the area close to the epicenter**

	1954–1967 (mm)	1967–1969 (mm)	1969–1972 (mm)	1972–1975 (mm)
No. 01	+7.7	+12.9	−9.6	+3.0
No. 02	+10.2	+10.2	−9.4	+3.8
No. 03	−0.4	+13.4	−20.3	+2.4
No. 04	+11.3	+20.6	−22.7	+8.6
No. 05		+23.0	−20.4	+12.1
No. 06	−3.6	+19.0	−24.1	+3.9
No. 07	−5.2	+11.5	−50.4	+3.7
No. 08		+31.1	−34.3	+6.2
No. 09			−31.5	+3.5
No. 10			−26.1	+7.8
Average	+2.7	+17.7	−24.9	+5.5

* The locations of observation points can be found in Fig. 4.

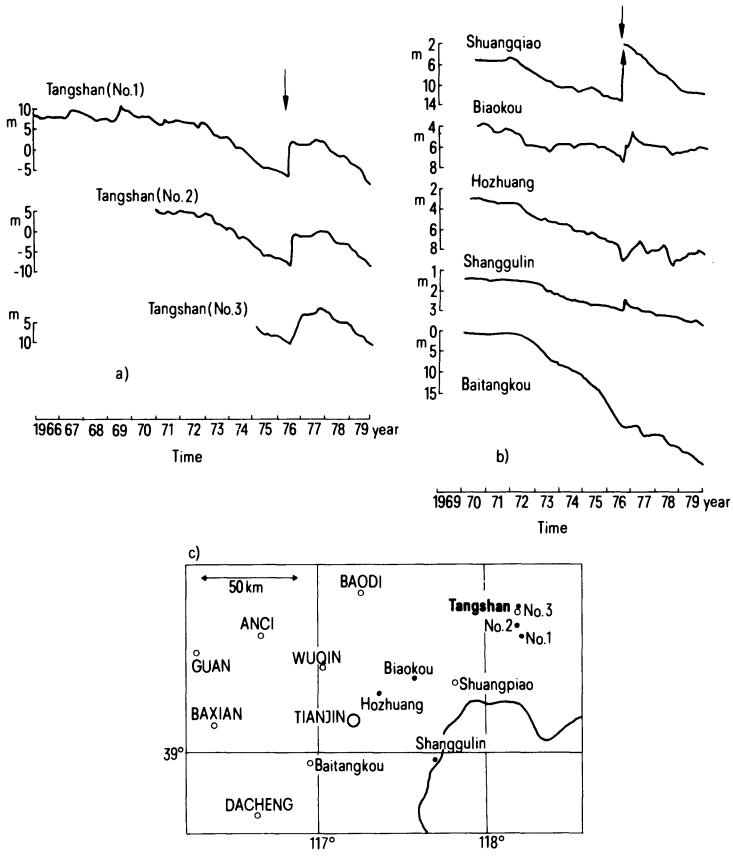

Figure 3

Watertable changes in Tangshan–Tianjin region: (a) data from wells in Tangshan region; (b) data from wells in Tianjin region; (c) the locations of wells in (a) and (b).

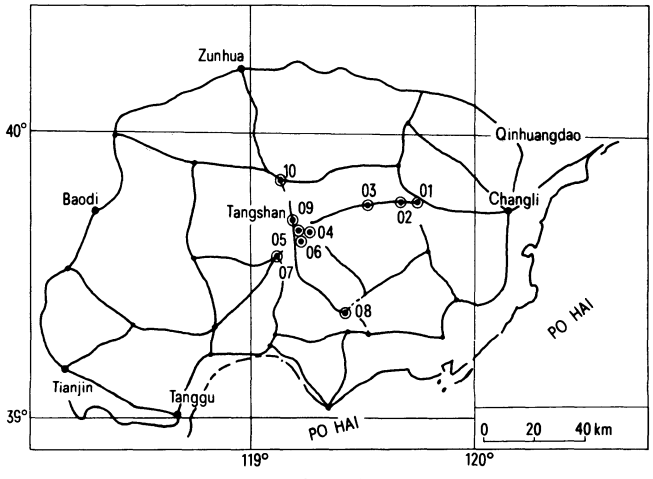

Figure 4

Leveling net in the Tangshan region.

1.2. The sensitivity analysis

From the theory of geoelectricity, changes in apparent resistivity observed by an array at the surface of a medium are associated with changes of true resistivity[3]) within the medium. The determination of the relationship between the observed surface changes and the change within the medium is a very complex procedure, which requires simultaneous measurements with different array separations with respect to the same central point in order to solve the inverse problem. Instead of this procedure, a simpler approach is to set up the relationship between these two variations by calculating the sensitivity of apparent resistivity to changes of true resistivity. For our purposes, a three-layer horizontal model is used.

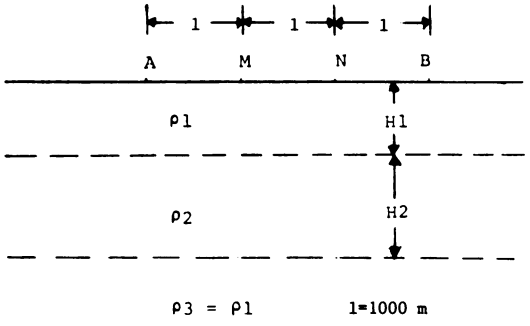

Figure 5
Three-layer model for the sensitivity calculation (A, B, M, N are current electrodes and potential electrodes, respectively).

Assume the medium is a homogeneous half space with resistivity ρ and a surface array with Wenner configuration and separation denoted by l. The apparent resistivity denoted by ρ_a for this case should be equal to ρ. Then assume that a change occurs somewhere inside the medium and the resistivity change is $\Delta\rho$. This part, for convenience, is supposed to be a horizontal layer in the medium with a thickness denoted by H_2 and its upper boundary denoted by H_1 (Fig. 5). Thus, in the end, a three-layer model is considered and the apparent resistivity, denoted by ρ_a', is calculated in terms of theoretical formulas of electrical prospecting.[4])

In this way, a problem dealing with a temporal variation is equivalent to a problem dealing with a spatial variation. In terms of the three-layer model, the sensitivity S of the variation in apparent resistivity $\Delta\rho_a/\rho_a$ to that in the true resistivity $\Delta\rho/\rho$ is defined by the following formula:

$$S = \frac{\Delta\rho_a/\rho_a}{\Delta\rho/\rho_1} \tag{2}$$

---

[3]) Definitions of true and apparent resistivity are given in (DAKHNOV, 1961), p. 85.

[4]) The program FORTRAN-SONDE presented by H. F. Morrison has been used in the calculations.

Where $\rho_a = \rho$, $\Delta\rho_a = \rho'_a - \rho_a$, $\Delta\rho = \rho_2 - \rho_1$. The numerical results for S were calculated as a function of H_1, H_2 and $\Delta\rho/\rho$, and S–H_1 curves are plotted in Fig. 6, which is a log–log diagram. In Fig. 6, the different curves correspond to different values of H_2. In these calculations l, H_1, H_2 are in units of meters and $l = 1000$ m.

The following features can be inferred from Fig. 6:

(a) Each S–H_1 curve has a maximum value of S at the point H_{1m}, i.e., the sensitivity S increases with H_1 when $H_1 < H_{1m}$ and decreases with H_1 when $H_1 > H_{1m}$. The smaller the value for H_2, the steeper the left part of the curve and the larger the H_{1m} value.

(b) The curve moves up when H_2 increases, i.e., the sensitivity increases with H_2.

(c) Regardless of the values for H_1 and H_2, the sensitivity S never exceeds 1. This means that if a certain amount of relative change (or fractional change) in apparent resistivity, $\Delta\rho_a/\rho_a$, is observed at the surface, the relative change in true resistivity, $\Delta\rho/\rho$, inside the medium must be larger than $\Delta\rho_a/\rho_a$ ($S < 1$), or equal to $\Delta\rho_a/\rho_a$ only when $H_1 = 0$ and H_2 goes to infinity ($S = 1$).

(d) For the assumed layered geometry S is always positive, i.e., $\Delta\rho_a/\rho_a$ and $\Delta\rho/\rho_1$ have the same sign. A decrease in ρ_a requires a decrease in ρ, and vice versa.

Applying these features to the Tangshan case in which there was (as shown in Fig. 2) a regional, coherent distribution of ρ_a anomalies, the negative anomalies with amplitude of 3–5% in the main stations require a compatible negative change of true

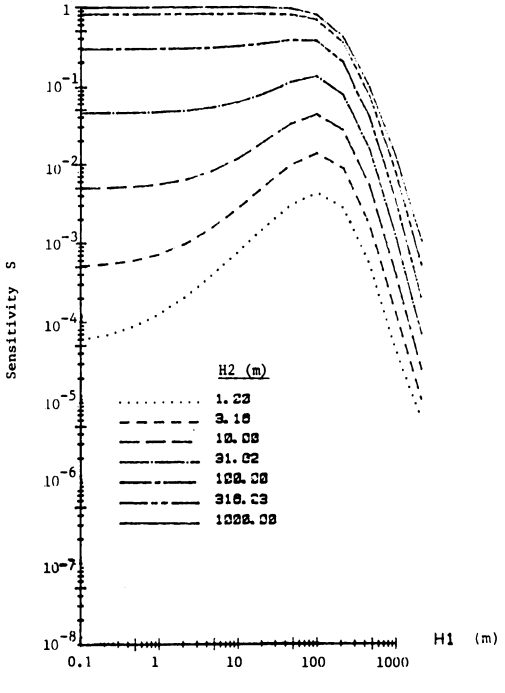

Figure 6
Sensitivities vs. H_1 (different curves denote different thickness H_2 of the changed layer; H_1, H_2 in units of meters, ρ_2, Ωm, S dimensionless).

resistivity with amplitude larger than 3–5% in the investigated volume beneath these stations.

Generally in electrical prospecting the concept 'investigated volume' for an array with a certain separation is represented by a horizontal layer with upper boundary at the surface ($z = 0$) and lower boundary at $z = H_0$ which is called the investigated depth. Usually, for convenience, H_0 simply takes on the value of the half separation between electrodes. In fact, from Fig. 6, the concept 'investigated depth' corresponds to the depth below which S becomes very small. We prefer to take the separation of electrodes as the investigated depth below which $S < 0.001$.

1.3. Archie's law and the variations of true resistivity of rock

Since any change of apparent resistivity observed at the surface must be due to the change of true resistivity within the medium, the next questions should be 'What factors could cause the change in the medium?' and 'What is the contribution of each factor?' Many laboratory experiments have been performed on various rock samples (BRACE *et al.*, 1965; BRACE and ORANGE, 1968a,b; BRACE, 1974; PARKHOMENKO, 1967) which deal with the effects of stress, temperature, mineral content and the salinity of pore water, on resistivity. Most of the experiments, however, were performed on samples of igneous rock rather than the sedimentary rock on which most of the stations in the studied region are situated. Therefore we prefer to answer the questions by using the well-known Archie's law (ARCHIE, 1942), which is especially applicable to the behavior of sedimentary rocks with the porosity in the range of 1–30% (KELLER and FRISCHKNECHT, 1966).

Archie's law is an empirical formula which describes the relationship between the bulk resistivity and the porosity of sedimentary rock in a very simple form:

$$\rho = \rho_0 \, \eta^{-m} \, S_d^{-n} \tag{3}$$

where

ρ is the bulk resistivity of the rock

η is the porosity of the rock

S_d is the degree of saturation of the rock

ρ_0 is the resistivity of electrolyte in pores and cracks

m and n are empirical constants (ARCHIE, 1942; DAKHNOV, 1961) usually $m \approx 1\text{-}2$, $n = 2$.

In equation (3), η is defined by

$$\eta = V_p / V_T \tag{4}$$

where V_T is the total volume of rock, V_p is the pore volume inside the rock, which forms an interconnected system, and S_d is defined by

$$S_d = V_w / V_p \tag{5}$$

where V_w is the volume of electrolyte in the pore volume.

When a rock is saturated, $V_w = V_p$, $S_d = 1$, and equation (3) becomes

$$\rho = \rho_0 \eta^{-m} \tag{6}$$

From equations (3)–(6), it can be seen that if the environmental conditions (such as the rock stress, temperature, or water table depth) change, then variations in the parameters, V_T, V_p, V_w and/or ρ_0, may occur, and as a consequence the resistivity ρ of the rock will change.

In the region studied in this paper the apparent resistivity at the monitoring stations ranges from 10–200 Ωm. Suppose the corresponding true resistivity is in the range of 1–1000 Ωm and take $\rho_0 = 0.1 \sim 50$ Ωm. Then from equation (3) η for the medium would be estimated to be in the range of a few per cent to a few tens of per cent, which is reasonable for sedimentary rocks.

To discuss the variation of true resistivity of rock by applying Archie's law, three classes of basic effects will be considered. They are (1) the effect of a change in total volume of rock, (2) the effect of a change in water-bearing volume of rock pores, and (3) the effect of a change in electrolyte resistivity. These three effects will be referred to as 'volume change effect', 'water content effect', and 'electrolyte resistivity change effect', respectively.

(*1*) *Volume change effect or stress–strain effect.* A general way of discussing each of these effects on the true resistivity is the process of partially differentiating both sides of equations (3) or (4) with respect to one of the parameters. In dealing with the volume change effect, only ΔV_T will be referred to (i.e., $\Delta V_w = 0$. By differentiating equations (3) and (4), it can be shown that for incompletely saturated rocks,

$$\frac{\Delta\rho}{\rho} = -m\frac{\Delta\eta}{\eta} - n\frac{\Delta S}{S} = -\frac{m}{\eta}\frac{\Delta V_T}{V_T} - n\left(\frac{\Delta V_w}{V_w} - \frac{\Delta V_p}{V_p}\right)$$

$$= \frac{n-m}{\eta}\frac{\Delta V_T}{V_T} = F_1\frac{\Delta V_T}{V_T}$$

where F_1 is defined as:

$$F_1 = \frac{n-m}{\eta} = \frac{\Delta\rho/\rho}{\Delta V_T/V_T} \tag{7}$$

For saturated rocks,

$$\frac{\Delta\rho}{\rho} = -m\frac{\Delta\eta}{\eta} = -\frac{m}{\eta}\frac{\Delta V_T}{V_T} = -F_2\frac{\Delta V_T}{V_T}$$

where F_2 is defined as:

$$F_2 = \frac{m}{\eta} = \frac{\Delta\rho/\rho}{\Delta V_T/V_T} \tag{8}$$

F_1 and F_2, ratios of $\Delta\rho/\rho$ over $\Delta V_T/V_T$, are also called magnification coefficients of resistivity over volumetric strain. In deriving equations (7) and (8), $\Delta V_p \approx \Delta V_T$ was assumed, i.e., almost the total volume change would be accomplished by changing the pore volume. From a practical point of view, this assumption is reasonable.

Three features can be inferred from equations (7) and (8):

(a) The volume change effect has different signs for these two cases, respectively. This means that an increase in the rock volume could cause an increase in true resistivity in the partially saturated case, but a decrease in the fully saturated case.

(b) Both F_1 and F_2 are inversely proportional to the porosity η. The smaller the porosity η, the larger F_1 and F_2.

(c) $F_2 \geqslant F_1$ because in general n, $m \geqslant 0$ and $n > m$. Take some examples: suppose $n = 2$, $m = 1.5$ and take the low estimate $\eta = 0.05$, then $F_1 = 10$ and $F_2 = 30$. If we expect the variation of true resistivity $\Delta\rho = -10\%$, a compressive volume strain $\Delta V_T/V_T$ of 10^{-2} would be needed in the unsaturated case or a dilatant strain $\Delta V_T/V_T$ of 3.3×10^{-3} in the saturated case. If η is taken to be 0.1, $\Delta V_T/V_T$ must increase to 10^{-1} and 3.3×10^{-2}, to produce the same $\Delta\rho/\rho$ as that in the previous example.

(*2*) *Water content change effect.* In dealing with the water content change, only ΔV_w will be referred to in differentiating equation (3) and this results in

$$\frac{\Delta\rho}{\rho} = -n\frac{\Delta V_w}{V_w} = -2\frac{\Delta V_w}{V_w} \tag{9}$$

where $\Delta V_w/V_w$ represents the relative change in the water-bearing volume of pore in the rock.

The water content change could be due to climate changes such as rainfall, snow, evaporation, or to cultural activities such as the pumping of water or the irrigation of farm land, any of which could cause occasional water table changes. Usually this kind of effect occurs at shallow depth (0–100 m). For some stations the water table changes show a periodicity of one year, and the true resistivity in the water-bearing part also changes periodically so that the apparent resistivity change has a similar behavior. One typical example of simultaneous observations in both apparent resistivity and water table taken from a station in north-western China, is shown in Fig. 7. Both observations are periodic, and the correlation coefficient between them is 0.93.

(*3*) *Electrolyte resistivity change effect.* Since the resistivity of pore electrolyte ρ_0 is a common factor both in equations (3) and (4), and ρ is directly proportional to ρ_0, we have

$$\frac{\Delta\rho}{\rho} = \frac{\Delta\rho_0}{\rho_0} \tag{10}$$

According to KELLER and FRISCHKNECHT (1966), ρ_0 depends on concentrations of ions and their mobilities in the electrolyte if the electrolyte contains n kinds of ions:

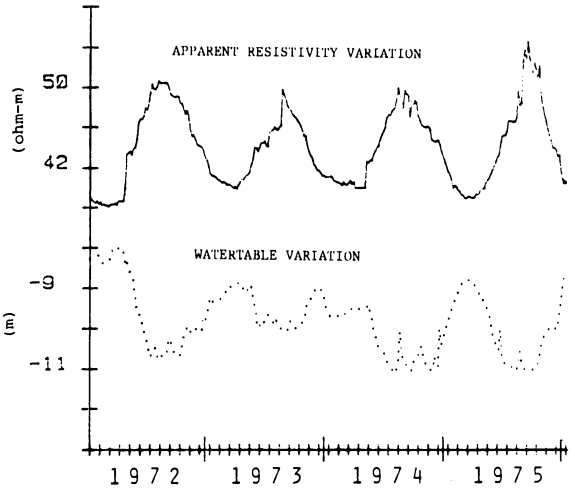

Figure 7

A typical example shows simultaneous observations in apparent resistivity and watertable, taken from Jiayuguan station in Gansu Province in North-western China during the period of 1972–1976. The solid line shows the ρ_a change with time, the unit for ρ_a is Ωm. The dotted line shows the watertable change; the unit for it is meter, and the minus sign means the watertable below the surface.

$$\frac{1}{\rho_0} = \sum_{i=1}^{n} C_i m_i F = F C_e M_e \tag{11}$$

where C_i ($i = 1, 2, \ldots, n$) is the concentration of ith kind of ion; m_i is the mobility of the ion and F is the Faraday constant ($F = 96\,500$ coulombs/mole). Because mobility varies little from one ion to another, $m_1 = m_2 = \cdots = m_n = M_e$, and $Ce = \sum_{i=1}^{n} C_i$ is the total number of various ions in pore water, and is called equivalent salinity of the electrolyte. Thus,

$$\frac{\Delta\rho}{\rho} = -\frac{\Delta C_e}{C_e} - \frac{\Delta M_e}{M_e} \tag{12}$$

indicates that the effect due to the change in electrolyte resistivity consists of two contributions: one from the relative change of the equivalent salinity in the electrolyte and another from the relative change of the mobility of the ions.

Keller and Frischknecht pointed out that the influence of temperature on rock resistivity is essentially the influence of temperature on the resistivity of the electrolyte in the pores in terms of the mobility change caused by the temperature variation of the viscosity of water. The relationship between temperature and rock resistivity is the following (KELLER and FRISCHKNECHT, 1966):

$$\rho_t = \frac{\rho_{t_0}}{1 + \alpha_t(t - t_0)} \tag{13}$$

where ρ_t and ρ_{t_0} denote the resistivities at the temperature t and t_0 (a reference temperature), respectively, α_t is the temperature coefficient of resistivity and has a value of about 0.025 per centigrade degree for most electrolytes.

From equation (13), the effect of temperature change (or say the effect of mobility change) can be obtained alone:

$$\frac{\Delta\rho_t}{\rho_t} = -\frac{\alpha_t \Delta t}{\rho_{t_0}/\rho_t} \approx -\alpha_t \Delta t \tag{14}$$

where $\rho_{t_0}/\rho_t \approx 1$. Equations (13) and (14) hold at moderate temperature which is appropriate in our study because within the electrically investigated volume the temperature is in the range of a few tens of degrees centigrade. Thus a 5% decrease of resistivity would require a 2° temperature increase.

1.4. Regional study of ρ_a anomaly in the Tangshan case

In the regional study of the ρ_a anomaly we wish to know which of the effects described in the last section would play important roles in producing a decrease of true resistivity in the investigated volume beneath each station. In other words, we need to check if these effects are reasonable, or, if they are compatible with relevant observations.

(*1*) *Regional compression.* Assuming that a regional strain was compressive which might be related to the preparatory process of the earthquake, and that the compression was uniform over the investigated region, the influence of volume compression on ρ_a could be estimated in the following way.

In general, the investigated volume beneath each station consists of two parts: one is the top part which is above the static water table and is in a state of partial saturation, and the other is the lower part which is below the static water table and is in a state of complete saturation. Thus, the change in ρ_a, should be the sum of the contributions of these two parts. Assume the average static water table is 30 m over the studied region, then we have $H_1 = 0$ and $H_2 = 30$ m for an estimate of the contribution of the top part (the notation H_1 and H_2 is the same as explained in Fig. 5), and likewise, $H_1 = 30$ m and $H_2 = 1000$ m for the lower part. For convenience, $\eta = 0.05$, $n = 2$ and $m = 1.5$ are taken for both the top part and the lower part, and a compressive volume strain $\Delta V_T/V_T = -10^{-5}$ is assumed over the entire investigated volume as well. For the top part, we have from equation (7) that $F_1 = 10$ and $\Delta\rho/\rho = -0.01\%$. The influence of the compression on ρ_a from this part can be estimated by

$$\left(\frac{\Delta\rho_a}{\rho_a}\right)' = S\left(\frac{\Delta\rho}{\rho}\right) = -0.0005\% \tag{15}$$

where S in this case ($H_1 = 0$, $H_2 = 30$ m) is about 0.05 from Fig. 6. For the lower part, we have from equation (8) that $F_2 = 30$ and $\Delta\rho/\rho = +0.03\%$. The influence of the compression in this part on ρ_a can be estimated by

$$\left(\frac{\Delta\rho_a}{\rho_a}\right)'' = S\left(\frac{\Delta\rho}{\rho}\right) \approx \frac{\Delta\rho}{\rho} = 0.03\% \tag{16}$$

where $S \approx 1$ ($H_1 = 30$, $H_2 = 1000$) from Fig. 6.

The total influence of compression on ρ_a would be

$$\frac{\Delta\rho_a}{\rho_a} = \left(\frac{\Delta\rho_a}{\rho_a}\right)' + \left(\frac{\Delta\rho_a}{\rho_a}\right)'' = -0.0005\% + 0.03\% \approx 0.03\%$$
$$= \left(\frac{\Delta\rho_a}{\rho_a}\right)'' \tag{17}$$

This estimate is made under the assumption that the static water table depth is small compared to the separation of the array (30:1000). In this case, the contribution to $\Delta\rho_a/\rho_a$ from the lower, fully saturated part is much larger than that from the top part which is partially saturated, because F and S are larger for the lower part than for the top part. Therefore the overall influence under compression is to increase ρ_a instead of decreasing it as might have been expected. A decrease in ρ_a would be possible if the static water level were so deep that the unsaturated top part occupied most of the investigated volume. In an extreme case, for example, assume the static water level is equal to the investigated depth ($H_1 = 1000$ m). Then, the total contribution would be

$$\left(\frac{\Delta\rho_a}{\rho_a}\right) = \left(\frac{\Delta\rho_a}{\rho_a}\right)' + \left(\frac{\Delta\rho_a}{\rho_a}\right)'' = -0.01\% + 0.0003\% \approx -0.01\%$$
$$= \left(\frac{\Delta\rho_a}{\rho_a}\right)' \tag{18}$$

Unfortunately the static water table in this example is not typical of most of the wells over that region. Therefore, we cannot expect to explain the regional ρ_a decrease by considering a regional compression over that region at all.

(2) *Regional dilatancy.* The dilatancy of brittle rock samples under high pressure attracted much attention in the early 1970s, and was invoked to explain the observations of a variety of precursors including resistivity (SCHOLZ *et al.*, 1973; BRACE, 1975).

An analysis of the effects of dilatancy has been done using the same parameters η, n, m, H_1 and H_2 as used in deriving equations (17)–(18) and only changing the sign for $\Delta V_T/V_T$ ($= +10^{-5}$). The results are the same as those in equations (17)–(18), respectively, except for changes of sign:

$$\left(\frac{\Delta\rho_a}{\rho_a}\right)' = +0.0005\%$$
$$\left(\frac{\Delta\rho_a}{\rho_a}\right)'' = -0.03\%$$
$$\left(\frac{\Delta\rho_a}{\rho_a}\right) = -0.03\% = \left(\frac{\Delta\rho_a}{\rho_a}\right)'' \tag{19}$$

It is obvious that, although the minus sign in equation (19) is as expected, the $\Delta V_T/V_T = +10^{-5}$ is too small to explain the observed anomaly in ρ_a of 3–5%. A large value $\Delta V_T/V_T = 10^{-3}$ is needed, but is not acceptable because it demands a very large surface uplift of the earth, which approaches a few meters according to a rough calculation with a source depth $h = 10$ km $= 10^4$ m

$$\left(\frac{\Delta h}{h} \approx \frac{1}{3}\frac{\Delta V_T}{V_T},\ \Delta h \approx \frac{1}{3}\frac{\Delta V_T}{V_T} h = 3.3 \text{ m}\right).$$

The uplift is three orders of magnitude larger than the observed uplift in the Tangshan case, shown in the last column of Table 1, which was 5.5 mm on the average in the area close to the epicenter relative to the outer area. It is of course conceivable that dilatant behavior is confined to a shallow but laterally extensive surface zone, whose thickness is three orders of magnitude less than the source depth, but this appears unlikely.

It should be pointed out that the estimate of $\Delta V_T/V_T = 10^{-3}$ was conservative because $\eta = 0.05$ was close to the extreme value (on the low side) for general sedimentary rock and $S = 1$ for the saturated lower part was on the high side. Thus, additional difficulty will be encountered with the dilatancy explanation if $\eta < 0.05$ and $S < 1$ are assumed.

Therefore, we would say that the dilatancy cannot be a major contribution in explaining the regional anomaly in ρ_a.

(*3*) *Regional temperature change.* In the last section, equation (14) seemed to show that the influence of temperature would be of importance because the electrolyte resistivity and therefore the bulk resistivity of the rock which contains the electrolyte would decrease by 2.5% with a temperature increase of 1°C. But the following analysis will indicate that the minimum change of temperature required to account for the regional anomaly in ρ_a cannot be attained due to energy constraints.

As mentioned in Section 2, the change in ρ_a at the surface requires a minimum change in true resistivity, which is equal to the change in ρ_a and should occur over the whole volume of the medium, or over the whole investigated volume. Suppose that such a change is caused by a temperature increase. From equation (14), it would require a minimum increase of 1–2°C in the entire investigated volume. Considering the anomaly as a regionally distributed feature, we should expect that a large scale region which is specified horizontally by the anomalous descending region shown in Fig. 2 and extending vertically to the source depth, would undergo at least the same minimum increase of temperature. The energy necessary to raise the temperature by 2°C may be estimated. The volume would be $300 \times 100 \times 11$ km$^3 = 3.3 \times 10^{20}$ cm^3 and the energy required would be 1.6×10^{28} ergs by taking the average density 2.84 g/cm^3 for the crust and a heat capacity of 0.2 cal/g·deg for crustal rock (DUNBAR, 1966). The energy estimated in this way is 25000 times larger than the energy of an earthquake with magnitude 8 (KASAHARA, 1981). If the postulated temperature increase were confined to a laterally extensive near surface zone whose thickness is three orders of magnitude less than the source depth, the energy discrepancy is reduced but not eliminated. Hence

the requisite energy is not available, though the direct negative evidence has not been available because the deepest temperature measurements for long periods in China are at depths of only a few meters.

A temperature variation considered to be related to the earthquake was found at a depth of 80 cm below the surface of the Earth at meteorological stations in an area very close to the epicenter during a very short period (half month) prior to the earthquake but no anomaly of temperature for a three-year period was reported (see 'The Tangshan Earthquake, 1976' [in Chinese], p. 194, published by the Seismological Press, Beijing, 1982).

(*4*) *Watertable changes.* A regional tendency in ρ_a as shown in Figs. 1 and 2 requires a regional rise in water table because $\Delta V_w/V_w > 0$ so that $\Delta\rho/\rho < 0$ when the water table increases. But as shown in Fig. 3, in the Tangshan–Tianjin–Beijing region, the observations of wells showed the opposite picture: the regional trend in levels decreased for several years, with an average amplitude of 10 m. Most scientists attributed this trend to the influences of climate and cultural activities because an arid period lasted for several years over this area while pumping continued to increase. Some scientists were of the opinion that the trend was at least partially related to the earthquake preparatory process. However, no one has disputed the validity of the observations.

In Table 2, some numerical results are given to show the influence of watertable change on ρ_a. It can be seen that for our separation of electrodes (1000 m) the apparent resistivity would increase about 10% if the water table, the thickness of waterbearing layer, and the amplitude of water table are taken as shown in Fig. 8.

Therefore, the regional decrease in ρ_a cannot be explained by the regional water table changes. And the sought for cause for the resistivity decrease must be sufficiently strong

Table 2

An example of the influence of a 10 m water table decrease on ρ_a

Separation of electrodes (m)	ρ_a (Ωm) $H_1 = 40$ m $H_2 = 40$ m	ρ'_a (Ωm) $H'_1 = H_1 + \Delta H = 50$ m $H'_2 = H_2 - \Delta H = 30$ m	$\Delta\rho_a/\rho_a = (\rho'_a - \rho_a)/\rho_a$
0.3	30.02	30.02	~0
3	29.91	29.91	~0
65	28.39	29.91	0.029
139	22.31	25.63	0.149
300	17.07	21.65	0.261
646	27.97	33.32	0.191
1392	52.59	61.07	0.161
3000	89.85	101.0	0.124
6463	133.78	144.5	0.08
13 925	170.39	177.2	0.04
30 000	190.37	193.1	0.014

$\rho_1 = 30$ Ωm, $\rho_2 = 5$ Ωm, $\rho_3 = 200$ Ωm. $\Delta H = 10$ m.

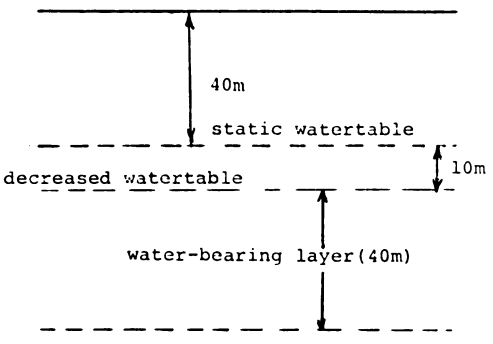

Figure 8
Schematic illustrations of water table structure in the Tangshan–Tianjin–Beijing region. The numbers for parameters in this figure are typical values.

to counteract the water table resistivity contribution, which in view of the opposite resistivity and water table trends may be viewed as noise in the measurements. To minimize the influence of this supposed noise contribution in future measurements, it is highly desirable to establish dipole separations which are significantly greater than the scales associated with the water table depth, as shown in Table 2.

(*5*) *Regional salinity change.* The last factor to be considered is the salinity change in the pore fluids. The regional salinity change is a possible explanation for the decrease in ρ_a. Based on Archie's law, an increase in the salinity would cause a proportional decrease in resistivity. Especially for a pore electrolyte with small salinity an appropriately large fractional change $\Delta\rho/\rho$ could be caused by a small change ΔC_e as long as $\Delta C_e/C_e$ is sufficiently large. The contribution of a salinity change to ρ_a depends in reality on where the salinity change occurs and whether the salinity change could occur in the real situation.

In the near surface, there is a very thin layer in which the salinity of pore electrolyte could change with time because of a fertilizing process. Since many arrays in the region of study were set up in proximity to farm land, we have first to consider the influence of this surface layer on ρ_a. Calculating the influence by taking a thin layer at the top of the earth with $H_1 = 0$ and $H_2 = 3$ m gives the sensitivity $S \approx 10^{-3}$, the resulting decrease in ρ_a is only -0.05% even though the averaged increase of salinity in that layer $\Delta C_e/C_e$ is taken to be 50%. The result is obviously far less than that required to explain the anomaly in ρ_a.

The existence of an increase in salinity at greater depth is unknown. If this increase at greater depth exists, the source of extra ions is still in question. Unfortunately, long-term observations of salinity over this region are lacking.

To summarize the discussions in this section, it can be seen that except for the possibility of a salinity increase at greater depth, definitely no other factors derived from differentiating Archie's law will provide an adequate explanation for the regional anomaly in ρ_a. Therefore, it is necessary to search for another explanation for the anomaly.

1.5. One speculation

In Archie's law, one factor left to be considered is the exponent m, which may be variable in the preparatory process of the earthquake. The m is called the structural coefficient by BARSUKOV (1979), who pointed out that m is related to the orientation of conducting paths, and according to SEN *et al.* (1981), 'm' is related to the shapes of pores or cracks. When the shapes deform or the orientation of conducting paths changes in the preparatory process of the earthquake the exponent, and therefore the resistivity, may change. Neither Barsukov nor Sen *et al.* specified possible causes for a change in 'm'.

Many experimental and theoretical studies (SPRUNT and NUR, 1977; PATERSON, 1981; ENGELDER, 1982; RENTON *et al.*, 1969) indicate the geometry of the pore structure changes during pressure solution. Pressure solution is the process with a long time scale occurring in stressed rocks with liquid filling in the pore or crack volume, which causes the deformation of rock cracks or pores by virtue of solid material dissolving from a stressed portion into the pore water and precipitation of solid material from the pore water in an unstressed portion. The larger the stress, the more extensive the dissolution. The pressure solution effect is likely accelerated near the ends of cracks or pores where the greatest stress concentration occurs. Therefore pressure solution is actually a process in which the geometry of the pores and cracks is modified by stress and the rate of the geometry change is controlled by stress. And with stress increasing it is possible that the geometry change will improve the connection between pores and cracks, so that the resistivity of the medium will decrease. The change in resistivity caused by geometry change could be attributed to the change in the exponent m in Archie's law.

One important characteristic of pressure solution is its long time scale which is to say that dissolving in a stressed region or precipitation in an unstressed region requires a certain period of time after a rock is stressed. Currently, it is not possible to quantitatively estimate the effect of pressure solution on resistivity as we did in Section 3 and Section 4, because the geometry change is a complicated process. Nor have experimental results on resistivity changes influenced by pressure solution been reported. However, the resistivity behavior following the Tangshan earthquake in Fig. 1, which we have not dealt with so far, exhibits a change in trend at the approximate time of the earthquake rather than an abrupt return to the original level immediately after the earthquake, which is the expected elastic response. This behavior suggests that the geometry of pores and cracks modified by stress is playing a role because of the long-term feature of geometry change in pressure solution.

1.6. Conclusions

Tentative conclusions of this study are as follows:

(1) The regional negative anomaly in ρ_a cannot be explained by effects of regional water table variation, or by strain and temperature change: the water table trend

gives an opposite contribution to ρ_a as does a hypothetical compression. The dilatancy change needed to give such a resistivity decrease based on Archie's law is much larger than that needed to explain the observed uplift by 2–3 orders of magnitude and the energy needed for a regional temperature increase of 1–2°C is too large, being four orders of magnitude greater than that of an earthquake with magnitude 8.

(2) The salinity change in pore electrolyte is left as a possible explanation for resistivity decrease according to Archie's law. But, at shallow depths the influence of salinity change is negligible while at greater depths the source of the additional ions is still in question even though the hypothesis holds. Data needed to test this hypothesis are lacking. Further simultaneous investigations of pore water salinity change are necessary.

(3) Since the geometry of pore and crack interconnections can be modified due to pressure solution, the effect of geometry change on resistivity may present an appropriate explanation for the decreasing tendency in ρ_a before the earthquake. Some observations showing long-term change of trend in ρ_a rather than an abrupt return to the original level immediately after the earthquake may serve as an indicator that the geometry of pores and cracks modified by stress is playing a role, because of the long-term feature of geometry change in pressure solution. From the theoretical viewpoint, the effect of geometry change by pressure solution can be associated with a change in the exponent m in Archie's law.

(4) Eliminating or significantly reducing the influence of the water table variation by increasing the electrode separation is very important. For resistivity inverse studies, a set of arrays with a range of electrode separations is essential.

Acknowledgments

I wish to acknowledge many helpful suggestions, discussions, and comments with Professor T. R. Madden and Dr E. Williams. Thanks are expressed to Professor F. H. Morrison for supplying the program of 1-D sounding problem. Discussions with Dr D. Morgan and J. Williams were also very helpful.

References

ARCHIE, G. E. (1942), *The Electrical Resistivity Log as an Aid in Determining Some Reservoir Characteristics*, Trans. Amer. Inst. Min. Engrs. *146*, 54.

BARSUKOV, O. M. (1972), *Variations of Electric Resistivity of Mountain Rocks Connected with Tectonic Causes*, Tectonophysics *14*, 273.

BARSUKOV, O. M. (1979), *A Possible Cause of the Electrical Precursors of Earthquakes*, Bull. (Izv.) Acad. Sci. U.S.S.R., Physics of Solid Earth, No. 8.

BRACE, W. F. (1974), *Electrical Resistivity of Sandstone*, Final report to the Defense Nuclear Agency, contract no. DNA-001-74-C-005.

BRACE, W. F. (1975), *Dilatancy-related Electrical Resistivity Change in Rocks*, Pure appl. Geophys. *113*, 207.

BRACE, W. F., and ORANGE, A. S. (1968a), *Electrical Resistivity Changes in Saturated Rocks During Fracture and Frictional Sliding*, J. geophys. Res. *73*, 1433.

BRACE, W. F., and ORANGE, A. S. (1968b), *Further Studies of the Effect of Pressure on Electrical Resistivity of Rocks*, J. geophys. Res. *73*, 5407.

BRACE, W. F., ORANGE, A. S., and MADDEN, T. R. (1965), *The Effect of Pressure on the Electrical Resistivity of Water-saturated Crystalline Rocks*, J. geophys. Res. *70*, 5669.

DAKHNOV, V. N. (1961), *The Application of Geophysical Method: Electrical Well Logging*, Colo. Sch. Mines Q. *57*, 95.

DUNBAR, C. O., *The Earth* (Weidenfeld and Nicholson, London 1966), p. 69.

ENGELDER, T. (1982), *A Natural Example of the Simultaneous Operation of Free-face Dissolution and Pressure Solution*, Geochim. cosmochim. Acta *46*, 69.

KASAHARA, K., *Earthquake Mechanics* (Cambridge University Press, Cambridge 1981), pp. 15–22.

KELLER, G. V., and FRISCHKNECHT, F. C., *Electrical Methods in Geophysical Prospecting* (Pergamon Press, New York 1966), pp. 16–33.

MAZZELLA, A., and MORRISON, F. H. (1974), *Electrical Resistivity Variations Associated with Earthquakes on the San Andreas Fault*, Science, N.Y. *185*, 855.

MJACHKIN, V. I., BRACE, W. F., SOBOLEV, G. A., and DIETERICH, J. H. (1975), *Two Models for Earthquake Forerunners*, Pure appl. Geophys. *113*, 167.

MORRISON, H. F., FERNANDEZ, RICARDO, and CORWIN, R. F. (1979), *Earth Resistivity, Self-potential Variations, and Earthquakes: a Negative Result for M = 4.0*, Geophys. Res. Letters *6*, 139.

PARKHOMENKO, E. I., *Electrical Properties of Rock* (English translation by G. V. Keller) (Plenum Press, New York 1967), pp. 119–184.

PATERSON, M. S. (1981), *Nonhydrostatic Thermodynamics and its Geologic Applications*, Review of Geophysics and Space Physics *11*, 355.

QIAN, J., GUI, X., MA, H., MA, X., GUANG, H., and ZHAO, Q., Observations of Apparent Resistivity in Shallow Crust Before and After Several Great Shallow Earthquakes. The contributed paper to the 'International Symposium on Earthquake Prediction' (UNESCO, Paris, 2–6 April 1979).

RENTON, J. J., HEALT, M. T., and CECIL, C. B. (1969), *Experimental Investigation of Pressure Solution of Quartz*, J. sedim. Petrol. *39*, 1107.

RIKITAKE, T., and YAMAZAKI, Y. (1969), *Electrical Conductivity of Strained Rocks (the Fifth Paper). Residual Strain Associated with Large Earthquakes as Observed by a Resistivity Variometer*, Bull. Earthq. Res. Inst. Tokyo Univ. *47*, 99–105.

SADOVSKY, M. A., NERSESOV, I. L., NIGMATULLAEV, S. K., LATYNINA, L. A., LUKK, A. A. SEMENOV, A. N., SIMBIREVA, I. G., and ULOMOV, V. I. (1972), *The Processes Preceding Strong Earthquakes in Some Regions of Middle Asia*, Tectonophysics *14*, 295.

SCHOLZ, C. H., SYKES, L. R., and AGGARWAL, Y. P. (1973), *Earthquake Prediction: A Physical Basis*, Science, N.Y. *181*, 803.

SEN, P. N., SCALA, C., and COHEN, M. H. (1981), *A Self-similar Model for Sedimentary Rock with Application to the Dielectric Constant of Fused Glass Beads*, Geophysics *46*, 781.

SPRUNT, E. S., and NUR, A. (1977), *Experimental Study of the Effects of Stress on Solution Rate*, J. geophys. Res. *82*, 3013.

WANG, C., *Characteristics of Variations in Watertable of Deep Wells Before and After Tangshan Great Earthquake.* The contributed paper to the 'International Symposium on Earthquake Prediction' (UNESCO, Paris, 2–6 April 1979).

YAMAZAKI, Y. (1974), *Coseismic Resistivity Steps*, Tectonophysics *22*, 159–171.

YAMAZAKI, Y. (1975), *Precursory and Coseismic Resistivity Changes*, Pure appl. Geophys. *113*, 219.

ZHANG, Z., XIE, J., XU, F., and PENG, S. (1981), *Vertical Deformations Associated with the Tangshan M = 7.8 Earthquake*, Acta Geophys. Sinica *24*, 182.

(Received 20th April 1984; revised 14th November 1984; accepted 14th November 1984)

PAGEOPH, Vol. 122 (1984/85)

0033-4553/85/060921-12$1.50 + 0.20/0

Piezomagnetic Monitoring in the South Pacific Region

By MICHAEL T. GLADWIN[1])

Abstract – Data from an array of piezomagnetic stations in the South Pacific Islands indicate that noise limitations on piezomagnetic stress monitoring reported for California (MUELLER and JOHNSTON, 1981; JOHNSTON *et al.*, 1984) are probably pessimistic since they seem to include significant diurnal residual. Raw station differences could be significant at the 1.0 nT level out to distances of several hundred kilometres. Two large earthquakes have occurred within the network, and no coseismic anomalies were observed. However, changes in observed magnetic field for several stations within 200 km of the earthquakes indicate that stress propagation effects are observable prior to the events, and that these effects dominate the simple elastic effects previously investigated which accompany the stress drops for moderate to large earthquakes.

Introduction

An array of twenty-five piezomagnetic monitoring stations was established during 1980/81 in the South Pacific region in an attempt to expose a piezomagnetic observation array to some very large earthquakes. Extensive studies in California have been reported (MUELLER and JOHNSTON, 1981; JOHNSTON, SMITH and MUELLER, 1976; DAVIS *et al.*, 1981; JOHNSTON, MUELLER and KELLER, 1981; JOHNSTON *et al.*, 1984). Many of the intrinsic difficulties of this type of measurement have been clearly identified by these studies, in particular, the problem of location of the instruments in significant anomaly fields and the limitations on significance imposed by the apparent rapid increase of observed noise on difference fields between stations with increased separation. No significant limitations of an instrumental nature have emerged to this time, and it is clear that proton precession magnetometers deployed in the Californian array have performed to predictable precision allowing reliable measurements at 0.2 nT.

The array established in the South Pacific was planned for a direct comparison with the California array. The object was to locate a series of high quality proton precession magnetometers in a region where large ($M > 7$) shallow events were common. The array is located to capture at least one event of magnitude 7 or greater every two years. Expected piezomagnetic anomalies for such events would be more clearly above the

[1]) Physics Department, University of Queensland, St Lucia, 4067, Australia.

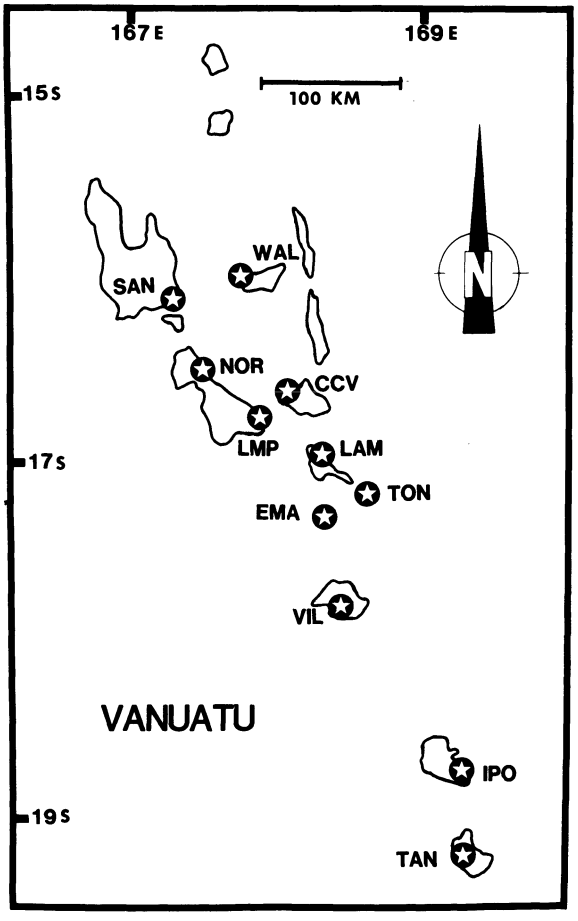

Figure 1
Location map of the stations in the Vanuatu sub-array. Eleven stations have been on line since June 1980.

operating noise levels if these were similar to those obtained in California. Thus, if such anomalies existed for large events, and scaled in some reasonable way for more extensive strain fields, they would be reliably observed. Actual performance of the array to this time indicates that resolution of 1 nT can be achieved in hour averages of simple differences out to station separations of several hundred km. At this level, large events have not been accompanied by co-seismic anomalies, but that other apparently propagating anomalies have been associated with the only two earthquakes which have occurred to this time in the array.

Instrumentation

The sites chosen for the array are shown in Figs. 1, 2 and 3. The Vanuatu sites were established in June 1980, and the Papua New Guinea and Solomon Islands sites in June

1981. The average stations separation for the Vanuatu region is 60 km, and for the northern array nearer 100 km.

At each site the proton precession sensor was located 2.4 m above ground, 30 m from an instrument hut. Geometrics model 826 magnetometers with high stability reference oscillators and 0.25 nT resolution are used throughout. Readings, synchronized across the array to within 10 seconds per year, are taken at each site every five minutes, and stored in the microprocessor controller for three hours. A satellite telemetry link (GOES W) for each site is used every three hours to transmit the data back to the US, and a summary data set is printed on site, for collection at the annual maintenance trip. The normal data stream is rich in station diagnostics so that all power supplies, operating temperatures, signal strength and oscillator reference frequencies are checked at each transmission. Stations are solar powered and generally very remote from civilization or mains power networks. At each maintenance visit the field magnetometers are calibrated by comparison with a standard magnetometer – worst case deviations of 0.3 nT have been observed.

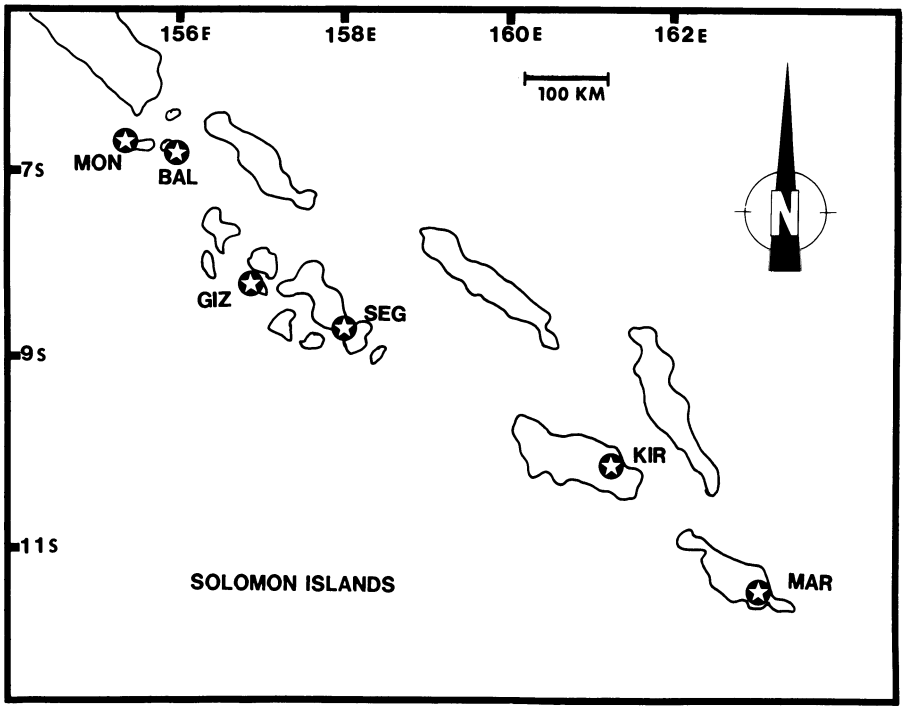

Figure 2
Location map of stations in the Solomon Islands sub-array. Six sites have been on line since May 1981.

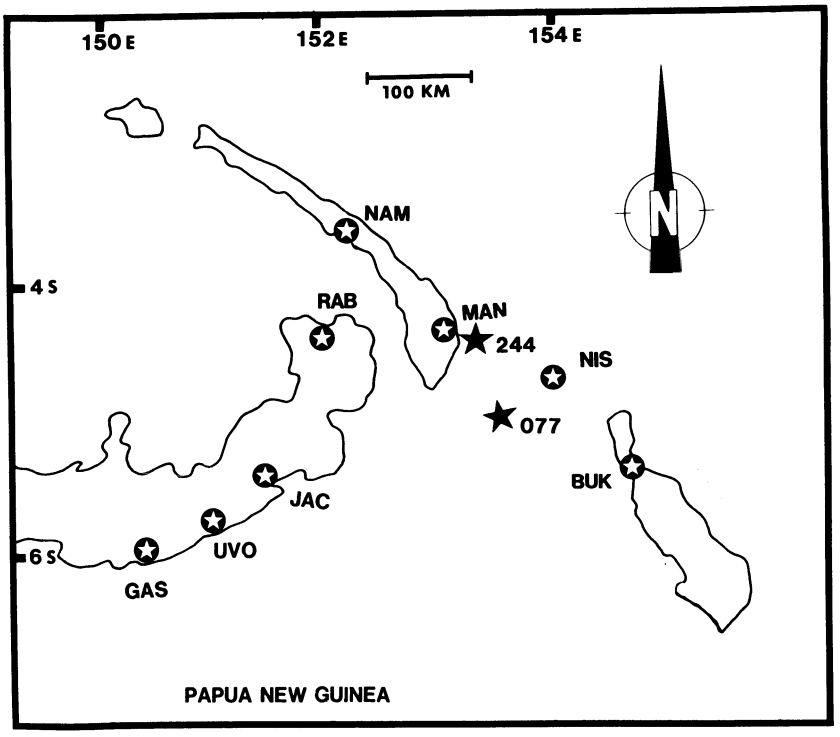

Figure 3
Location map of the Papua New Guinea sub-array. Eight stations have been on line since June 1981. Hypocentres of the two events discussed are shown.

Results

A. Performance and noise limitations

Magnetometer records are dominated by large scale solar activity superimposed on the Sq diurnal variation. The effectiveness of a simple (non-vector) array is limited by the common mode rejection of the array of these two noise sources. DAVIS and JOHNSTON (1983) have shown that an improvement of perhaps a factor of three can be obtained on noisy sites by use of Weiner predictive filtering, but that this efficacy is only obtainable with vector data at some nearby reference site. The improvement at low noise sites is considerably less.

A simple measure of the effectiveness of differencing without predictive filtering has been used by MUELLER and JOHNSTON (1981) and JOHNSTON *et al.* (1984). They examine a parameter which they call 'the standard deviation of hourly averages' of instantaneous differences and for the Californian data have found that for station separations beyond 50 km, this parameter increases at 0.007 nT/km. If this value

measured the random noise in the data it would impose a severe limitation on the predictive capability of an array for large event stress fields in the scale range 100–300 km because anomalies would need to exceed a few nanoTeslas to be above the noise. However, for the South Pacific array, it is clear that the JOHNSTON *et al.* (1984) procedure does not provide an appropriate measure of the noise limitation. Figure 4 shows the standard deviations of each hour of data for a series of ten station difference pairs. Most of the more than 6000 standard deviations shown are well below 0.5 nT and

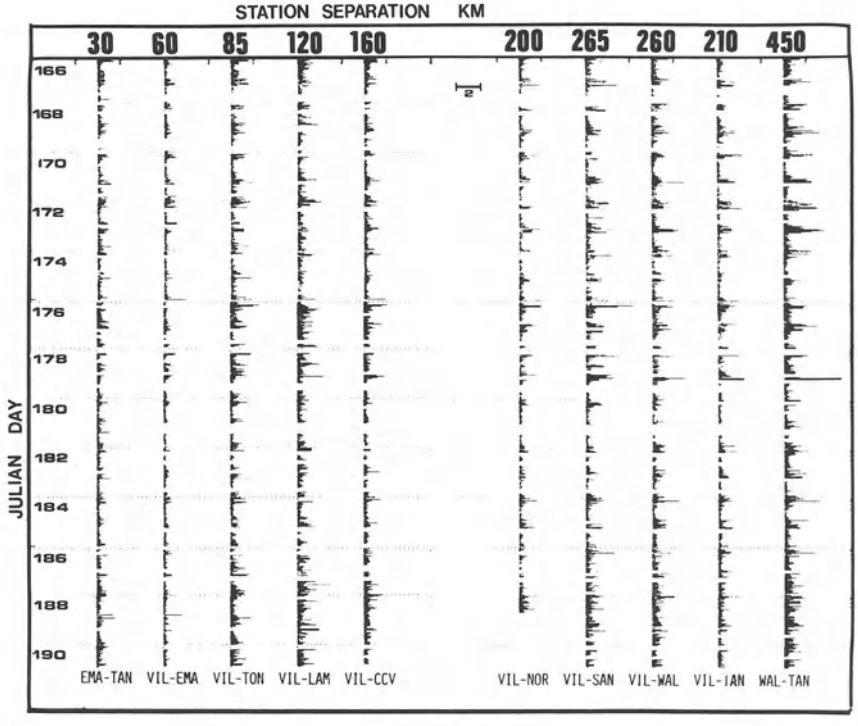

Figure 4

Standard deviations of all hour averages of station pairs for a series of station separations in the Vanuatu array. The bulk of the data show deviations less than 1 nT. Scale in nT is shown in the top centre of the figure.

there is no obvious increase of noise with station separation. A more extensive set is summarized in Fig. 5, plot A, which clearly shows that hour averages of differences have standard deviations of less than 0.5 nT out to distances of 500 km.

The increase of noise with distance in the Californian data compared with the South Pacific data cannot be explained by the geographical location of the South Pacific array. The data shown was taken at magnetic latitudes between 15 and 20 degrees South, where the Sq variation is perhaps three times larger than in California. The result remained true at the northern end of the array which extends to magnetic latitude 10°S where there is maximal Sq variation and the noise effects of the equatorial electrojet are strong.

We believe that the explanation for the Johnston *et al.* increase of noise with station separation is found in the fact that their noise estimate was calculated using hour averaged data for a minimum of four days (i.e. at least 96 hour averages). The standard deviation produced by this procedure would be dominated by any residual diurnal variation in the data. Their measure is reported in terms of 'standard deviation of hour averages' since it was produced from hour-averaged data. The standard deviation produced by their procedure actually approximates the standard deviation for the four day data set which, if the data shown in fig. 4 of JOHNSTON *et al.* (1984) is typical, includes residual diurnal variation. Since their measure includes the diurnal variation, the effects of which will certainly increase with station separation (particularly for dominantly north–south oriented arrays as in California and the South Pacific) it should not be taken at face value as a good indication of the limitations of piezomagnetic monitoring.

The standard deviations shown as plot A of Fig. 5 were produced from the data set of Fig. 4 by evaluating an average value, over 96 samples, of the standard deviation of one-hour samples. The Mueller and Johnston noise estimate is shown on Fig. 5 as plot B, increasing linearly with station separation at a rate of 0.007 nT per km, though most of the raw data shown in fig. 2 of DAVIS and JOHNSTON (1983) seems to indicate that the noise for this data subset decreases with station separation out to 100 km. It should be

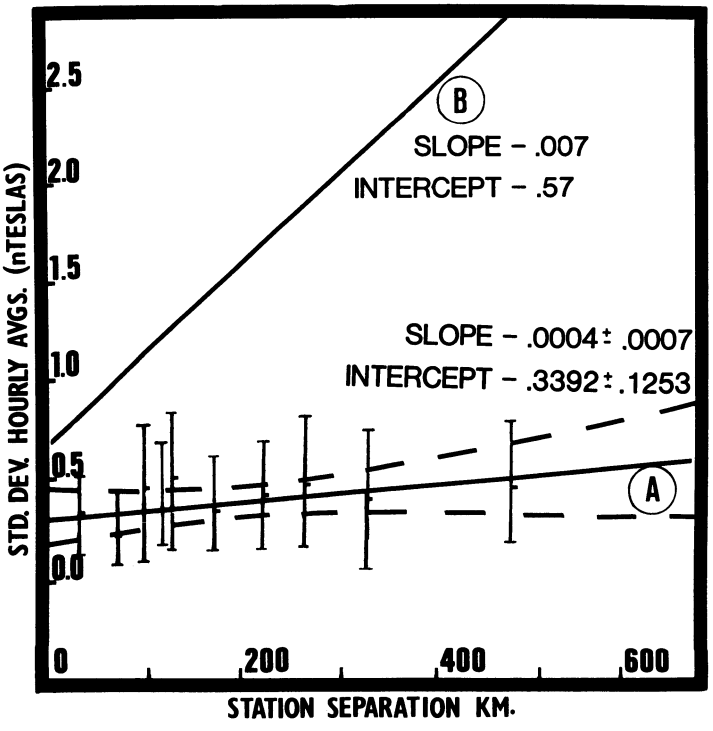

Figure 5
Mean values of standard deviations of hourly averages in the Vanuatu array against station separation.

noted that in the South Pacific data set an increase of approximately the same magnitude (0.006 nT per km) results if diurnal effects are included by the use of four day data sets. A realistic estimate of the actual noise limitation is therefore probably somewhere between plot A and plot B on Fig. 5, with the Mueller and Johnston estimate taken as a 'worst case' value.

DAVIS and JOHNSTON (1983) have shown that more advanced processing using predictive filtering is effective in removal of some of the dependence of noise in the differenced data on station separation for the Californian array. It also removes the more obvious effects of secular variation. The procedure also removes the dominant diurnal effect in the original data, since it is based on day-averaged data. The residual variances are approximately the same as plot A on Fig. 5.

Use of simple multiple day averages is not as effective as might be expected in reduction of diurnal noise effects because the average is highly sensitive to details of the shape of the diurnal residual in the difference, and to treatment of missing or bad data. An alternative procedure suitable for identification of static anomalies is presented below.

B. Observed field anomalies

Two earthquakes of significance have occurred in the Papua New Guinea part of the array in the period to May 1983. The first event on day 244, 1982 was a well behaved dip-slip event ($Mb = 5.9$, $Ms = 6.4$) at a depth of 45 km with a dip angle of 81 degrees (P.D.E. determination). The second at depth 88 km on day 077, 1983 was reported as $Mb = 6.4$ and $Ms = 7.9$. The location of the events are shown on Fig. 3 in relation to the five nearest stations. Detailed examination of the records for near stations revealed no clear co-seismic anomaly in either case. It has not yet been confirmed that an anomaly larger than 1 nT was to be expected based on simple elastic theory.

A most striking result was obtained in relation to the two events by detailed examination of differences of the various stations in the area over several months prior to the earthquakes. This result is presented in simple format in Fig. 6, which shows a model of the observed static magnetic field anomalies at each of the five nearest stations, where the total field value of each site is assumed constant except when a clear shift occurs in a set of differences and the shift can be identified as unique to one of the sites. Each of the thirteen shifts shown is inferred from examination of station differences from all nearest neighbours. To be included as an event a station must show clear offsets from its nearest neighbours while the nearest neighbours themselves are required to remain stationary relative to each other and to more distant stations. Early examination of averaged station differences revealed the unreliability of simple averaging procedures in such noise prone environments. The average value of a set of differences is extremely sensitive to the shape and amplitude of the diurnal variations (here about 30–40 nT) which over long intervals change quite significantly. The averages are also sensitive to the treatment chosen for lost data values, particularly if these are not randomly distri-

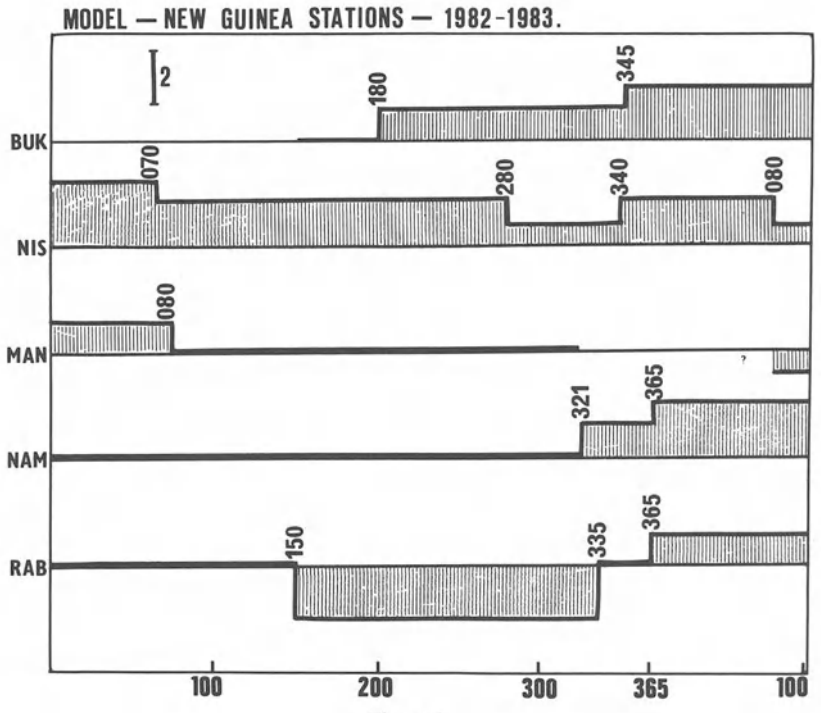

Figure 6

Model of observed magnetic field anomalies at the five nearest stations to the two earthquakes shown on Fig. 3. The vertical scale in nanoTeslas is shown at the top left. The days on which the inferred changes occurred are shown on the plots. In most cases the changes occurred non-synchronously.

buted in the averaging interval. Thus at events included in Fig. 6, instantaneous differences (and not the average values of these differences) were examined, and it was required that all values in a given interval be shifted to confirm an anomalous total field value.

An example of this procedure is presented in Fig. 7, which shows every data point (5 minute samples) for three different two-day intervals for the station pair Rabaul (RAB) and Namatanai (NAM). Diurnal variations are still evident on each difference set, but although there is some variation in shape, the static shift is easily identified. The technique remains robust for considerable shape variation, but for gross shape anomalies possible steps must be rejected as unconfirmed. Most of the structure seen on running averages is found by this procedure to be spurious, relating to inadequate storm rejection or missing data. The shift indicated in Fig. 7 on the Rabaul station beginning at day 150 and extending to day 320 was identified from the fact that before day 150 and during all days out to day 320, a clear shift occurred on each and every difference including the Rabaul station, but on no other difference pairs. The third difference trace labelled 'AFTER' shows instantaneous differences following another event, this time identified at Namatanai on day 320, which produced RAB–NAM differences systematically less negative than prior to day 320. Figure 8 provides a more

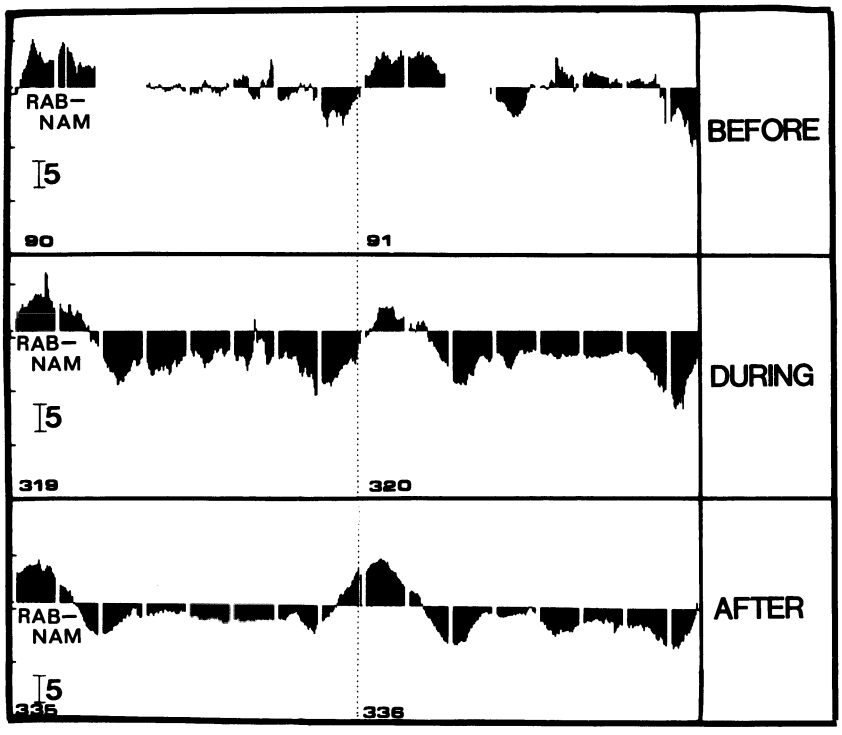

Figure 7

Example data for the event identification procedure. Three segments of data are overlaid. The top set shows all data points in a two-day period (days 90, 92) in the difference pair Rabaul–Namatanai (RAB–NAM), before a step identified at Rabaul on day 150. The second trace (days 319, 320) is shown as typical during the Rabaul anomaly, and demonstrates that all readings have been offset. The third trace (Days 335, 336) shows a reduced difference which was caused by a subsequent offset which occurred on day 321 on the Namatanai data.

conventional presentation of a selected set of these differences, where a 10 day running mean has been used. The scale shown in the upper left hand corner (3 nT) is common to all plots.

Figure 8 also illustrates the unreliability of determining shifts from smoothed station differences without examining individual records of both the differences and of the single stations. Several very evident steps (e.g. RAB–NIS day 116, 1982) in this plot can be easily attributed to transient sources such as storms, changes in the diurnal shape, or bad or missing data, and were not included in Fig. 6. There is no evidence to suggest that these shifts are an expression of secular drift. The region has quite low secular drift and all shifts shown occur as rapid steps in the data. At this time no analysis of secular variation equivalent to JOHNSTON *et al.* (1984) for the Californian array has been attempted.

Thirteen unambiguous shifts of magnitude greater than 1.0 nT occurred at the five stations in the interval shown. All stations were checked for absolute calibration within one week of the day 077 event. With one exception the events shown on Fig. 7 occurred

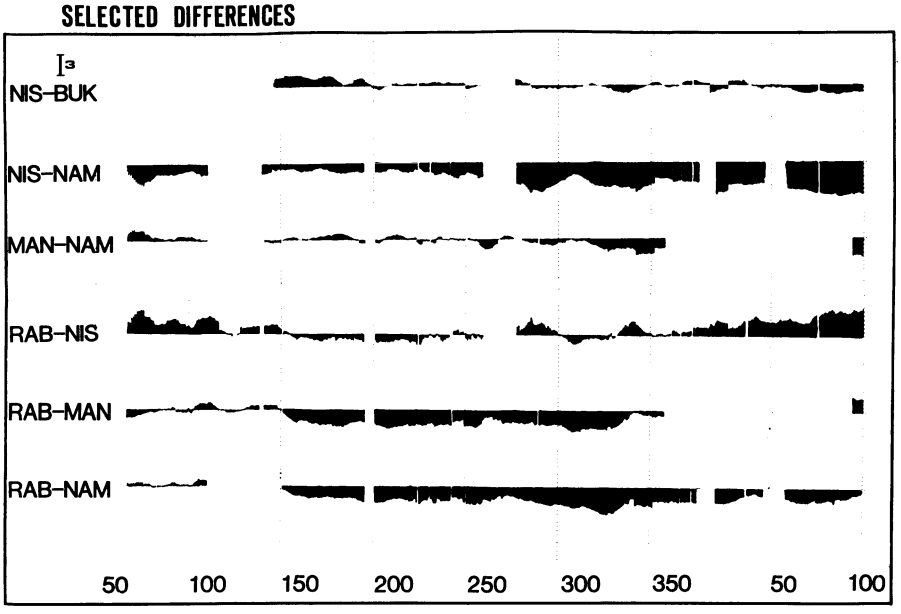

Figure 8
Selected station differences in the conventional running averaged format.

asynchronously at the various stations (the day on which each step occurred is shown on the figure), e.g. 070 (1982) at Nissan (NIS) and 080 (1982) at Manga (MAN) or the sequence NIS on day 280, NAM on day 320, RAB on day 335, NIS on day 340, BUK on day 345, NAM on day 365. In all cases, the steps show rapid onset at individual stations (less than one day), and given the fact that stations are dominantly sensitive to the stress field on the immediate 5–10 km adjacent to the stations, there is evidence of an aseismic propagation of stress fields with drift velocities in the range 5–15 km per day. No reasonable model of a single event of slip on a fault in an elastic half space can explain this asynchronous behaviour or the slow onset at each station.

A full analysis of these propagation effects is in progress. The existence of propagating stress relief steps could well be the mechanism by which stress is concentrated at major asperities which eventually fail in large seismic events. Algorithms are under development to provide detailed isolation of the time signature of the changing magnetic field during the transition and of the inferred large scale stress fields necessary to explain the observed time sequence at the various stations.

Conclusions

It is possible that the shifts shown in Fig. 6 are not of tectonomagnetic origin, but equally it is not possible to dismiss the viability of piezomagnetic stress monitoring until all of these events are explained by other (non-instrumental) causes. The anomalous

offsets occur over a scale which relates well to earthquakes of magnitude about 7, and no equivalent offsets have occurred elsewhere in the array over the prior two-year interval.

The observations suggest that it is inappropriate to use simple single event elastic models in analysing large event piezomagnetic data. All evidence in the present data indicates that large scale propagation of aseismic stress fields occurs prior to large events. These propagation phenomena are probably related to the accumulation of stress concentrations at potential large event epicentres.

This implies that greater success in piezomagnetic modelling for earthquake studies and prediction may be obtained by abandoning the simple consideration of quasi-static elastic strain fields centred on the final event in favour of an investigation of the dynamics of the stress accumulation process preceding the rupture. Piezomagnetic monitoring sites are dominantly sensitive to the stress in their near vicinity, and for the large events examined asynchronous propagation of stress relief through the station sites is the normal effect observed rather than the exception. Further sequences of static offsets are being investigated which may relate the very recent (December, 1983) Solomon Islands event to the southward bound sequence of events discussed here.

Acknowledgments

The work has been generously supported by the Australian Research Grants Scheme, and initially by the United States Geological Survey (Contract 14-08-0001-17771) which provided sixteen sites in the array. Data collection from the satellite was provided by U.S.G.S. personnel, in particular K. Breckenridge, S. Silverman and S. Miranda. Detailed comments on the manuscript by Dr M. J. S. Johnston and Dr P. Davis for comparison with Californian data were very productive.

Major contributions to the successful implementation of the array were made by R. Hart, F. Beckey, M. Francis, F. Peters and R. Gwyther, and in the early years R. Bergman and K. McIvor. The assistance of the Governments of Vanuatu, Papua New Guinea and the Solomon Islands through their Geological Departments is gratefully acknowledged.

References

DAVIS, P. M., JACKSON, D. D., SEARLS, C. A., and MCPHERRON, R. L. (1981), *Detection of Tectonomagnetic Events Using Multichannel Predictive Filtering*, J. geophys. Res. *86*, 1731–1737.

DAVIS, P. M., and JOHNSTON, M. J. S. (1983), *Localised Geomagnetic Field Changes Near Active Faults in California 1974–1980*, J. geophys. Res. *88*, 9452–9460.

JOHNSTON, M. J. S., MUELLER, R. J., and KELLER, V. (1981), *Preseismic and Coseismic Magnetic Field Measurements Near Coyote Lake, California, Earthquake of August 6, 1979*, J. geophys. Res. *86*, 921–926.

JOHNSTON, M. J. S., MUELLER, R. J., WARE, R. H., and DAVIS, P. M. (1984), *Precision of Magnetic Measurements in a Tectonically Active Region*, J. Geomagn. Geoelect. *36*, 83–95.

JOHNSTON, M. J. S., SILVERMAN, S. A., MUELLER, R. J., and BRECKENRIDGE, K. S. (1984), *Secular Variation and its Local Variations*, in press.

JOHNSTON, M. J. S., SMITH, B. E., and MUELLER, R. J. (1976), *Tectonomagnetic Experiments and Observations in Western U.S.A.*, J. Geomagn. Geoelect. *28*, 85–97.

MUELLER, R. J., and JOHNSTON, M. J. S. (1981), *Precision of Magnetic Measurements in a Tectonically Active Region*, Trans. Am. geophys. Un. *62*, 1054.

(Received 16th December 1983, revised 15th August 1984, accepted 17th August 1984)

PAGEOPH, Vol. 122 (1984/85) 0033-4553/85/060933-14$1.50 + 0.20/0

Groundwater Microtemperature in Earthquake Regions

By HIDEKI SHIMAMURA[1]), MORIO INO[2]), HISAYOSHI HIKAWA[3]) and TAKAYA IWASAKI[1])

Abstract – Microtemperature measurements of groundwater with a relative precision better than 1/1000°C have been made in several seismically active areas in Japan. The measured temperatures show clear coseismic signals as well as a correlation with atmospheric pressure. Simultaneous observations at various depths have shown that these temperature changes were not induced by simple groundwater level changes. Also, distinctive signals occurred before several earthquakes and seem to be caused by a different mechanism than the coseismic signals. The microtemperature at some observation sites shows excellent correlation with records of nearby sensitive borehole strainmeters. Simultaneous recording of microtemperature and strain has been initiated in some boreholes.

Key words: Groundwater temperature, Crustal strain, Coseismic signal, Earthquake precursor, Atmospheric pressure.

1. Introduction

A very precise digital system to measure the microtemperature change of deep groundwater has been developed (SHIMAMURA, 1980). The principal aim of the apparatus is to monitor movements of groundwater which may be caused by crustal strain changes related to faulting and earthquake generation. In our earlier work a quartz thermometer installed 200 m deep in a 380 m deep well in the Usu volcanic region, Hokkaido, showed preseismic temperature variations (SHIMAMURA and WATANABE, 1981). The temperature increased by about 300 m°C (1 m°C = 1/1000°C) during a half year, the biggest observed change of all our microtemperature measurements. Also, the rate of temperature increase decreased notably before intense earthquake swarms.

Several coseismic temperature changes were also reported by SHIMAMURA and WATANABE (1981). These signals have a similar distinctive shape marked by a sharp temperature spike of several tens of m°C with positive polarity (temperature increase) and accompanied by an offset with either positive or negative change of 1 to 10 m°C. SHIMAMURA and WATANABE (1981) concluded that the spikes were not of tectonic

[1]) Laboratory for Ocean Bottom Seismology, Geophysical Institute, Hokkaido University, Sapporo 060, Japan.

[2]) Earthquake Preparedness Division, Shizuoka Prefectural Government, Shizuoka 420, Japan.

[3]) Earthquake Prediction Information Division, Japan Meteorological Agency, Tokyo 100, Japan (present address: Sapporo District Meteorological Observatory Japan Meteorological Agency, Sapporo 060, Japan).

origin, but that the offsets were. The positive and negative steps corresponded to two separate earthquake groups of different locations and focal mechanisms.

NOTSU *et al.* (1980) also observed coseismic temperature changes in a 7 m deep well in the Usu volcanic region using a thermistor installed with a Radon concentration measuring instrument. Their study was probably the first instrumental observation of a coseismic temperature change. They observed sixteen temperature changes with amplitudes of 0.2 to 1.0°C by a thermometer which had a sensitivity of ±0.1°C. Most of the changes accompanied nearby volcanic earthquakes. The recorded polarity of the observed changes, which had a shape of a dull spike, was always positive.

The coseismic temperature signals observed by NOTSU *et al.* (1980) are probably different from those observed by SHIMAMURA and WATANABE (1981). The instrument in the latter study had higher resolution in both time and temperature, and so it could record a spike and a step separately. Thus, the consistently positive coseismic signals of NOTSU *et al.* (1980) probably correspond to the spikes of SHIMAMURA and WATANABE (1981), since the spikes have much larger amplitudes than do the steps. Unfortunately the two studies were at different times so no direct comparison is possible. The only other published studies of microtemperature changes of groundwater are by SHIMAMURA (1980, 1983).

Although crustal strain is generally thought to relate more directly to water level measurements than to microtemperature measurements, we prefer microtemperature observations because (a) if there are more than two aquifers, the water level does not respond simply, (2) water level is easily affected by precipitation and cultural activities, and (3) aquifer table (outside the well casing) is sometimes different from water level (inside casing) (e.g. WEEKS, 1979). Our strategy of microtemperature observations has been (1) initially to install inexpensive sensitive thermometers in existing wells, (2) to distinguish signal from noise, and (3) to find wells which record signals of tectonic origin.

2. *Experimental apparatus*

The system was specially designed for geophysical boreholes, which allow very stable long-term observations. The temperature sensor uses a quartz crystal which enables a stable measurement with a precision of better than 1/1000°C. The system has digital recording with a dynamic range of 240 dB, temperature range of −50°C to 150°C, and a resolution of 10^{-5}°C (SHIMAMURA, 1980). The thermometer system was tested for sensitivity to ambient air pressure, and no effect was seen.

Most units operate on AC power, although all have battery back-up. Those not on AC power use D cell batteries or 40 ampere-hour automobile batteries, enabling unattended observation up to six months. They have operated reliably over an ambient temperature range of −30°C to 40°C. The instrument is also not affected by vibrations of the size expected in strong earthquakes.

Since we are interested in relative temperature changes with high precision, the absolute accuracy of the microtemperature measurements is not important. The long-term stability of the measurements can be estimated from the aging of the quartz crystal (SHIMAMURA, 1980). Drift rates are less than ± 20 m°C per year. However, in many wells the observed temperatures did not change by more than 10 m°C over one to two years of observation. The observation at Usu volcano by SHIMAMURA and WATANABE (1981), with a 300 m°C change in a half year, is an exception. These data suggest good stability of the quartz crystal since it is unlikely that real temperature changes were exactly compensated by the aging rates of the quartz crystals. Aging rates of the quartz crystals are inherently random.

No data exist to determine the optimum depth for installing the instrument. Thus nearly all sensors were placed at the bottom of wells, regardless of the position of screens (perforations) in the well casing, in order to get as far from the ground surface as possible. The temperature outside of the casing can be sensed through the steel wall with a time constant of tens of minutes, depending on the diameter of the well.

3. Field observations

About fifty instruments have been installed in various regions in Japan, at an Antarctic base, and in Iceland. Most units have been deployed in earthquake prone regions. The first installation was in the Teshikaga region of eastern Hokkaido (Fig. 1), Japan, in 1978. During the past forty years, shallow earthquakes with magnitudes 6.0, 5.7, 6.2, 6.1, 6.5, and 5.7 have occurred in 1938, 1959, 1959, 1959, 1967, and 1967 respectively. The depths of the earthquake foci were between 0 and 20 km (Japan Meteorological Agency: J.M.A.). This area is one of the most active for shallow earthquakes in Japan.

The Teshikaga area was also chosen because of the large number of wells which had been drilled for geothermal exploration. Most wells were drilled in rock covered by sediments 100 to 700 m thick. The sites lie within a 10 km square area thought to be the source region of the recurrent shallow earthquakes of the Teshikaga area. The well KUR is nearly on the trace of the fault generated by the magnitude 6.0 earthquake in 1938 (TSUYA, 1938). The instrument at KUR was installed to record possible temperature changes due to frictional shear heating caused by fault movement (e.g. LACHENBURCH, 1980). To the northwest of KUR, the fault cuts the bottom of Kusyaro Lake (poisonous gas generated during faulting killed nearly all the fish).

Temperature gradients in the KUR well are generally higher than in non-geothermal areas in Japan. A gradient of 10 to 20°C/100 m is common in the region. The hydrology of the area is apparently complex, because the groundwater temperature differs greatly from site to site, i.e. from less than 40°C to more than 90°C, at the same depth of 400 m.

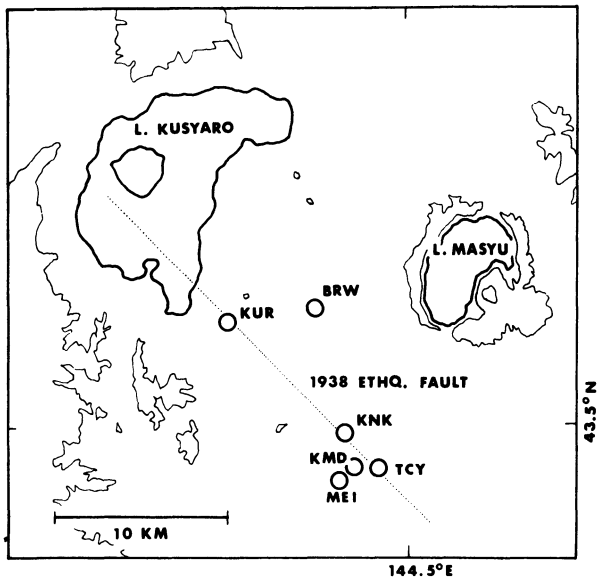

Figure 1
Locations of microtemperature observation sites in eastern Hokkaido. The sites are concentrated near the 1938 earthquake fault, shown by the dotted line. The earthquake fault lies under Kusyaro Lake. Both Kusyaro Lake and Masyu Lake are caldera lakes. Contour lines of 500 m elevation are shown by thin lines. The southeastern end of the earthquake fault is not precisely known.

The observed microtemperature vs. time is a function of atmospheric pressure at some sites (SHIMAMURA, 1983). In May 1980 we added observation site TCY, a flowing well with a rate of about 3 liter/min and mean temperature of 23°C. TCY has a response to atmospheric pressure (Fig. 2) about ten times larger than the response of KUR (KUR_{210} in Fig. 2) and more than a hundred times larger than that of well MEI, where the pressure effect is barely seen. The TCY site is near the extension of the earthquake fault, although the southeastern end of the fault is not precisely known (TSUYA, 1938). The well is 800 m deep, and the sensor is installed 68 m deep.

The pressure coefficient in all wells is negative, however the amplitude varies from well to well. Pressure coefficient is the microtemperature variation divided by the atmospheric pressure variation; its units are m°C/mbar. The pressure coefficient of each well is tabulated in Table 1. Flowing wells generally have larger pressure coefficients than non-flowing wells. However, the non-flowing wells themselves have coefficients differing by more than a factor of ten. We have no explanation of why the sensitivities are so different among the wells. The changes in the flow rates were not accurately measured, so the atmospheric pressure effect on flow is unknown.

As is seen in Fig. 2, at KUR and TCY a few millibar change of atmospheric pressure induces noticeable change in the microtemperature, e.g. 10–30 m°C. Hence, a few millibar change in tectonic stresses in the earth crust probably could be recorded by the instruments. This suggests the possibility of monitoring very small changes of the crustal stress by microtemperature measurement. In some wells microtemperature changes correlated with earth tides have been observed.

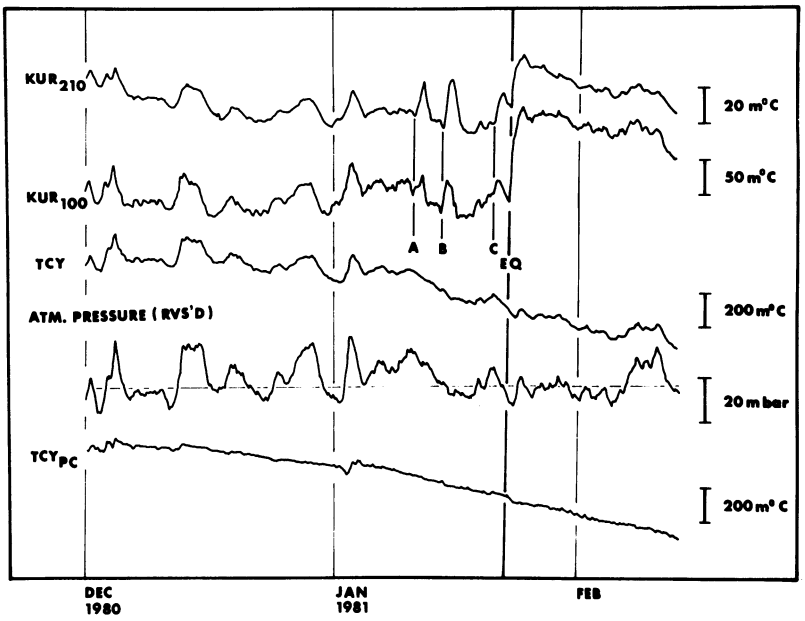

Figure 2

Comparison of KUR_{210}, bottom sensor, and KUR_{100}, middle sensor. Both records are before compensating for atmospheric pressure. In general the KUR_{100} signal is 3.6 times larger, but for the coseismic signal it is 4.5 times larger. The coseismic signal was recorded when the Jan. 23 earthquake (M 7.1) occurred. A very small negative coseismic signal is seen at EQ of TCY_{PC}, a pressure compensated record of TCY. Atmospheric pressure is also shown; the polarity is reversed. A, B and C are possible precursory signals.

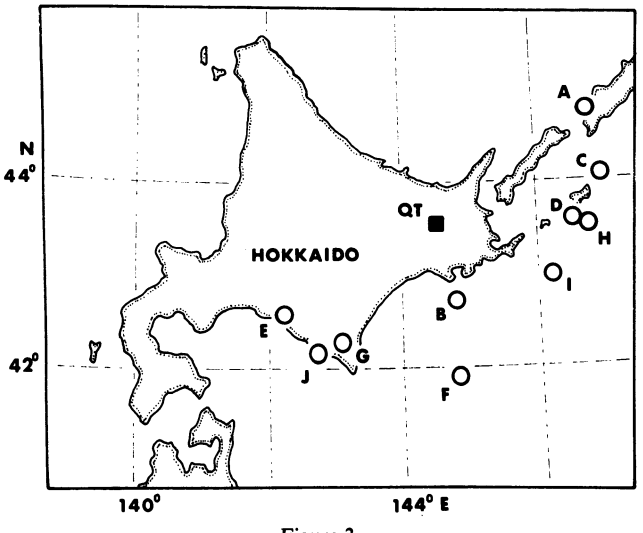

Figure 3

Epicenters of earthquakes A–K which caused microtemperature steps in the Teshikaga thermometer array. The observation site Fig. 1 is indicated by QT. Earthquake dates and magnitudes are A – 6 Dec., 1978, M 7.7; B – 14 Dec., 1979, M 5.7; C – 10 Feb., 1980, M 5.4; D – 23 Feb., 1980, M 6.8; E – 23 Jan., 1981, M 7.1; F – 20 May, 1981, M 5.2; G – 14 July, 1981, M 4.6; H – 3 Sept., 1981, M 6.5; I – 23 Nov., 1981, M 6.0; J – 21 Mar., 1982, M 7.1; K – 6 May, 1983, M 7.7.

4. *Coseismic signals*

The first large coseismic change in groundwater temperature was observed at KUR on December 6, 1978 by an analog thermometer (SHIMAMURA, 1980). After the installation of the digital system, a number of additional coseismic temperature signals were also observed (SHIMAMURA, 1983). However, no earthquakes have occurred in the Teshikaga area since the start of microtemperature observations, so only signals by earthquakes with epicentral distances more than 90 km are reported here. Most of these earthquakes (Fig. 3) resulted from thrust movements at the boundary between the subducting Pacific plate and the Eurasian plate.

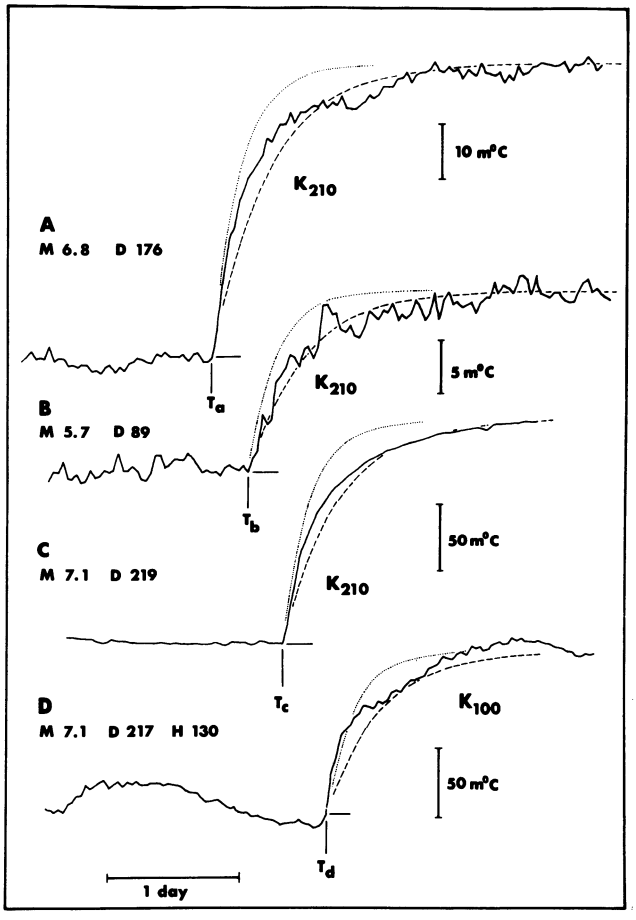

Figure 4

Coseismic KUR signals for sensors at 100 m (K_{100}) and 210 m (K_{210}) depths in expanded time scale. Dotted lines indicate exponential increase with time constant of 5 hours, and broken lines, of 10 hours. The observed microtemperature increased with a time constant of about 5 hours at first, and later with a time constant more than 10 hours. T_a to T_d are the times of earthquakes, which coincided with the onsets of the observed records within a sampling interval. Earthquake dates and depths are A – 23 Feb., 1980, 30 km; B – 14 Dec., 1979, 70 km; C – 21 Mar., 1982, 40 km; D – 23 Jan., 1981, 130 km. Earthquake magnitude, epicentral distance, and focal depth of each earthquake are shown on each trace.

The coseismic changes are shown with an expanded time axis in Fig. 4. Most recorded steps show a temperature increase. The sign of the temperature change is probably dependent on the focal mechanisms of the earthquake sources and the azimuths to the sources. Alternatively the polarity may depend on characteristics of the aquifer; we have not been able to distinguish the causes.

The magnitudes of the observed microtemperature steps observed at KUR correlate with epicentral distance and earthquake magnitude (SHIMAMURA, 1983). Figure 5, an updated version of a similar figure in SHIMAMURA (1983), shows that the new microtemperature data appear to follow the lines determined by the old data.

Some wells in the Teshikaga region show no clear coseismic signal. The reason is not known. For example, the TCY well, which has the largest atmospheric pressure coefficient (Table 1), has not recorded clear coseismic signals except for a few small

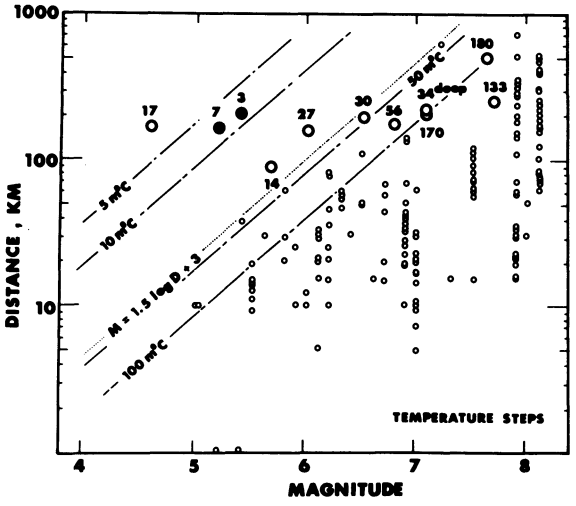

Figure 5

Observed microtemperature steps of KUR (KUR_{210}) sensor. The recorded amplitudes (m°C) are indicated by large circles with numerals. Open circles are positive steps and closed circles are negative steps. Small circles are the compilation of visible coseismic signals of hot springs and groundwater by S. Hiraga (personal communication). The point labelled '34 m°C' was recorded from a deep earthquake 170 km away. The correspondences between earthquakes (Fig. 3) and temperature steps are K – 180, A – 170, J – 170, E – 34, D – 56, H – 30, I – 27, B – 14, C – 3, F – 7, G – 17.

Table 1

Atmospheric pressure coefficients of the microtemperature records

Site (sensor)	Depth of sensor	Depth of well	Pressure coefficient (m°C/mbar)	Comments
KUR_{210}	210 m	210 m	0.53–0.59	Not flowing
KUR_{100}	100 m	210 m	1.9–2.1	Not flowing
KMD	30 m	495 m	1.8–2.2	Flowing
MEI	480 m	760 m	Less than 0.05	Not flowing
TCY	68 m	800 m	5.7–6.1	Flowing

ones that can be seen only after removal of the atmospheric pressure effect (Fig. 2). The MEI well has recorded neither coseismic signals nor the effects of atmospheric pressure. The MEI record has shown a temperature change of less than 5 m°C. Although MEI is only about 1.5 km from TCY, the records are quite different. Both wells are near the southeastern extension of earthquake fault, but their coseismic signals are much smaller than KUR signals.

5. *Possible precursors*

As was stated in the previous section, the microtemperature changes were interpreted to be due to either atmospheric pressure or earthquakes. In addition to these two kinds of signals, a third kind of signal has sometimes been observed at KUR. These signals have similar shape, consisting of a single pulse of a few days duration. Figure 6 shows two examples, A and B. Figure 2 shows three different examples marked A, B, and C. The maximum precursory signal amplitude was 30 m°C. These signals were not related to any observable non-earthquake events. They have never appeared except one or two months before large earthquakes. However, not all large earthquakes were accompanied by these signals.

The precursory signals have a characteristic dependence on the sensor depth. A second quartz sensor was originally installed at 100 m depth at KUR for comparison with the bottom sensor at 210 m in July 1980. The sensors were identical and the

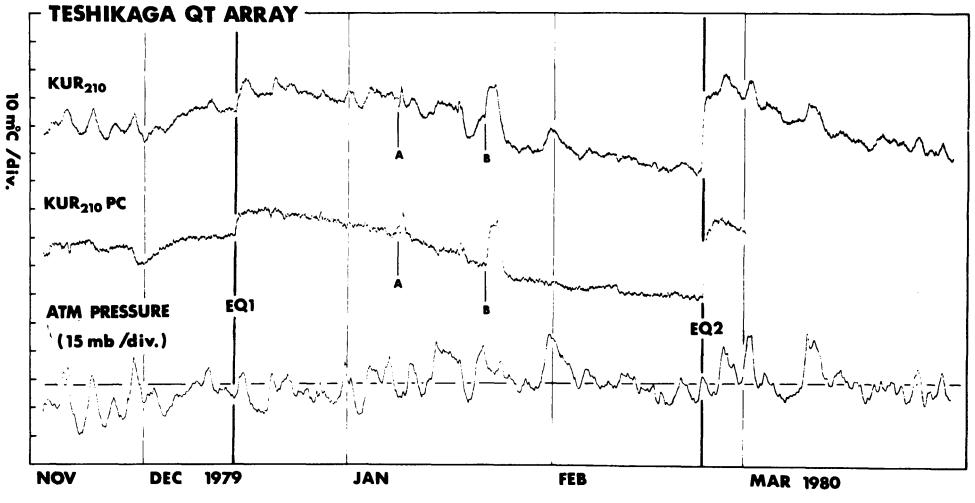

Figure 6

KUR microtemperature record (upper trace), atmospheric pressure compensated record (middle trace), and atmospheric pressure, whose polarity was reversed (lower trace). Small coseismic signals such as EQ1 are visible only on the trace of the pressure compensated record. EQ1 is 14 Dec., 1979 earthquake, *M* 5.7, distance 89 km. EQ2 is 23 Feb., 1980 earthquake, *M* 6.8, distance 176 km. Signals A and B are possible precursors.

recorder was common. While the signals induced by atmospheric pressure are similar, the amplitudes from the upper sensor are about 3.6 times larger than those of the lower sensor (Fig. 2). However, the ratio of the amplitudes of the coseismic signals is 4.5, as seen in Fig. 2 (SHIMAMURA, 1983). The difference of the ratios suggests that the mechanisms generating coseismic signals and atmospheric pressure signals are different.

The same ratio for the precursory signals at the upper and lower sensors is 1.5–1.6, quite different from both the ratio of the atmospheric pressure effect and the ratio of the coseismic signals (Fig. 2). Thus for these precursory signals, the lower sensor has a better 'signal-to-noise' ratio than the upper sensor. The difference in the amplitude ratio (KUR_{100}/KUR_{210}) strongly suggests that the mechanism of precursory signals is different from the mechanisms of atmospheric pressure effects and coseismic effects.

Although the KUR signals are different from signals observed in the Usu volcanic region, we think that both signals are probably precursors of earthquakes. The association of the Usu earthquakes with a volcanic environment may account for the difference of precursor shapes. In the Teshikaga region we have recorded only a few precursory signals, but the number of large earthquakes was also small and the earthquake magnitudes were greater than 6.8.

6. *Comparison of strainmeter and microtemperature records*

Identical thermometers have been installed since 1979 also in the Tokai area southwest of Tokyo where a magnitude 8 earthquake is expected. In a 130 × 60 km area, eleven thermometers have been deployed (Table 2). The depths of the wells are 100 to 495 m, and almost all sensors were put at well bottoms. The area has been seismically quiet since installation of the thermometers, and no coseismic-appearing signals have been recorded. All observation wells are in heavily populated areas, and typically several hundred houses lie within 500 m of a well. However, the micro-

Table 2
Observation sites of the quartz thermometers

Observation site	Latitude	Longitude	Observation period	Sensor depth	Well depth	Comments
(HOKKAIDO)						
KUR (Kurotaki)	43°33′04″N	144°22′04″E	17/11/1978 –	210 m	210 m	Second sensor added 7/1980
MEI (Meisei)	43°28′15″N	144°12′00″E	11/4/1979 –	480 m	760 m	Sensor shifted to 220 m 5/1981
KMD (Kamata)	43°28′48″N	144°27′50″E	11/7/1979 –	110 m	495 m	Sensor depth 30 m until 7/1980
TCY (Tsujiya)	43°28′49″N	144°28′37″E	10/5/1980 –	68 m	800 m	Self flowing 3 litre/min., 24°C
USU (Showashinzan)	42°32′08″N	140°51′42″E	12/10/1979 –	200 m	376 m	
KMU (Kamikineusu)	42°14′19″N	142°58′02″E	4/7/1983 –	101 m	101 m	With borehole strainmeter
(TOKAI)						
OMZ (Omaezaki)	34°35′58″N	138°13′50″E	22/6/1979 – 24/4/1980	100 m	100 m	Second sensor added 11/1979
YSD (Yoshida)	34°45′24″N	138°16′17″E	22/6/1979 – 5/10/1982	135 m	135 m	With Radon observation
ARA (Arainmachi)	34°41′05″N	137°34′43″E	21/11/1979 –	393 m	393 m	With seismograph
MKB (Mikkabi)	34°48′20″N	137°33′26″E	5/10/1981 –	46 m	46 m	With borehole strainmeter
HIZ (Higashiizu)	34°48′45″N	139°13′28″E	15/3/1982 –	246 m	246 m	With borehole strainmeter
AJR (Ajiro)	35°02′34″N	139°05′45″E	11/3/1983 –	108 m	108 m	With borehole strainmeter

temperature records do not show cultural influences, except for a few sites such as YSD where pumping is heavy nearby.

J.M.A. has installed 16 sensitive borehole volumetric strainmeters, which were designed by SACKS and EVERTSON (1970), in the Tokai area. The depths of the installations are 50 to 250 m. The microtemperature records of OMZ and ARA resemble the records of the J.M.A. strainmeters at Omaezaki and Mikkabi respectively (Fig. 7). OMZ (100 m depth) is 2 km northeast of Omaezaki well (208 m depth), and ARA (395 m depth) is about 14 km south of Mikkabi (51 m depth). The scaling between the curves is about 1 m°C microtemperature increase for 1×10^7 extension strain.

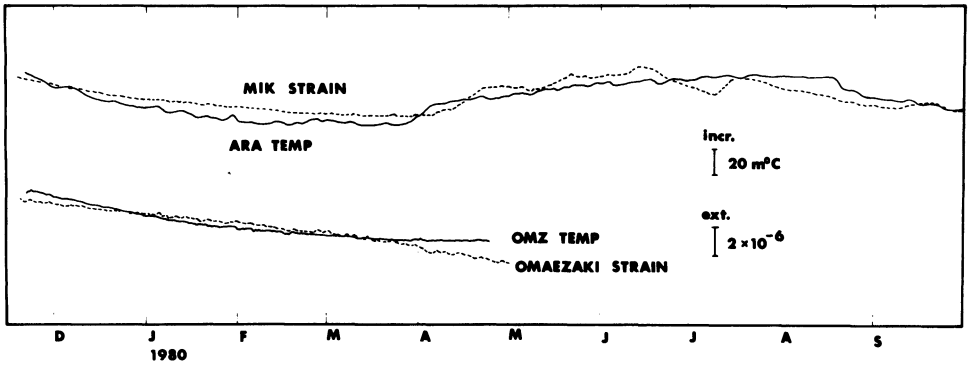

Figure 7
Comparison of the microtemperature records and the borehole strainmeter records. Solid lines show microtemperature of ARA (395 m deep) and OMZ (100 m). Broken lines show volumetric strainmeter records of Mikkabi (MIK, 51 m) and Omaezaki (208 m). ARA and Mikkabi are 14 km apart; OMZ and Omaezaki are 2 km apart. The microtemperature records are daily mean values.

7. *Discussion*

By microtemperature observations, we have studied movements of groundwater which might be related to earthquake generation. In most earlier work the groundwater flow was studied by observing groundwater levels. But we have observed both microtemperature and water level in a few wells and observed no correlation. Our work is the first to evaluate the correlation of microtemperature with atmospheric pressure. There are, however, some earlier studies of the relation of groundwater level to atmospheric pressure. In one such study JOHNSON *et al.* (1973) observed that the water level of a well was inversely correlated to atmospheric pressure.

In a qualitative sense, a simple vertical shift of the entire groundwater mass with groundwater level would seem to account for the temperature changes. The reason is that at a fixed depth in a well, temperature increases when the water level rises because water temperature normally increases with depth. However, this explanation is inconsistent with our microtemperature observations. The average temperature gradient

at KUR is twelve times larger at the upper sensor level than at the lower level (Fig. 8), and thus a vertical shift would produce a ratio much larger than the observed ratio of 3.6.

The actual situation may be more complex. When a well penetrates a sequence of strata, the barometric efficiency is more complex than for a well with a single aquifer. (Barometric efficiency is the specific weight of water times the ratio of water level change to atmospheric pressure change.) Generally each layer will have its own barometric efficiency determined by its hydraulic parameters, and as a whole, an integrated barometric efficiency governs. Thus the integrated barometric efficiency may be the cause of the discrepancy between the ratios of 12 and 3.6.

Even though coseismic groundwater level changes have been noted in several studies (STERNS, 1928; BRANCHARD and BYERLY, 1935; REXIN *et al.*, 1962; RATCLIFFE, 1972), and some of them recorded not only P waves but also PP, PPP, S, LQ, and LR1, we believe that our coseismic microtemperature changes are not caused by motion of the groundwater level. If the water level change governs the microtemperature change, the observed ratio of the coseismic signals, 4.5, should be equal to the observed ratio of the atmospheric pressure changes, 3.6, but it is not. Another explanation could be that microtemperature responses are frequency dependent.

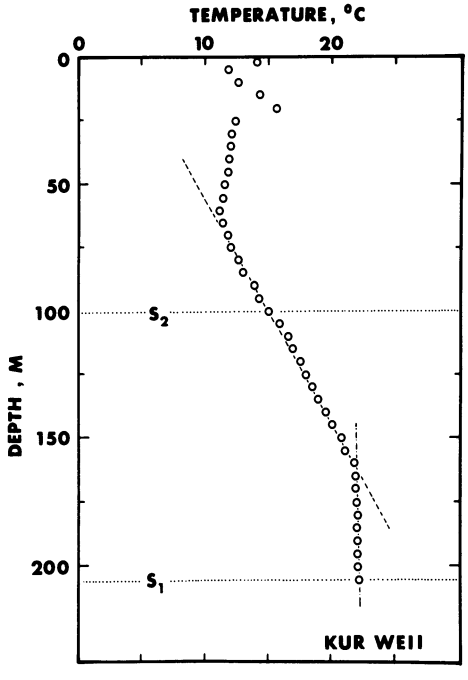

Figure 8

Temperature profile of the KUR well. Sensors KUR_{210} and KUR_{100} are deployed at depth S_1 and S_2, respectively. The temperature gradient is about 120 m°C/m at S_2 and about 10 m°C/m at S_1. The temperature between 0 and 25 m is variable according to the secular changes of the air temperature.

However, the periods of coseismic and atmospheric pressure signals are both several hours. The difference in the temperature change ratios therefore suggests that the mechanism generating coseismic signals is different from the mechanism generating atmospheric pressure signals. Adiabatic compression of either rocks or groundwater by the strain of earthquakes can cause a temperature increase. However, calculation has shown that the temperature change is far smaller than 1 m°C and thus cannot explain the observed temperature steps.

The thermometers have sensed some possible precursory signals from large earthquakes 200 km away. The distances were around 3–4 times typical fault lengths of magnitude 7 earthquakes, so it is not implausible for sensitive thermometers to sense signals from these earthquake sources. Unfortunately we have not yet observed signals from the earthquake fault located near the thermometers, because the region has been seismically inactive during the past several years. Our study has so far shown that a relatively small number of wells record coseismic and preseismic microtemperature signals.

It is very interesting that the ratio of precursory temperature changes for sensors at different depths is 1.5–1.6, much different than the ratio for coseismic signals. The difference is evidence that the mechanism of transmission of precursory signals may be different from that of main shocks. The succession of isolated pulses in the precursory signals may be related to a mechanical process which goes on before a large earthquake.

The interpretation of the microtemperature records is difficult because groundwater movements are uncertain. A horizontal groundwater flow may exist because of atmospheric pressure and seismic waves; the non-uniform geothermal gradient (Fig. 8) suggests that vertical permeability is probably high in this region. Sometimes the well itself acts as a short-circuit between aquifers, disturbing the observation of aquifers, but at KUR the observation well is completely cased by a steel pipe without any opening or screen from the ground surface to the well bottom. In order to improve the interpretation of the microtemperature record, measurements in the future should be made at several depths in a well together with *in-situ* strain and piezometric measurements.

The reason for the large differences in the microtemperature records from nearby observation wells is not understood. For example at TCY, which is near the extension of a seismic fault, the microtemperature is greatly affected by atmospheric pressure. Since TCY is a flowing well, its large microtemperature pressure coefficient seems to contradict previous hydrological studies where confined aquifers tend to show the largest barometric efficiency. On the other hand, coseismic signals recorded at TCY were much smaller than those recorded at KUR. The MEI well is also unusual. It is close to TCY and to the extension of the seismic fault, but does not have any response to atmospheric pressure or seismic signals.

The similarity of strainmeter records and microtemperature records, such as for Mikkabi or Omaezaki, has given us confidence in both kinds of measurements. To make a more direct comparison, another thermometer was installed in October 1981 in the Mikkabi well on top of the J.M.A. volumetric strainmeter. Six thermometers were

also installed in the borehole strainmeter wells in Iceland in September 1982. In three other strainmeter wells, two in the Tokai area, Ajiro and Higashiizu, and one on Hokkaido, KMU, the thermometers were installed in 1983 (Table 2).

8. *Conclusions*

The main aim of the microtemperature observations is to sense groundwater movements that may be related to crustal stress and earthquake generation. One advantage of microtemperature measurement is that it can sense the temperature through the steel well casing, thus allowing the use of existing wells.

The main results of the observations are:

(1) The microtemperature shows a strong response to atmospheric pressure; however, the barometric coefficient varies by 100 times or more. The thermometers can be expected to be sensitive enough to measure changes in crustal stresses related to earthquake generation.

(2) The groundwater microtemperature shows coseismic changes. However, the signals are quite different from well to well. The most clear coseismic signals were recorded by a well which is nearly on the 1938 earthquake fault. Wells having a high sensitivity to atmospheric pressure generally do not have coseismic sensitivity. The coseismic atmospheric pressure signals are not simply induced by alterations of groundwater level. Coseismic and atmospheric pressure signals probably come from different mechanisms.

(3) Distinctive signals seem to precede some earthquakes. They have similar pulse-like shapes and last a few days. Their shapes and amplitudes suggest a different causal mechanism than for coseismic signals.

(4) In some sites, the microtemperature records resemble strainmeter records in boreholes 2–15 km away. We have been installing more thermometers in wells with borehole strainmeters to study the effect more clearly.

Acknowledgments

The authors wish to thank Dr S. Hiraga for supplying a figure, Dr H. Wakita, Dr N. Fujii, Dr K. Notsu and Mr T. Urabe for fruitful discussions, and J.M.A. for supplying the strainmeter records.

References

BRANCHARD, F. G., and BYERLY, P. (1935), *Well gauges as seismographs*, Nature *135*, 303–304.

JOHNSON, A. G., KOVACH, R. L., and NUR, A. (1973), *Pore pressure changes during creep events on the San Andreas Fault*, Jour. Geophys. Res. *78*, 851–857.

LACHENBURCH, A. H. (1980), *Frictional heating, fluid pressure, and the resistance to fault motion*, J. Geophys. Res. *85*, 6097–6112.

NOTSU, K., ABIKO, T., and WAKITA, H. (1980), *Coseismic temperature changes of well water related to volcanic activities of Usu volcano*, Journal of Physics of the Earth *28*, 617–624.

RATCLIFFE, C. A. (1972), *A seismometer with a water well as a sensing element*, IEEE Transactions on Geoscience Electronics *GE10-2*, 92–95.

REXIN, E. E., OLIVER, J., and PRENTISS, D. (1962), *Seismically induced fluctuations of the water level in the Nunn-Bush well in Milwaukee*, Bull. Seism. Soc. America *52*, 17–25.

SACKS, I. S., and EVERTSON, D. W. (1970), *A sensitive borehole strain-rate meter*, Carnegie Institution Year Book *68*, 448–453.

SHIMAMURA, H. (1980), *Precision quartz thermometers for borehole observations*, Journal of Physics of the Earth *28*, 243–260.

SHIMAMURA, H., and WATANABE, H. (1981), *Coseismic changes in groundwater temperature of the Usu volcanic region*, Nature *291*, 137–138.

SHIMAMURA, H. (1983), *Ground-water microtemperature measurements, coseismic signals and atmospheric pressure effects*, Annales Geophysicae *1*, 235–238.

STERNS, H. T. (1928), *Record of earthquake made by automatic recorders on wells in California*, Bull. Seism. Soc. America *18*, 9–15.

TSUYA, H. (1938), *Report on Kusyaro earthquake which occurred on May 29, 1938*, Bull. Seism. Soc. Japan, *10*, 19–47 (in Japanese).

WEEKS, E. P. (1979), *Barometric fluctuations in wells tapping deep unconfined aquifers*, Water Resources Research, *15*, 1167–1176.

(Received 10th January 1984; revised 18th October 1984; accepted 29th November 1984)

PAGEOPH, Vol. 122 (1984/85) 0033-4553/85/060947-19$1.50 + 0.20/0

Pore Pressure Diffusion and the Mechanism of Reservoir-Induced Seismicity

By PRADEEP TALWANI and STEVE ACREE[1])

Abstract – The study of reservoir-induced seismicity offers a controlled setting to understand the physics of the earthquake process. Data from detailed investigations at reservoirs in South Carolina suggested that the mechanism of transmission of stress to hypocentral locations is by a process of diffusion of pore pressure (Pp). These results were compared with available worldwide data. The 'seismic' hydraulic diffusivity, α_s, was estimated from various seismological observations, and was found to be a good estimate of the material hydraulic diffusivity, α. Application of these results to a dedicated experiment to understand RIS at Monticello Reservoir, S.C., suggested that the diffusing Pp front plays a dual role in the triggering of seismicity. The spatial and temporal pattern of RIS can be explained by the mechanical effect of diffusion of Pp with a characteristic hydraulic diffusivity within an order of magnitude of 5×10^4 cm^2/s, corresponding to permeability values in the millidarcy range. The triggering of seismicity is due to the combined mechanical effect of Pp in reducing the strength and, possibly, the chemical effect in reducing the coefficient of friction between the clays in the pre-existing fractures and the rocks that enclose these fractures.

Key words: Mechanism, reservoir, induced seismicity.

1. Introduction

The incidence of reservoir-induced seismicity (RIS) is usually confined in both space and time, and it is now being routinely monitored on dense local networks. The seismic data so collected provide a controlled setting to study the mechanism of RIS in particular and the physics of the earthquake process in general. Until recently it was thought that RIS was triggered by the loading of a reservoir and/or by the effect of pore pressure (Pp) in lowering the strength of rocks at hypocentral depths. As case histories accumulated, Pp was considered to be the primary factor. It was assumed that the rocks are close to failure and small perturbations in the *in situ* stress field due to Pp changes trigger the observed RIS. It has been further assumed that the coefficient of friction μ is constant and lies between 0.6 and 0.85.

Pore water can play a two-fold role in the earthquake process, the first, a mechanical effect as pore pressure, and second, a chemical effect as stress-aided corrosion. There is evidence to suggest that pore water or pore pressure diffuses along pre-existing fractures, bedding planes, etc. (WITHERSPOON and GALE, 1977); or it can be associated with new crack propagation through stress corrosion (ANDERSON and GREW, 1977). We suggest that the mechanical effects of pore pressure control the spatial and temporal

[1]) Geology Department, University of South Carolina, Columbia, S.C. 29208

pattern of RIS, whereas the actual onset of seismicity may be influenced by the chemical effect of water in reducing the coefficient of friction in clays (filling pre-existing fractures). We shall be primarily concerned with the first effect, although we recognize that stress corrosion as it applies to hydration of clay minerals under increasing pore pressure is an important factor in RIS.

In the last ten years, we have monitored RIS at four locations in South Carolina, including, since its inception in October 1975 and December 1977, Lake Jocassee and Monticello Reservoir, respectively. The observation of a linear growth rate of epicentral area following impoundment at Lake Jocassee and other locations of RIS, suggested that the mechanism of transmission of the pressure front to hypocentral locations was by a process of pore pressure diffusion. We do not have any direct observation of a propagating pressure front. However, our conclusions are based on the inference that the onset and migration of RIS is associated with such a pressure front.

By monitoring the epicentral growth, and assuming it to be associated with the diffusion of pore pressure, we calculate a parameter, which we label 'seismic' hydraulic diffusivity, α_s. We then suggest that by making some simple yet reasonable assumptions, α_s can be estimated from a wide variety of RIS data.

We have examined the available published literature on RIS and wherever possible estimated the 'seismic' hydraulic diffusivity α_s. Considering the uncertainties in various published data the surprising result from observation of 22 case histories was the relatively narrow range of values estimated for α_s. Over 30 estimates of α_s were within one order of magnitude of 5×10^4 cm^2/s. We show that these estimates of 'seismic' hydraulic diffusivity (α_s) are within an order of magnitude of the material hydraulic diffusivity (α). The parameter α is not commonly used in hydrogeological literature. However, it is directly related to a more commonly used hydraulic property, permeability, k by the equation $\alpha = k/\mu\phi\beta$ where μ, ϕ and β are fluid viscosity, porosity of the rocks and compressibility of the fluid respectively. If μ, ϕ and β are known, then k can be estimated from α. Thus we have a simple, albeit an indirect method of estimating the *in situ* 'crustal' permeability. Even allowing for uncertainties in the estimation of α_s, and ϕ, we obtained a narrow range of 'crustal' permeabilities associated with RIS. These lie in the millidarcy range, in agreement with those inferred at this scale by BRACE (1984).

These ideas of diffusion of pore pressure, narrow range of hydraulic diffusivity, and inferred permeabilities were tested in an elaborate experiment at Monticello Reservoir, a site of ongoing RIS. Besides an in depth investigation of seismological, hydrological, and geological factors, two deep boreholes were drilled in the active hypocentral regions. Borehole investigations included the measurement of *in situ* stress, orientation and density of fractures, pore pressure, etc. (ZOBACK and HICKMAN, 1982; SEEBURGER and ZOBACK, 1982; MOOS and ZOBACK, 1983). A comparison with detailed fault plane solutions suggested that the seismicity was occurring on pre-existing fractures (TALWANI, 1981b). Thus for earthquakes to occur, the frictional resistance on a fracture has to be overcome. BYERLEE's (1978) laboratory data

indicated that at pressures corresponding to shallow crustal depths, $\tau = 0.85\ \sigma_n$, where τ and σ_n are the shearing and normal stress at which frictional resistance is overcome on a fracture. The significance of this result was that the coefficient of friction μ, was constant (=0.85) and independent of rock type or surface conditions. For higher pressures μ was found to be 0.6. This result was labelled Byerlee's law by BRACE and KOHLSTEDT (1980). MEISSNER and STREHLAU (1982) noted that Byerlee's data were based on relatively short time scales, low temperatures and obtained with small samples, and cautioned against extrapolation to crustal dimensions. In his paper, BYERLEE (1978) did note that the coefficient of friction was drastically reduced in the presence of clays.

In our analyses of the *in situ* stress data at Monticello Reservoir, we were led to the conclusion that to explain the observed RIS there, BYERLEE's law (1978) for friction between rock and rock may not be applicable and that the seismicity is probably associated with the effect of pore pressure on clays filling the pre-existing fractures.

These results have possible applications in regions where the growth of aftershock zones or the migration of seismicity is relatable to fluid flow.

2. *Background about theories of RIS*

GOUGH and GOUGH (1970) suggested that the observed increase in seismicity at Lake Kariba following its impoundment could have been triggered by loading or due to the effect of increased fluid pressure. They preferred the former mechanism. However, in the last decade there is a considerable body of data that very persuasively suggests that changes in the pore pressure are the main cause of the observed seismicity. HUBBERT and RUBEY (1959) showed that an increase in subsurface pore pressure reduces the effective normal stress on fault planes. These results were used by SNOW (1972) who showed that filling of a reservoir built on an infinite halfspace was conducive to RIS in strike slip and normal fault environments and inhibitive in a thrust fault environment. In all cases, however, the effect of increase in pore pressure was to decrease the effective strength of rocks leading them to failure. However, if the logic of Snow's arguments was followed, we should not expect RIS in areas of thrust faulting except by unloading of the reservoir. The work of HUBBERT and RUBEY (1959) and SNOW (1972) has been incorporated by GUPTA and RASTOGI (1976) in their book, *Dams and Earthquakes*, and will not be pursued further here. Snow's arguments were incorporated in a review paper by SIMPSON (1976) and by WITHERS (1977) and WITHERS and NYLAND (1978), who used consolidation theory to calculate the time history of stress below a freshly impounded reservoir. Making many simplifying assumptions, they concluded, as did SNOW (1972), that RIS was most likely in strike slip and normal fault regimes. In another theoretical study, BELL and

NUR (1978) showed that anisotropy in rock permeability and relative changes in ground-water played an important role in RIS.

The role of pore pressure diffusion as a mechanism of stress transmission was recognized over a decade ago (e.g. NUR and BOOKER, 1972; SCHOLZ *et al.*, 1973) and was used to explain the onset time of seismicity following injection in wells at Matsushiro (OHTAKE, 1974), Rangeley (RALEIGH *et al.*, 1976) and Dale (FLETCHER and SYKES, 1977). HOWELLS (1974) suggested that it could explain RIS, and TALWANI (1976) used the concept to account for the observed time lag between lake level rise and onset of seismicity at Clark Hill reservoir. Subsequently, TALWANI and RASTOGI (1978) and TALWANI (1981a) evaluated the then available worldwide data and suggested that pore pressure diffusion is the preferred mechanism for RIS. This conclusion was based on the observation of a linear growth of epicentral area with time at Lake Jocassee (TALWANI *et al.*, 1976). If we assume that an increase in epicentral area is directly caused by diffusion of pore pressure to hypocentral locations (with little change in depth), then 'seismic' hydraulic diffusivity can be estimated from the epicentral growth rate. It can also be estimated from other seismological parameters such as the time lag between the filling (or draining) of a reservoir and the onset of seismicity, and the time lag between the start (or cessation) of injection in a well and the onset (or cessation) of seismicity (OHTAKE, 1974; FLETCHER and SYKES, 1977; TALWANI and RASTOGI, 1978; TALWANI, 1981a). This method of calculation of 'seismic' hydraulic diffusivity is subject to various uncertainties. These include uncertainties in the location of 'ground zero' from where the pore pressure front originates. Assuming the transmission of pore pressure along fractures, the 'ground zero' would be on a line where those fracture(s) intersect the bottom of the reservoir. With the available data from the case histories this is seldom determinable. Therefore we plot the data as available, and note that the uncertainty in 'ground zero' location is proportional to the dimensions of the reservoir. The hypocentral locations for the earlier cases of RIS (accurate to a few km) are not known with the same accuracy as those with modern microearthquake networks (accurate to within a km). Another uncertainty lies in the difficulty in choosing the time of water level rise (or fall), (the onset of the pore pressure front). In calculating α_s we further assume that the pore pressure follows a straight line path.

In our calculations of α_s, we have estimated the uncertainties in hypocentral locations and in the calculation of the time lags. These are represented by error bars in the parameters L and t (see next section). If the pore pressure front does not follow a straight line path, but one twice as long, it will lead to an error of 0.4 of an order of magnitude in the estimate of α_s.

Owing to the various uncertainties discussed above, and the simplifying assumptions, this method is obviously an approximation, however, its main justification lies in the coherent results obtained. We show below that the hydraulic diffusivity obtained from seismological parameters (α_s) is a meaningful estimate of the material hydraulic diffusivity. This method of estimating α_s is now being increasingly used (e.g. KEITH *et al.*, 1982; ZOBACK and HICKMAN, 1982).

3. *Calculation of* α_s

After the first felt event in October 1975, the seismicity at Lake Jocassee has been monitored continually since November 1975. After a few felt events that occurred between 8 and 10 November 1975, the seismicity increased, with a M_L 3.2 event occurring on 25 November 1975. The epicentral region, which was initially in the vicinity of the dam, increased from November 1975 to February 1976, decreased in March and then increased again in April and May 1976, when it was the largest (Fig. 1). Subsequent activity in the next seven years has been confined, for the most part, to lie within the epicentral envelope defined by the seismicity in May 1976.

In Fig. 2, we note that the epicentral area growth for the period November 1975 to February 1976, is linear with time. The growth rate is about 40 km^2/100 days (or about 4.6×10^4 cm^2/s). The growth between March and May 1976 is again linear, the growth rate is now about 5.0×10^4 cm^2/s.

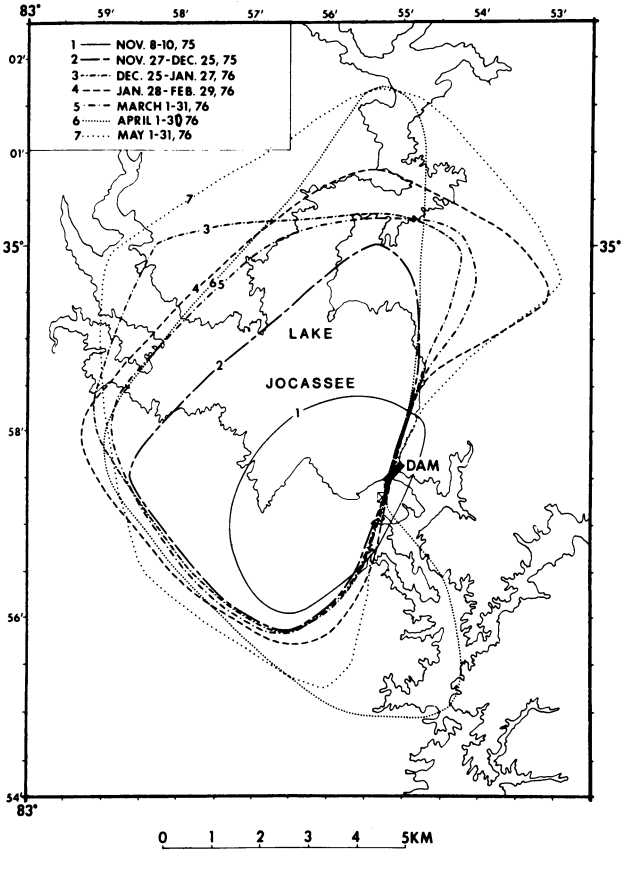

Figure 1

The epicentral growth of seismicity at Lake Jocassee in the first six months after its inception in November, 1975. Note the decrease in the epicentral area in March 1976 (curve 5) after the growth in the previous months.

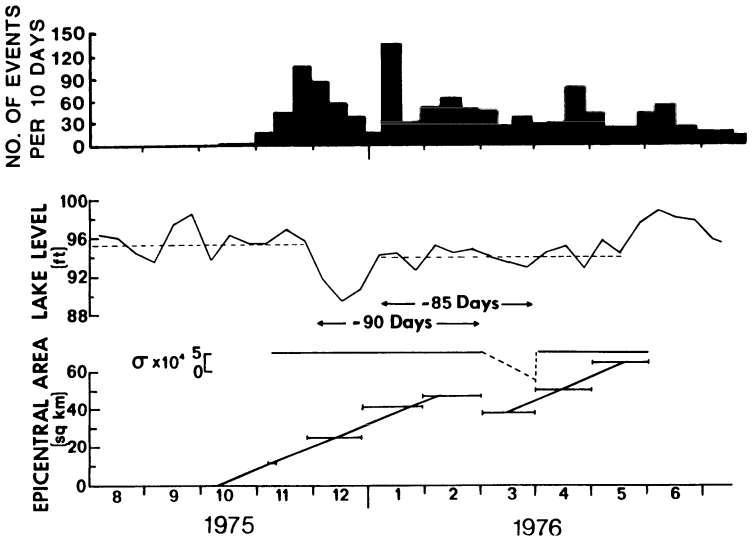

Figure 2
Epicentral growth at Lake Jocassee as a function of time compared with the lake level and the number of events per 10 day periods. The growth rate corresponds to a hydraulic diffusivity of 5×10^4 cm^2/s. The decrease in epicentral area in 3/76 is related to lake level decrease in 12/75 (top).

In Fig. 2 the epicentral growth was compared to the lake level (the ten day average of the 8 a.m. readings). Water level was suddenly lowered after the M_L 3.2 event on 25 November 1975, and raised again in January 1976. There appears to be a corroborative decrease in growth of the epicentral area about three months after the decrease in the lake level. This decrease in March 1976 was located on the periphery of the epicentral envelope, about 5 to 6 km away from the dam.

The linear growth rate of the epicentral area (Fig. 2) suggested a relationship of the kind $L^2 \sim t$, or that $L^2/t = \alpha_s$, a constant we call 'seismic' hydraulic diffusivity. Such dependence is expected from the diffusion equation describing flow of some kind. Thus, the observed linear growth rate of the epicentral area lends support to the diffusion mechanism as the transmitter of pore pressure.

To check this conclusion, we can calculate the time it will take to change the pore pressure at a distance of 5 to 6 km due to a change in the lake level (e.g. 12/75) for a hydraulic diffusivity of 5×10^4 cm^2/s. The required time is 58 to 83 days. For a hydraulic diffusivity of 4.6×10^4 cm^2/s, the corresponding delay is 64 to 93 days. These time periods agree well with the observed delays (Fig. 2).

There are very few examples where epicentral growth as a function of time due to RIS is well documented. However, there are several examples where the hypocentral distance from the location of impoundment, L, is known, and the time lag between impoundment, and the onset of seismicity, t, is also known. In such cases, assuming that the earthquakes have been caused by pore pressure diffusion, α_s, the 'seismic'

hydraulic diffusivity can be easily estimated ($=L^2/t$). For Monticello and Clark Hill reservoirs in South Carolina this method gave α_s values of the order of 10^4 cm^2(s.

Encouraged by these results, α_s was also estimated for cases of seismicity associated with the injection of fluids in boreholes and where the seismicity was known to have spread linearly along fault planes. The results of various methods used are presented below.

4. *Estimation of α_s from epicentral growth*

Besides Lake Jocassee, data on the initial growth of epicentral area of RIS were available at Koyna, India (GUHA *et al.*, 1974). Hsingfengkiang, China WANG *et al.*, 1976) and at Oroville, California (LESTER *et al.*, 1975).

The seismicity that followed the impoundment in 1962 of Shivaji Sagar Lake by Koyna Dam in the Peninsular shield of India is among the best known examples of RIS. Before impoundment no tremors had been reported for the region. Although seismicity was first felt in 1962, no epicentral data are available before 1964. The seismicity grew in space and magnitude until two significant events occurred in 1967. These were the magnitude 5 and 6.3 events that occurred on 13 September and 10 December respectively. The epicentral growth rate and hence α_s observed at Koyna were not uniform. For the period from 1962 to mid-July 1967, α_s was about 5×10^3 cm^2/s. However, following the 13 September event and before the 10 December main shock, the growth rate was higher, yielding $\alpha_s \doteq 9 \times 10^4$ cm^2/s $\pm 2 \times 10^4$ cm^2/s including uncertainties in L and t. The main event occurred on 10 December, and the pursuant growth rate for the first three months of 1968 was even higher, $\alpha_s \sim 2 \times 10^5$ cm^2/s. Thus it appears that the larger two events caused changes in the surrounding rocks that resulted in an increase in α_s. Such an increase would be associated with the formation of new fractures.

Such a noticeable change was not observed at Hsingfengkiang, China. There, after impounding the reservoir in October 1959, small shocks occurred concurrently, and the epicentral area grew and on 19 March 1962 a magnitude 6.1 earthquake occurred (WANG *et al.*, 1976). The epicentral growth for this ~2.5 year period implied $\alpha_s \sim 5 \times 10^4$ cm^2/s $\pm 1 \times 10^4$ cm^2/s. The epicentral region continued to grow and for the remaining part of the year α_s was $\sim 6 \times 10^4$ cm^2/s $\pm 1 \times 10^4$ cm^2/s.

The results of aftershock studies immediately following the M_L 5.7 Oroville, CA earthquake of 1 August 1975 were presented by LESTER *et al.* (1975). The rapid epicentral growth rate in the first week was followed by a slower growth rate in the following months, with the corresponding values of α_s, $5.7 \times 10^{\times}$ and 3.8×10^4 cm^2/s, respectively. SAVAGE *et al.* (1976) also carried out an aftershock survey in the month following the main shock. α_s calculated from their data also shows a similar decrease, decreasing from 5.1×10^5 cm^2/s to 3.2×10^4 cm^2/s.

In summary, the 'seismic' hydraulic diffusivities calculated from an estimate of

epicentral growth rate, α_s, range from 5×10^3 to 6×10^5 cm^2/s, with most values clustering around 5×10^4 cm^2/s. The larger values ($\sim 10^5$ cm^2/s) were obtained immediately after the main shock and are probably associated with increased fracturing following the main shock, and the lower values ($\sim 10^4$ cm^2/s) are more representative of the hypocentral region.

5. *Estimation of α_s from time lag between change in lake level and onset of seismicity*

A careful perusal of various listed cases of RIS reveals that there is always a time lag between filling (or draining) of a reservoir and the onset of seismicity. In most cases, however, adequate epicentral data are not available. If we make the assumption that the diffusion of pore pressure is the operative mechanism of transmitting pore pressure changes to hypocentral depths, it is possible to estimate α_s from the observed time lag. WITHERSPOON and GALE (1977) have shown that water flow in fractured rocks occurs principally through joints, faults and other planar features. Here we assume that due to the generally observed anisotropy in rocks, diffusion is also restricted to the plane of the fault or fracture. With these assumptions the rate of diffusion of the pore pressure front which is associated with seismicity can be estimated directly. The hydraulic diffusivity is obtained from the distance L, between the source of the pressure front (the reservoir) and the location of seismicity, and from the delay t, between generating this front (filling or draining the reservoir) and the onset of seismicity, by the simple relation, $\alpha_s = L^2/t$. This method is simple and generates reasonable values, as illustrated by the following examples.

Figures 3 and 4 show the location of epicenters for the period 12/77–3/78 and cumulative number of earthquakes following the impoundment of Monticello Reservoir in December 1977. Fault plane solutions indicate that the seismicity is occurring in a thrust fault environment. In such an environment the filling of a reservoir is associated with two effects. The increased load of water inhibits seismicity, whereas the delayed effect of pore pressure favors it. Thus observed seismicity is primarily due to changes in pore pressure. We note that there is a lag of about three weeks between the start of filling and the start of seismicity. After completion of filling, in early February 1978, the increasing inhibiting effect of loading stopped, and there was a marked increase in the seismicity for about three weeks, after which a steady increase was noted. This three week lag was associated with the diffusion of pore pressure to hypocentral locations at depths of 1 to 2 km. By the method outlined above, the corresponding values of α_s are 5.5×10^3 cm^2/s $\pm$ 0.4×10^3 cm^2/s and 2.2×10^4 cm^2/s $\pm$ 0.2×10^4 cm^2/s.

Similar estimates were made for all the reservoirs where adequate data were available. (The details are being published elsewhere.) Forty-two such values were obtained and they ranged between 5×10^3 and 5×10^5 cm^2/s (Fig. 5). This result is in good agreement with the values obtained from the growth rate of epicentral area.

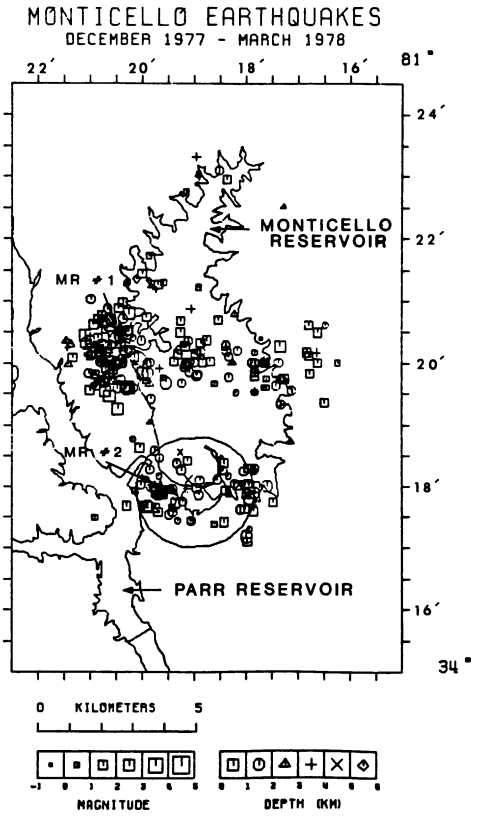

Figure 3
Spatial distribution of seismicity at Monticello Reservoir, from its inception in the last week of December 1977 through March 1978. MR nos 1 and 2 show the locations of the two 1 km deep wells.

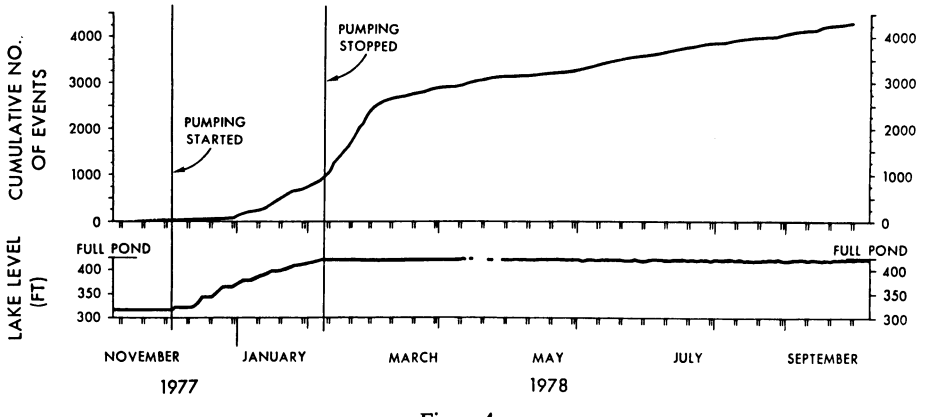

Figure 4
Cumulative seismicity at Monticello Reservoir (top) compared with the lake level. The reservoir was filled by pumping from the lower Parr Reservoir.

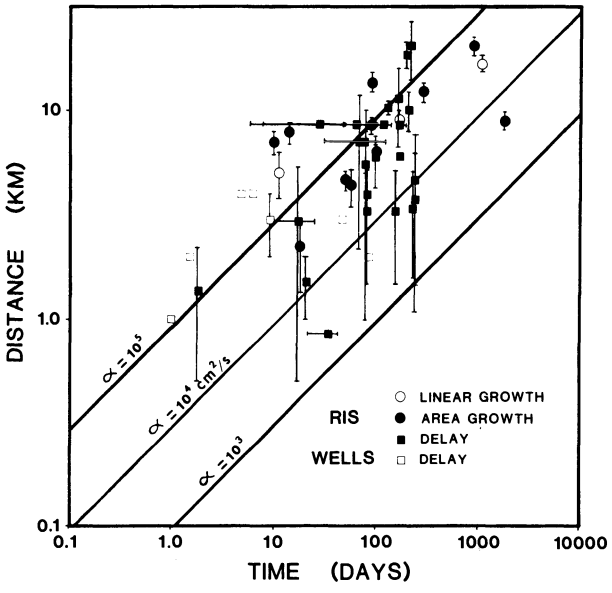

Figure 5
Hydraulic diffusivity associated with RIS calculated by different methods. Uncertainties in the calculation of time lags and hypocentral distances are represented by error bars.

6. *Estimate of α_s from linear growth of seismicity*

In some cases a more or less linear epicentral growth is observed, indicating earthquake migration along a fault. If this pattern is associated with the reservoir at one end, α_s can be estimated in a manner similar to that described in the previous section. Here if L is the distance that the earthquake front has propagated, in time t, the 'seismic' hydraulic diffusivity, is as before, $\alpha_s = L^2/t$. Such an epicentral spreading was observed at Kariba, S. Rhodesia, now Zimbabwe (GUPTA and RASTOGI, 1976), and at Nurek, in Tadjikistan, Russia (SOBOLEVA and MAMADALIEV, 1976; SIMPSON and NEGMATULLAEV, 1981). The calculated values of α_s were $5.3 \times 10^4 \pm 0.8 \times 10^4$ and $2.9 \times 10^4 \pm 0.5 \times 10^4$ cm^2/s, respectively.

7. *α_s from time lag between fluid injection in deep wells and onset of seismicity*

There are many known cases of seismicity associated with the injection of fluids in deep wells (HEALY *et al.*, 1968; OHTAKE, 1974; FLETCHER and SYKES, 1977; RALEIGH *et al.*, 1976). In such cases again we make similar assumptions about the time lag and distance of seismicity from the well to hypocentral locations. In these cases, both the t and L are known very accurately.

For example, seismicity was found to be located about 4 km from the bottom of the 1800 m deep cased well at Matsushiro, Japan (OHTAKE, 1974). Spurts of seismicity were correlatable with sudden increases in fluid pressure and followed them by 9.3, 6.2 and 4.8 days. The seismicity was in the vicinity of the Matsushiro fault – the location of a large swarm of seismicity about 4 to 5 years earlier. The calculated values of α_s ($\sim 10^5$ cm^2/s) are high and possibly reflect the fractured state of the hypocentral region after the Matsushiro swarm.

Similar estimates of α_s were obtained from other cases of induced seismicity associated with the injection of fluids in a well (or between cessation of injection and associated cessation of seismicity) at Dale, N.Y. (FLETCHER and SYKES, 1977); Denver arsenal well (HEALY *et al.*, 1968); and the Rangeley, Colorado well (RALEIGH *et al.*, 1976). The calculated value of α_s in all cases ranged between 5×10^3 and 4×10^5 cm^2/s.

In summary, α_s, the 'seismic' hydraulic diffusivity calculated from seismological data – for all cases of RIS where usable data were available, was found to be within one order of magnitude of 5×10^4 cm^2/s. We examine the significance of this result in the following section.

8. α_s *and the material diffusivity*

To a first approximation, for one-dimensional diffusion of pore pressure p,

$$(\partial^2 p/\partial z^2) = (1/\alpha)(\partial p/\partial t) \tag{1}$$

where z is distance, t the time and α is the diffusivity of the material in which diffusion occurs. This equation has a solution of the form

$$(p(z,t)/p_0) = 1 - \mathrm{erf}(z/2\sqrt{\alpha t}) \tag{2}$$

where p_0 is the pore pressure applied at $z = 0$, $t = 0$, and maintained for $t > 0$; and $p(z,t)$ is the pore pressure at distance z after time t. The behavior of the solution (equation 2) is illustrated in Fig. 6 for $\alpha = 10^4$ cm^2/s. We label M the ratio $p(z,t)/p_0$ on the left-hand side of equation (2). It is the ratio of the diffused pore pressure at depth z after time t to the applied pore pressure, p_0.

Now in the case of RIS, the activity is triggered by the perturbation in the ambient pore pressure at the hypocenter due to the diffusing pore pressure front. The seismicity occurs at some threshold, i.e., some value of $p(z,t)$; hence at a particular value of M. For example, if the applied pore pressure p_0 is 10 bars and the stress field conditions are such that seismicity is triggered at a depth of 2 km when the perturbing pore pressure is 5 bars, then, $p(2,t) = 5$ bars, $M = 0.5$ and from Fig. 6, $t = 50$ days.

However, *a priori*, we do not know the particular value of M at which an earthquake is triggered, so that the diffusivity that will be estimated from seismic data,

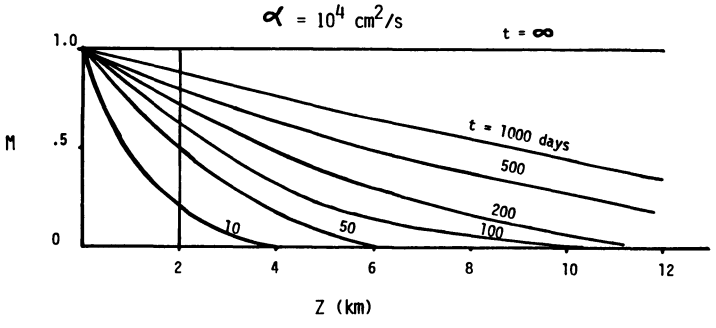

Figure 6
Variation of ratio M for hydraulic diffusivity of 10^4 cm^2/s plotted as a function of time and distance.

α_s ($L = 2$ km, $t = 50$ days, $\alpha_s = 9.3 \times 10^3$ cm^2/s) will not equal the material diffusivity, α ($= 10^4$ cm^2/s). Suppose that the earthquake had been triggered at $M = 0.2$ or 0.61, at the same depth (2 km), the corresponding times are 10 and 100 days, and estimated values of α_s are 4.6×10^4 and 4.6×10^3 cm^2/s respectively.

Clearly any *calculated* value of hydraulic activity from seismic data will depend on M. Recall, $M = p(z,t)/p_0$ is some fraction of the applied pore pressure perturbation p_0, and the value of M at which seismicity is triggered is dependent on the ambient stress conditions. So the question arises, is the hydraulic diffusivity calculated from seismic data at all meaningful? To answer that, rewrite equation (2).

$$M = p(z,t)/p_0 = 1 - \mathrm{erf}(z/2\sqrt{\alpha t})$$
$$= 1 - \mathrm{erf}(z^2/4\alpha t)^{1/2}$$

Now, z^2/t is the 'seismic' hydraulic diffusivity, α_s, and α is the material diffusivity; then

$$M = 1 - \mathrm{erf}(\alpha_s/4\alpha)^{1/2} \quad \text{or} \quad \alpha_s/\alpha = 4[\mathrm{erf}^{-1}(1 - M)]^2 \tag{3}$$

Figure 7 shows the variation of α_s/α, the ratio of the 'seismic' hydraulic diffusivity to the 'true' material diffusivity, for different values of M. We note that for extreme values of M (0.9 and 0.03), α_s is 0.1α and 10α respectively. Thus the estimated 'seismic' hydraulic diffusivity α_s, is within an order of magnitude of the 'true' material diffusivity α.

9. *Permeability and hydraulic diffusivity*

The hydraulic diffusivity, α, is related to the permeability of a medium, k, by the relation (BODVARSSON, 1970; TALWANI, 1981a)

$$\alpha = k/\{\mu[\phi\beta_f + (1 - \phi)\beta_r]\} \tag{4}$$

where μ, ϕ, β_f and β_r are fluid viscosity, porosity of the rocks, and the compressibilities of fluid and rock respectively. If diffusion is in the fluid filled fractures, equation (4)

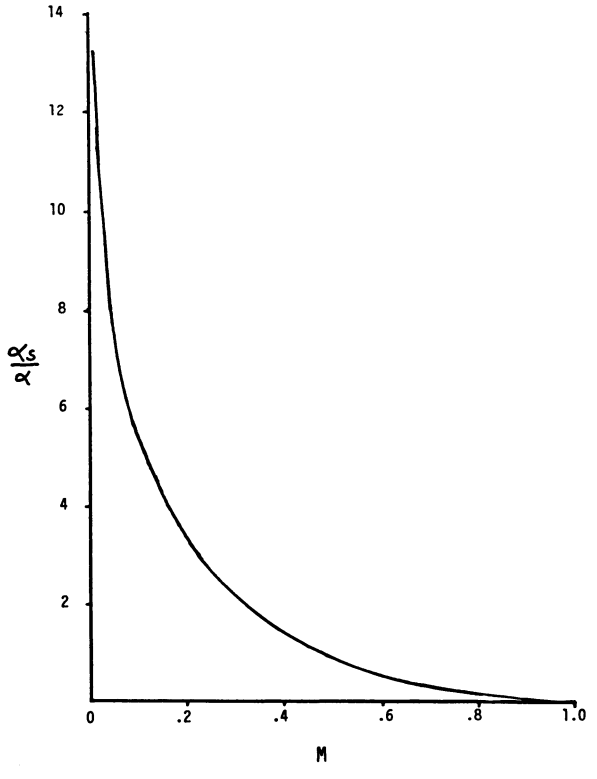

Figure 7
Relation between 'seismic' and 'material' diffusivity as a function of M.

can be simplified (see e.g., SCHOLZ *et al.*, 1973 or BRACE, 1980), to $\alpha = k/(\mu\phi\beta_f)$. If we assume typical values of these parameters,

μ = viscosity of water = 10^{-2} poise = 10^{-8} bar sec.

ϕ = porosity of fractured rock = 10^{-2} to 10^{-3}, say 3×10^{-3} (BRACE, 1980, 1984)

β_f = effective compressibility of fluid = 3×10^{-5} bar^{-1}

then, $\alpha \sim 10^4$ to 10^5 cm^2/s implies a permeability value of 10^{-11} to 10^{-10} cm^2 or 1–10 millidarcies. If we allow for two orders of magnitude uncertainty in α_s due to uncertainties in parameters or our incomplete knowledge of the stress field conditions at hypocentral location, the range of α becomes 10^3–10^6 cm^2/s (clearly bracketing all our data – Fig. 5). Further allowing for an order of magnitude uncertainty in our estimate of the porosity of the fractured rocks, these values imply a maximal range of 10^{-13} to 10^{-9} cm^2 (0.01 to 100 md). Our data (Fig. 5) however suggest a narrower range, 10^{-12} to 10^{-10} cm^2 (0.1 to 10 md) as being more representative of the true range of permeabilities in crustal rocks. These values are in general agreement with those given by BRACE (1984), who noted that for crustal phenomena, estimates made *in situ* on a kilometer scale may be the most meaningful. These values are of the

same order as those for the more permeable intervals in boreholes, where the values range from 10^{-9} to 10^{-15} cm^2 (BRACE, 1984).

Thus, although the permeability of rocks encountered in nature varies from the nanodarcy to the darcy range (10^{-17} to 10^{-8} cm^2) (BRACE, 1984), RIS is usually associated with rocks having a permeability in the millidarcy range (0.1 to 10 md or 10^{-12} to 10^{-10} cm^2).

10. Application to RIS at Monticello Reservoir

As we have shown above, the process of pore pressure diffusion adequately accounts for the *time lag* between the impoundment of a reservoir (or lake level fluctuations) and the onset of seismicity. The working model (SNOW, 1972; SIMPSON, 1976; TALWANI, 1976; WITHERS and NYLAND, 1978) has been that the stress field is very close to critical and small increases in the pore pressure decrease the effective normal stress sufficiently to drive the rocks to failure. Different workers have assumed different levels of cohesive strength ranging from laboratory values to assumed zero cohesion for pre-existing fractures.

The first test of these models was provided by the experiment at Monticello Reservoir (ZOBACK and HICKMAN, 1982). *In situ* stresses, pore pressure and permeability values were obtained in two boreholes. In explaining the seismicity, Zoback and Hickman assumed the coefficient of friction μ to be 0.6 to 0.8, and cohesion to be zero. The value of μ was based on the work of BYERLEE (1978).

On examining cores collected in the two boreholes, three different groups of fractures were encountered. One set was subhorizontal open fractures – along exfoliation joints. The other set consisted of steeply dipping fractures filled with fluorides, pink zeolites and carbonates. In other cores, the material filling the fractures was mixed illite and smectites, including montmorillonite. These deposits were similar to others in the region resulting from hydrothermal action of hot water.

The presence of the expandable clays (montmorillonite, etc.) has also been noted in fault zones. CHU *et al.* (1981) note that the clay composition in the fault gouge between the depths of 300 and 1000 feet from the San Andreas fault zone is fairly uniform. The predominant components are montmorillonite (40%), kaolinite (40%) and 10% each of illite and chlorite (LIECHTI and ZOBACK, 1979). X-ray diffraction of a clay sample from Monticello Reservoir revealed the presence of montmorillonite clay. We do not know how widespread is the presence of montmorillonite and other expandable clays. WU *et al.* (1979) note that clay minerals have been encountered in fault zones to depths of 2 km, whereas WANG *et al.* (1978) suggest that clay rich fault gouge may exist down to 10 km on the San Andreas fault.

In old metamorphic terranes like the South Carolina Piedmont, where there is evidence of large scale hydrothermal activity, it is not unreasonable to expect that clays may be present in fractures at observed hypocentral depths.

There has been a series of excellent papers describing the frictional and other properties of materials in simulated or real fault gouge. See, for example, ENGELDER *et al.* (1975), SUMMERS and BYERLEE (1977), WANG and MAO (1979), CHU *et al.* (1981), MORROW *et al.* (1982), among others. Two U.S.G.S. Conference Reports on Experimental Studies on Rock Friction (EVERNDEN, 1977) and Analysis of Actual Fault Zones in Bedrock (EVERNDEN, 1979) also contain relevant data.

For rock on rock, BYERLEE (1978) showed for a wide range of rocks and at a wide range of stress conditions, that at normal stress (σ_n) above 2 kb shear stress (τ) required to activate rock on rock sliding is given by $\tau = 0.5 + 0.6\ \sigma_n$, and for normal stress below 2 kb, $\tau = 0.85\ \sigma_n$. The coefficient of friction (μ) being constant (0.6 to 0.85) for large varieties of materials led this relationship to be referred to as Byerlee's law (BRACE and KOHLSTEDT, 1980). However, for fault gouge and other clays, μ was found to be 0.4 to 0.2, and decreased to 0.2 and below when the clays were saturated (WANG and MAO, 1979). Increasing pore pressure may further reduce the coefficient of friction in montmorillonite (BIRD, 1984). Similar results were obtained by MORROW *et al.* (1982). This decrease in μ is due to the hydration of the clay minerals.

These observations suggested a possible explanation for the observed seismicity near Monticello Reservoir. From a detailed analysis of fault plane solutions occurring in various earthquake clusters near the Monticello Reservoir and a comparison with *in situ* fractures encountered in the boreholes, TALWANI (1981b) demonstrated that the seismicity is occurring along pre-existing fractures.

In Fig. 8, we have plotted in Mohr circle configuration the measured stresses at a depth of 312 m in deep well no. 2 and at a depth of 961 m in deep well no. 1.

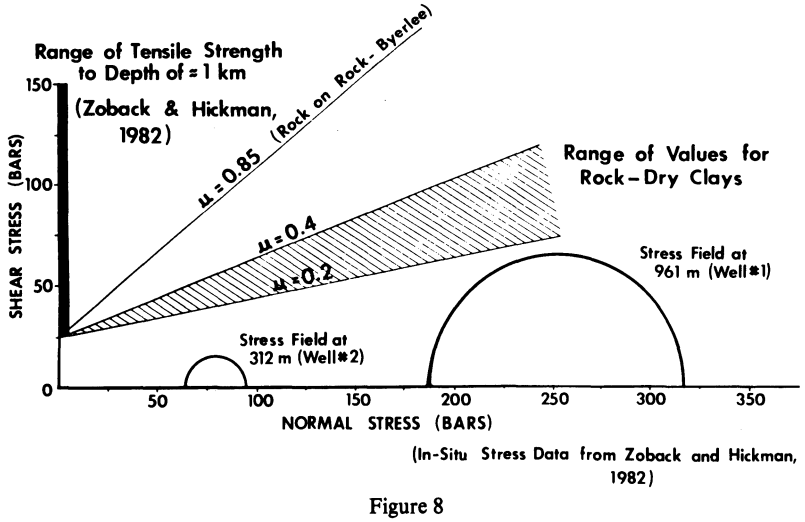

Figure 8

In situ stress data for Monticello Reservoir compared with failure envelopes for different coefficients of friction. Tensile strengths are those observed in well no. 2 and decrease to zero for pre-existing fractures.

The tensile strength measured by ZOBACK and HICKMAN (1982) ranges from 26 bars to 152 bars and has been indicated. Failure envelopes corresponding to $\mu = 0.85$ (Byerlee's value for these stress levels) and $\mu = 0.2$ and 0.4 (μ for dry clays) are also indicated for a tensile strength of 25 bars (corresponding to the lowest observed value). We note that the failure envelope lies over the stress values. Small changes in pore pressure (say by 10 bars) will shift the Mohr circles to the left, but not account for the observed seismicity, if we assume a coefficient of friction according to Byerlee's law.

We suggest that what in fact changes is the coefficient of friction. As the lake is impounded, pore pressure diffusion occurs, increasing pore pressure in the fractures. If the fractures were initially dry, then WANG and MAO's (1979) laboratory data suggest that there is a reduction in μ to 0.2–0.1 for pure clays. The experimental results of MORROW *et al.* (1982) confirm a similar trend at a variety of confining pressures with mixed clay fault gouge. This is accompanied by a reduction in the cohesive strength. If the rock was already saturated, there is still a reduction in the strength and μ with increasing pore pressure (BIRD, 1984). The failure envelope will now approach the Mohr circle and lead to earthquakes.

Following development by BRACE and KOHLSTEDT (1980), ZOBACK and HICKMAN (1982) examined their *in situ* stress data at Monticello deep wells 1 and 2 in an attempt to explain the observed RIS. By assuming a coefficient of friction ranging between 0.6 and 0.8, they concluded that the observed (thrust fault) seismicity should be concentrated at depths to 500 m only. However, well constrained hypocentral depths extend to at least 2 km. In view of the discussion in the previous paragraph, we suggest that the actual coefficient of friction lies in the range 0.2 to 0.4 instead of between 0.6 and 0.8 as predicted by Byerlee's law.

In Fig. 9 we compare the *in situ* stress data of ZOBACK and HICKMAN (1982) with the range of $S_{h\max}$ where seismicity would occur if the coefficient of friction lay in the range 0.2 to 0.4. These stress measurements were taken in July 1978 at Monticello deep well 1 and in January 1979 and August 1980 at Monticello deep well 2, some 7 to 32 months after the onset of induced seismicity at the reservoir. Earthquakes occurring in the vicinity of the wells would have already produced localized stress drops of up to 100 bars as estimated by ZOBACK and HICKMAN (1982). These data, therefore, may reflect the released stress state in these areas. We note that now the *in situ* stress data with the assumption of lower coefficients of friction are compatible with the observed hypocentral depths.

11. Conclusions

It is now generally accepted that changes in pore pressure are the primary causes of observed RIS. In this paper we suggest that the mechanism by which changes in pore pressure are transmitted to hypocentral depths is by diffusion. Analyses of available RIS data further suggest that there is a characteristic range of 'seismic' hydraulic diffusivity (10^3–10^5 cm^2/s) and permeability (0.1–10 millidarcy)

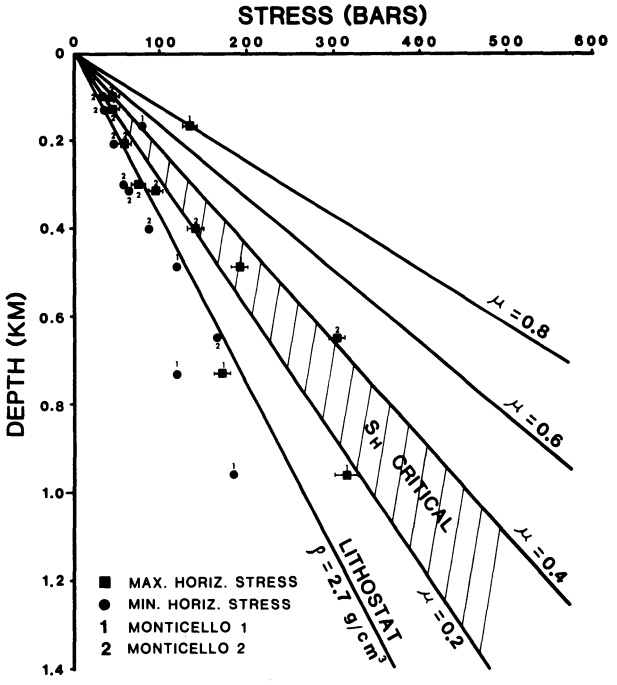

Figure 9

Hydraulic fracturing stress measurements at Monticello Reservoir deep wells 1 and 2 as a function of depth. The area labelled S_H critical indicates the magnitude of maximum horizontal stress expected to result in reverse faulting along appropriately oriented fault planes assuming a coefficient of friction between 0.2 and 0.4. Stress data from ZOBACK and HICKMAN (1982).

values. Field data at Monticello Reservoir also indicate that the diffusing pore pressure plays a dual role in triggering seismicity, one by decreasing the coefficient of friction between the clays in the pre-existing fractures and the rocks that enclose these fractures, and two by decreasing the strength.

These results have a possible application in our understanding the physics controlling the growth of aftershock zones of tectonic earthquakes.

Acknowledgments

This work emerged from observations of RIS in South Carolina funded by US Geological Survey Contracts 14-08-001-14553, 17670, 19252 and 21229. We also thank former students who helped in collecting the seismic data that led to the development of the ideas in this paper – Don Stevenson, David Amick and Kevin Hutchenson. Pradeep Talwani also acknowledges helpful discussions with Professors Dickerson, Benedict and Aswani of the College of Engineering at the University of South Carolina and B. K. Rastogi of National Geophysical Research Institute, Hyderabad, India. We also thank Mr Bhatnagar and Mr Gladden of Duke Power

Company – owners of Jocassee Dam, and Mr Whorton of South Carolina Electric and Gas Company – owners of Monticello Resevoir, for their unfailing cooperation.

REFERENCES

ANDERSON, O. L., and GREW, P. C. (1977), *Stress Corrosion Theory of Crack Propagation with Application to Geophysics*, Rev. Geophys. Space Phys. *15*, 77–104.

BELL, M. L., and NUR, A. (1978), *Strength Changes due to Reservoir-induced Pore Pressure and Stresses and Application to Lake Oroville*, J. geophys. Res. *83*, 4469–4483.

BIRD, P. (1984), *Hydration-phase Diagrams and Friction of Montmorillonite under Laboratory and Geologic Conditions, wit[h] Implications for Shale Compaction, Slope Stability, and Strength of Fault Gouge*, Tectonophysics *107*, 235–260.

BODVARSSON, G. (1970), *Confined Fluids as Strain Meters*, J. geophys. Res. *75*, 2711–2718.

BRACE, W. F. (1980), *Permeability of Crystalline and Argillaceous Rocks*, Int. J. Rock Mech. Min. Sci. and Geomech. Abstract *17*, 241–251.

BRACE, W. F. (1984), *Permeability of Crystalline Rocks: New in situ Measurements*, J. geophys. Res. *89*, 4327–4330.

BRACE, W. F., and KOHLSTEDT, D. L. (1980), *Limits on Lithospheric Stress Imposed by Laboratory Experiments*, J. geophys. Res. *85*, 6248–6252.

BYERLEE, J. W. (1978), *Friction of Rocks*, Pure appl. Geophys. *116*, 615–626.

CHU, C. L., WANG, C. Y., and LIN, W. (1981), *Permeability and Frictional Properties of San Andreas Fault Gouges*, Geophys. Res. Lett. *8*, 565–568.

ENGELDER, J. T., LOGAN, J. M., and HANDIN, J. (1975), *The Sliding Characteristics of Sandstone on Quartz Fault-gouge*, Pure appl. Geophys. *113*, 69–86.

EVERNDEN, J. F., ed. (1977), *Proceedings of Conference II: Experimental Studies of Rock Friction with Application to Earthquake Prediction*, U.S.G.S., 701 pp.

EVERNDEN, J. F., ed. (1979), *Proceedings of Conference VIII: Analysis of Actual Fault Zones in Bedrock*, U.S.G.S Open File Report 79-1239, 595 pp.

FLETCHER, J. B., and SYKES, L. R. (1977), *Earthquakes Related to Hydraulic Mining and Natural Seismic Activity in Western New York State*, J. geophys. Res. *82*, 3767–3780.

GOUGH, D. I., and GOUGH, W. I. (1970), *Load-induced Earthquakes at Lake Kariba – II*, Geophys. J. Roy. astr. Soc. *21*, 79–101.

GUHA, S. K., GOSAVI, P. D., NAND, K., PADALE, J. G., and MARWADI, S. C. (1974), *Koyna Earthquakes (October, 1963 to December, 1973)*, Report of the Central Water and Power Research Station, Poona, India, 340 pp.

GUPTA, H. K., and RASTOGI, B. K., *Dams and Earthquakes* (Elsevier Scientific Publishing Co., Amsterdam 1976).

HEALY, J. H., RUBEY, W. W., GRIGGS, D. T., and RALEIGH, C. B. (1968), *The Denver Earthquakes*, Science, N.Y. *161*, 1301–1310.

HOWELLS, D. A. (1974), *The Time for a Significant Change of Pore Pressure*, Eng. Geol. *8*, 135–138.

HUBBERT, M. K., and RUBEY, W. W. (1959), *Role of Fluid Pressure in Mechanics of Overthrust Faulting, I*, Bull. geol. Soc. Am. *70*, 115–166.

KEITH, C. M., SIMPSON, D. W., and SOBOLEVA, O. V. (1982), *Induced Seismicity and Style of Deformation at Nurek Reservoir, Tadjik SSR*, J. geophys. Res. *87*, 4609–4624.

LESTER, F. W., BUFE, C. G., LAHR, K. M., and STEWART, S. W. (1975), *Aftershocks of the Oroville Earthquake of August 1, 1975*, Calif. Div. of Mines and Geol., Sp. Report 124 (eds. R. W. Sherburne and C. J. Hauge), 131–138.

LIECHTI, R., and ZOBACK, M. (1979), *Preliminary Analysis of Clay Gouge from a Well in the San Andreas Fault Zone in Central California.* Proc. Conf. VIII: Analysis of Actual Fault Zones in Bedrock (ed. J. F. Evernden), U.S.G.S. Open File Report 79-1239, 268–275.

MEISSNER, R., and STREHLAU, J. (1982), *Limits of Stresses in Continental Crusts and their Relation to the Depth-frequency Distribution of Shallow Earthquakes*, Tectonics *1*, 73–89.

MOOS, D., and ZOBACK, M. D. (1983), *In situ Studies of Velocity in Fractured Crystalline Rocks*, J. geophys. Res. *88*, 2345–2358.

MORROW, C. A., SHI, L. Q., and BYERLEE, J. D. (1982), *Strain Hardening and Strength of Clay-rich Fault Gouges*, J. geophys. Res. *87*, 6771–6780.

NUR, A., and BOOKER, J. R. (1972), *Aftershocks Caused by Pore Fluid Flow?*, Science, N.Y. *175*, 885–887.

OHTAKE, M. (1974), *Seismic Activity Induced by Water Injection at Matsushiro, Japan*, J. Phys. Earth *22*, 163–174.

RALEIGH, C. B., HEALY, J. H., and BREDEHOEFT, J. D. (1976), *An Experiment in Earthquake Control at Rangely, Colorado*, Science, N.Y. *191*, 1230–1237.

SAVAGE, W. U., TOCHER, D., and BIRKHAHN, P. C. (1976), *A Study of Small Aftershocks of the Oroville, California, Earthquake Sequence of August 1975*, Eng. Geol. *10*, 371–385.

SCHOLZ, C. H., SYKES, L. R., and AGGARWAL, Y. P. (1973), *Earthquake Prediction: A Physical Basis*, Science, N.Y. *181*, 803–810.

SEEBURGER, D., and ZOBACK, M. D. (1982), *The Distribution of Natural Fractures and Joints at Depth in Crystalline Rock*, J. geophys. Res. *87*, 5517–5534.

SIMPSON, D. W. (1976), *Seismicity Changes Associated with Reservoir Loading*, Eng. Geol. *10*, 123–150.

SIMPSON, D. W., and NEGMATULLAEV, S. K. (1981), *Induced Seismicity at Nurek Reservoir, Tadjikistan, USSR*, Bull. seis. Soc. Am. *71*, 1561–1586.

SNOW, D. T. (1972), *Geodynamics of Seismic Reservoirs*, in Proc. Symp. Flow Fractured Rock, German Soc. Soil. Rock Mech., Stuttgart, T2-J, 19 pp.

SOBOLEVA, O. V., and MAMADALIEV, U. A. (1976), *The Influence of the Nurek Reservoir on Local Earthquake Activity*, Eng. Geol. *10*, 293–305.

SUMMERS, R., and BYERLEE, J. (1977), *A Note on the Effect of Fault Gouge Composition on the Stability of Frictional Sliding*, Int. J. Rock Mech. Min. Sci. and Geomech., Abstract 14, 155–160.

TALWANI, P. (1976), *Earthquakes Associated with the Clark Hill Reservoir, South Carolina – A Case of Induced Seismicity*, Eng. Geol. *10*, 239–253.

TALWANI, P. (1981a), *Hydraulic Diffusivity and Reservoir Induced Seismicity*, final technical report, U.S.G.S., Reston, Va., 48 pp.

TALWANI, P. (1981b), *Association of Induced Seismicity with Pre-existing Fractures at Monticello Reservoir, South Carolina*, Earthquake Notes *52*, no. 1, 28–29.

TALWANI, P., and RASTOGI, B. K. (1978), *Mechanism for Reservoir Induced Seismicity*, Earthquake Notes *49*, no. 4, 59.

TALWANI, P., STEVENSON, D., CHIANG, J., and AMICK, D. (1976), *The Jocassee Earthquakes – A Preliminary Report*, third technical report, U.S.G.S., Reston, Va., 92 pp + Appendix 1–35.

WANG, C. Y., and MAO, N. (1979), *Shearing of Saturated Clays in Rock Joints at High Confining Pressures*, Geophys. Res. Lett. *6*, 825–828.

WANG, C. Y., LIN, W., and WU, F. T. (1978), *Constitution of the San Andreas Fault Zone at Depth*, Geophys. Res. Lett. *5*, 741–744.

WANG, M. Y., YAG, M.-Y., HU, Y.-L., LI, T.-C., CHEN, Y.-T., CHIN, Y., and FENG, J. (1976), *Mechanism of the Reservoir Impounding Earthquakes at Hsingfengkiang and a Preliminary Endeavour to Discuss their Cause*, Eng. Geol. *10*, 331–351.

WITHERS, R. J. (1977), *Seismicity and Stress Determination at Man-made Lakes*, Ph.D. thesis, University of Alberta, Edmonton, Alberta.

WITHERS, R. J., and NYLAND, E. (1978), *Time Evolution of Stress under an Artificial Lake and its Implication for Induced Seismicity*, Can. J. Earth Sci. *15*, 1526–1534.

WITHERSPOON, P. A., and GALE, J. E. (1977), *Mechanical and Hydraulic Properties of Rocks Related to Induced Seismicity*, Eng. Geol. *11*, 23–55.

WU, F. T., ROBERSON, H. E., WANG, C. Y., and MAO, N. H. (1979), *Fault Zones, Gouge, and Mechanical Properties of Clays under High Pressure*, Proc. Conf. VIII: Analysis of Actual Fault Zones in Bedrock, U.S.G.S. Open File Report 79–1239, 344–376.

ZOBACK, M., and HICKMAN, S. (1982), *In situ Study of the Physical Mechanisms Controlling Induced Seismicity at Monticello Reservoir, South Carolina*, J. geophys. Res. *87*, 6959–6974.

(Received 22nd December 1983; revised 26th November 1984; accepted 16th December 1984)

PAGEOPH, Vol. 122 (1984/85) 0033-4553/85/060966-16$1.50 + 0.20/0

Regression Analysis of Reported Earthquake Precursors. I. Presentation of Data

MANSOUR NIAZI[1])

Abstract – Around 700 reported precursors of about 350 earthquakes, including the negative observations, have been compiled in 11 categories with 31 subdivisions. The data base is subjected to an initial sorting and screening by imposing three restrictions on the ranges of main shock magnitude ($M \geqslant 4.0$), precursory time ($t \leqslant 20$ years), and the epicentral distance of observation points ($X_m \leqslant 4.10^{0.3M}$). Of the 31 subcategories of precursory phenomena, 18 with 9 data points or more are independently studied by regressing their precursory times against magnitude. The preliminary results tend to classify the precursors into three groups:

1. The precursors which show weak or no correlation between time and the magnitude of the eventual main shock. Examples of this group are foreshocks and precursory tilt.
2. The precursors which show clear scaling with magnitude. These include seismic velocity ratio (V_p/V_s), travel time delay, duration of seismic quiescence, and, to some degree, the variation of b-value, and anomalous seismicity.
3. The precursors which display clustering of precursory times around a mean value, which differs for different precursors from a few hours to a few years. Examples include the conductivity rate, geoelectric current and potential, strain, water well level, geochemical anomalies, change of focal mechanism, and the enhancement of seismicity reported only for larger earthquakes. Some of the precursors in this category, such as leveling changes and the occurrence of microseismicity, show bimodal patterns of precursory times and may partially be coseismic.

In addition, each category with a sufficient number of reported estimates of distance and signal amplitude is subjected to multiple linear regression. The usefulness of these regressions at this stage appears to be limited to specifying which of the parameters shows a more significant correlation. Standard deviations of residuals of precursory time against magnitude are generally reduced when observation distance enters as a second independent variable. The effect is more pronounced for water well level and conductivity rate changes.

While a substantial portion of the data seem to suffer from personal bias, hence should be regarded as noise, the observations of a number of strain sensitive phenomena such as strain, water well level, and conductivity rate changes, appear to be internally more consistent. For instance, their precursory times suggest a scaling relationship with the strain energy surface density associated with the main shock. The scaling is not identical for all three phenomena so that they may constitute the imminent, short- and intermediate-term manifestation of the same process, i.e. strain loading, respectively.

Introduction

The continuing accumulation of reports of precursory observations to strong earthquakes, often discovered retrospectively, has made the task of systematically

[1]) TERA Corporation, 2150 Shattuck Avenue, Berkeley, California 94704.

interpreting these observations increasingly desirable. In the final analysis, one would expect all such potential precursors to accommodate one or possibly more physical models intimately related to the mechanics of rock failure under different loading conditions. Until such time that scientific experimentation may lead to such a capability, systematic classification of the reported precursors in terms of their precursory lead time and success rate for the purpose of tentative empirical interpretation remains extremely important. This classification provides the potential to:

1. Identify the noisy, less reliable phenomena which either may be of common occurrence regardless of the tectonic condition or may have shown only coincidental correspondence with some strong earthquakes.
2. Understand interdependence of various precursors.
3. Differentiate long-, medium- and short-term phenomena.
4. Recognize regional sensitivities to various observations.
5. Quantify the precursory potential of each phenomenon in probabilistic terms on the basis of success rate (track record), which should in turn guide us in expanding the more promising monitoring programs.
6. Construct an empirical scheme with an updating capability by which future probabilistic forecasting may be attempted.
7. Most importantly, provide insight regarding the physical processes which govern the preparation stages which occur in the source region prior to strong earthquakes.

We have compiled the reported precursory information on a worldwide scale and have taken the initial steps in the screening and analysis of the data. This study, consisting of compilation, sorting, and screening of the available data and the statistical study of magnitude precursor lead times and observation distance, is also a prerequisite for the estimation of probability gains by which forecasting significance of each precursor, in a probabilistic sense, is to be quantified. In the second phase of this study some of these results are being applied to specific seismogenic provinces.

Worldwide observations

Nearly 700 worldwide observations of widely different precursory phenomena have been compiled. While a number of earlier listings (RIKITAKE, 1975, 1979; BILHAM, 1981; KANAMORI, 1981) have been used, an extensive literature search was also conducted for more recent accounts of individual scientists' identification of one or more phenomena on the basis of their own observations. This compilation also includes negative reports of a number of unsuccessful searches for specific precursors in the observation records prior to certain earthquakes (MCEVILLY and JOHNSON, 1973; KANAMORI and FUIS, 1976; BOLT, 1977; STEPPE *et al.*, 1977; LINDH *et al.*, 1978). Nearly all data have been identified retrospectively. The current procedures used in searching for precursory phenomena are expected to introduce personal, and to some

extent cultural, bias in the data, the effect of which may only be evaluated after a long period of monitoring. The inclusion of negative findings is, however, expected to reduce the bias. The data base (NIAZI, 1982) is designed to include information relevant to both earthquake source characteristics (date, location, depth, magnitude, focal mechanism) and precursors' specifics (type, lead time, distance from the source, or extent of area, amplitude, and observation depth) whenever available.

The reported anomalies are broadly classified into 11 categories which, along with their number of observations, are listed below.

Category	Number of observations	Category	Number observations
Leveling and gravity	25	Geoelectric	61
Tilt, strain and creep	129	Geochemical	59
Tidal coefficients	2	Source mechanism	16
Seismicity anomaly	273	Hydrological	26
Seismic velocity	84	Macroanomaly	7
Geomagnetism	9		

The macroanomaly category consists of the precursory phenomena not covered by the other 10 categories and includes change of odor and color of springs and water wells, and abnormal animal behavior.

The total number of subdividions with one or more observations is 31, as shown in Table 1. A tabulation of the reported data in each subdivision appears in NIAZI (1982).

Screening procedure

Three selection criteria were adopted:

1. The analysis is confined to the main shocks of magnitude 4 and greater.
2. The analysis is restricted to those observations reported at epicentral distances not exceeding $X_m = 4 \times 10^{0.3M}$, where M is the local or surface wave magnitude of the eventual main shock, and X_m is in kilometers.
3. Data for which reported precursory times are longer than 20 years (7300 days) are ignored.

A magnitude threshold at 4 for the main shock is imposed rather arbitrarily. While forecasting smaller earthquakes may have scientific merit, it is of little practical value. With very few reported observations, there is a large possibility of noise contamination which could mask potential trends in the data, easily outweighing the loss of information resulting from their exclusion. The extent of the region where sufficiently strong precursory signals would be observed is rather small. It is difficult to relate relatively frequent events of magnitude less than 4 with enough certainly to a particular precursory observation without first establishing a relevant baseline.

Table 1

Frequency distribution of reported premonitory phenomena

Category	Code	All	Refined	Neg.	Time and mag.	Time and dist.	Ampl. dist. and mag.	Ampl. time and mag.	All four parameters
Uplift or subsidence	A1	25	25		24	18	11	13	10
Tilt	B1	91	85		83	82	76	77	76
Strain	B2	34	31	2	29	26	22	25	22
Creep rate	B3	4	4	1	3	2	1	1	1
Tidal coefficients	C1	2	2		2	2	2	2	2
Anomalous seismicity	D0	14	12		12	—	—	—	—
Foreshocks	D1	109	100		99	8	1	1	1
Quiescence	D2	55	51		50	2	—	—	—
Enhanced seismicity,	D3	38	38	9	28	19	—	—	—
Migration and clustering	D4	9	9		9	—	—	—	—
Microseismicity	D5	30	30		30	2	—	1	—
b-value	D6	17	14		14	—	—	7	—
Volcanic tremor	D7	1	1		1	1	—	—	—
V_p/V_s	E1	59	56	1	55	1	1	46	1
V_p	E2	7	7	3	4	—	—	3	—
V_s	E3	3	2		2	—	—	2	—
Travel time delay	E4	15	14		14	13	11	12	11
Magnetic field	F1	8	8		8	8	7	7	7
Radio waves	F2	1	1		1	—	—	—	—
Geoelectric current and potential	G1	21	20		20	8	6	17	6
Conductivity rate	G2	22	18		18	18	18	18	18
Resistivity	G3	18	15		14	8	4	10	4
Radon count	H1	48	37	1	36	31	19	23	19
Other geochemical observations	H2	11	10		9	8	5	6	5
Focal mechanism	11	11	11		11	—	—	—	—
Spectra	12	5	5		5	1	—	—	—
Well water level	J1	15	15		15	14	7	7	7
Spring output	J2	2	1		1	1	1	1	1
Groundwater temperature	J3	5	5		5	5	3	3	3
Fluid ejection	J4	4	4		4	4	—	—	—
Macroanomalies	K	7	7		2	—	—	—	
Total		691	638	17	613	284	195	282	194

It would be logical to exclude precursors distant from the site of anticipated earthquakes, despite quantitative arguments. Regardless of how the precursory signal attenuates with distance, or what physical model is adopted for the analysis of signal's decay, the precursor observed many hundreds of kilometers away would have little pratical importance to the site of interest. In defining an upper bound for the acceptable distance for a credible precursory observation, we may be guided by a number of

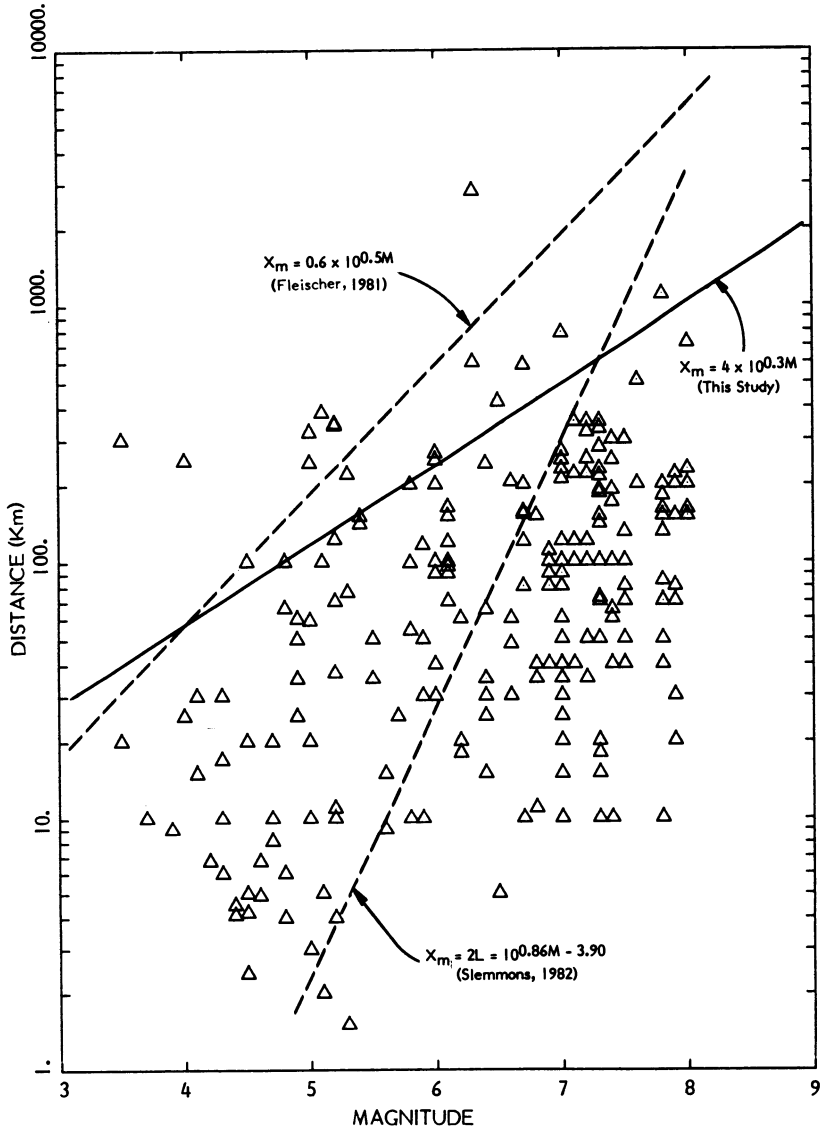

Figure 1
Precursor study, distance vs. magnitude (all types). Straight lines represent various options for truncation of large distances (see the text).

models, physical or empirical, suggested for scaling the earthquake's source dimensions. Two such examples are shown in Fig. 1. FLEISCHER (1981) has suggested an upper bound to the distance at which a radon anomaly should have sufficient strength to be observed. The derivation is based on a simplified dislocation model, and leads to very large distances of many thousands of kilometers for an earthquake of $M = 8.0$.

SLEMMONS' (1982) revised regression coefficients of fault dimension versus magnitude for strike-slip earthquakes, interpreted very conservatively, result in a fraction of one kilometer for $M = 4$. To avoid discarding many reported observations at short distances and, at the same time, to avoid retaining irrelevant observations at large distances, we have defined a compromise upper bound for application in this study. The adopted formula L (km) $= 4 \times 10^{+0.3M}$ results in a bounding epicentral distance of 1000 km for $M = 8$, in agreement with Slemmons' result, which is then reduced in steps of two for each decreasing unit of magnitude. The upper bound distances obtained by each of three models are compared graphically in Fig. 1 with real data for reported observation distances against main-shock magnitude.

In applying a temporal cut-off of 20 years, we are taking into account the relatively imprecise nature of older observations and placing the primary emphasis of this study upon the intermediate- and short-term features of precursory phenomena. Long-term precursors are expected to be more sensitive to the regional loading rate. Application of these criteria reduced the number of observations to 638.

Classification of precursory data

Despite a number of attempts to classify precursory phenomena, no firm criteria for such a classification have yet been established. Previous work is grouped into two categories. In one category, the long-, medium-, and short-term precursory phenomena are characterized as such without regard to the magnitude of the eventual main shock (for example see AKI, 1981). In the second category, the precursory lead time is characterized by its semi-log scaling relationship with the magnitude of the future earthquake. RIKITAKE (1975, 1979), for instance, in examining 391 reported precursors, suggests three classes of precursors according to how well their precursory times scale with magnitude. The suggested relationship of the form $\log t = a + bM$ can best be explained by the dilatancy diffusion model (NUR, 1972; SCHOLZ *et al.*, 1973; WHITCOMB *et al.*, 1973; see also MYACHKIN *et al.*, 1975, for diagnostic features of an alternative model). Since its initial suggestion, this magnitude scaling relationship has been used as a yardstick for measuring the validity of precursory reports. In fact, the searching process is occasionally guided by such a yardstick.

Several objections to this procedure, termed 'fishing for anomalies' by REYNERS (1981), may be raised.

1. It is biased toward a specific physical model of the prefailure preparation process, not yet unequivocally validated.
2. It fails to take into account the predominant influence of certain precursors in establishing a linear trend or in contributing to the noise.
3. It assigns identical weight to all data points regardless of their distance from the source, signal strength and success rate.

The gradual compilation of a broader data base would enable us to gain the capability of overcoming some of these objections. With this objective in mind, we

focused on the analysis of individual observation categories or their subgroups whenever they contained more than 9 observations. However, we were not able to resolve some of the uncertainties which were inherent in the reported observations or which would require further experimental work. Examples are:

1. Occasional simultaneous reports of contradictory precursors such as quiescence and enhancement of seismicity.
2. The interdependence of several precursors which may be physically related such as resistivity, geoelectric current and chemistry of groundwater.
3. The correlation of some of the precursors with nontectonic factors such as seasonal fluctuations of gravity and groundwater level, and of geochemical observations with precipitation.

Data analysis

As a first test of the data, we have examined each precursor category with 9 or more observations for magnitude scaling of the precursory lead times. Of the 31 categories, only 18 contain sufficient data points for this test. Table 2 shows the coefficients of

Table 2

$\log(t) = a + bM$

Category (see Table 1)	No. of obs.	a	b	σ	R^2
+A1	(21)	2.89	0.03	0.45	0.00
B1	(83)	−2.14	0.52	1.15	0.18
+B2	(27)	2.25	−0.04	0.88	0.00
D0	(12)	−1.58	0.74	0.19	0.94*
D1	(99)	0.85	0.05	1.24	0.00
D2	(50)	0.52	0.36	0.54	0.28*
+D3	(28)	0.70	0.32	0.28	0.18
D5	(30)	0.52	0.34	0.72	0.14
D6	(14)	−0.09	0.36	0.97	0.18
E1	(55)	−0.86	0.58	0.24	0.86*
E4	(14)	−1.71	0.71	0.32	0.76*
G1	(20)	0.06	0.17	0.52	0.14
G2	(18)	−1.80	0.10	0.29	0.10
G3	(14)	1.75	0.05	0.71	0.01
+H1	(35)	1.33	0.03	0.82	0.00
H2	(9)	0.80	0.16	0.46	0.10
I1	(11)	0.78	0.28	0.41	0.23
J1	(15)	−0.20	0.21	1.01	0.02

* Denotes significant correlation.

+ sign in front of category indicates that regression is only applied to precursory times of one day or longer.

regression between the logarithm of precursory time and the magnitude of the main shock for each category. The units of time and distance used in the calculation of coefficients of Table 2 and those of later tables are day and kilometer, respectively.

From the examination of Table 2 we note that all categories but one (strain) are associated with positive b which would indicate a tendency of longer precursory times for larger earthquakes. This tendency, however, is quite varied for different categories. Furthermore, the scatter is often too large to render a meaningful positive trend for the entire population of data. Some categories, for instance, show no convincing correlation between time and magnitude of the eventual main shock. Examples of this lack of correlation are foreshocks (D1, $R^2 = 0.00$) and precursory tilt (B1, $R^2 = 0.00$). A number of potential precursors, on the other hand, exhibit a significant correlation between precursory time and magnitude. These include seismic velocity ratio V_p/V_s (E1, $R^2 = 0.86$), travel time delay (E4, $R^2 = 0.76$), and, to some degree duration of seismic quiescence (D2, $R^2 = 0.26$). The not-so-well-specified category of anomalous seismicity also shows significant correlation (D0, $R^2 = 0.94$).

Another group of precursors displays a band of precursory times scattered around a mean value, irrespective of the magnitude of the pending earthquake. The coefficient b for this group is generally small. The mean precursory time for these categories varies from a few hours to few years. The mean value of changes for the earth's conductivity rate change (G2) is a few hours; for geoelectric current and potential (G1) it is approximately two weeks; for strain (B2) and widely scattered geochemical anomalies (H1 and H2) it is a few months; for a change of the focal mechanism (I1) it is about a year; and for the enhancement of seismicity (D3), as reported only for larger earthquakes, it is around a few years.

Some of the reported precursory times of this group may show a bimodal character, one extremely short or perhaps coseismic, and the other of short- to intermediate-term character. Leveling changes, microseismicity occurrences, and to some extent the resistivity changes (A1, D5, G3), fall within this bimodal pattern. The earlier precursors for leveling and microseismicity changes peak a few years prior to the main shock. Their later occurrences appear to be within a one-hour window preceding it, and would not exclude possible coseismic occurrences. Resistivity change may exhibit a bimodal character for very large earthquakes and not for small or medium size events.

The coefficients of simple regression of the data, together with σ (the standard deviation of the residuals) and correlation coefficient for each category, are given in Table 2.

Precursor time vs. observation distance

The reported observation (epicentral) distances for large earthquakes with extended sources are not well defined. Also, for a number of precursory phenomena describing average regional or local behavior such as quiescence, b-value variation, seismic velocity, etc, this distance would generally refer to the lateral extent of the anomalous

region. Nevertheless, an examination of the reported distance and its possible dependence on magnitude may be expected to lead to a better understanding of the pattern of migration, or likely distance ranges in which they may be observed. Any trend in the observation distance, magnitude dependent or not, would provide further constraint on the physical mechanism describing particular aspects of earthquake preparation processes.

As explained before, we arbitrarily screened out some of the large distances which were thought to be out of proportion with the expected source dimension of the designated main shock ($X_m > 4.0 \times 10^{0.3M}$). A total of 16 out of 300 data points were discarded for this reason. Table 3 lists the regression coefficients of the reported distances vs. precursory times for 13 subcategories and 5 categories for which 8 or more observations were reported. Again we note that in only 4 categories, correlations are significant. These categories are marked by an asterisk in Table 3.

As an example, the reported observations of precursory tilt are shown in Fig. 2. These observations cover relatively wide ranges of magnitude, distance and precursory time. Most of the observations associated with larger main shocks are reported at distances of 20–200 km. There is a tendency for the data of smaller earthquakes to

Table 3

$\log (t) = a + c \log (\text{dist.})$

Category (see Table 1)	No. of obs.	a	c	σ	R^2
+A1	17	2.52	0.30	0.43	0.07
+B1	66	1.21	0.22	0.79	0.01
+B2	24	2.80	−0.55	0.83	0.18
+(B1–2–3)	92	2.25	−0.33	0.83	0.04
D1	8	−0.33	1.02	0.21	0.08
D3	19	3.12	−0.022	0.28	0.00
(D1–2–3–5–7)	32	0.58	1.02	1.25	0.18
E4	13	1.58	0.89	0.43	0.59*
(E1–4)	14	1.60	0.86	0.42	0.61*
F1	8	1.57	0.63	1.00	0.12
G1	8	0.29	0.56	0.38	0.29*
G3	8	3.96	−1.05	0.86	0.08
(G1–3)	16	0.79	0.44	0.76	0.04
G2	18	−1.31	0.055	0.30	0.06
+H1	29	2.29	−0.46	0.77	0.10
+H2	8	0.76	0.74	0.32	0.48*
+(H1–2)	37	2.07	−0.33	0.72	0.06
+J1	13	1.56	0.01	0.75	0.00
+(J1–2–3–4)	23	1.91	−0.12	0.68	0.00

* Denotes significant correlation.

+ sign indicates that regression in only applied to precursory times of one day or longer.

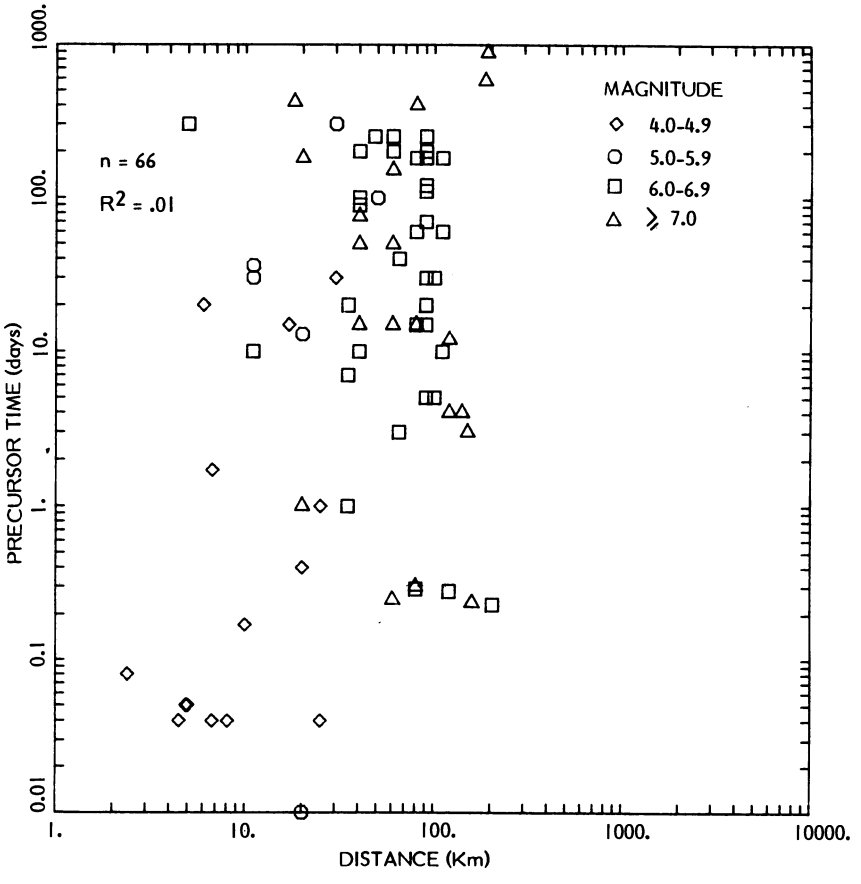

Figure 2
Precursor study, type B1 (tilt).

cluster at near distances with very short precursory times. Most of the reported precursory tilts for small earthquakes, and some for larger events, may be coseismic. As can be noted from Table 3, the coefficients of correlation for these data, as well as for 11 other simple or composite categories, are positive.

Precursory times of the strain observations (Fig. 3), reported almost entirely for events of magnitude 5 and above, on the other hand display a negative correlation with observation distance. While such a correlation may be quite fortuitous, if upheld by future observations, it may be more readily attuned to a physical model of failure. We tentatively interpret this tendency to mean that the deformation at inception is localized and consequently grows in amplitude and extent. For stations close to the center of deformation (i.e., presumably closer to the epicenter of the future event) the maturity time appears longer. It may be significant that this pattern of precursory time-observation distance with a negative slope also is observed in the examination of other

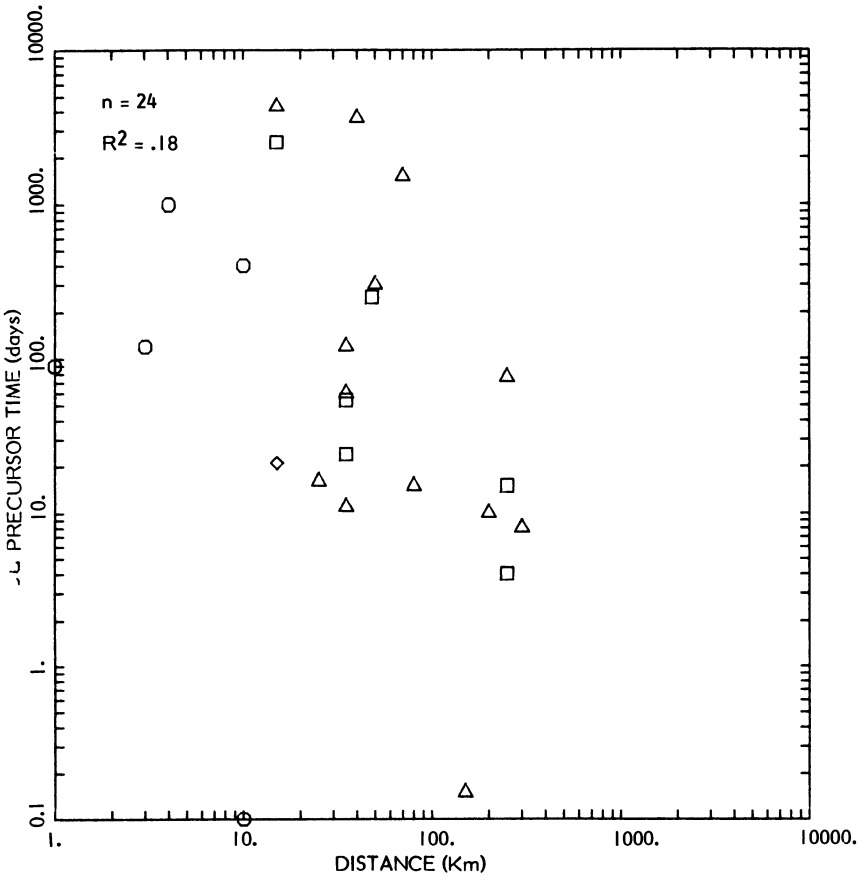

Figure 3
Precursor study, type B2 (strain). The magnitude symbols are the same as in Fig. 2.

strain sensitive phenomena. An alternative interpretation of this tendency for resistivity precursors has recently been advanced by RIKITAKE and YAMAZAKI (1984).

Figure 4 shows the distribution of well water level data and conductivity rate changes. Because of the limited resolution of recording time and very small precursory times (the mean value for 18 observations is 1.56 hours), many of the conductivity observations may be coseismic. The well water level observations are clustered around 100 km (few tens to few hundred kilometers) and have a mean precursory time of about 38 days. The combined data of Fig. 4 tend to indicate systematic scaling of distance with magnitude which may be significant, particularly in view of the facts that (1) no data have been discarded on account of large observation distance from well water level observations and (2) the four discarded observations of conductivity rate changes fit the general pattern reasonably well. As can be noted in Fig. 4, the straight lines which roughly represent the observations of magnitude bins for the combined sets of data

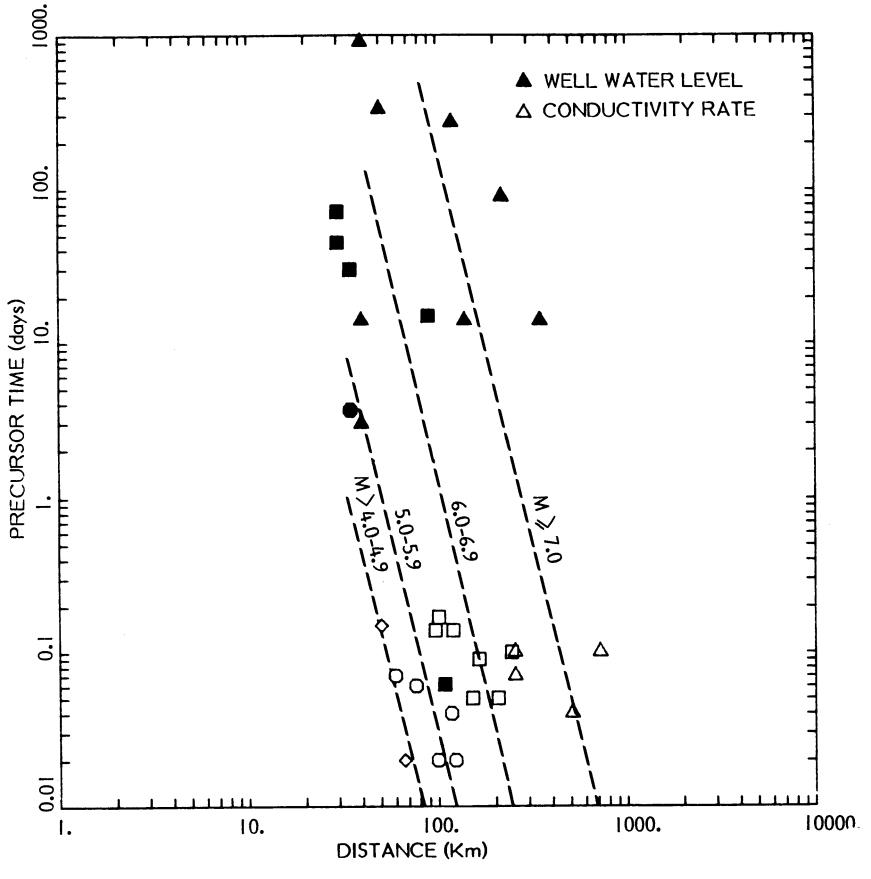

Figure 4
Precursor study, water well level and conductivity rate. The magnitude symbols are the same as in Fig. 2.

move outward in a parallel fashion with the increase of magnitude, in general agreement with a relationship of the form

$$\log t + \log x^2 \approx M$$

in terms of strain energy Σ this relationship may be written as

$$t \approx \frac{\Sigma}{x^2} \approx \text{strain energy surface density.}$$

The coefficient of proportionality may be expected to vary for different phenomena depending on the tectonic characteristics of the region. This model also appears to fit precursory strain observations (Fig. 3) fairly well, indicating at the same time possible flattening of slopes at shorter distances. Therefore, a tentative interpretation of these data may be that the available observations on precursory strain, water well level and

conductivity rate variation are related to the same physical process. As such they can be intermediate-term, short-term and imminent manifestations of the strain loading process. Their precursory time scale in somewhat different ratio with the strain energy surface density of the pending main shock.

Table 2 showed that the correlation between the logarithm of precursory times and magnitude for 15 of the 19 categories, for which 9 or more observations were available, fell below 0.5. The four categories with correlation coefficient above 0.5 are abnormal seismicity (D0), quiescence (D2), V_p/V_s variation (E1), and travel time anomaly (E4). Inclusion of epicentral distance as a second variable (cf. Tables 2 and 4) reduces the estimated standard deviations, but the reduction is more noticeable for well level change, J1 (27%) and conductivity rate, G2 (15%).

Multiple linear regressions

A more systematic examination of the described pattern may be achieved by the method of multiple linear regression. As seen in Table 1, after initial refinement and exclusion of negative observations of the 691 data points, there remained 282 observation points containing amplitude, time and magnitude; 195 points containing amplitude, distance, and magnitude; and 194 points containing amplitude, distance, time and magnitude information. To these, we applied multiple linear regression. Only categories with 10 or more data points were used in the analysis. Results of regressions are tabulated in Tables 4 and 5. The tested models in these tables are

$$\log (t) = a + bM + c \log (\text{dist.}), \text{ and}$$

$$\text{Ampl} = a + bM + c \log (\text{dist.}) + d \log (t),$$

respectively. The last two columns of Tables 4 and 5 give the standard deviation of residuals and correlation coefficient of the fit. In each, multiple regression independent variables which showed more significant correlation with log (t) or magnitude are printed in *italic*.

Precursory times of less than one day are ignored for the categories marked by a '+'. In Table 5, the regression coefficients are also given when either precursory time ($d = 0$) or observation distance ($c = 0$) was left out of the analysis.

While units of amplitude vary from one to the next category, every effort has been made to use a consistent amplitude scale for each category, in the form of either percent variation or absolute value. Geochemical anomalies including radon counts, creep rate, resistivity, spring flow rate, tidal coefficients, and velocity anomalies are thus given in percentage change from background levels. Measurements for other precursory observations are expressed as follows: amplitude of leveling changes, groundwater level (centimeter), strain (microstrain), tilt (microradian), temperature variation (degreees centrigrade), geomagnetic transients (nanotesla), and geoelectric current and potential (microvolt/km and microvolt).

Table 4

$\log(t) = a + bM + c \log(\text{dist.})$

Category (see Table 1)	No. of obs.	a	b	c	σ	R^2
+A1	(17)	2.91	0.07	*0.26*	0.43	0.07
B1	(82)	−2.11	*0.39*	0.48	1.14	0.19
+B2	(24)	1.21	0.31	*−0.83*	0.79	0.26*
D3	(19)	0.22	*0.39*	0.02	0.27	0.10*
E4	(13)	−1.08	*0.53*	0.36	0.28	0.83*
G2	(18)	−1.43	*0.44*	−1.14	0.24	0.35*
+H1	(29)	1.14	0.26	*−0.74*	0.73	0.18
+J1	(13)	0.66	*0.16*	−0.13	0.74	0.02

* Denotes significant correlation.

+ sign in front of category indicates that regression is only applied to precursory times of one day or longer.

Table 5

$\text{Ampl} = a + bM + c \log(\text{dis}) + d \log(t)$

Category (see Table 1)	No. of obs.	a	b	c	d	σ	R^2
A1	(11)	−2.28	*1.07*	−2.12		9.52	0.01
	+(10)	−52.39	*5.86*		2.99	9.71	0.06
	+(10)	−51.96	*5.87*	−0.19	2.98	9.71	0.06
B1 × 10^4	(76)	1.13	−0.06	*−0.32*		0.93	0.04
	+(61)	−0.20	*0.04*		0.04	0.40	0.02
	+(60)	−0.13	0.14	*−0.42*	0.06	0.39	0.11
B2 × 10^4	(22)	0.19	0.01	*−0.03*		0.03	0.17
	+(23)	0.58	−0.01		*0.02*	0.05	0.25*
	+(20)	−0.16	0.00	−0.01	*0.02*	0.03	0.32*
E1	(46)	10.72	*−8.85*		11.94	11.03	0.08
E4	(11)	−7.92	1.17	*1.77*		2.30	0.37*
	(12)	−9.65	*1.39*		0.86	2.32	0.30*
	(11)	−7.87	1.12	*1.74*	0.09	2.30	0.37*
G1	+(17)	50.58	33.08		*−147.82*	75.49	0.24
G2 × 10^4	(18)	−0.03	*0.11*	−0.30		0.43	0.01
	(18)	−0.17	*0.02*		−0.02	0.43	0.00
	(18)	−0.23	*0.17*	−0.46	−0.14	0.43	0.02
G3	(10)	−101.2	11.36		*24.35*	14.00	0.44*
H1	(19)	25.71	−8.26	*59.90*		115.25	0.07
	+(22)	−74.18	14.94		*68.43*	107.91	0.21
	+(18)	−158.92	−15.15	116.33	*100.64*	92.23	0.44*

* Denotes significant correlation.

+ sign in front of an observation indicates that regression is only applied to precursory times of one day or longer.

In general, as seen from the underlined coefficients in Table 4, precursory time for the reported observations of tilt (B1), enhanced seismicity (D3), travel time anomaly (E4), conductivity rate (G2), and well level change (J1) show more significant correlation with magnitude than with distance; whereas leveling (A1), strain (B2), and radon count (H1) show the reverse. When all three independent variables are used, signal amplitude within each category generally shows a positive correlation with precursory time (with the exception of geoelectric observations) and with magnitude (with the exception of groundwater radon count), but negative correlation with observation distance (with the exception of geoelectric and radon observations). The available foreshock and tilt observations appear quite random, and thus in their present unrefined form are least useful for premonitory purposes.

Discussion

We have here confined the discussion to the presentation of those earthquake precursory reports readily accessible through the technical literature. Some 700 observations have been examined. In the course of this analysis, the reported data have been tabulated into 31 groups (NIAZI, 1982) for the convenience of future use. The data base suffers from substantial noise. However, for a number of categories a baseline estimate may yet be afforded. An attempt is currently underway to apply some of these results to the problem of probabilistic forecasting of earthquakes under restricted conditions. Results will be discussed in Part II of this study.

Acknowledgments

This study was supported by the United States Geological Survey under Grant 14-08-0001-19908. Constructive comments of Professor Keiiti Aki, Dr Dan Moore and Dr Christian Mortgat were helpful. Technical support of Ms Ann Bornstein is acknowledged.

REFERENCES

AKI, K., *A Probabilistic Synthesis of Precrusory Phenomena*, in *Earthquake Prediction* (Ewing Symposium 1981), pp. 566–574.

BILHAM., R., *Delays in the Onset Times of Near-Surface Strain and Tilt Precursors to Earthquakes*, in *Earthquake Prediction* (Ewing Symposium 1981), pp. 411–421.

BOLT, B. A. (1977), *Constancy of P Travel Times from Nevada Explosives to Oroville Dam Station, 1970–1976*, Bull. seism. Soc. Am. *67*, 27–32.

FLEISCHER, R. L. (1981), *Dislocation Model for Radon Response to Distant Earthquakes*, Geophys. Res. Letters *8*, 477–480.

KANAMORI, H., *The Nature of Seismicity Patterns Before Large Earthquakes*, in *Earthquake Prediction* (Ewing Symposium 1981), pp. 1–19.

KANAMORI, H., and FUIS, G. (1976), *Variation of P-Wave Velocity Before and After the Galway Lake Earthquake (M_L 5.2) and the Goat Mountain Earthquakes (M_L 4.7), 1975, in the Mojave Desert, California*, Bull. seism. Soc. Am. *66*, 2017–2037.

LINDH, A. G., LOCKNER, D. A., and LEE, W. H. K. (1978), *Velocity Anomalies: An Alternative Explanation, Bull. Seism. Soc. Am.* **68**, 721–734.

MCEVILLY, T. V., and JOHNSON, L. R. (1973), *Earthquakes of Strike-Slip Type in Central California: Evidence on the Question of Dilatancy*, Science *182*, 581–584.

MYACHKIN, V. I., BRACE, W. F., SOBOLEV, G. A., and DIETRICH, J. H. (1975), *Two Models for Earthquake Forerunners*, Pure appl. Geophys. *113*, 169–181.

NIAZI, M. (1982). *Probabilistic Approach to Earthquake Forecasting, I: Compilation, Evaluation and Preliminary Anaysis of Data*, TERA Report 14-08-0001-19908 to U.S. Geological Survey.

NUR, A. (1972), *Dilatancy, Pore Fluids and Premonitary Variations of ts/tp Travel Times*, Bull. seism. Soc. Am. *62*, 1217–1222.

REYNERS, M., *Long- and Intermediate-Term Seismic Precursors to Earthquakes – State of the Art*, in *Earthquake Prediction* (Ewing Symposium 1981), pp. 333–347.

RIKITAKE, T. (1975), *Dilatancy Model and Empirical Formulas for an Earthquake Area*, Pure appl. Geophys. *113*, 000–000.

RIKITAKE, T. (1979), *Classification of Earthquake Precursors*, Tectonophysics, *54*, 293–309.

RIKITAKE, T., and YAMAZAKI, Y. (1984), *The Nature of Resistivity Precursors*, Proceedings of U.S.–Japan Seminar on Practical Approaches to Earthquake Prediction and Warning.

SCHOLZ, C.H., SYKES, L. R., and AGGARWAL, Y. P. (1973), *Earthquake Prediction: A Physical Basis*, Science, *181*, 803–810.

SLEMMONS, D. B. (1982), *Determination of Design Earthquake Magnitudes for Microzonation*, Proceedings of 3rd International Earthquake Microzonation Conference, Seattle, Vol. 1, pp. 119–130.

STEPPE., J. A., BAKUN, W. H., and BUFE, C. G. (1977), *Temporal Stability of P-Velocity Anisotropy Before Earthquakes in Central California*, Bull. Seism. Soc. Am. *67*, 1075–1090.

WHITCOMB, J. H., GARMANY, J. D., and ANDERSON, D. L. (1973), *Earthquake Prediction: Variation of Seismic Velocities Before the San Fernando Earthquake*, Science, *180*, 632–635.

PAGEOPH, Vol. 122 (1984/85) 0033-4553/85/060982-16$1.50 + 0.20/0

Assessment of Earthquake Hazard by Simultaneous Use of the Statistical Method and the Method of Fuzzy Mathematics

By DE-YI FENG[1]), JING-PING GU[2]), MING-ZHOU LIN[3]), SHAO-XIE XU[4]), and XUE-JUN YU[5])

Abstract – A probabilistic method and a retrieval method of fuzzy information are simultaneously studied for assessment of earthquake hazard, or earthquake prediction. Statistical indices of regional seismicity in three adjacent time intervals are used to predict an earthquake in the next interval. The indices are earthquake frequency, the maximum magnitude, and a parameter related to the average magnitude (or *b*-value) and their time derivatives. Applying the probabilistic method, we can estimate a probability for a large earthquake with magnitude larger than a certain threshold occurring in the next time interval in a given region. By using the retrieval method of fuzzy information we can classify time intervals into several classes according to the regional seismic activity in each time interval and then evaluate whether or not the next time interval belongs to seismically hazardous time interval with a large earthquake. Some examples of applying both methods to the North section of the North–South Seismic Zone in China are shown. The results obtained are in good agreement with actual earthquake history. A comparison of the probabilistic method with the method of fuzzy mathematics is made, and it is recommended that earthquake hazard be assessed by simultaneous use of both methods.

Key words: earthquake hazard, statistical indices, total probability, fuzzy sets, fuzzy information, descriptors, membership function.

1. Introduction

This paper consists of two parts. In the first part a probabilistic method will be described and in the latter part a retrieval method of fuzzy information will be discussed. Also a brief discussion based on a comparison of the two methods will be given in the end.

The probabilistic method is based on 18 statistical indices of regional seismicity and provides an indicator for the occurrence of an earthquake with magnitude above a certain threshold, which is called the total probability in this paper. The probability method basically helps to judge whether or not a large earthquake occurs. However, we often need more detailed information. For example, we sometimes need to estimate which kind of event most likely takes place among several kinds of event. Thus we will

[1]) Seismological Bureau of Tianjin, Tianjin, China.
[2]) Seismological Institute of Lanzhou, State Seismological Bureau, Lanzhou, China.
[3]) Seismological Bureau of Shanghai, Shanghai, China.
[4]) Institute of Geophysics, State Seismological Bureau, Beijing, China.

apply one of the methods of fuzzy mathematics, a retrieval method of fuzzy information, to the evaluation of earthquake hazard following FENG *et al.* (1983).

Since ZADEH (1965) advanced the fuzzy set theory, it has developed rapidly with application in various scientific domains (KAUFMANN, 1971; GUPTA *et al.*, 1977; DUBOIS and PRADE, 1980; WANG and CHANG, 1980). The method has many advantages in simplicity, convenience, and easy operation. This is the reason why we apply a method of fuzzy mathematics in the present paper. The result shows that a simultaneous application of the probabilistic method and the method of fuzzy mathematics may be useful in an earthquake prediction.

2. *A probabilistic method for earthquake hazard assessment*

2.1. *Method*

The basic data we use in this paper is an earthquake catalogue in a certain region. First we define several statistical indices which can be obtained from the catalogue and then calculate a conditional probability of a large earthquake occurrence in a certain time interval based on values of each statistical index in the previous time intervals. The conditional probability for each statistical index is the fundamental quantity used in this method. We define the total probability P_j, an indicator of occurrence of a large earthquake in the jth time interval, as a product of two probabilities, P_{j1} and P_{j2}. The probability P_{j1} can be obtained as a weighted mean of the conditional probabilities for different indices, and the probability P_{j2} concerns a combination of values of the conditional probabilities. The next step is to calculate the total probabilities for the past time intervals and set an appropriate threshold for the values of the total probability. When the total probability exceeds this threshold, we can judge that a large earthquake is likely to occur in the next time interval.

2.1.1. *Statistical indices of regional seismicity*

We will use six fundamental statistical indices of regional seismicity after FENG *et al.* (1981). They are the number of earthquakes N with magnitude above a certain threshold M_0, the maximum magnitude $M^{\max}$, the average magnitude $\bar{M}$, and their time derivatives $\dot{N}$, $\dot{M}^{\max}$, and $\dot{\bar{M}}$. The average magnitude will be replaced by a coefficient r in this study, which is defined as follows:

$$r = \log\left(1 + N \Big/ \sum_{s=1}^{\infty} sN_s\right), \tag{1}$$

where N_s is the number of earthquakes with magnitudes between $M_0 + \Delta M(s-1)$ and $M_0 + \Delta Ms$, and ΔM is a magnitude interval which is taken as 0.5 in this paper. The average magnitude may be approximated as:

$$\bar{M} \simeq \left[\sum_{s=1}^{\infty} (M_0 + (s - 1/2)\Delta M)N_s\right] \Big/ N$$

$$= M_0 - \Delta M/2 + \Delta M \left(\sum_{s=1}^{\infty} sN_s\right) \Big/ N.$$

The average magnitude may also be replaced by the b-value since the most likelihood estimate of the b-value is expressed as (UTSU, 1965; AKI, 1965):

$$b = 0.4343/(\bar{M} - M_0 + \Delta M/2).$$

Let us divide the whole time period $t_n - t_0$ into n equal intervals, so we have $t_n - t_0 = n\Delta t = (t_{n-1} - t_0) + \Delta t$. Here t_0 is the beginning time, and the time step Δt can be taken as a unit time (month, year, decade, and so on). The six fundamental indices for the jth time interval are:

$$r_j, \dot{r}_j = r_j - r_{j-1}, \qquad N_j, \dot{N}_j = N_j - N_{j-1},$$

$$M_j^{\max}, \dot{M}_j^{\max} = M_j^{\max} - M_{j-1}^{\max}, \qquad (j = 1, 2, \ldots, n).$$

2.1.2. *Probability for a large earthquake occurrence estimated from a single statistical index*

We can assume that an occurrence of a 'large' earthquake with magnitude above M_1 depends on the six fundamental indices in the past three adjacent time intervals. Consequently, we have 18 statistical indices for calculating the probability of having at least one earthquake with magnitude above M_1 in the jth time interval. They are: r_{j-i}, $\dot{r}_{j-i}$, N_{j-i}, $\dot{N}_{j-i}$, $M_{j-i}^{\max}$, and $\dot{M}_{j-i}^{\max}$ ($i = 1$, 2, and 3). For example, we take the statistical indices in January, February, and March to calculate the probability of having at least one earthquake with magnitude above M_1 in April. In the following discussion we will simply call an earthquake with magnitude above the threshold M_1 a 'large earthquake'.

For simplicity, let us denote by a variable x, any one of the indices, r, $\dot{r}$, N, $\dot{N}$, $M^{\max}$, or $\dot{M}^{\max}$. When the kth index x^k ($k = 1, \ldots, 6$) ranges from x_o^k to x_p^k, we divide the range into p equal intervals: $x_1^k = (x_0^k, x_1^k)$, ..., $x_p^k = (x_{p-1}^k, x_p^k)$ where $x_h^k = x_{h-1}^k + \Delta x$ ($h = 1, 2, \ldots, p$). By using Bayes' theorem, we can obtain the conditional probability of having a large earthquake in the jth time interval under the condition that the value of x_{j-1}^k falls in an interval Δx_h^k:

$$P(e|h) = P(e)\,P(h|e)/(P(e)\,P(h|e) + P(q)\,P(h|q)), \tag{2}$$

where signs 'e' and 'q' denote the cases with and without a large earthquake, respectively. For example, $P(e)$ indicates a probability that a large earthquake occurs in any time interval and $P(h|e)$ shows a conditional probability that a value of the statistical index x_{j-i}^k falls into an interval Δx_h^k under the condition that a large earthquake occurs in the jth time interval. In equation (2) suffixes k, j, and $j - i$ are omitted for simplicity.

Let us introduce the following symbols:

n_q : the total number of time intervals without a large earthquake,

n_e : the total number of time intervals with a large earthquake,

n_q^h : the number of time intervals without a large earthquake under the condition that a certain statistical index x has a value within interval Δx_h,

n_e^h : the number of time intervals with a large earthquake under the condition that a certain statistical index x has a value within interval Δx_h.

Since we have

$$P(e) = n_e/(n_e + n_q) = n_e/n,$$

$$P(q) = n_q/(n_e + n_q) = n_q/n,$$

$$P(h|e) = n_e^h/n_e, \text{ and } P(h|q) = n_q^h/n_q,$$

we obtain from equation (2)

$$P(e|h) = n_e^h/(n_e^h + n_q^h) \tag{3}$$

and

$$P(q|h) = 1 - P(e|h)\,. \tag{4}$$

For the kth index x_{j-i}^k for time interval $j - i$ ($i = 1$, 2, and 3), we can calculate the probabilities $P(e|h_{j-i}^k)$ and $P(q|h_{j-i}^k)$ for all intervals Δx_h^k ($h = 1, 2, 3, \ldots, p$) where $k = 1$, 2, 3, 4, 5, and 6 represent the indices r, $\dot{r}$, N, $\dot{N}$, $M^{\max}$, and $\dot{M}^{\max}$, respectively.

2.1.3. Synthesized probability

By assuming a statistical independency of the indices in different time intervals, we can obtain the probability of having a large earthquake in the jth time interval under the condition that the indices x_{j-i}^k fall in intervals $\Delta x_{h,\,j-i}^k$ ($i = 1$, 2, and 3) as follows (UTSU, 1977; AKI, 1981):

$$P_{kJ} = P(e) \prod_{i=1}^{3} P(e|h_{j-1}^k) \Bigg/ \left[P(e) \prod_{i=1}^{3} P(e|h_{j-i}^k) + p(q) \prod_{i=1}^{3} P(q|h_{j-i}^k) \right], \tag{5}$$

where $P(e|h_{j-i}^k)$ represents the conditional probability that a large earthquake occurs in time interval j under the condition that a value of statistical index k for time interval $j-i$ falls into Δx_h^k. Similarly by assuming a statistical independency of different indices, we can obtain a synthesized probability of an occurrence of a large earthquake under the condition that the indices x_{j-i}^k fall in intervals $\Delta x_{h,j-i}^k$ ($k = 1$, 2, 3, 4, 5, and 6). However, some of the indices such as r and $\dot{r}$ are not statistically independent. Thus we will use a weighted mean of the conditional probabilities for different statistical indices. The

synthesized probability of having a large earthquake in the jth time interval can be expressed by weights W_k for indices x^k as

$$P_{j1} = \sum_{k=1}^{6} W_k P_{k,j} . \tag{6}$$

We put a larger weight for a more effective index in the following way. We count a number of time-intervals when an index x^k gives the maximum $P_{k,j}$ among the six statistical indices. If the index x^k gives the maximum $P_{k,j} S_k$ times, its weight can be given by $W_k = S_k/n$. Here n is the total number of time intervals.

2.1.4. *Total probability for large earthquakes*

We have so far been concerned with a conditional probability based on a single statistical index. Instead of using Bayes' theorem to synthesize the conditional probabilities for different indices, we simply took a weighted mean of the different conditional probabilities, because some of the indices are not statistically independent. Since we neglected an effect of a combination of different statistical indices, we will take care of its possible effect by introducing another probability P_{j2}. Again by assuming a statistical independency, we define the total probability P_j, an indicator of an ocurrence of a large earthquake in the jth time interval, as a product of two probabilities.

$$P_j = P_{j1} P_{j2} . \tag{7}$$

The probability P_{j2} is defined by Q_j, the number of indices that give probabilities $P_{k,j}$ (defined by equation (5)) larger than their average value $\bar{P}_k = 1/n_q \sum_{j=1}^{n_q} P_{k,j}$ for time intervals without a large earthquake. Thus Q_j takes a value of 1, 2, 3, 4, 5 or 6. In a way similar to that used in deriving equation (3), we can derive a conditional probability of having a large earthquake in the jth time interval under condition that Q_j takes a value of h. If we only consider time intervals with $Q_j = h$ and denote by n_e^h and n_q^h, the numbers of time intervals with and without a large earthquake, respectively, then we can use equation (3) to obtain the probability P_{j2} for a case of $Q_j = h$. Thus we obtain:

$$P_{j2} = P(e|h).$$

2.1.5. *Critical probability*

Let us try to judge if a large earthquake will occur in the jth time interval on the basis of a value of P_j. We define a threshold P^* called a critical probability for this purpose. We shall judge that a large earthquake will occur when $P_j \geq P^*$ and that no large earthquake will occur when $P_j < P^*$.

In order to determine the critical probability P^*, we apply the following standards for judging the effect of earthquake prediction. The notations which will be used in the following are listed in Table 1.

Table 1

Symbols for seismicity statistics

Number of events		Predicted cases: Occurrence of event	Non-occurrence	Sum
Actual cases	Occurrence of event	n_e^p	n_e^f	n_e
	Non-occurrence	n_q^p	n_q^f	n_q
	Sum	n^p	n^f	n

(1) The precision standards R and K are measures of the accuracy of earthquake prediction.

$$R = 1 - n_e^f/n_e - n_q^p/n_q, \tag{8a}$$

$$K = 1 - [(n^p - n_e^p) + (n^f - n_q^f)]/n. \tag{8b}$$

(2) Precursor value $I(a,b)$ is a quantity of information obtained by the earthquake prediction:

$$I(a,b) = H(b) - H_a(b), \tag{9}$$

where $H(b)$ and $H_a(b)$ are entropy before and after the earthquake prediction, respectively. The maximum entropy indicates complete disorder as well known in statistical mechanics. Thus a decrease in entropy is associated with obtaining information.

$$H(b) = -P(n_e)\log P[n_e) - P(n_q)\log P(n_q),$$

$$H_a(b) = P(p)\,[-P(e|p)\log P(e|p) - P(q|p)\log P(q|p)]$$

$$+P(f)\,[-P(e|f)\log P(e|f) - P(q|f)\log P(q|f)],$$

$$P(e) = n_e/n, \qquad P(q) = n_q/n,$$

$$P(p) = n^p/n, \qquad P(e|p) = n_e^p/n^p, \qquad P(q|p) = n_q^p/n^p,$$

$$P(f) = n^f/n, \qquad P(e|f) = n_e^f/n^f, \qquad P(q|f) = n_q^f/n^f.$$

(3) We also introduce the information rate defined by:

$$g = I(a,b)/H(b). \tag{10}$$

We can determine a suitable critical probability P^* by maximizing these values of standards R, K, $I(a,b)$ and g.

2.2. *Examples*

Two examples of applying the proposed statistical method to regional seismicity data will be given in this section. First, we have studied earthquakes in the North section

(namely, the Yinchuan–Songpan section) of North–South Seismic Zone in China. This section is located between 32.8°N and 38.5°N and between 104°E and 106.5°E and trends NNE. We used an earthquake catalogue 'Earthquake of Gansu (1954–1979)' (SEISMOLOGICAL INSTITUTE OF LANZHOU, 1981). The unit time interval was taken as one month. By taking $M_0 = 2.6$ and $\Delta M = 0.5$, the statistics of six fundamental indices were obtained from the earthquake catalogue of the given section for a period from April 1970 to July 1979. We calculated the total probabilities of having an earthquake with magnitude 4.5 and above (i.e. $M_1 = 4.5$) for months from August, 1970 to August, 1979. The obtained weights for indices r, $\dot{r}$, N, $\dot{N}$, $M^{\max}$, and $\dot{M}^{\max}$ for the calculation of P_{1j} are 0.23, 0.07, 0.28, 0.14, 0.17, and 0.11, respectively.

The result is listed in Table 2 for different critical probabilities P^*. From Table 2 we determined a value of the critical probability as 0.4 to satisfy most of the standards, R, K, $I(a,b)$, and g. In this case, earthquakes with magnitude above the threshold occurred in 28 time intervals among 31 predicted intervals. Prediction of non-occurrence of moderate to large earthquakes are correct for 71 intervals among the predicted 77 intervals. The results may not be surprising because we used the whole time period to calculate P_j. For verification of the method it is necessary to split the whole time period into two intervals: learning and testing periods.

We also tried to evaluate seismic hazard for a 37 month testing period (August 1976–August 1979) on the basis of the data in a 76 month learning period (April 1970–July 1976). We used the same critical probability as before ($P^* = 0.4$). The result is shown in Fig. 1. We can correctly predict 5 months 'having $M \geq 4.5$ earthquake', approximately correctly predict 3 months 'having $M \geq 4.5$ earthquake' with delay in one month, and correctly predict 24 months 'without $M \geq 4.5$ earthquake'. For two months, we predict an occurrence of $M \geq 4.5$ earthquakes, but no moderate to large earthquakes occur. For another two months, prediction of occurrence of $M \geq 4.5$ earthquake is given neither in those months nor one month before, but $M = 4.5$ earthquakes occurred.

Table 2

Results of earthquake prediction in the North section (Yinchuan–Songpan) area of North–South Seismic Zone by the probabilistic method (total number of time intervals $n = 108$, number of intervals with magnitude 4.5 and above $n_e = 34$, number of intervals without earthquakes with magnitude 4.5 and above $n_q = 74$)

$\|^*$	n^p	n_e^p	n^f	n_q^f	K	R	$I(a, b)$	g
0.2	50	32	58	57	0.82	0.711	0.109	0.401
0.3	39	31	69	66	0.92	0.804	0.142	0.524
0.4	31	28	77	71	0.92	0.783	0.147	0.539
0.5	29	27	79	72	0.92	0.767	0.147	0.542
0.6	25	23	83	72	0.88	0.649	0.112	0.413
0.7	16	16	92	74	0.83	0.471	—	—
0.8	11	11	97	74	0.79	0.324	—	—

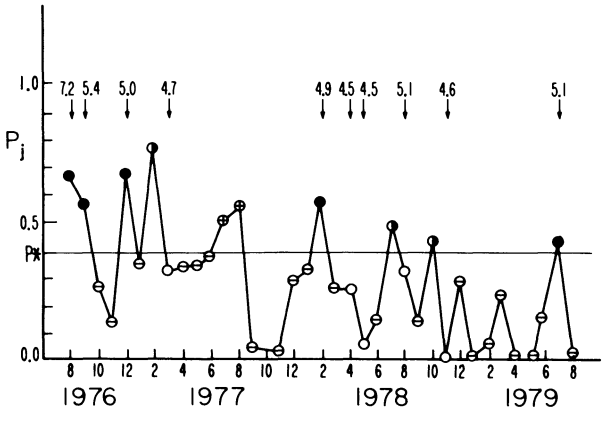

Figure 1

Results of earthquake prediction for the North section (Yinchuan-Songpan area) of North–South Seismic Zone by the probabilistic method. The closed circles and open circles with bar indicate correctly predicted intervals with and without earthquakes with magnitude 4.5 and above, respectively. The half-filled circles show approximately correctly predicted time intervals followed by an occurrence of earthquakes with a delay of one month. The open circles indicate incorrectly predicted intervals with earthquakes. The open circles with cross show incorrectly predicted intervals without earthquakes.

The second example is an attempt to predict earthquakes of $M \geq 7.0$ occurring in the Yunan and Sichuan provinces of Western China. Now the time interval is taken as one year. We used an earthquake catalogue in 1920–1976 (STATE SEISMOLOGICAL BUREAU, 1977). By taking $M_0 = 4.0$ and $\Delta M = 0.5$, we calculated the total probabilities of having $M \geq 7.0$ earthquake for years 1927–1976 (i.e. $n = 50$). The weights are calculated for six indices r, $\dot{r}$, N, $\dot{N}$, $M^{\max}$, and $\dot{M}^{\max}$ as 0.25, 0.10, 0.28, 0.3, 0.13, and 0.11, respectively. When we set $P^* = 0.1$, we get $K = 0.92$. Prediction of an occurrence of large earthquakes is made in 18 intervals. Large earthquakes occurred in 14 intervals and all are successfully predicted. Prediction of non-occurrence is made in 32 time intervals and all are correct. By using the same critical probability we attempted to predict an occurrence of large earthquakes in 1975–1977 on the basis of seismicity data in 1920–1974. The obtained prediction shows that large earthquakes occur in 1976 but that no large earthquake occurs in 1975 and 1977. This result is rather insensitive to the choice of the critical probability since the obtained total probabilities are 0.03, 0.67, and 0.00 for 1975, 1976 and 1977, respectively. This is in good agreement with the actual case: in 1976 the Longling ($M = 7.6$) and Songpan ($M = 7.2$) earthquakes occurred, but in 1975 and 1977 no large earthquake of $M \geq 7.0$ occurred.

3. *Retrieval method of fuzzy information for earthquake hazard assessment*

3.1. *Method*

In assessing earthquake hazard, a classification method for retrieving information based on the theory of fuzzy sets can be used following FENG *et al.* (1982). When a

series of small earthquakes occurs in some region, they are regarded as a series of information. They may reflect a probability of occurrence of an earthquake in the future time interval and also magnitude of the earthquake. We will use in the following sections four statistical indices, i.e. N, $\dot{N}$, $M^{\max}$, and $\dot{M}^{\max}$ of the six used in the previous section.

The essential part of this method is to classify each time interval into several classes with different seismic hazard according to the statistical indices of the previous intervals. We take these classes as fuzzy subsets and use so called membership functions for the classification of each time interval. We will first describe the retrieval method of fuzzy information in general and then discuss how to apply the method to earthquake prediction.

3.1.1. Fuzzy information retrieval

The information retrieval process can be considered as a matching process of inquiry with document. Every document is denoted by a group of independent descriptors and retrieval is made on the basis of these descriptors. If a batch of 'file storage' consists of n documents $D_1, D_2, \ldots, D_n$, and each document D_j is described by descriptors $x_j^1, \ldots, x_j^v$, then D_j can be represented by the following vector:

$$D_j = (z_j^1, z_j^2, \ldots, z_j^v)$$

where

$$z_j^k = \begin{cases} 1, \text{ when there is descriptor } x^k \text{ in } D_j \\ 0, \text{ otherwise.} \end{cases}$$

As a result, all documents may be characterized by a matrix of $n \times v$ rank. Usually number n is very large and the document retrieval through matrix $[z_j^k]_{n \times v}$ is very inefficient and actually impractical. Therefore, the fuzzy information retrieval may be applied usefully (LOU *et al.*, 1983).

Suppose that the documents D_j ($j = 1, \ldots, n$) can be classified into s classes according to their properties:

$$G_1, G_2, \ldots, G_s,$$

where each G_m may be taken as a fuzzy subset in the domain of $D_1, D_2, \ldots, D_n$. Let us assume that we can calculate the probability of occurrence of descriptor x^k in the mth class, P_{mk}, based on a preliminary classification of the documents. The probabilities P_{mk} ($m = 1, \ldots, s$; $k = 1, \ldots, v$) can be arranged in the following matrix:

$$M_1 = \begin{bmatrix} P_{11} & P_{12} & \ldots & P_{1v} \\ \ldots\ldots & \ldots\ldots & \ldots\ldots & \ldots\ldots \\ P_{s1} & P_{s2} & \ldots & P_{sv} \end{bmatrix}. \tag{11}$$

If the matrix M_1 is given, then the membership function of G_m can be obtained by the formula below:

$$y_j^m = y^m(z_j^1, \ldots, z_j^v) = \sum_{k=1}^{v} z_j^k P_{mk} \Big/ \sum_{k=1}^{v} z_j^k .$$

The membership function y_j^m indicates a possibility that document D_j belongs to class m. The relative values of membership functions of all n documents may be arranged in the following matrix:

$$M_2 = [y_j^m]_{n \times s} = \begin{bmatrix} y_1^1 & \cdots & y_1^s \\ \cdots\cdots & & \cdots\cdots \\ y_n^1 & \cdots & y_n^s \end{bmatrix}. \tag{12}$$

Some threshold is necessary to classify the documents by using the membership functions. Let us denote by L the threshold. Then the fuzzy set G_m can be obtained from the ordinary set of documents $\{D_j\}$ as follows:

$$G_m \{D_j | y_j^m \geq \mathrm{L}\} \ (m = 1, 2, \ldots, \mathrm{s}).$$

For the purpose of setting an appropriate threshold we introduce new fuzzy sets $R_{lm} = G_l \cap G_m (l \neq m;\ l, m = 1, 2, \ldots, s)$ formed from the given fuzzy sets $G_1, \ldots, G_s$. Their membership functions are defined as follows:

$$y_j^{lm} = y^{lm}(z_j^1, \ldots, z_j^v) = \min (y_j^l, y_j^m). \tag{13}$$

The corresponding matrix of membership functions is as follows:

$$M_3 = [y_j^{lm}] = \begin{bmatrix} y_1^{12} & \cdots & y_l^{s-1,s} \\ \cdots\cdots & & \\ y_n^{12} & \cdots & y_n^{s-1,s} \end{bmatrix}. \tag{14}$$

The matrix has C_m^2 columns and n rows, where C_m^2 indicates a number of combination of two classes among m classes. Because each document belongs to at least one class, we can get the following condition that the threshold L has to satisfy, with the help of matrix M_3:

$$L < \min_{lm} \max_{j} y_j^{lm}. \tag{15}$$

It is worth pointing out that each document is not definitely classified into only one class, but it can belong to several classes. This is in conformity with the principle of document storage.

3.1.2. Application to earthquake hazard assessment

We consider a unit time interval as a 'document' and take seismicity indices in a given time interval to be descriptors for describing its characteristics. Let us classify the time intervals into s classes G_m ($m = 1, 2, \ldots, s$). For example, the intervals may be classified according to the maximum magnitude of earthquakes, the location of the largest event, and so on.

In a way similar to that discussed in Section 2, we will try to make a prediction at any time interval based on the statistical indices of three previous time intervals. We will use the following 12 indices, N_{j-i}, $\dot{N}_{j-i}$, $M_{j-i}^{\max}$, and $\dot{M}_{j-i}^{\max}$ $(i = 1, 2, 3)$ for the prediction of the jth time interval. Let n_e be the number of the time intervals with earthquakes of the mth class and n_q be the number of intervals without earthquakes of the mth class. Under condition that a value of the kth index x_{j-i}^k in the $j - i$th time interval lies in interval Δx_h^k, let n_e^h times the jth time interval has earthquakes of the mth class and n_q^h times no earthquake of the mth class. Then from equations (2) and (3), we can get a conditional probability of occurrence of earthquakes of the mth class under condition that index x^k has a value within interval Δx_h^k. Further from equation (5) we can obtain a synthesized probability of occurrence of earthquakes of the mth class in the jth time interval estimated from the kth index (descriptor x^k) as follows:

$$P_{kj}^m = P(e_m) \prod_{i=1}^{3} P(e_m|h_{j-i}^k) \Big/ \left[P(e_m) \prod_{i=1}^{3} P(e_m|h_{j-i}^k) + P(q_m) \prod_{i=1}^{3} P(q_m|h_{j-i}^k) \right], \quad (16)$$

where symbols 'e_m' and 'q_m' denote the cases with and without earthquakes of the mth class, respectively. We will use these synthesized probabilities P_{kj}^m $(k = 1, 2, 3, \text{and } 4)$ as parameters describing the jth time interval. Each time interval D_j can be represented by the following matrix:

$$D_j = [P_{k,j}^m]_{s \times 4}.$$

If we determine weights W_k^m for the different statistical indices in a way similar to that used in deriving equation (6), the membership function of G_m-class can be defined by

$$y_j^m = \begin{cases} W_k^m P_{kj}^m & \text{when } W_k^m P_{kj}^m \leq 1, \\ 1 & \text{otherwise}. \end{cases} \quad (17)$$

Once the membership functions are determined, matrices M_2 and M_3 can be obtained from equations (12) and (13) and the classification of the time intervals into s classes is straightforward.

3.2. Examples

Two examples of evaluating the earthquake hazard in the North section of North–South Seismic Zone in China will be shown in this section. First, we attempted to estimate roughly a location of a large event on the basis of seismicity data of a whole region in relatively long time intervals. We tried to classify the seismicity in each year into three classes, G_1: $M \sim 7$ earthquakes occurring in the north region (Gansu and Ninxia provinces), G_2: $M \sim 7$ earthquakes occurring in the south region, i.e. the northern part of Sichuan province (an area north of 30°N), and G_3: non-occurrence of $M \sim 7$ earthquakes in both regions. We choose ten-year time windows for calculation of the following statistical indices: the total number of earthquakes N, the difference of the

total numbers between two adjacent time windows $\dot{N}$, an average of the maximum magnitude of earthquakes in each year $\overline{M^{\max}}$, and the difference in $\overline{M^{\max}}$ of the two adjacent time windows $\overline{M^{\max}}$. These indices are calculated by displacing the time window year by year for the data of earthquakes of magnitude $M \geq 4.0$ for 1923 to 1980. We calculated $P^m_{j,k}$ and W^m_k based on all the data except for that in 1981. The matrices M_2 and M_3 are calculated as follows.

$M_2 =$

G_1	G_2	G_3
0.31	0.38	0.69
0.27	0.40	0.73
0.61	0.40	0.60
0.38	0.00	1.00
0.55	0.00	1.00
0.49	0.38	0.62
0.21	0.38	0.79
0.52	0.37	0.63
0.47	0.37	0.63
0.67	0.38	0.62
0.30	0.38	0.70
0.38	0.40	0.60
0.38	0.40	0.62
0.38	0.10	1.00
0.48	0.40	0.60
0.43	0.38	0.62
0.34	0.22	0.78
0.49	0.40	0.60
0.47	0.00	1.00
0.55	0.00	1.00
0.79	0.40	0.60
0.30	0.38	0.70
0.93	0.07	0.93
0.29	0.34	0.71
0.32	0.22	0.78
0.19	0.32	0.81
0.22	0.80	0.78
0.23	0.26	0.77
0.36	0.13	0.87
0.08	0.04	0.96
0.09	0.21	0.91
0.14	0.30	0.70

$M_3 =$

G_{12}	G_{13}	G_{23}	Years
0.31	0.31	0.38	1934
0.27	0.27	0.40	1935
0.40	0.60	0.40	1936
0.00	0.38	0.00	1937
0.00	0.55	0.00	1938
0.38	0.49	0.38	1939
0.21	0.21	0.38	1940
0.37	0.52	0.37	1941
0.37	0.47	0.37	1942
0.38	0.62	0.38	1943
0.30	0.30	0.38	1944
0.38	0.38	0.40	1945
0.38	0.38	0.40	1946
0.10	0.38	0.10	1947
0.40	0.48	0.40	1948
0.38	0.43	0.38	1949
0.22	0.34	0.22	1950
0.40	0.49	0.40	1951
0.00	0.47	0.00	1952
0.00	0.55	0.00	1953
0.40	0.60	0.40	1954
0.30	0.30	0.38	1955
0.07	0.93	0.07	1956
0.29	0.29	0.34	1957
0.22	0.32	0.22	1958
0.19	0.18	0.32	1959
0.22	0.22	0.78	1960
0.23	0.23	0.26	1961
0.13	0.36	0.13	1962
0.04	0.08	0.04	1963
0.09	0.09	0.21	1964
0.14	0.14	0.30	1965

0.37	0.37	0.63	0.37	0.37	0.37	1966
0.42	0.74	0.58	0.42	0.42	0.58	1967
0.28	0.23	0.77	0.23	0.28	0.23	1968
0.28	0.23	0.77	0.23	0.28	0.23	1969
0.20	0.27	0.80	0.20	0.20	0.27	1970
0.20	0.67	0.80	0.20	0.20	0.67	1971
0.20	0.23	0.80	0.20	0.20	0.23	1972
0.25	0.78	0.75	0.25	0.25	0.75	1973
0.16	0.43	0.84	0.16	0.16	0.43	1974
0.49	0.59	0.61	0.49	0.49	0.59	1975
0.36	0.46	0.64	0.36	0.36	0.46	1976
0.14	0.29	0.86	0.14	0.14	0.29	1977
0.18	0.50	0.82	0.18	0.18	0.50	1978
0.17	0.26	0.83	0.17	0.17	0.26	1979
0.17	0.49	0.83	0.17	0.17	0.48	1980
0.29	0.76	0.71	0.29	0.29	0.71	1981

Maximum values in columns for G_{12}, G_{13}, and G_{23} in matrix M_3 are 0.49, 0.93, and 0.78, respectively. Accordingly the threshold value L should be taken smaller than 0.49 in this case; we took $L = 0.48$. The retrieval prediction shows fairly good agreement with actual seismicity as shown in Table 3. Only two exceptions are obtained; years 1943 and 1976 are erroneously classified to G_1 and G_3 respectively. The result for 1981 is based on the data in intervals 1969–1978, 1970–1979, and 1971–1980 which are not included in determining $P^m_{k,j}$ and W^m_k, but it agrees with actual activity. That is, an earthquake of magnitude 6.9 occurred in Luhao, located in the south region, on 24 January 1981.

For the second example, we used the same data set as was used for the probabilistic method in the North (Yinchuan–Songpan) section of North–South Seismic Zone in China. The unit time interval is taken as one month and all the $M \geq 2.6$ earthquakes are used. In this case we calculated statistical indices N, $\dot{N}$, $M^{\max}$, and $\dot{M}^{\max}$ for months from

Table 3

Comparison between the predicted (fuzzy retrieved) seismic risk and actual seismicity for M 7 earthquakes

Class of seismicity	Retrieved and predicted years	Years of actual occurrence
G_1 North region	1936, 1943, 1954, 1956	1936, 1954, 1956
G_2 South region	1960, 1967, 1973, 1981	1960, 1967, 1973, 1976, 1981
G_3 Non-occurrence	1934, 1935, 1937–1942, 1943–1953, 1955, 1957, 1958, 1959, 1961–1966, 1968–1972, 1974–1980	1934, 1935, 1937–1953, 1955, 1957–1959, 1961–1966, 1968–1972, 1974, 1975, 1977–1980

January 1966 to December 1980. The time intervals are classified into five classes G_1, G_2, G_3, G_4, and G_5 corresponding to the ranges of the maximum magnitude $M^{max} < 4.0$, $M^{max} = 4.0$–4.9, $M^{max} = 5.0$–5.9, $M^{max} = 6.0$–6.9, and $M^{max} \geq 7.0$, respectively. The results are too numerous to show all here. We only show the results for 1976 and those for January 1981. We choose the year 1976 since an $M = 7.2$ earthquake occurred in August. Also the result for January 1981 is based on the data which is not used to calculate $P^m_{k,j}$ and W^m_k. The matrices M_2 and M_3 for January–December 1976 and January 1981 are obtained as follows:

$M_2 =$

G_2	G_3	G_4	G_5	G_1
0.300	0.130	0.072	0.077	0.700
0.523	0.376	0.049	0.127	0.477
0.461	0.294	0.013	0.088	0.539
0.325	0.247	0.049	0.113	0.675
0.497	0.197	0.063	0.018	0.502
0.461	0.183	0.055	0.000	0.539
0.400	0.238	0.040	0.000	0.600
0.244	0.315	0.149	0.547	0.756
0.509	0.722	0.210	0.000	0.491
0.499	0.187	0.036	0.048	0.551
0.600	0.408	0.160	0.053	0.400
0.394	0.484	0.135	0.195	0.606
0.474	0.208	0.122	0.150	0.526

$M_3 =$

G_{23}	G_{21}	G_{31}	Month
0.130	0.300	0.130	Jan
0.376	0.477	0.376	Feb
0.294	0.461	0.294	Mar
0.183	0.461	0.183	Apr
0.197	0.497	0.197	May
0.183	0.461	0.183	Jun
0.238	0.400	0.238	Jul
0.244	0.244	0.315	Aug
0.509	0.491	0.491	Sep
0.187	0.449	0.187	Oct
0.408	0.400	0.400	Nov
0.394	0.394	0.484	Dec 1976
0.208	0.474	0.280	Jan 1981

Since all the elements in columns corresponding to G_4 and G_5 are smaller than those for G_3 and G_1, respectively, it is necessary to consider only the elements corresponding to G_{23}, G_{21}, and G_{31}.

From M_3 we can find the maximum values for columns G_{23}, G_{21}, and G_{31} are 0.509, 0.497, and 0.491, respectively. Therefore we should assume a threshold value L smaller than 0.491. Taking $L = 0.484$, we can classify 13 time intervals into five classes according to the element of M_2. If some time interval has two or more elements larger than L, it is classified into the class with the maximum earthquake magnitude. The results are shown in Table 4. The predicted earthquake risks are in good agreement with the actual cases. An earthquake of $M = 4.0$–4.9 is predicted in May, 1976, but it occurred in June, with a delay of one time interval.

Table 4

Comparison between predicted seismic risk and actual seismicity for Songpan–Yinchuan section, China

Class of earthquakes	Retrieved and predicted months	Months of actual earthquake occurrence
G_2 $M = 4.0$–4.9	February, May, November in 1976	February, June, November in 1976
G_3 $M = 5.0$–5.9	September, December in 1976	September, December in 1976
G_4 $M = 6.0$–6.9	None	None
G_5 $M \geq 7.0$	August in 1976	August in 1976
G_1 $M < 4.0$	January, March, April, June, July, October in 1976 and January in 1981	January, March, April, May, July, October in 1976 and January in 1981

4. Discussion

Figure 2 gives a comparison between the statistical method and the method of fuzzy mathematics in earthquake hazard assessment described above. We can see that both methods may be simultaneously applied to a given region by using the same statistical indices of regional seismicity. The statistical indices and the number of time intervals used for predicting earthquakes can be chosen arbitrarily. If these indices and the number of intervals are chosen appropriately, both methods can be useful and effective in seismic hazard evaluation and in earthquake prediction. In general, the retrieval method of fuzzy information has several advantages. It allows earthquake risks to be divided into several classes; also, a large number of statistical indices are unnecessary.

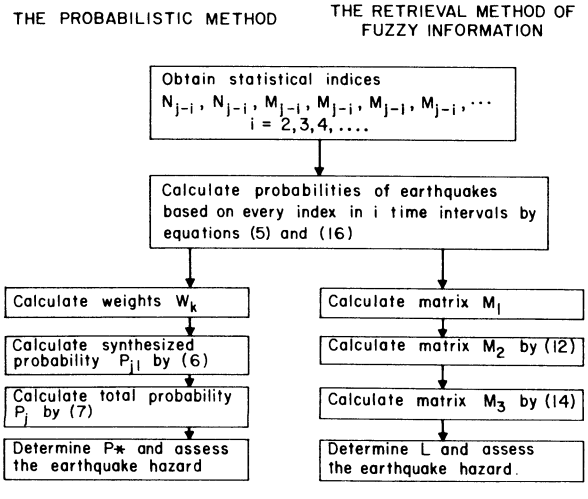

Figure 2
Flow chart for earthquake prediction by the two proposed methods.

The present results suggest that the simultaneous application of the fuzzy mathematics method and the statistical method in earthquake hazard assessment and earthquake prediction has promise. Moreover, fuzzy mathematics may also be useful for prediction-oriented studies. For example, fuzzy clustering analysis, fuzzy similarity, and fuzzy multifactorial evaluation have been investigated by using statistical indices of seismicity and observational data of precursors such as crustal deformation, radon content in underground water, and earth resistivity (FENG *et al.*, 1983).

Acknowledgment

The authors are grateful to Dr Kunihiko Shimazaki for his encouragement in this study and helpful suggestions in reviewing the manuscript.

REFERENCES

AKI, K. (1965), *Maximum Likelihood Estimate of b in the Formula* log $N = a - bM$ *and its Confidence Limits*, Bull. Earthq. Res. Inst., Tokyo Univ. *43*, 237–239.

AKI, K. (1981), *A Probabilistic Synthesis of Precursory Phenomena*, Maurice Ewing Ser. *4*, 566–574.

DUBOIS, D., and PRADE, H., *Fuzzy Sets and Systems: Theory and Application* (Academic Press, New York 1980).

FENG, DE-YI, GU, JING-PING, LUOO, RUI-MING, and SHENG, GUO-YING, (1981), *The Statistical Indices of Seismicity and the Probability Prediction for the Time of Earthquake Occurrence* (in Chinese), J. Seismol. Res. *4*, 1–9.

FENG, DE-YI, GU, JING-PING, ZHONG, TING-JIAO, LIN, MING-ZHOU, LOU, SHI-BO, and CHEN, HUA-CHENG, (1982), *The Application of Retrieval Method of Fuzzy Information in Earthquake Prediction Based on Seismic Activity* (in Chinese), Earthquakes *5*, 11–13.

FENG, DE-YI, LOU, SHI-BO, LIN, MING-ZHOU, CHEN, HUA-CHENG, GU, JING-PING, and ZHONG, TING-JIAO, *The Methods of Fuzzy Mathematics and their Applications* (in Chinese) (Seismological Press 1983).

GUPTA, M. M., SARIDIS, G. N. and GAINES, B. R. (editors), *Fuzzy Automata and Decision Processes* (North-Holland, New York 1977).

KAUFMANN, A., *Introduction to Theory of Fuzzy Subsets* (Academic Press, New York 1971).

LUO, SHI-BO, FENG, DE-YI, CHEN, HUA-CHENG, GU, JING-PING, YU, XUE-JUN, YU, MING-ZHOU, and ZHONG, TING-JIAO, (1983), *The Application of Retrieval Method of Fuzzy Information in Earthquake Prediction Researches* (in Chinese), Fuzzy Mathematics *1*, 113–120.

SEISMOLOGICAL INSTITUTE OF LANZHOU, *Earthquakes in Gansu (1954–1979)* (Seismological Institute of Lanzhou, State Seismological Bureau 1981).

STATE SEISMOLOGICAL BUREAU, *A Summary of Seismological Catalogue of China* (Seismological Press 1977).

UTSU, T. (1965), *A Method for Determining the Value of b in a Formula* log $n = a - bm$ *Showing the Magnitude–Frequency Relation for Earthquakes* (in Japanese), Geophys. Bull., Hokkaido Univ. *13*, 99–103.

UTSU, T. (1977), *Probabilities in Earthquake Prediction* (in Japanese), J. Seismol. Soc. Japan *30*, 179–185.

WANG, P. P., and CHANG, S. K., *Fuzzy Sets: Theory and Applications Policy Analysis and Information Systems* (Plenum Press, New York 1980).

ZADEH, L. A. (1965), *Fuzzy Sets*, Inf. Control *8*, 338–353.

(Received 29th October 1983)

PAGEOPH, Vol. 122 (1984/85)

Acknowledgement

The geophysical community and the Editorial Board of Pure and Applied Geophysics (PAGEOPH) are grateful for the time and effort offered by the scientists listed below who have reviewed papers submitted to vol. 122, N. 1–6, 1984/85.

KEIITI AKI, Editor-in-Chief
RENATA DMOWSKA, Executive Editor

KATSUYUKI ABE
D. J. ANDREWS
MASATAKA ANDO
WILLIAM BAKUN
ENRIQUE E. BANDA
I. BARNES
JOHN BEAVAN
ANTHONY BEDFORD
ARI BEN-MENAHEM
JAMES G. BERRYMAN
ROGER BILHAM
BRUCE A. BOLT
M. G. BONILLA
J. D. BREDEHOEFT
J. D. BYERLEE
Y. CHUNG
STEVEN COHEN
SHAMITA DAS
SUBHENDU K. DATTA
PAUL DAVIS
P. DELANEY
ERNST R. DEUTSCH
RANDALL M. DOLE
A. C. ERINGEN
J. H. FETH
DAVID V. FITTERMAN
ROBERT L. FLEISHER
GLENN R. FLIERL
YOSHIO FUKAO
ROLANDO GARCIA
MICHAEL GLADWIN
VALERIE M. GODLEY
YOZO HAMANO
J. W. HANDIN
RICHARD O. HANSEN
J. W. HARDEN
AKIRA HASEGAWA
THOMAS HEATON
THOMAS L. HENYEY
YOSHIMORI HONKURA
GREGORY A. HOUSEMAN
YOSHIAKI IDA
BRIAN ISACKS
DAVID JACKSON
JERZY JANKOWSKI
MALCOLM JOHNSTON
LUCILE JONES
YAN Y. KAGAN
MASARU KAIZU
HIROO KANAMORI
ROBERT KARLIN
TERUYUKI KATO
BRIAN L. N. KENNETT
CHI-YU KING
ANNE S. KIREMIDJIAN
R. W. KLUSMAN
J. KORRINGA
JUNJI KOYAMA
KEI KURITA
D. L. LAMAR
P. J. LAMOTHE
JOHN LATHAM
THORNE LAY
PETER C. LEARY
VICTOR C. LI
J. G. LIOU
DAVID A. LOCKNER
STEVEN P. LUND
THEODORE MADDEN
MITSUHIRO MATSU'URA
GARY M. MAVKO
DENNIS D. McCARTHY
MARCIA K. McNUTT
P. M. MERIFIELD
KAORU MIYASHITA
TAKASHI MIYATAKE
HITOSHI MIZUTANI
KIYOO MOGI
A. MOGRO-CAMPERO
PETER MOLNAR
H. F. MORRISON

R. J. MUNROE
J. NOORISHAD
MITIYASU OHNAKA
MASAKAZU OHTAKE
NAOTO OSHIMAN
ROBERT L. PARKER
WILLIAM PRESCOTT
GEORGE PURCARU
G. M. REIMER
JAMES R. RICE
PAUL G. RICHARDS
RAYMOND ROBLE
S. A. ROJSTACZER
BARBARA ROMANOWICZ
JOHN W. RUDNICKI
ANDY RUINA
KACPER RYBICKI
JAMES C. SAVAGE
TETSUZO SENO
M. H. SHAPIRO
KUNIHIKO SHIMAZAKI
DAVID SIMPSON
W. F. SLAWSON
A. R. SMITH
L. SMITH
SEAN C. SOLOMON
ANNIE SOURIAU
JOHN M. STANLEY
WILLIAM D. STUART
R. SUGISAKI
TAKASHI TADA
PRADEEP TALWANI
A. B. TANNER
T. TENG
SIMON T. TSE
T. C. URBAN
TOKUJI UTSU
ROB VAN DER VOO
HIROSHI WAKITA
C. WANG
R. H. WARE
M. H. WILKENING
H. A. WOLLENBERG
TENG-FONG WONG
F. T. WU
KEN'ICHIRO YAMASHINA
TAKESI YUKUTAKE